Computer simulation of heteroepitaxial oxide/oxide and metal/oxide interfaces

Sayle, D. C.

Award date:
1992

Awarding institution:
University of Bath

Computer Simulation Of Heteroepitaxial Oxide / Oxide and Metal / Oxide Interfaces

Submitted by D.C. Sayle for the degree of PhD at the University of Bath 1992

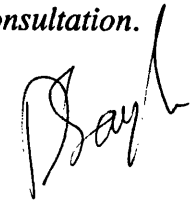

ProQuest LLC
789 East Eisenhower Parkway
P.O. Box 1346
Ann Arbor, MI 48106-1346

Abstract

In this thesis we have developed a procedure which can be routinely employed to investigate the interface between two dissimilar oxide materials at the atomic level using computer simulation techniques. This method has yielded good quantitative information about the interfacial stability, structure and mechanisms by which the interface is stabilised or destabilised.

Chapter 1 provides an introduction to the current state of experimental and theoretical techniques which have been employed to study heteroepitaxial interface systems. Chapters 2 and 3 outline the potential models and theoretical methods employed in this thesis.

The remainder of the thesis presents calculated results. In chapter 4, the BaO//MgO interface is exploited as a model system representative of a heteroepitaxial interface. We employ this simple system to investigate factors deemed either deleterious or conducive to the stability of the interface such as the accommodation of the incommensuration between the lattice parameters of the two materials, the effect of charged defects and reduced ion densities at the interface region. Finally we investigate the formation of thin BaO films on the MgO substrate. In chapter 5 the range of materials investigated is extended to include the perovskites $BaTiO_3$ and $SrTiO_3$.

The application of a Near Coincidence Site Lattice theory is employed in chapter 6, to identify new interface configurations with low associated misfits between any two oxide materials. The results of the simulation are in excellent agreement with experimental observations in predicting the occupancy levels of MgO twist grain boundaries. In chapter 7 we address interfaces between MgO and the high T_c superconductor $YBa_2Cu_3O_{6.5}$, to ascertain the effect an interface may have on the superconducting properties.

Finally in chapter 8 we focus our attentions on the metal - oxide interface. We employ a classical image charge approach to describe the long range attractive interactions between the oxide and the metal and include a cutoff into the potential to effectively screen the image terms. We employ this modified image interaction to model the Au(100)//MgO(100), Au(110)//MgO(110) and Au(111)//MgO(111) interfaces. The calculated contact angle of 126° is in good agreement with the experimentally measured value of 139° for the Ag//MgO interface.

Acknowledgements

First, I would like to thank my supervisor Dr. S.C. Parker for his help and encouragement throughout the course of this work.

Next I would like to thank my CASE supervisor, Dr. J.H. Harding for his help in assembling this thesis and thought provoking discussions.

I am grateful to the Science and Engineering Research Council and the United Kingdom Atomic Energy Authority for financial support and provision of computer time. Also I am grateful to Biosym Technologies Ltd. for the provision of the Insight II software.

The contributions of my friends and colleagues are numerous and gratefully acknowledged. I would specially like to thank Alison, Mark, Philip, Toby, Pete, Graeme and Nick.

Finally I would like to thank my parents for financial assistance.

Cho người vợ yêu quí của tôi

To My Parents

Contents

Chapter 1

Introduction

1.1 Introduction

Surfaces and interfaces dominate many of the technologically important processes in solid materials, such as catalysis, thin film superconducting devices, and oxidation. Atomistic modelling of oxide materials has made a significant contribution to the understanding of the structure and properties of surfaces and interfaces (Davies et al. 1989, Kenway 1991 and Titiloye et al. 1991) and may ultimately assist the design and fabrication of many device applications including thin film superconductors and elucidate catalytic processes and oxidation mechanisms such that they may be enhanced (catalysts) or inhibited (corrosion).

The majority of interface calculations have so far been limited to surfaces or internal interfaces within a single material with only two exceptions (Tasker and Stoneham 1987, Cotter et al. 1988). The interface between an oxide and a metal however has attracted more attention and several workers have addressed the problem using simulation techniques (Duffy et al. 1992, Finnis 1991, Blochl et al. 1989 and Freeman et al. 1989). However, because of the complex nature of the interactions between the oxide and the metal, progress has been hampered by the lack of suitable potentials.

The limited number of calculations on heteroepitaxial systems, together with their fundamental importance in many technologically important areas has therefore inspired an investigation into the modelling of these interfaces using atomistic simulation.

The aim of this thesis is to develop the methodology for modelling heteroepitaxial oxide interfaces, at the atomic level, which will enable future workers to routinely model interface systems between two dissimilar oxide materials and ultimately assist in the

design of commercially viable products.

To achieve this aim, the BaO//MgO interface is employed in this thesis as a model system representative of an incommensurate heteroepitaxial interface, to elucidate the factors which contribute to the stability or instability of a interface system.

The major problem one must first address when modelling heteroepitaxial interface systems is the accommodation of the incommensurate relationship between the lattice parameters of the two oxide materials. The resulting misfit between the two materials must be removed to ensure the periodic boundary conditions imposed by the simulation are satisfied by ensuring the primitive unit cells in adjacent cells are commensurate. Furthermore the size of the primitive unit cell must be small enough such that it can be suitably accommodated within the current computational resources available. This can be achieved by a compression or expansion of one or both of the materials to be interfaced which inevitably introduces an instability into the system. Nature however has the advantage of a near infinite unit cell and the incommensuration therefore poses no technical problem. However, experimental observations have shown that the primitive unit cell is not infinite as other factors such as relaxation, defect concentrations and dislocations are also known to contribute to the interfacial structure and ensure high periodicity (small primitive unit cell size) in heteroepitaxial interfaces.

A second objective of this thesis is to consider the metal-oxide interface. The primary focus of this work is to address the major component of the adhesive interaction across the interface. It has been verified by Stoneham and Tasker (1986) that one of the dominant terms in the adhesion arises from the Coulombic interaction of the oxide ions with their images in the metal. This is a classical electrostatic description to model the interactions of ions neighbouring a dielectric discontinuity. We have therefore employed

classical image charge theory to model the long range interactions across the metal - oxide interface.

1.2 Recent Developments

1.1.2 Experimental Interfaces

As many technologically important processes are dominated by the existence of a surface or interface it is perhaps not surprising that the literature on interfaces is extensive, indeed many journals are dedicated entirely to the physics and chemistry of surfaces and interfaces. Furthermore with the advent of high temperature superconductivity and their device applications, a review on the current state of interface technology would be impractical. This section is therefore considers recent work of direct relevance to the simulation work performed in this thesis.

One of the most important interface substrates is MgO which has enjoyed much attention, with workers focusing on both its surface and interface properties. The relaxation of the (100) surface has been probed by techniques such as low energy electron diffraction (LEED) (Welton-Cook and Berndt 1982), reflection high energy electron diffraction(RHEED) (Makasym 1985) , helium diffraction (Reider 1982) and more recently extended energy loss fine structure (EELFS) (Santoni et al. 1988). The results obtained for the relaxation and rumpling of the MgO surface by these various techniques varies by as much as 20%. This discrepancy has been suggested by Duriez et al. (1990) to be a consequence of sample preparation. This must ultimately affect the characteristics of the interface if the surface is to be used, for example, as a substrate for a superconducting thin film device and thus may affect the device performance. This will obviously affect any comparisons made between the experimentally observed interfaces and the calculated interface structures, where the starting point is a perfect MgO(100) surface with no relaxation or rumpling. However these experimental

observations suggest that the starting configuration for the MgO substrate for our calculations should exhibit the experimentally observed relaxation and rumpling. Work by Moeckly et al. (1990) showed that thermal annealing of the MgO substrate results in surface steps on the substrate which favours cube on cube epitaxy of the $YBa_2Cu_3O_{7-x}$ grains with the c-axis of $YBa_2Cu_3O_{7-x}$ normal to the substrate. Furthermore the large associated misfit (8-10%), as a result of the cube on cube epitaxy, must be accommodated. This is achieved by the formation of a polycrystalline, mosaic structure including a periodic array of dislocations at the interface. This work therefore shows that the preparation of the substrate surface affects not only the epitaxial relationships between the substrate and overlayer but also the defect chemistry and structural configuration of the overlaying material near the interface region.

A further point to consider when creating a thin film interface are the various processing techniques available to deposit the overlayer. Various deposition methods have been employed to create superconducting thin films (Kramer et al. 1988, Kwo et al. 1987, Ravi et al. 1990, Tong Lee et al. 1989) and must control the quality of the thin film and ultimately the effectiveness of the application for which it is intended. Furthermore, the conditions of sample preparation are critical to the quality of the film formed by the particular deposition method. Work of Chang et al. (1990) showed that superconducting $YBa_2Cu_3O_{7-x}$ thin film growth on $SrTiO_3$ by pulsed laser deposition led to the film surface to be rough, a smooth surface was achieved by choosing a suitable substrate temperature and deposition rate such that the coalescence is just completed at the final film thickness.

The next stage after preparation of the interface is the characterisation; such as the structural features of the interface. LEED has been used by Cotter et al. (1988) to identify the arrangements of the atoms of the overlaying material on the substrate and

XPS to quantify the coverage of the overlayer. Experimental results such as these are valuable in ascertaining the interfacial structural configuration to enable comparisons to be made with our calculated interfacial structural configurations. For high T_c superconducting materials, high resolution imaging is perhaps one of the most powerful techniques for elucidating the interface structure since the average separation of heavy atom columns along the most relevant crystal zones is larger than the resolving power of present day microscopes ($\approx$ 1.7Å). A recent review, summarising the viability of electron microscopy and electron diffraction techniques as applied to high T_c-superconducting materials, is given by Amelinckx et al. (1991). Furthermore electron microscopy is superior to most other techniques when "local" rather than "average" information is required.

In summary the characteristics of the superconducting thin film is dependent on substrate preparation, thin film deposition method and deposition conditions. Atomistic simulation can aid the experimentalists in providing details of the interface at the atomic level of effect substrate has on the interface for example epitaxial constraints and the accommodation of misfit. In addition, the effect of defects and reduced ionic density at the interface can be simulated and will therefore provide a notable complement to the experimental results. The next section gives a brief description of the current state of static lattice simulation in relation to surface or interfaces.

1.1.3 Lattice simulation

The last twenty years has seen considerable growth in the use of computer simulation methods to model the properties of condensed matter. Initially Norgett and Lidiard (1968) showed that atomistic simulation could be reliably employed to calculate the bulk defect properties of alkaline earth halides. More recently simulation has been used to study multicomponent systems including the ceramic superconductors (Islam and

Ananthamohan 1991).

Most energy minimisation simulations neglect the vibrational contribution by considering only the lattice energy and hence predict crystal properties at 0K. Calculations at elevated temperatures however have been facilitated by Parker and Price (1988) who developed a computer code based on lattice statics and dynamics to calculate the solid state phase diagrams of minerals (Price et. al. 1987). The inclusion of temperature effects has also led to some interesting and perhaps surprising observations for example some zeolites are predicted (Tschaufeser 1992) to contract on heating and this has recently been confirmed by experiment (Tschaufeser private communication).

Time is not included in static simulation and hence each atomistic simulation will determine only one local energy minima. A major advantage however is the use of sophisticated potentials.

An alternative technique is Molecular Dynamics or MD (Rahman 1979) which provides detailed dynamical information. MD was initially developed in the 1950's to study liquids (Alder and Wainwright 1959) but is ideally suited to study superionic conductivity within ionic crystals (Gillan 1985, Watson et. al. 1992). The simulation of diffusion (Pickett et. al. 1990, Catlow et. al. 1991) requires many steps to be statistically significant thus MD requires much cpu time. The vast majority of molecular dynamics studies have omitted the effects of polarisability, which in many cases might reduce the reliability of the predictions of the simulations.

The development of surface codes (Tasker 1978, Duffy and Tasker 1983a) has lead to a clearer understanding of the atomic processes that occur at surfaces and interfaces of

inorganic solids. These codes have been employed to investigate the structure, stability of, and atom transport along tilt grain boundaries (Duffy and Tasker 1982, Duffy 1983b) which have obvious implications to corrosion (Atkinson and Taylor 1979, Atkinson and Taylor 1986) due to enhanced diffusion along the grain boundaries.

More recently much effort has been directed towards modelling the metal - oxide interface. Duffy et al. (1992) have employed modified classical image interactions to describe the long range attractive contribution to the interfacial energy. The image terms are modified by suppressing fluctuations of the induced image charge density which have wavelengths greater than the Fermi wavevector and thereby eliminating the singularities that have plagued classical image models (Duffy et al. 1992). A similar approach is taken by Finnis (1991, 1992) which is also based on image theory. In this work the metal is modelled as a discrete lattice of polarisable spheres which are constrained to be equipotential. Such a model, known as the Discrete Classical Model, automatically introduces the crystal structure and eliminates the divergence which arises in the classical model. An alternative approach to modelling the metal - oxide interface is by calculating the electronic properties of the metal - oxide interface using Local Density Approximation techniques (Blochl et al. 1989, Freeman et al. 1989, Schonberger and Andersen, 1992). Such calculations provide information about the energy and adhesion of the boundary, however they require substantial computational resources.

Chapter 2

Potential Models

2.1 Introduction

The success of any calculation on a perfect or defective crystal surface or interface is critically dependent on the potential model that describes the interatomic interactions in the crystal. Indeed, the greatest uncertainties in the numerical results are often due to the potential model, rather than problems with the simulations itself. It would therefore seem appropriate to consider a sophisticated quantum simulation as a theoretical treatment of heteroepitaxial interfaces, such as the Car-Parrinello approach (Car and Parrinello 1985) which has enabled researchers to calculate the structures of semiconductor interfaces (Payne et al. 1987, Needels et al. 1987) without defining a potential model. This method is not however applicable to the study of heteroepitaxial interface systems mainly because the simulation of such systems requires an extensive unit cell to be treated explicitly and the computational requirement of a full quantum mechanical treatment of such systems is prohibitively large. Consequently the classical approach, namely atomistic simulation, was employed, in which the Born model (Born, 1954) of ionic solids is used to describe the interactions between ions.

2.2 Potentials

The starting point for any atomistic simulation is the identification of a suitable potential function which will enable the energy of a perfect crystal to be calculated. There is no problem in principle in defining a potential; if an energy surface exists, an algorithm that approximates it constitutes the potential. The interatomic potential, Ψ, for a system of n particles, describes the ground state energy of a solid as a function of the nuclear coordinates r_i to r_n.

$$\Psi = \Psi(r_i....r_n) \qquad (2.1)$$

This can be broken down into a series of summations;

$$\Psi(r_i....r_n) = \Psi_o + \sum_{i,j=1}^{N} \Psi_1 (|r_i - r_n|) + \sum_{i,j,k=1}^{N} \Psi_2 (r_i,r_j,r_k) + ...$$

$$+ \sum_{(i...n)=1}^{N} \Psi_n (r_i.....r_n) \qquad (2.2)$$

The first term, Ψ_o, represents the energies required to create the ions in the electronic configuration it has in the crystal and is therefore a function of the local environment. The environmental dependence of the first term is ignored and so it merely defines the energy zero. The second term refers to a sum over all pairs of atoms, the third over all triplets, with the summation continuing, in principle at least, up to 'n-body' terms. Additions of equivalent terms (e.g. ij and ji) are avoided.

The majority of simulations, including the work in this thesis, approximates Ψ to include contributions only from the pair potential terms, which can be decomposed as follows;

$$\sum_{i,j=1}^{N} \Psi_1 (|r_i - r_j|) = \sum_{i,j=1}^{N} \frac{q_i q_j}{4\pi\epsilon_o r_{ij}} + \sum_{i,j=1}^{N} \Phi(r_{ij}) \qquad (2.3)$$

The first term is the Coulomb potential between a pair of atoms with charges q_i and q_j and separation r_{ij}. $\Phi(r_{ij})$ is the short range potential acting between the atoms, which includes contributions from many terms, including covalency, non-bonded repulsion, and dispersion.

The inclusion of many-body terms in the simulation will inevitably increase the computational demands, however by truncating equation (2.2), we have assumed that the potential is a function of the inter-nuclear distance only, and not of its direction. This is incorrect, even for ionic solids. One consequence is that for solids in which all ions are on sites of the same symmetry implies that two of the elastic constants, c_{12} and c_{44} are equal (the Cauchy relation). This is not found experimentally for MgO or BaO, where the difference between them is very large MgO ($c_{12} = 9.3 \times 10^{11}$dyn/cm^2, $c_{44} = 15.7 \times 10^{11}$ dyn/cm^2) or BaO ($c_{12} = 5.0 \times 10^{11}$ dyn/cm^2, $c_{44} = 3.4 \times 10^{11}$ dyn/cm^2). Nevertheless, for the purposes of calculating defect parameters (Harding 1990) and surface relaxations(Lewis and Catlow 1985b, Lewis 1985c), the approximation has been very successful.

In this work we are mostly concerned with the application of atomistic simulation to heteroepitaxial interface systems, where inevitably the misfit between the overlaying material and substrate will have to be accommodated by either an expansion or a contraction of the materials at the interfacial plane. The inclusion of three body terms may therefore have a larger effect on the relaxational behaviour and interfacial stability than surface relaxation or defect energy calculations as a result of this artificial expansion or contraction at the interfacial plane. Three body terms are not however included in any of the work in this thesis, however a useful extension to this work would be to modify the computer codes such that the three body terms may be included to

ascertain what effect (if any) higher order terms have on the interfacial behaviour.

Several types of analytical functions can be employed to model $\Phi(r_{ij})$ and are discussed below. It is possible to use numerical potentials, i.e. tabulations of Φ as a function of r. Numerical potentials have not been employed in this work, however work by Lawrence (1988) examines the relative merits of employing numerical potentials compared to analytical potentials in a theoretical treatment of Cr_2O_3. For the Coulomb term, the r^{-1} function is exact, however for other terms, the functions are approximate. The next section describes a few of the candidates available which are employed to describe Φ.

2.2.1 Two-body bonded interactions

The simplest, and most widely used function applied to a bonding pair of atoms is the *bond harmonic* function;

$$\Phi(r_{ij}) = 1/2K[(|r_i-r_j|)-r_o]^2 \qquad (2.4)$$

where r_o is the equilibrium bond distance and K is the bond force constant. Functions of this type are quite adequate for small deviations from the equilibrium bond distance, however the anharmonicity of real systems is not represented in this expression. Greater reliability over a wider range of separations can be achieved by using the *Morse* function, which has the form;

$$\Phi(r_{ij}) = D\{1 -\exp[-\beta(|r_i-r_j| - r_o)]\}^2 \qquad (2.5)$$

where D is the dissociation energy of the bond, r_o the equilibrium bond length and β is a variable parameter, which can be determined by spectroscopic data. The Morse potential is employed to describe the bonding interactions between atoms of organic molecules in

modelling the diffusion of molecules in zeolite frameworks (Titiloye et al. 1989)

2.2.2 Two-body non-bonded interactions

The most widely used function is the *Lennard-Jones* potential (employed almost exclusively for molecular dynamics simulations) which is of the form;

$$\Phi(r_{ij}) = A/(|r_i - r_j|)^{12} - C/(|r_i - r_j|)^6 \qquad (2.6)$$

where the first term represents the Pauli repulsion and the second, the leading dispersion term. A and C are variable parameters.

Finally, the potential function employed in this thesis, is the Buckingham potential, in which the r^{-12} term of the Lennard-Jones potential is replaced by an exponential repulsive term, giving;

$$\Phi(r_{ij}) = A\exp[(-|r_i-r_j|)/\rho] - Cr^{-6} \qquad (2.7)$$

The parameters A,ρ and C, have to be derived for each material which is discussed later. A and ρ, represent the related ion size and hardness (Busing 1970), and the attractive Cr^{-6} term included to take account of the Van der Waals, dispersive and covalent interactions. The Cr^{-6} term is occasionally omitted from the potential, with the contribution from this term incorporated into the calculation by a suitable adjustment of the A parameter.

2.3 Many Body Terms

2.3.1 Three body bond bending functions

The importance of including many-body terms to simulations is increasingly recognised to increase the reliability of such calculations, particularly when modelling partially covalent systems such as zeolites and other silicate materials (Titiloye et al. 1989, Tschaufeser 1992). In the case of silicates, the expression usually chosen for the three-body component is a simple harmonic about the equilibrium tetragonal bond angle, given by;

$$\Psi_2(r_i,r_j,r_k) = K/2(\Delta\Theta)^2 \qquad (2.8)$$

where K is the bond-bending force constant and $\Delta\Theta = \Theta - \Theta_o$ is the deviation of the bond angle from the equilibrium Θ_o.

2.3.2 Four body torsional terms

When modelling molecules (especially macromolecules) it is often necessary to include a four-body potential which depends on the torsional angle φ. In a system of atoms 1,2,3 and 4, the torsional angle is defined as the angle subtended by the intersection of planes defined by atoms 1,2,3 and 2,3,4 (figure 2.1). Several functions may be used to describe the potential, for example;

$$\Psi_3(r_i,r_j,r_k,r_l) = K[1 \pm \cos(n\varphi)] \qquad (2.9)$$

A final step in obtaining a potential model is the derivation of the potential parameters which is discussed in section 2.4.

All these potential models described above have been employed with much success to

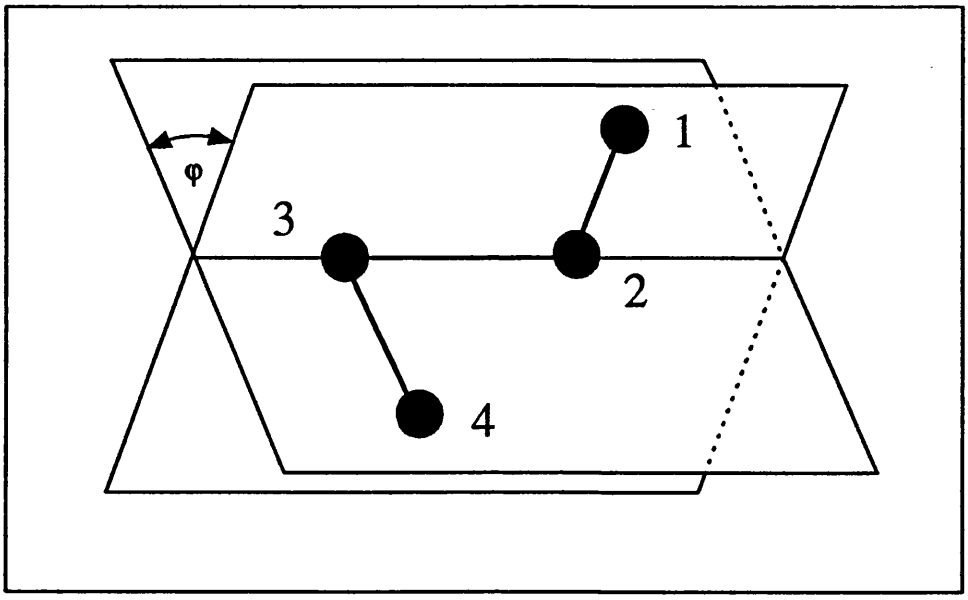

Figure 2.1 Quartet of atoms illustrating the torsional angle φ in the four body potential.

model a wide range of systems. However, in ionic solids, the many body term is represented by the electronic polarisation, which cannot be neglected. The many body effect arises because the magnitude of the polarisation is determined by the electronic field of the total crystal. In the next section we discuss the inclusion of ionic polarisation in the potential model.

2.3.3 Ionic polarisability

The simplest type of model, the *rigid ion model*, does not incorporate ionic polarisability. Rigid ion models can be applied to defect studies (Gillan and Dixon 1980) if the short range parameters are fitted to accurately reproduce the static dielectric constants of the material. This type of potential however limits the ability of the model to accurately calculate, for example, dynamical lattice properties (Woods et al. 1960) and segregation energies (Colbourn and Mackrodt 1985). Furthermore the rigid ion model implies the high frequency dielectric constant is unity and therefore the model is unable to reproduce, for example, the optic modes of the phonon spectrum.

The inclusion of ionic polarisability inevitably increases the number of potential parameters required, and the number of degrees of freedom of the system which will ultimately reduce the maximum possible calculation size available for limited computer resources. These constraints are the major reason that polarisability is usually neglected in molecular dynamics or Monte Carlo simulations. For some of the more computationally intensive interface calculations in this thesis, a return to the rigid ion model is necessitated due to computational resource limitations.

A description of two approaches to model ionic polarisability is now given. First, the point polarisable ion model and second, the shell model.

2.3.3a Point Polarisable Ion Model

This is the simplest of the two approaches and models the polarisability in terms of a point dipole whose magnitude, μ, is proportional to the effective field, E, acting on the ions;

$$\mu = \alpha E \tag{2.10}$$

where α is the ionic polarisability. The key features of this model are firstly the ionic polarisability is fixed and secondly, it is computationally inexpensive. For isolated ions or small molecules, the model is adequate, however the model can fail badly for ionic solids (Lyddane and Herzfield 1958, Faux 1971, Norget 1971). In these systems the coupling between the short range repulsion and polarisability is strong, since polarisation is a displacement of the valence electrons which will inevitably affect the short range interaction between ions. The omission of this coupling results in a poor description of the dielectric and defect properties. This coupling and hence the modification of polarisability with changes in electric field, is however, adequately described by the shell model.

2.3.3b The Shell Model

The shell model is based on the model developed by Dick and Overhauser (1958) and is used to reproduce the electronic polarisability in this work. A simple diagrammatic illustration is shown in figure 2.2. The ion is represented by two parts, a massless 'shell' of charge Y, coupled to a core of charge X (in which the mass of the ion is concentrated), by a harmonic spring with force constant k. The interaction between the core and shell is given by;

$$\Phi_i(r_i) = k_i r_i^2 \tag{2.11}$$

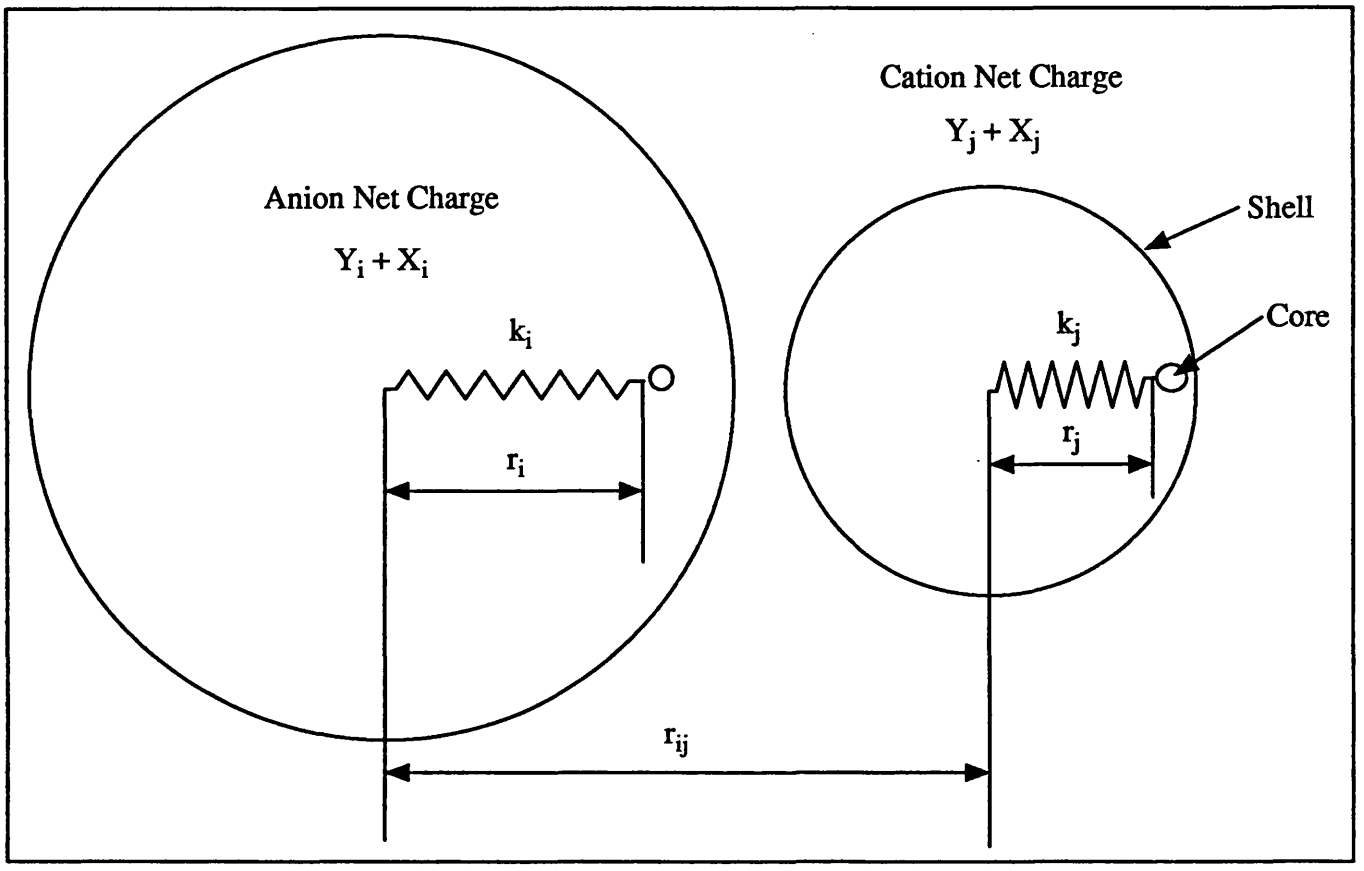

Figure 2.2 Diagrammatic representation of the shell model (based on the model developed by Dick and Overhauser (1958)).

where the polarisability of the free ion is

$$\alpha_i = Y_i^2/K_i \qquad (2.12)$$

$K_i = k_i + r_i$ with $k_i \gg r_i$. The parameters Y and k are obtained by empirical fitting to dielectric data, elastic constants or dispersion curves. Polarisation is described in terms of the displacement of the shells relative to the core. The model includes the required coupling between these terms and the polarisation because the short-range repulsions are generally taken to act between the shells only, The Coulomb forces act between all cores and shells except for the core and shell belonging to the same ion. The core positions represent the positions of the ionic nuclei, however, no significance should be attached to the shell positions or indeed any physical interpretation of the model. The commonest is to assume that the shells represent the valence electrons, this interpretation is incorrect as many of the fitted shell charges are positive!

The relative merits of the shell model description of polarisability in ionic solids are discussed in more detail by Catlow and Mackrodt (1982) and Catlow (1986).

The next step is to obtain values for the variable parameters.

2.4 Potential Parameters

The variable parameters required for the description of the short range potential energy terms can be obtained, either by empirically fitting to experimental data, or by approximate quantum mechanical calculations (non-empirical) i.e. calculating numerically the short range potential energy terms. Empirical potentials must ultimately rely on the validity of the analytical forms used for the potential when they are

extrapolated to interatomic separations that differ substantially from those used in the parameterisation. Non-empirical potentials offer the promise of greater reliability, to describe the short range potential energy terms for a wide range of interatomic separations. This assumes theoretical methods of sufficient accuracy can be developed. The major advantage is that they will be more applicable to systems which exhibit substantial deviations in interatomic separations, such as in defect calculations where interstitial sites can be up to 1Å closer than the corresponding equilibrium separation. Empirical potentials do however perform well in comparison to their non-empirical counterparts as the deficiencies in the analytical form of the empirical methods may be compensated, in part, by the fitting procedure. A disadvantage empirical methods have compared to non-empirical methods is that if no experimental data exists, the potential cannot be derived, furthermore the accuracy of the empirical potential can not exceed the accuracy of the experimental data. The two ways in which the short range potentials are derived are now described.

2.4.1 Empirical Derivation of Short Range Parameters

In this work the analytical term employed to describe the short range potential energy terms is the Buckingham expression (2.7).

$$\Phi(r_{ij}) = A\exp[(-|r_i-r_j|)/\rho] - Cr^{-6} \qquad (2.7)$$

The parameters A, ρ and C are determined by a least squares fitting routine (figure 2.3) to the available experimental data, for example, crystal structure, dielectric and elastic properties and phonon frequencies.

The potential parameters used for BaO and MgO in the BaO(100)//MgO(100) interface studies in this work were derived by Lewis and Catlow (1985c) and are given in table

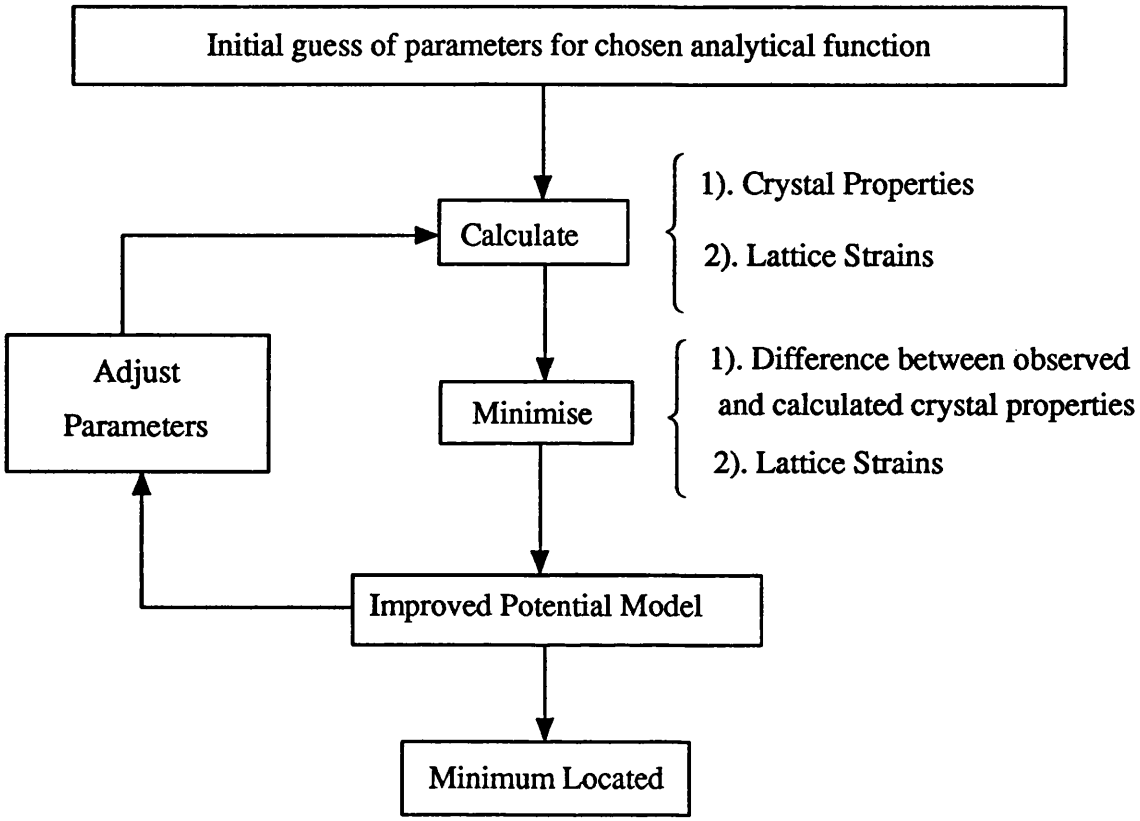

Figure 2.3 Representation of the fitting procedure employed to derive the empirical potential parameters of the two-body analytical functions.

Short Range Parameters

$\Phi(r_{ij}) = A\exp[(-|r_i-r_j|)/\rho] - Cr^{-6}$

Interaction	A(eV)	ρ(Å)	C(eV/Å^6)
Ba^{2+}-O^{2-}	905.7	0.3976	0.0
Mg^{2+}-O^{2-}	1428.5	0.2945	0.0
O^{2-}-O^{2-}	22764.3	0.149	27.879
Mg^{2+}-Ba^{2+}	—	—	—

Shell Parameters

Ion	Y	k(eV/Å^2)
Ba^{2+}	9.203	443.46
Mg^{2+}	Rigid Ion	
O^{2-}	-3.0	51.836

Table 2.1 Empirical potential parameters for BaO and MgO.

2.1. To reduce the number of variables, cation-cation interactions (Ba^{2+}-Ba^{2+}, Mg^{2+}-Mg^{2+} and Ba^{2+}-Mg^{2+}) are neglected as a result of insufficient experimental data. This does not severely inhibit the accuracy of the potential model as the cation-cation interactions are small, particularly at the large interatomic cation-cation distances in the MgO and BaO crystals (i.e. lattice parameter $\times \sqrt{2}$). In addition, the repulsion will be totally dominated by the Coulombic interaction. The cation-cation distances across the interface (Ba^{2+}-Mg^{2+}) however may be smaller than in the bulk crystal (chapter 4) and it may therefore be necessary to include this interaction into the calculation.

The potentials employed for $SrTiO_3$ were derived by Lewis and Catlow (1985c) and James (1978) and are given in table 2.2. Lewis and Catlow (1983) potentials are employed to model $BaTiO_3$ and are given in table 2.3. Finally the potentials employed for the superconductor $YBa_2Cu_3O_{6.5}$ were derived by Baetzold (1988) and are given in table 2.4.

2.4.2 Non-Empirical Potential Derivation

The potential models employed in this thesis are all empirical and therefore a detailed description of non-empirical potential derivations is not given.

Two approaches have been employed to calculate the potential energy terms numerically. The first is the "electron gas method" which is based on methods developed by Wedepohl (1967) and applied by Gordon and Kim (1972). This method, which is described in detail by Harding (1982), has the advantage of being computationally inexpensive and is based on the statistical treatment of electrons in an atom or ion as a degenerate Fermi gas. The second method is a 'direct' calculation based on ab-initio molecular orbital methods, usually Hartree-Fock self consistent field techniques (Fowler and Madden 1983). The procedure is to represent the interacting

Short Range Parameters

$\Phi(r_{ij}) = A\exp[(-|r_i-r_j|)/\rho] - Cr^{-6}$

Interaction	A(eV)	ρ(Å)	C(eV/Å^6)
Sr^{2+}-O^{2-}	1400.0	0.35	0.0
Sr^{2+}-Ti^{4+}	---	---	---
Sr^{2+}-Sr^{2+}	---	---	---
Ti^{4+}-O^{2-}	656.74	0.40431	0.0
Ti^{4+}-Ti^{4+}	---	---	---
O^{2-}-O^{2-}	22764.0	0.149	27.88

Shell Parameters

Ion	Y	k(eV/Å^2)
Sr^{2+}	Rigid Ion	
Ti^{4+}	Rigid Ion	
O^{2-}	-2.38856	23.80

Table 2.2 Empirical potential parameters for $SrTiO_3$.

Short Range Parameters

$\Phi(r_{ij}) = A\exp[(-|r_i-r_j|)/\rho] - Cr^{-6}$

Interaction	A(eV)	ρ(Å)	C(eV/Å^6)
Ba^{2+}-O^{2-}	1214.4	0.3522	8.0
Ba^{2+}-Ti^{4+}	---	---	---
Ba^{2+}-Ba^{2+}	---	---	---
Ti^{4+}-O^{2-}	877.2	0.38096	9.0
Ti^{4+}-Ti^{4+}	---	---	---
O^{2-}-O^{2-}	22764.0	0.149	43.0

Shell Parameters

Ion	Y	k(eV/Å^2)
Ba^{2+}	1.848	29.1
Ti^{4+}	-35.863	65974.0
O^{2-}	-2.389	18.41

Table 2.3 Empirical potential parameters for $BaTiO_3$.

Short Range Parameters

$\Phi(r_{ij}) = A\exp[(-|r_i-r_j|)/\rho] - Cr^{-6}$

Interaction	A(eV)	ρ(Å)	C(eV/Å^6)
Y^{3+}-Y^{3+}	---	---	---
Y^{3+}-Ba^{2+}	---	---	---
Y^{3+}-Cu^{2+}	---	---	---
Y^{3+}-O^{2-}	20717.5	0.24203	0.0
Ba^{2+}-Ba^{2+}	2663.7	0.2588	0.0
Ba^{2+}-Cu^{2+}	168128.6	0.22873	0.0
Ba^{2+}-O^{2-}	3115.5	0.33583	0.0
Cu^{2+}-Cu^{2+}	---	---	---
Cu^{2+}-O^{2-}	3799.3	0.24273	0.0
O^{2-}-$^+O^{2-}$	22764.0	0.1490	75.0

Shell Parameters

Ion	Y	k(eV/Å^2)
Y^{3+}	Rigid Ion	
Ba^{2+}	9.1173	426.1
Cu^{2+}	Rigid Ion	
O^{2-}	-3.2576	49.8

Table 2.4 Empirical potential parameters for $YBa_2Cu_3O_{6.5}$.

ions, and a few of their close neighbours, quantum mechanically and then to employ an array of point charges to represent the remainder of the lattice. The point charges are positioned at lattice sites and their charges chosen such that the correct Madelung field energy is obtained. The relative positions of the two interacting species is varied and the energy calculated at each point to obtain a potential energy surface.

2.5 Summary

In this chapter we have reviewed the various analytical forms that have been employed to describe the interatomic interactions in a system. We have shown that pairwise interactions alone have been successfully employed to model ionic systems, however for systems with a higher degree of covalency, higher order terms must be included. For ionic systems, polarisation terms must be included into the calculation, this is successfully achieved by implementing the shell model. Finally the two methods of deriving the potential parameters are described and the parameters for all the materials considered in this thesis are given.

In the next chapter, the computer codes, which employ the potential models described in this chapter, to calculate the interfacial energies and ionic behaviour, are described.

Chapter 3

Theoretical Methods

3.1 Introduction

In this chapter we describe the theoretical methods employed in this thesis to calculate bulk and planar defect energies, interfacial stability and ionic behaviour of the heteroepitaxial interface systems considered in this thesis.

3.2 Calculation of the Bulk Defect Formation Energies.

The bulk defect calculations presented in this thesis are based on the Mott-Littleton method (Mott and Littleton 1938) and developed by Lidiard and Norgett (1972) and Norgett (1972, 1974) and implemented in the **HADES** (Harwell Automatic Defect Evaluation System) code (Norgett 1972, 1974). For the calculations in this work, its successor, the **CASCADE** (Cray Automatic System for the CAlculation of Defect Energies) code (Leslie 1982) was employed.

The approach for calculating the defect energy is to divide the crystal surrounding the defect into two regions. An inner region I, where all the ions are allowed to relax explicitly and an outer region II, which is treated by a suitable continuum approximation. Region II is also subdivided into an inner region IIa and an outer region IIb (figure 3.1a). Where the region I region IIb interactions are purely Coulombic. The total energy of the system E, can be written as;

$$E = E_1(\underline{x}) + E_2(\underline{x},\underline{\zeta}) + E_3(\underline{\zeta}) \qquad (3.1)$$

in which $E_1(\underline{x})$ is the energy of the inner region, $E_3(\underline{\zeta})$ the energy of the outer region and $E_2(\underline{x},\underline{\zeta})$, the interaction energy between regions I and II. $\underline{x}$ are the independent coordinates describing the configuration of region I (which are calculated explicitly), $\underline{\zeta}$,

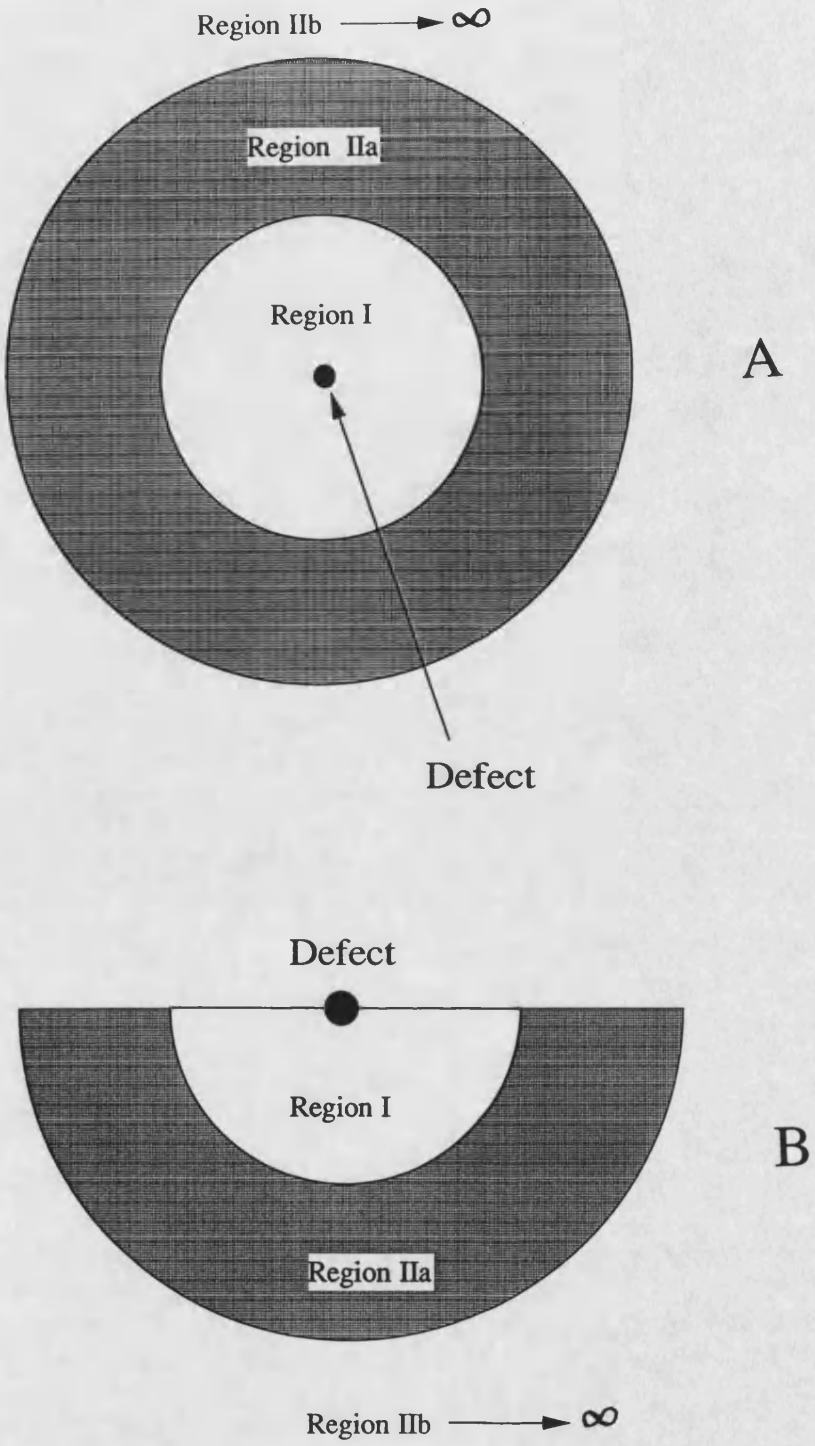

Figure 3.1 Two-region strategy used for defect calculations. Region I is the explicitly relaxed region surrounding the defect. Region IIa is constructed for charged defects. Region IIb extends to infinity. (a) bulk calculations and (b) surface calculations.

are the displacements in region II and are formally distinguished from $\underline{x}$. $E_3(\underline{\zeta})$ cannot be solved exactly because it contains an infinite number of displacements. We assume however that the distance between the defect and the innermost ions of region II is sufficiently large that we can consider the outer region consists of the perfect crystal, with harmonic displacements of the ions arising from the electric field generated by the defect. Therefore $E_3(\underline{\zeta})$ can be represented by a quadratic function of $\underline{\zeta}$;

$$E_3(\underline{\zeta}) = 1/2(\underline{\zeta}.\underline{A}.\underline{\zeta}) \tag{3.2}$$

Substituting this expression into (3.1) and assuming the equilibrium condition, we obtain;

$$\frac{\partial E(\underline{x}, \underline{\zeta})}{\partial \underline{\zeta}} = \left. \frac{\partial E_2(\underline{x}, \underline{\zeta})}{\partial \underline{\zeta}} \right|_{\underline{\zeta} = \underline{\zeta}_o} + \underline{A} \cdot \underline{\zeta} = 0 \tag{3.3}$$

We thus obtain an expression for $E_3(\underline{\zeta})$;

$$E_3(\underline{\zeta}) = 1/2(\underline{\zeta}.\underline{A}.\underline{\zeta}) = -\left(\frac{\underline{\zeta}}{2} \right) \left. \frac{\partial E_2(\underline{x},\underline{\zeta})}{\partial \underline{\zeta}} \right|_{\underline{\zeta} = \underline{\zeta}_o} \tag{3.4}$$

for $\underline{\zeta} = \underline{\zeta}_o$, the value of the outer displacements at equilibrium with a given set of displacements of the inner region.

The total energy of the system as a function of $E_1(\underline{x})$ and $E_2(\underline{x}, \underline{\zeta})$ can be written;

$$E = E_1(\underline{x}) + E_2(\underline{x}, \underline{\zeta}) - \left(\frac{\underline{\zeta}_o}{2} \right) \frac{\partial E_2(\underline{x}, \underline{\zeta})}{\partial \underline{\zeta}} \Bigg|_{\underline{\zeta} = \underline{\zeta}_o} \tag{3.5}$$

The total relaxed energy of the system, E, can be determined by direct minimisation with respect to $\underline{x}$, the displacements in region I, i.e. $dE/d\underline{x} = 0$. This can be done, but, since there is no analytical expression for these displacements, it is difficult to apply in view of the complicated nature of E as a function of $\underline{x}$. An easier method is ensuring the force on each ion is zero;

$$\frac{\partial E}{\partial \underline{x}} \Bigg|_{\underline{\zeta} = \underline{\zeta}_o} = 0 \tag{3.6}$$

We now calculate the energy of the defect by considering an explicit two-body representation for E, the energy of the perfect lattice;

$$E_L = \sum_{i>j} \Psi_{ij}(|\underline{R}_i - \underline{R}_j|) \tag{3.7}$$

where Ψ_{ij} is some suitable pair potential (chapter 2.2) and $\underline{R}$ the appropriate lattice coordinates. Similarly the energy of the lattice containing the defect is given by;

$$E_D = \sum_{i>j} \Psi_{ij}(|\underline{r}_i - \underline{r}_j|) \tag{3.8}$$

where $\underline{r}$ are the displaced coordinates. The energy of the defect, therefore, is simply given as the difference in the lattice energy with and without the defect;

$$E = \sum_{i>j} \left[\Psi_{ij}(|\underline{r}_i - \underline{r}_j|) - \Psi_{ij}(|\underline{R}_i - \underline{R}_j|) \right] \tag{3.9}$$

The identification of equation (3.1) or (3.5) with equation (3.9) is not as straightforward as it appears, whilst E_1 is evidently given by;

$$E_1 = \sum_{\substack{i \in I \\ j \in I}} [\, \Psi_{ij}(|\underline{r}_i - \underline{r}_j|) - \Psi_{ij}(|\underline{R}_i - \underline{R}_j|) \,] \tag{3.10}$$

a simple summation for the outer region is not a adequate description of E_3 because it is not a quadratic function of the displacements. It can be shown that E_3 is given by;

$$E_3 = \sum_{\substack{i \in II \\ j \in II}} [\, \Psi_{ij}(|\underline{r}_i - \underline{r}_j|) - \Psi_{ij}(|\underline{R}_i - \underline{R}_j|) \,] + \sum_{\substack{i \in I \\ j \in II}} [\, \Psi_{ij}(|\underline{R}_i - \underline{r}_j|) - \Psi_{ij}(|\underline{R}_i - \underline{R}_j|) \,] \tag{3.11}$$

It contains a contribution which corresponds to a displaced region II with region I ions at their perfect lattice sites (i.e. $(|\underline{R}_i - \underline{r}_j|)$ where : $i \in I$ and $j \in II$. E_2 is given by;

$$E_2 = \sum_{\substack{i \in I \\ j \in II}} [\, \Psi_{ij}(|\underline{r}_i - \underline{r}_j|) - \Psi_{ij}(|\underline{R}_i - \underline{r}_j|) \,] \tag{3.12}$$

The final expression for E is therefore;

$$E = \sum_{\substack{i \in I \\ j \in I}} [\Psi_{ij}(|\underline{r}_i - \underline{r}_j|) - \Psi_{ij}(|\underline{R}_i - \underline{R}_j|)] + \sum_{\substack{i \in I \\ j \in II}} [\Psi_{ij}(|\underline{r}_i - \underline{r}_j|) - \Psi_{ij}(|\underline{R}_i - \underline{r}_j|)]$$

$$- \frac{1}{2} \sum_{\substack{i \in I \\ j \in II}} \left[\frac{\partial}{\partial \underline{r}_j} \Psi_{ij}(|\underline{r}_i - \underline{r}_j|) - \frac{\partial}{\partial \underline{r}_j} \Psi_{ij}(|\underline{R}_i - \underline{r}_j|) \right] . (\underline{r}_j - \underline{R}_j) \qquad (3.13)$$

The interactions in region I are purely local and are treated explicitly for the ionic crystal considered. In the neighbourhood of region I, the interactions between region I and region II comprises of both short range and long range terms which can be calculated by direct summation. Away from the region I, region II boundary (i.e. region IIb), the interaction is purely Coulombic. The treatment of this long range region I-region IIb interaction is via a continuum approximation developed from the classical polarisation theory of Mott and Littleton (1938). The contribution to the total energy of the system from the region I region IIb interactions is given, for cubic systems by;

$$E_{2b} = - \frac{Q^2}{2} \sum_{j \in IIb} q_j \frac{M_j}{|\underline{R}_j|^4} \qquad (3.14)$$

Where Q is the defect charge, V_m the molar volume, $\underline{R}_j$ the distance from the defect and M_j, the Mott-Littleton parameter for the sublattice, given by;

$$M_j = \left(\frac{\alpha_j}{\Sigma_k \alpha_k} \right) \left(1 - \epsilon^{-1} \right) \qquad (3.15)$$

where α_k is the polarisability of the k^{th} sub-lattice. For the more general case of a dielectrically anisotropic crystal, E_2 can be written as;

$$E_{2b} = - \frac{Q^2}{2} \sum_{j \in II_b} \left[\frac{\left(\sum M_j^{\alpha\beta} . R_j^{\alpha} . R_j^{\beta} \right)}{|R_j|^6} \right] \qquad (3.16)$$

where the sum over all j refers to ions in regionII and α and β refer to Cartesian coordinates.

The success of this model depends on the majority of the relaxation occurring near to the centre of the defect and decreasing rapidly away from the defect. The calculation of point defect energies at surfaces and interfaces is now described.

3.3 Calculation of Point Defect Energies at Near interface regions of ionic crystals

The calculation of point defect energies at surfaces or near interface regions of ionic crystals can be calculated using the computer code CHAOS (Computer simulation **HA**des **O**n Surfaces) (Duffy and Tasker 1983a). It is based on the HADES program (section 3.2) with necessary modifications (described below) to account for the existence of a surface or interface (figure 3.1b). The defect energy is given as the difference in energy between the defective lattice and the perfect lattice.

The relaxed structure of the perfect (no defects) relaxed surface or interface is obtained from the MIDAS program (section 3.4). The existence of the surface or interface necessitates modifications relating to the 2-dimensional periodicity of the reference configuration. In HADES, the Madelung energies are calculated using a 3-dimensional Ewald Summation (Ewald 1921) which is inappropriate to surface or interface

calculations. In CHAOS, a two dimensional lattice summation method developed by Parry (1975a, 1975b) is employed. The Ewald method for calculating the Madelung energies in systems maintaining 3-dimensional periodicity is described in section (3.6) and the Parry method which addresses the calculation of the Madelung energies in systems maintaining 2-dimensional periodicity is discussed in section 3.6.1

The calculation of the ionic displacements and energy of the continuum is also modified as a result of the surface or interface. For HADES, the energy of the continuum is calculated (assuming cubic symmetry) by a discrete $\underline{R}^{-4}$ summation (equation 3.14) but this assumes there is no structural deviation from the perfect crystal structure away from the defect (i.e. region II). This is true for three dimensional lattices, however for surface or interface calculations, the modification of ionic positions or indeed interplanar spacings at the surface or interface regions must be addressed. In CHAOS, the energy is calculated by a combination of a discrete sum of planar integrals around the interface for all planes in regions I and II defined by the MIDAS code, and a volume integral over the remainder of the crystal. The planar integrals therefore take explicit account of the dilation of the crystal at the interface;

$$E_{IIb} = -\frac{Q^2}{2}\left(E_{Planar} + E_{Volume} \right) \tag{3.17}$$

$$E_{Planar} = \sum_{\substack{p \in I \\ p \in IIa}} \sum_{j} q_j \cdot M_j \int_{\tau}^{\infty} \frac{1}{(\underline{R}^2 - \underline{R}_p^2)} \cdot 2\pi \underline{R} d\underline{R} \tag{3.18}$$

$$E_{Volume} = \sum_{j} q_j \cdot M_j \int_{R\text{IIb}}^{\infty} \frac{1}{|\underline{R}|^4} \cdot 2\pi \underline{R}^2 d\underline{R} \qquad (3.19)$$

where $\underline{R}_p$ is the perpendicular distance from the origin and plane p, M_j the Mott-Littleton displacement factor for sublattice j, Q_j, the total defect charge and $\tau = (R\text{IIb}^2 - r_p^2)^{1/2}$ (R-cutoff radius).

The response of interface or surface ions, to an electric field, is identical to bulk ions (i.e. they have the same Mott-Littleton coefficients). This is clearly an approximation as the environment at the surface deviates from the bulk. For ionic materials with little surface relaxation such as MgO(100) the effect is minimal, however for materials with large surface relaxations such as dipolar surfaces and especially interfaces, this approximation may not be trivial. CHAOS has been extended to accommodate this effect by calculating the Mott-Littleton coefficients for the bulk and surface ions. The modified coefficients are then used to determine the displacements and polarisation energies of the ions close to the surface or interface. This necessarily increases the computational time and was not included in the work in this thesis, it would however provide a useful extension to this work to include this effect.

A surface or interface implies a discontinuity in the dielectric constant and therefore the energy associated with the defect must also include a contribution from the image charged induced as a result of the defect. The image charge induced at the interface between two materials of dielectric constants ϵ_1 and ϵ_2 is given by;

$$q_i = q_{def}(\epsilon_1 - \epsilon_2)/(\epsilon_1 + \epsilon_2) \qquad (3.20)$$

where q_{def} is the charge of the defect and $\epsilon_1 > \epsilon_2$. The field due to the image charge must be included when calculating the displacements of the ions in region IIa and the polarisation energy of region IIb. The image charge is induced via the defect a distance d/2 above the uppermost ion from the top plane of the material containing the defect where d is the interplanar spacing. At present the CHAOS program adopts a dielectric constant of 1 for the second material and is therefore only directly applicable to free surfaces. For defect calculations at interfaces this will obviously introduce inaccuracies in the treatment of the continuum polarisation energy and the magnitude of the image charge especially for defects at or near the interface region. The size of region I in the calculations presented in this thesis was therefore made as large as possible to reduce the inaccuracies introduced as a result of the image interaction.

3.4 Calculation of Surface and Interface Behaviour.

The ionic crystal structures near surfaces, twist grain boundaries and heteroepitaxial interfaces were modelled using the computer code MIDAS (Tasker 1978) (Minimisation for Interfacial Defects And Surfaces). Extended planar defects that maintain two dimensional periodicity can also be considered provided that the net charge on the crystal is zero. Energies calculated using this code are energies at constant surface area.

The program considers the crystal as a stack of planes periodic in two dimensions (figure 3.2). The stack is divided into two regions (using a scheme not dissimilar to that developed by Norgett in the HADES code). A region I, where the ions are allowed to relax independently of each other, and a region II, where the ions are held fixed relative to each other. Region II may however move as a whole, enabling the crystal to 'expand' or 'contract'. Region II is included to ensure the potential of an ion at the bottom of region I is correctly calculated. The top of region I is the free surface (figure 3.2a) unless two such blocks are placed together enabling the cohesive energy of the perfect

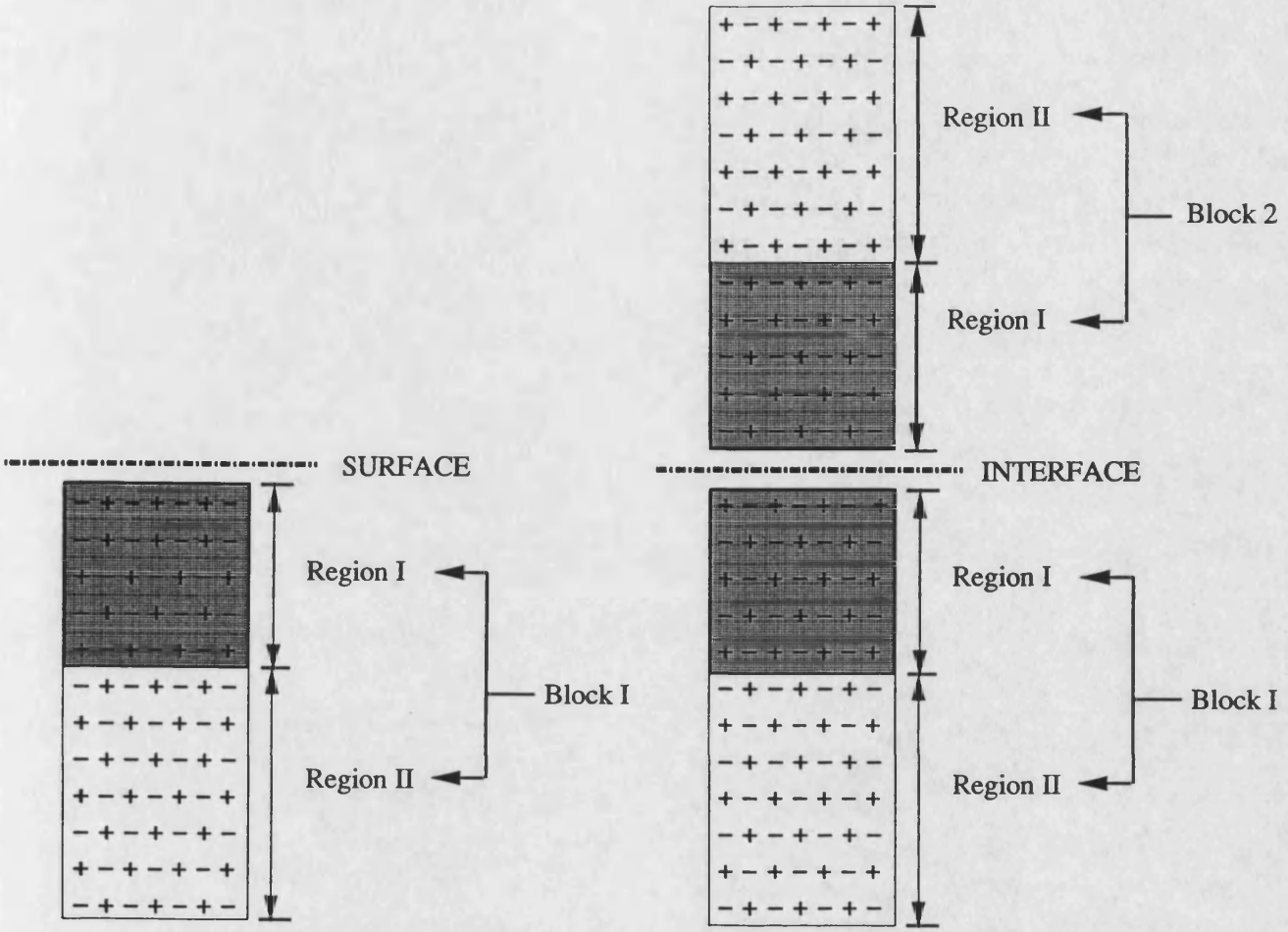

Figure 3.2 Schematic representation of the crystal regions for (a) interface calculations and (b) surface calculations.

crystal to be calculated (figure 3.2b). An interface can be created by a vector displacement or rotation of block I with respect to block II. If block I is displaced relative to block II by a vector within the interfacial plane a stacking fault is produced and a vector displacement perpendicular to the interface results in the formation of a shear plane. Rotations of block I with respect to block II about an axis perpendicular to the interfacial plane results in a twist grain boundary and parallel to the interfacial plane a tilt grain boundary is formed. The program also enables two dissimilar crystal structures to be placed together enabling a heteroepitaxial interface to be simulated. The vector displacements and rotations also apply to these systems enabling the modelling of epitaxy.

The surface energy E_s, per unit area can be defined as;

$$E_s = \sum_{\lambda=1}^{b} \frac{E_{(\lambda)} - E_{(b)}}{\text{Area}} \qquad (3.21)$$

where the energy is summed over all ions in plane λ, b is a bulk plane and $E_{(b)}$ is the bulk energy. Where available, this can be compared directly to the experimental determined surface energy.

3.5 Energy Minimisation

The real power of static simulation comes from adjustment of the ion positions to a minimum energy configuration. An initial configuration is specified for the system, the energy $E(\underline{x})$ is calculated, using the interatomic potentials, which are a function of all the structural variables, $\underline{x}$. The structure is then adjusted, using an iterative scheme such that the system achieves a minimum energy configuration.

Minimisation algorithms are classified according to the searching procedure they follow. The simplest methods employ the energy function alone and search over all configurational space until the minimum is located. This technique is suitable for systems with few variables, however for the systems considered in this work they are prohibitively slow. Much greater efficiency is achieved using gradient techniques which are employed to guide the system down the potential energy surface to a position of minimum energy. Figure 3.3 shows diagrammatically a one dimensional potential energy surface, where the energy is shown as a function of some structural variable ($\underline{x}$). The system runs from the starting configuration (a) to a minimum energy position (b). A major problem is the identification of a local minimum (position (b)) instead of a global minimum position (position (c)). To ascertain whether a local minimum has been identified, the initial structural configuration is altered slightly and the minimisation procedure repeated. The final energies of the systems are then compared to check whether a lower energy configuration has been identified. For many contemporary studies however the global minimum is unlikely to be located especially in this work. Indeed high resolution electron microscopy has been employed to show experimentally that local (higher energy) structures which deviate from the "average" or "global" energy minima structural configurations of many materials especially the high T_c superconductors (Amelinckx et al. 1991). Perhaps more fundamentally, surfaces and interfaces are metastable compared to the bulk crystals.

Three energy minimisation algorithms are now described

3.5.1 Steepest Descent

In this method the first derivatives of the energy $\partial E/\partial \underline{x}$ with respect to all the structural variables $\underline{x}$ are calculated and are employed to direct the minimisation. The values of $\underline{x}^{(n+1)}$ is related to $\underline{x}^{(n)}$ where n is the number of iterations by;

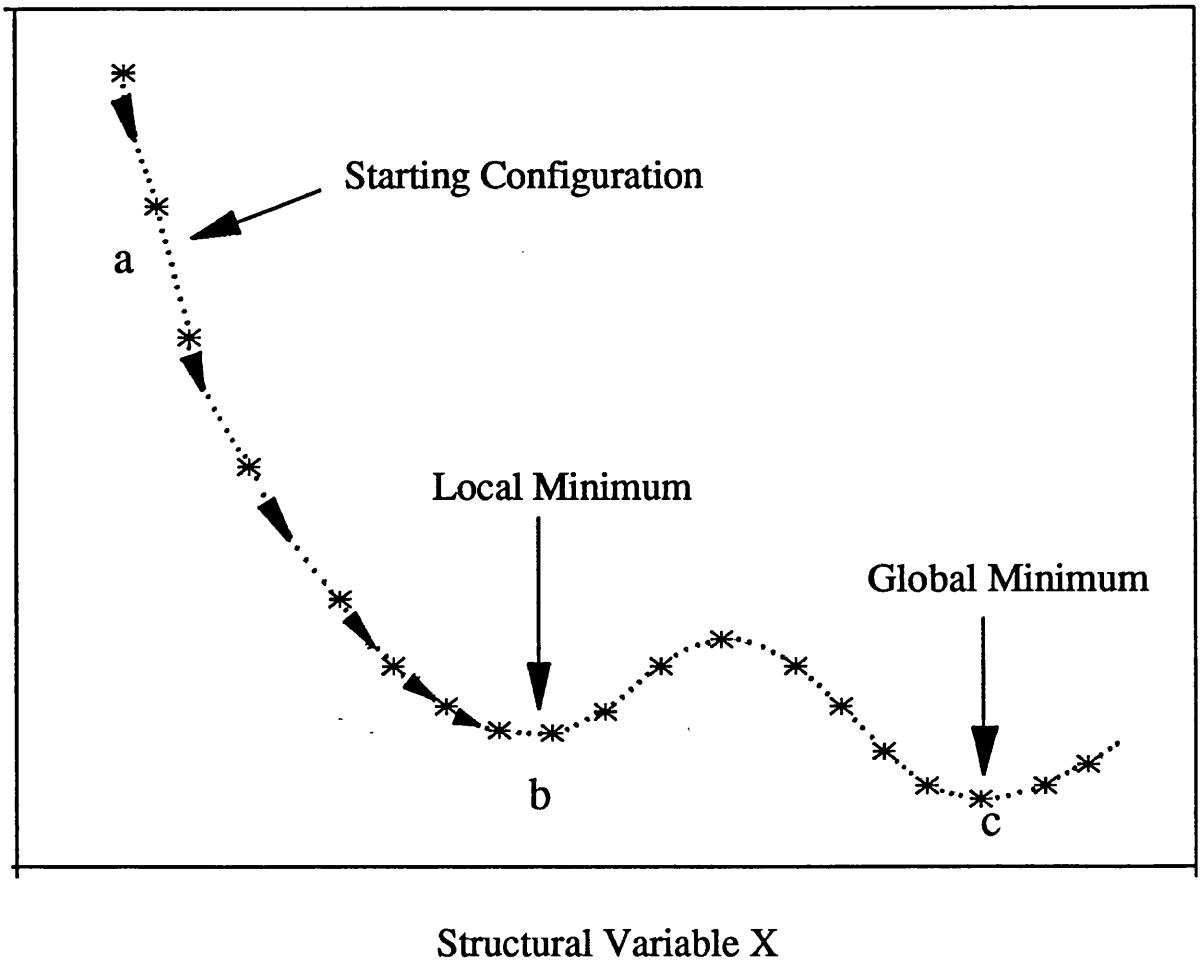

Figure 3.3 Energy minimisation with respect to some structural variable (x). The system runs downhill from the starting point (a) to a local minimum (b) despite the presence of a global minimum position (c).

$$\underline{x}^{(n+1)} = \underline{x}^{(n)} + C^{(n)}\underline{s}^{(n)} \tag{3.22}$$

where

$$\underline{s}^{(n)} = -\underline{g}^{(n)} \tag{3.23}$$

and

$$\underline{g}^{(n)} = \frac{\partial E}{\partial \underline{x}^{(n)}} \tag{3.24}$$

and $C^{(n)}$ is a numerical constant chosen each iteration to optimise the efficiency of the minimisation.

3.5.2 Conjugate Gradients

In this method, the displacement vector $\underline{s}^{(n)}$ uses information on the previous values of the gradients to speed the convergence;

$$\underline{s}^{(n)} = -\underline{g}^{(n-1)} + \underline{\beta}^{(n)}\underline{s}^{(n-1)} \tag{3.25}$$

where

$$\underline{\beta}^{(n)} = \frac{\underline{g}^{T(n-1)}.\underline{g}^{(n-1)}}{\underline{g}^{T(n-2)}.\underline{g}^{(n-2)}} \tag{3.26}$$

$\underline{g}^{(n)}$ are vectors whose components are the derivatives with respect to individual coordinates and the superscript, T, indicates the transpose of the vector.

3.5.3 Newtons Method

The final method considered is based on the Newton method, which employs the second derivatives to guide the minimisation to ensure more rapid convergence. The minimisation proceeds according to the expression;

$$\underline{\mathbf{x}}^{(n+1)} = \underline{\mathbf{x}}^{(n)} - \underline{\mathbf{H}}^{(n)}.\mathbf{g}^{(n)} \qquad (3.27)$$

where the matrix $\underline{\mathbf{H}} = \underline{\mathbf{W}}^{-1}$, in which the elements $\underline{\mathbf{W}}_{ij}$ are the second derivatives;

$$\underline{\mathbf{W}} = \frac{\partial^2 E}{\partial \underline{\mathbf{x}}^2} \qquad (3.28)$$

The improved speed of convergence is easily lost in the extra computational power required to calculate and invert the second derivative matrix for each iteration. However algorithms are available which enable the second derivative matrix to be updated without recalculation and inversion. The algorithms are approximate and it is therefore necessary to recalculate $\underline{\mathbf{H}}$ every few iterations. The most widely used of these is the Davidson-Fletcher-Powell algorithm (Davidson 1959, Fletcher and Powell, 1963) in which the matrix, $\underline{\mathbf{H}}$, is updated each iteration according to the formula;

$$\underline{\mathbf{H}}^{(n+1)} = \underline{\mathbf{H}}^{(n)} - \frac{(\underline{\mathbf{H}}^{(n)} . \Delta\mathbf{g}^{(n)}) . (\Delta\mathbf{g}^{T(n)} . \underline{\mathbf{H}}^{(n)})}{(\Delta\mathbf{g}^{T(n)} . \underline{\mathbf{H}}^{(n)} . \Delta\mathbf{g}^{(n)})} - \frac{(\Delta\underline{\mathbf{x}}^{(n)} . \Delta\underline{\mathbf{x}}^{T(n)})}{(\Delta\underline{\mathbf{x}}^{T(n)} . \Delta\mathbf{g}^{(n)})} \qquad (3.29)$$

where

$$\Delta\mathbf{g}^{(n)} = \mathbf{g}^{(n+1)} - \mathbf{g}^{(n)} \qquad (3.30)$$

and

$$\Delta \underline{x}^{(n)} = \underline{x}^{(n+1)} - \underline{x}^{(n)} \qquad (3.31)$$

The number of iterations over which $\underline{H}$ is recalculated is also crucial to the speed of minimisation, calculations have shown (chapters 4,5,6 and 7) the optimum iterations over which $\underline{H}$ should be recalculated varies from 5 to 20 for the various systems considered, with the minimisation time reduced by up to 50% within this range. There is unfortunately no method of determining the optimum number of iterations over which $\underline{H}$ should be recalculated without performing the minimisation.

One major limitation with the Newton method, is the enormous computational memory requirement in storing the inverse of the second derivative matrix. The alternative is therefore a return to the gradient techniques, which have a much lower memory requirement at the expense of computational time required.

The final section in this chapter addresses the calculation of the long range Coulombic terms by application of the Ewald method for systems with 3-dimensional periodicity and the Parry method for systems with 2-dimensional periodicity. These methods for calculating the Coulombic terms enable a substantial reduction in the computational time required for the calculations to be made and are inherent in all the static simulation codes and therefore the methods deserve a mention.

3.6 Summation of the 3-Dimensional Coulombic Terms

The calculation of the lattice energies of the systems investigated in this thesis include contributions from pair potential energy terms only. From equation 2.3, the total potential energy $U(r_{ij})$ is given by;

$$U(r_{ij}) = \sum_{i,j=1}^{N} \frac{q_i q_j}{4\pi\epsilon_o r_{ij}} + \sum_{i,j=1}^{N} \Phi(r_{ij}) \qquad (3.32)$$

The first term in equation 3.32 is the long range Coulombic interaction which accounts for about 80% of the lattice energy. Computational difficulties arise in summing all these terms. The deceptively simple r^{-1} term is very slow to converge and therefore requires a prohibitively large region II. The summation of these terms can however be evaluated without such a large region II by using the Ewald summation technique (Ewald 1921). This technique is now described.

1/r can be expressed in integral form;

$$\frac{1}{r} = \frac{2}{\pi^{1/2}} \int_0^{\infty} \exp(-r^2t^2)dt \qquad (3.33)$$

where t is a variable.

This identity can be separated into two terms by splitting the integral at a point η;

$$\frac{1}{r} = \frac{2}{\pi^{1/2}} \int_0^{\eta} \exp(-r^2t^2)dt + \frac{2}{\pi^{1/2}} \int_{\eta}^{\infty} \exp(-r^2t^2)dt \qquad (3.34)$$

where η is a variable parameter, chosen to optimise the speed of convergence of the system. The first term (I_1) of equation 3.34 can be transformed into reciprocal space by Fourier analysis;

$$I_1 = \frac{2}{\pi^{1/2}}\int_0^{\eta} \exp(-r^2t^2)dt \quad = \quad \frac{4\pi}{V}\sum_{\underline{G}} \frac{1}{G^2} \exp(-G^2/4\eta).\exp(-i\underline{G}.\underline{r}) \qquad (3.35)$$

where $\underline{G}$ is the reciprocal lattice vector and V, the volume of the unit cell. The second term in equation 3.34 can be evaluated in real space;

$$I_2 = \frac{2}{\pi^{1/2}}\int_{\eta}^{\infty} \exp(-r^2t^2)dt \quad = \quad \frac{1}{r} \operatorname{erfc}(\eta r) \qquad (3.36)$$

where erfc($\underline{r}$) is the complimentary error function and is related to the standard error function by;

$$\operatorname{erfc}(\underline{r}) = 1 - \operatorname{erf}(\underline{r}) \qquad (3.37)$$

The total Coulombic contribution to the lattice energy therefore becomes;

$$\sum_{ij} \frac{q_iq_j}{r_{ij}} = \frac{4\pi}{V}\sum_{\underline{G}} \frac{\exp(-G^2/4\eta)}{G^2} \cdot \sum_{ij} q_iq_j\exp(-i\underline{G}.\underline{r}_{ij})$$

$$+ \sum_{ij} q_iq_j \frac{\operatorname{erfc}(r_{ij}\eta)}{r_{ij}} \qquad (3.38)$$

The summation is now rapidly convergent with increasing $\underline{G}$ and r. The self interaction energy terms must be subtracted.

3.6.1 Summation of the 2-Dimensional Coulomb Terms

The treatment of the Coulombic terms in a two-dimensional lattice is calculated by an analogous method, first considered by Parry (1975a, 1975b). The identity (equation 3.33) is again split into two parts; a real space summation and a reciprocal summation. The real space contribution is given by equation 3.36 without the self interaction term. The reciprocal space summation is different to the 3-dimensional case as there remains a $\underline{G} = 0$ contribution. In the 3-dimensional case, this term disappears because of the charge neutrality of the unit cell. At surfaces the contribution from the Coulombic terms are summed on each plane of the crystal and unless the planes are charge neutral, the $\underline{G} = 0$ term must be included. Furthermore the surface relaxation causes a rumpling effect in the surface ions and therefore induces a dipole perpendicular to the surfaces of crystals with charge neutral planes such as MgO{1 0 0}. The reciprocal lattice contribution to the Coulomb energy is given by;

$$I_2 = \frac{\pi}{A}\left(-2\underline{u}_{ij}\mathrm{erf}(\eta\underline{u}_{ij}) - \frac{2\exp(-\eta\underline{u}_{ij})}{\eta\pi^{1/2}}\right) + \frac{\pi}{A}\sum_{\underline{G}\neq 0}\frac{1}{\underline{G}}(B+C)\exp(i\underline{G}.\underline{p}_{ij}) \qquad (3.39)$$

Where A is the area of the unit cell, $\underline{G}$ is the reciprocal lattice vector and

$$B = \exp(\underline{G}.\underline{u}_{ij})\mathrm{erfc}[(\underline{G}/2\eta) + \eta\underline{u}_{ij}] \qquad (3.40)$$

$$C = \exp(-\underline{G}.\underline{u}_{ij})\mathrm{erfc}[(\underline{G}/2\eta) - \eta\underline{u}_{ij})] \qquad (3.41)$$

$\underline{r}_{ij}$ is resolved into two components, $\underline{u}_{ij}$ perpendicular to the interface and $\underline{p}_{ij}$ in the interfacial plane. $2\eta/\pi^{1/2}$ is subtracted from equation 3.39 to remove the self interaction term and the infinite sums are truncated when a suitable accuracy criterion is met.

3.7 Summary

The development of these methodologies now allow atomistic simulation methods to address important problems including the structure and stabilities of interfaces. The aim of the following chapters is to establish the methodology for simulating such interfaces. However, despite the efficiency of the simulation methods described in this chapter, the focus of attention will be on considering model systems, starting with the BaO//MgO interfaces.

Chapter 4

The BaO(1 0 0)//MgO(1 0 0) Interface

4.1 Introduction

The aim of the work in this chapter, is to develop and test the methodology for modelling ceramic interfaces, so that future studies can address the problem of modelling thin film devices at the atomic level of more commercially viable materials than considered here. Many factors such as epitaxial constraints imposed on interfaces with high associated misfits, defects and dislocation, ionic interactions across the interface and relaxation, all contribute to the stability of the interface and are addressed in this chapter.

Interfaces between materials with high associated misfits are constrained to accommodate the misfit resulting in a high strain energy which will destabilise the interface. This has led many workers to investigate interfaces with low associated misfits (Eibl et al. 1990a, Eibl et al. 1990b, Kwo et al. 1987). Stable interfaces between materials which must accommodate a high misfit value have been identified (Tong Lee et al. 1989, Li et al. 1989b, Ramesh et al. 1990). However, the inclusion of high defect concentrations or dislocations are required to facilitate the stability of these interfaces (Tasker and Stoneham 1987, Ramesh et al. 1990, Li et al. 1989b, Mykura et al. 1980). The defect concentration may also prove deleterious to the material properties (Allan and Mackrodt 1989b, Johnston et al. 1987) and will therefore reduce the commercial viability of these materials. The favourable interactions across the interface of oppositely charged ions contribute to the stability of the interface, however, similar charged ions in close proximity are deleterious to the stability. The removal of these ions together with relaxation of the interface will optimise the favourable interactions whilst reducing any deleterious interaction from like charged ions. These factors are all ideally suited to investigation using computer modelling techniques which can probe the interface at the

atomic level, and monitor the interfacial behaviour when the system is allowed to relax.

The BaO(100)//MgO(100) interface is examined, as a model system, to investigate the factors outlined above, which are expected to be conducive to the stability of a heteroepitaxial interface. Initially we investigate the bulk and surface properties of BaO and MgO (The lattice parameter and structural symmetry of the two materials are essential to the epitaxial relationships and resulting structural configuration which will be adopted by the BaO(100)//MgO(100) interface). We next examine the accommodation of misfit strain energy in the BaO overlayer, as a function of BaO thin film thickness on the MgO substrate. The effect of neutral (reduced density calculations) and charged defects (vacancy formation energies) at the interface regions and their influence on interfacial stability is investigated and the results are compared to vacancy formation energies calculated for a pure MgO surface (Duffy et al. 1984) to ascertain the effect the interface has on defect energies. Finally we investigate the formation of a BaO monolayer on an MgO surface built up from sequential additions of neutral BaO units. This allows the thin film to form without any constraints imposed on the BaO to accommodate a certain configuration.

4.2 Surface Methodology

By far the most stable surface of rocksalt structured solids is the (100). An alternative low index surface is the (111) which also has a higher packing arrangement, yet it is rarely seen experimentally and then only with substantial reconstruction (Handwerker et al. 1988). This section explains (following Tasker (1979)) the absence of many low index surfaces by showing them to be unstable.

The formation of a stable surface will occur only if the Madelung sums converge with

increasing crystal size. This convergence only holds when the crystal is both electrically neutral and has no dipole moment perpendicular to the surface (Tasker, 1979). Indeed, Bertaut (1958) showed that a dipole moment perpendicular to the surface would lead to an infinite surface energy. These surfaces (including rocksalt (111)) are unstable and are not observed without substantial reconstruction or adsorption of foreign ions to remove the dipole.

The necessity of substantial reconstruction, can be illustrated by considering the continuum approximation of the interaction between charged planes;

The electrostatic potential at any plane P, (figure 4.1a) due to two planar sublattices one of overall charge +q and the second of charge -q at a perpendicular distance z and (z+δz) respectively, reduces to a simple form in the continuum approximation, when z is greater than a few interatomic spacings (δz):

$$V(z) = \frac{2\pi qz}{A} - \frac{2\pi q(z+\delta z)}{A} = -\frac{2\pi q\delta z}{A} \qquad (4.1)$$

A is the area of the unit cell in the plane. For N sets of planes, the electrostatic potential increases without limit and is given by;

$$V(z) = \left(\frac{2\pi q\delta z}{A}\right) N \qquad (4.2)$$

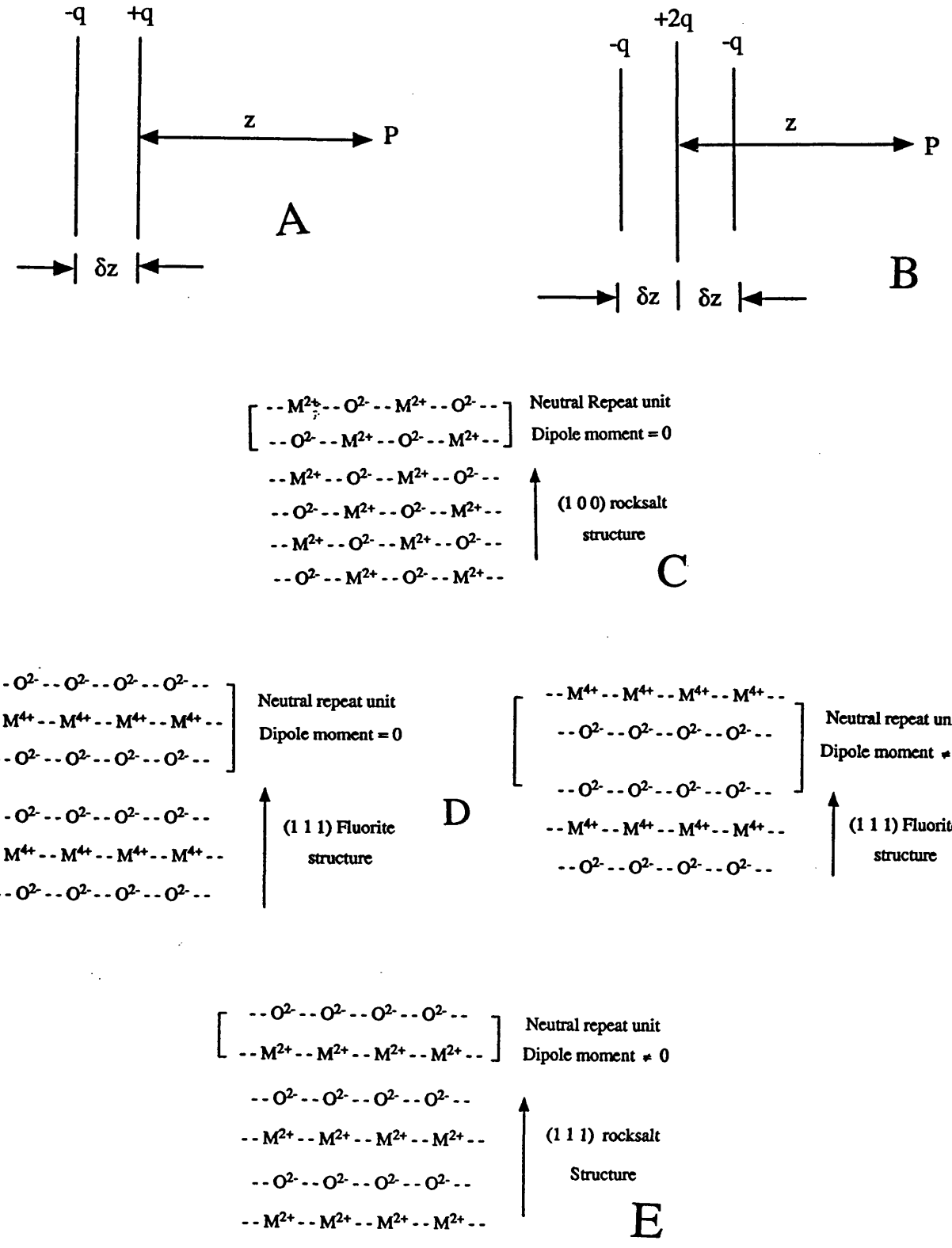

Figure 4.1 (a) Schematic of two charged planes of a type 3 surface, to explain the divergence of the potential at any plane in the crystal at an infinite distance from the plane. (b) Schematic of three charged planes representing a type 2 surface, to show that the potential is zero for large z. (c) Schematic of a type 1 surface. (d) Type 2 surfaces. (e) Type 3 surface.

These types of surfaces are, following Tasker (1979), designated type 3 surfaces and are generally unstable.

A second case exists where the crystal is constructed of a neutral block of planes (figure 4.1b). The potential at any plane P is given by;

$$V(z) = \frac{2\pi(2qz)}{A} - \frac{2\pi(q[z-\delta z])}{A} - \frac{2\pi(q[z+\delta z])}{A} = 0 \qquad (4.3)$$

Here the contributions to the potential from the planes in the neutral repeat unit cancel and the potential becomes zero at large distances. These surfaces are designated type 2 surfaces. A final case exists where each plane maintains electroneutrality. These surfaces are designated type 1 surfaces and the potential cancels on each plane. This also explains why reliable interatomic potentials are critical to our calculations, as the relaxation of a surface will result in the formation of a small dipole, the effect of which is independent of depth.

These points are illustrated in figures 4.1(c)-(e) showing three types of stacking sequences: type 1, type 2 and type 3. Figure 4.1(c), representing a type 1 structure, has an equal number of cations and anions, to give crystal planes of overall electroneutrality. It has no dipole moment perpendicular to the surface and the potential, equation (4.1) cancels for each plane. Additional neutral planes added to the surface, will make no contribution to the energy of the ions in the bulk of the crystal. The lattice sums required for the Madelung energy to converge at any ion site, require only a few planes either side of the site. Examples of this surface include rocksalt (100) and (110) and perovskite (100).

Figure 4.1(d), represents a type 2 structure. Two configurations can be envisaged, although only one will be stable. The surface terminating with a single anion plane consists of a neutral three plane repeat unit and hence there is no dipole moment perpendicular to the surface. Each plane will contribute a term to the potential sum which cancels over the three plane repeat unit. Addition of further three plane repeat units to the surface will again make no contribution to the energy of the ions in the bulk of the crystal. This type of surface is similar to a type 1 surface, except that each repeat, has a finite thickness. In contrast, the surface terminating with the cation plane produces a dipole moment in the repeat unit perpendicular to the surface. The addition of neutral repeat units continue to propagate the dipole an infinite distance into the crystal. The Madelung sums cannot be truncated and the summation diverges with increasing crystal size to give infinite surface energies. Examples of stable type 2 surfaces are fluorite (111) with terminating anion plane.

Figure 4.1(e), represents a type 3 structure. It consists of alternating charged planes which introduces a dipole moment perpendicular to the surface. These surfaces are unstable and generally not observed in ionic crystals. CoO and UO_2 have been observed to accommodate type 3 structures however both these substances can support complex defect structures (Hall et al. 1985). The rocksalt (111) surface is an example of a type 3 structure.

4.3 Crystal Structure

Both MgO and BaO exhibit the rocksalt structure of general formula MO, where M is the metal cation and with lattice parameters 2.10Å and 2.77Å respectively. The lattice is face-centred cubic, with each M^{2+} cation surrounded by six O^{2-} anions in a regular

octahedral arrangement. In MgO, the anion is roughly twice the size of the cation, whereas in BaO they are almost the same size.

4.3.1 Surface topography

The potentials employed for modelling the MgO and BaO were those derived by Lewis and Catlow (1985c). The calculation of properties that are not included in the fitting procedure used to derive the potentials provide a useful test of their reliability. A stringent test of these potentials is the modelling of surfaces, as the existence of a surface implies the existence of a discontinuity. The oxygen potential will therefore be affected by the local environment as, for MgO or BaO, the oxygen coordination changes from six to five resulting in a less compressed oxygen wavefunction. This argument suggests that surface specific potentials may be necessary.

The calculated surface energy for MgO(100) is 1.23 Jm^{-2}. This compares with an experimentally determined value of 1.43 Jm^{-2} (Causer, 1986). The surface energy of BaO is calculated to be 0.35 Jm^{-2}. The calculated surface structure of MgO reveals a 3% relaxation of the surface ions into the bulk together with a 1% rumpling (alternate inward and outward movement of both types of ions at the surface plane) with magnesium displaced into the bulk crystal. Many studies of the relaxation and rumpling of the MgO(100) surfaces have been performed. A review by Henrich (1985) suggests the surface to be very nearly a truncation of the bulk crystal structure, with any relaxation or rumpling limited to a few percent of the bulk lattice constant.

The excellent agreement between the calculated and experimentally determined surface energies and the correlation between the calculated and observed relaxation and rumpling of ions at the surface region, suggests the potentials employed are reliable in

modelling surfaces. For surface and interface calculations, the ions are in different crystal environments from which they were derived and therefore the ability of these potentials to accurately model surfaces suggests we can also confidently employ them to model interfaces.

4.4 Epitaxial Constraints

To investigate the BaO//MgO interface, we first consider epitaxial constraints to ensure lattice periodicity at the interface region.

The non-commensurate relationship between the lattice parameters of BaO (2.77Å) and MgO (2.10Å) leads to a prohibitively large two dimensional unit cell. Following Cotter et al. (1988, 1989) epitaxial matching can be achieved by considering the near equality between $\sqrt{2}\ a_o$(MgO) and a_o(BaO) resulting in a 7% misfit between the two lattices. This relationship requires the BaO overlayers to be rotated 45° with respect to the MgO substrate. Three distinct configurations arise (Figure 4.2). Firstly with the barium and oxygen of the BaO lattice constrained to sit above the magnesium sublattice of the MgO crystal surface. Secondly, with the barium and oxygen constrained to sit above the oxygen sublattice. Finally with the BaO sited above the interstitial sites of the MgO lattice.

The bulk regions of the MgO and BaO lattices forming the interface must exhibit their natural lattice parameter as the energy required to compress or expand a real crystal with perhaps 10^8 layers is prohibitive. The two materials must also be in complete commensuration (as grain boundaries) at the interface region. With the small size of the unit cell it is not possible to accommodate both these criterion. The MgO crystal was therefore allowed to exhibit its natural lattice spacing and BaO monolayers were

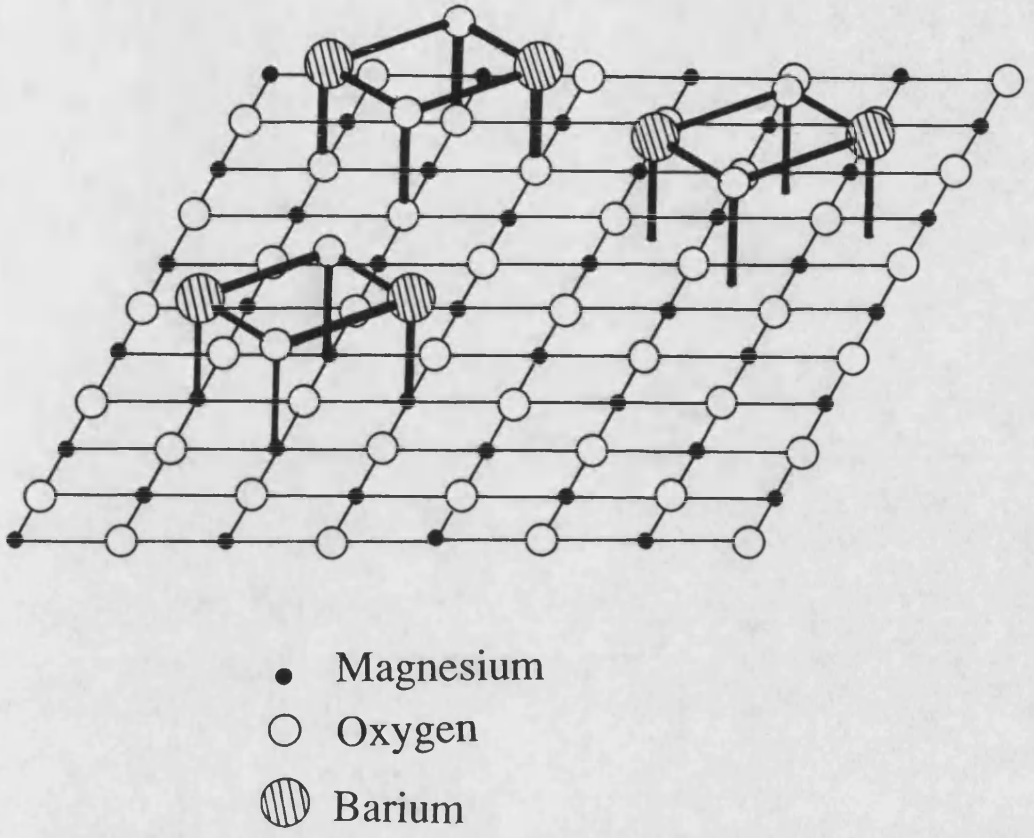

Figure 4.2 Diagrammatic representation of three configurations of BaO overlayers on an MgO(100) substrate. The BaO is constrained to adopt positions above the oxygen sublattice of the MgO, above the magnesium sublattice and also at interstitial positions.

sequentially added to the MgO substrate accommodating the full 7% mismatch. The strain energy is therefore intrinsically calculated for every BaO layer added.

The energies of adding successive BaO layers to the MgO substrate can be considered in two ways; type A and type B. Type A indicates the feasibility of adding further BaO layers to increase the BaO thin film thickness and is given by;

$$E_A = E_{interface(nBaO)} - E_{interface((n-1)BaO)} \quad (4.4)$$

where n is the number of BaO layers added to the MgO substrate. Type B depicts the stability of the interface as a function of layers and is given by;

$$E_B = (E_{interface(nBaO)} - E_{MgO})/n \quad (4.5)$$

The calculated energies of adding BaO monolayers to the MgO substrate are given in figure 4.3a for 1-8 BaO layers added to the MgO substrate.

The undulations in figure 4.3a (type A) up to four BaO layers, can be attributed to the relaxation of the system leading to the reduction of both the strain imposed on the BaO lattice and the unfavourable barium-magnesium interactions across the interface. The undulation is clearly dampened by the fifth BaO layer added. This can be attributed to the reduction in the freedom the BaO layers have to relax at the interface region because of the hindrance from the BaO layers above. The stability of the interface will steadily decrease with further layers as the strain energy will not be alleviated by the relaxation. One must note that these energies are not absolute interfacial stabilities but indicate the relative stabilities of various layers.

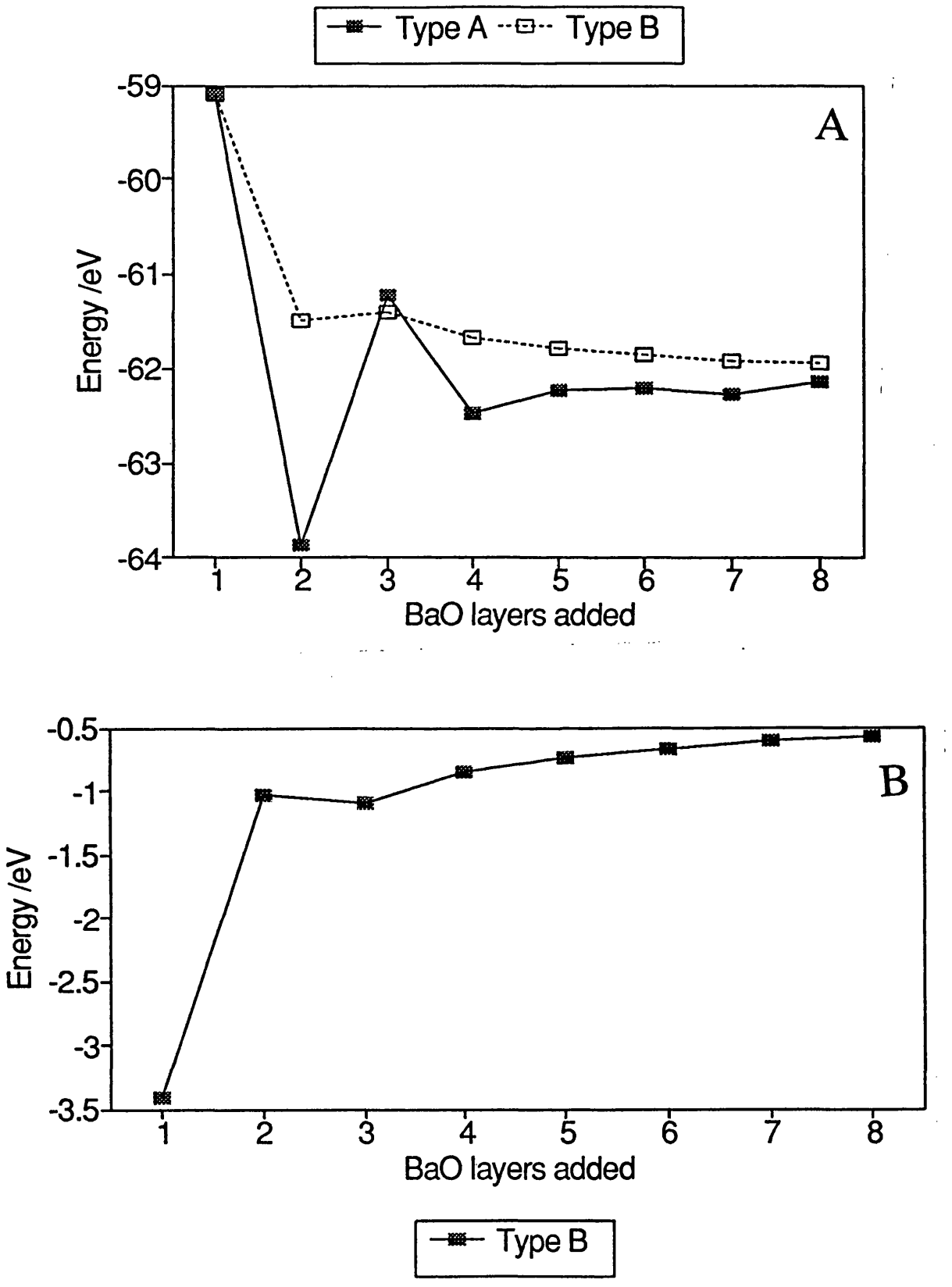

Figure 4.3 Calculated energies of adding successive BaO layers to an MgO substrate. (a) Type A and type B. (b) type A relative to pure MgO and pure BaO. The energy values (figure 4.3a) are calculated for 2 BaO units on the MgO (the energy for 2 BaO units in bulk BaO is calculated to be -62.52 eV).

Figure 4.3b shows the energy of the interface relative to pure MgO and pure BaO. In this calculation the energy of a BaO unit (the energy value for a bulk BaO crystal) is subtracted from the type B energies. This figure represents the energy required to remove the BaO overlayer from the MgO surface for one to eight BaO layers added and can therefore be compared directly to experimental results as it illustrates the stability of the interface. The results suggest however that the interface is unstable with respect to pure BaO and MgO for all BaO layer coverages i.e. the energies are negative. This does not preclude that the interface does not exist as the simulation may have located a metastable interface and not a global energy minimum. This can be considered analogous to purely siliceous zeolites which are metastable structures and are unstable with respect to quartz. Another factor which has not been considered is the energy of a BaO thin film may be lower than the bulk value. This is addressed in chapter 6.

The configuration considered in these calculations is with the BaO constrained to sit above the magnesium sublattice of the MgO. Configurations with the BaO over the magnesium or oxygen sublattices gave similar energies after relaxation (in accordance with Cotter et al. (1988, 1989)). However, the distance between the BaO overlayers and the MgO substrate is calculated to be 5.4Å with BaO accommodating oxygen sublattice positions compared to 2.1Å with the BaO accommodating the magnesium sublattice positions. This suggests the instability at the interface, attributed to the anion-anion repulsion at the interface, causes the interface to fall apart when BaO lies above the oxygen sublattice positions. The configuration with the BaO constrained to occupy the sites above the interstitial positions of the MgO lattice gave energies which were lower (more unstable) than with the BaO above the magnesium sublattice of the MgO crystal. The misfit for all these interfaces is identical therefore the difference in energy must be

attributed entirely to the favourable interactions and relaxation across the interface.

4.5 Interfacial Defects

The inclusion of defects at the interface is sometimes essential to ensure interfacial stability. In simulating the NiO//BaO interface, Tasker and Stoneham (1987) included a large number of defects in the NiO, in particular cation vacancies and Ni^{3+} ions. Tasker concluded that the defect concentrations are essential for stabilising the interface, which would fall apart if the full stoichiometric oxides were maintained.

There are two main driving forces for defect formation. Firstly the image terms (Jennings and Jones 1988) will stabilise charged defects near an interface of higher dielectric constant (Harding 1990). Second, epitaxial constraints may require additional vacancies in the structure (Tasker et al. 1985). The removal of a periodic array of ions at the interface will enable good charge matching throughout the interface and reduce the energy penalty of bringing like charges together. Early simulation of twist grain boundaries in rocksalt structured oxides indicated that boundaries with the twist axis oriented along the [001] direction are only barely stable with respect to the free surfaces (Wolf 1981, 1982). This is in contrast to (Sun and Balluffi 1982a) who identified stable MgO(001) twist grain boundaries experimentally. The discrepancy was later rectified by Duffy (1986) who attributed the stability to a reduced density of ions at the boundary plane. The restructured interface was calculated to have a lower energy than the interface containing the full complement of ions and stable with respect to the free surfaces. The vacancies are therefore not defects, since the reduced density is a consequence of the lowest energy structure.

4.5.1 Reduced density calculations

In this section, we examine the effects of reduced interfacial density and interfacial defects on the interfacial energy for the BaO//MgO interface, conforming to the $\sqrt{2}$ a_o(MgO)= a_o(BaO) configuration.

Uncharged BaO and MgO units were removed from the interface to create five different interface configurations H1-H5 which are represented diagrammatically in figure 4.4 (for type 'H' the BaO is constrained to accommodate sites above the magnesium sublattice of the MgO substrate and for type 'O', the BaO is constrained to accommodate sites above the oxygen sublattice of the MgO substrate). Configurations H1 and H2 involve the removal of BaO units from the interfacial region and H3, H4 and H5 have MgO units removed from the interface region. The defect energy is the energy difference between the pure and defective interface and is calculated as a function of defect concentration at the interface region.

The defect concentration is measured by considering the ratio of BaO to MgO ions at the interface. For example, the pure interface (no defects) conforming to the $\sqrt{2}$ a_o(MgO)= a_o(BaO) configuration, exhibits a BaO/MgO ratio of 1:2 or 0.5. If an MgO unit were removed from the interface region for every unit cell for example type H3, the ratio or 'local' interfacial stoichiometry changes to 1:1 or 1.0. Further complications arise when one considers the removal of an MgO unit every unit cell by removing a magnesium from the first MgO plane at the interface region together with an oxygen ion from the second MgO plane, type H4 or type H5. The stoichiometric ratio of BaO to MgO in this case is therefore 2:3 or 0.666 as two BaO and MgO planes must be considered either side of the interface. The defect energy calculated at a BaO/MgO stoichiometry of 1:2 is the defect energy at infinite dilution.

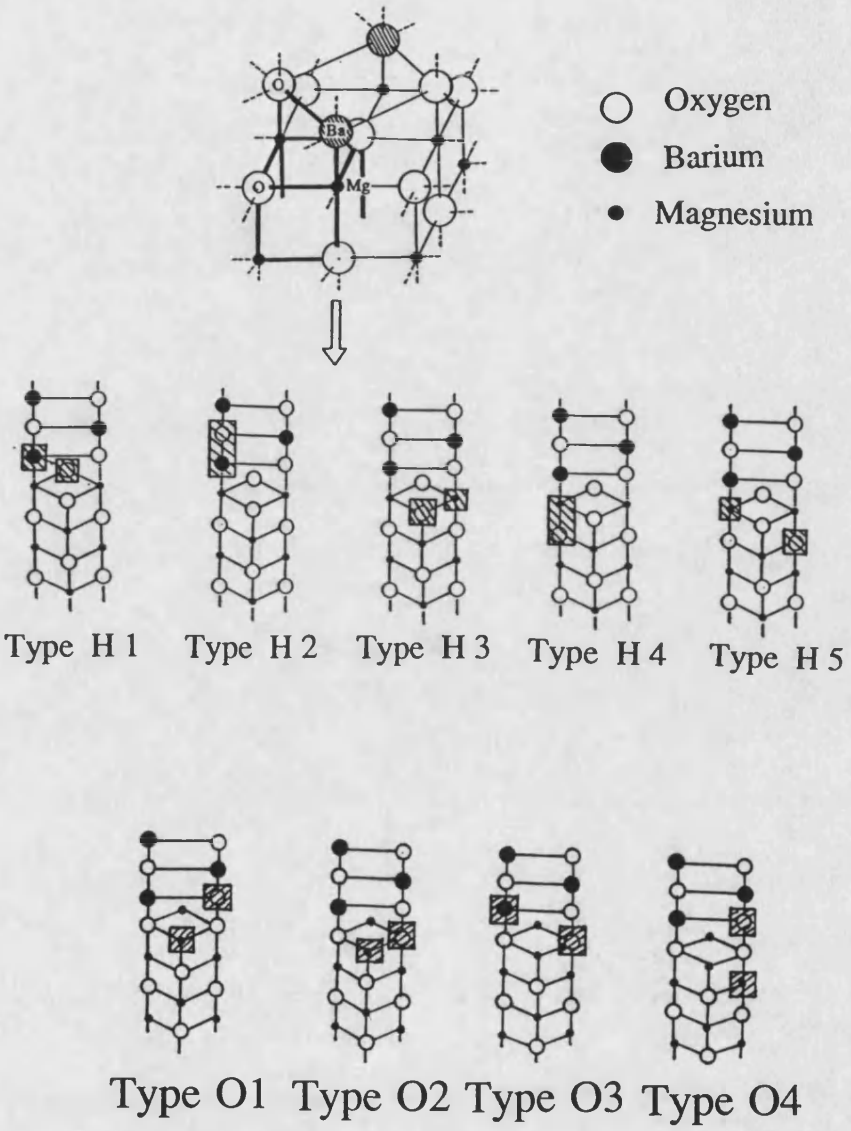

Figure 4.4 Diagrammatic representations of the interface defect configurations. H1-H5 with BaO constrained to sit above the magnesium sublattice and O1-O4 with BaO constrained to sit above the oxygen sublattice of the MgO substrate.

Figure 4.5 show the calculated defect energies, as a function of BaO/MgO stoichiometry, for defect types H1 and H2 (BaO units removed from the interface region). Figure 4.5a shows the defect energy, as a function of local BaO/MgO stoichiometry, for defect type H1. The figure shows that at a BaO/MgO stoichiometry of 1:3, the defect energy is -0.035 eV. At lower defect concentrations, the interface is destabilised with respect to the perfect interface, leading to a maximum defect energy at a BaO/MgO stoichiometry of 5:11. At infinite defect dilution the defect energy is calculated to be +3.36 eV. A negative defect energy at a BaO//MgO ratio of 1:3 suggests that the defects actually stabilise the interface. Closer inspection of the relaxation at the interface region reveals that the structure is almost identical to the interface with a full density of ions (the relaxation results in the density of the ions at the interface region being restored from relaxations of ions to the interface region from the bulk of the MgO and BaO crystals). This suggests that the minimisation procedure has identified an alternative local energy minimum for the perfect (no defects) interfaces even though the initial configuration accommodated defects. This argument is strengthened when one considers the defect energy is very close to zero (-0.035 eV) and local minima configurations are expected to be similar in energy. For the potential models employed in this work to direct the system back to the original perfect interface configuration from a very different initial interfacial configuration, is a useful result as it shows the adequacy of the minimisation method employed in this work. Figure 4.5b shows the calculated defect energies as a function of BaO//MgO stoichiometry at the interface region, for defect type H2. The figure shows a distinct minimum at a BaO/MgO stoichiometry of 3:8 with an associated defect energy of +0.49 eV.

Figure 4.6 shows the calculated defect energies, as a function of BaO/MgO stoichiometry, for defect types H3, H4 and H5 (MgO units removed from the interface

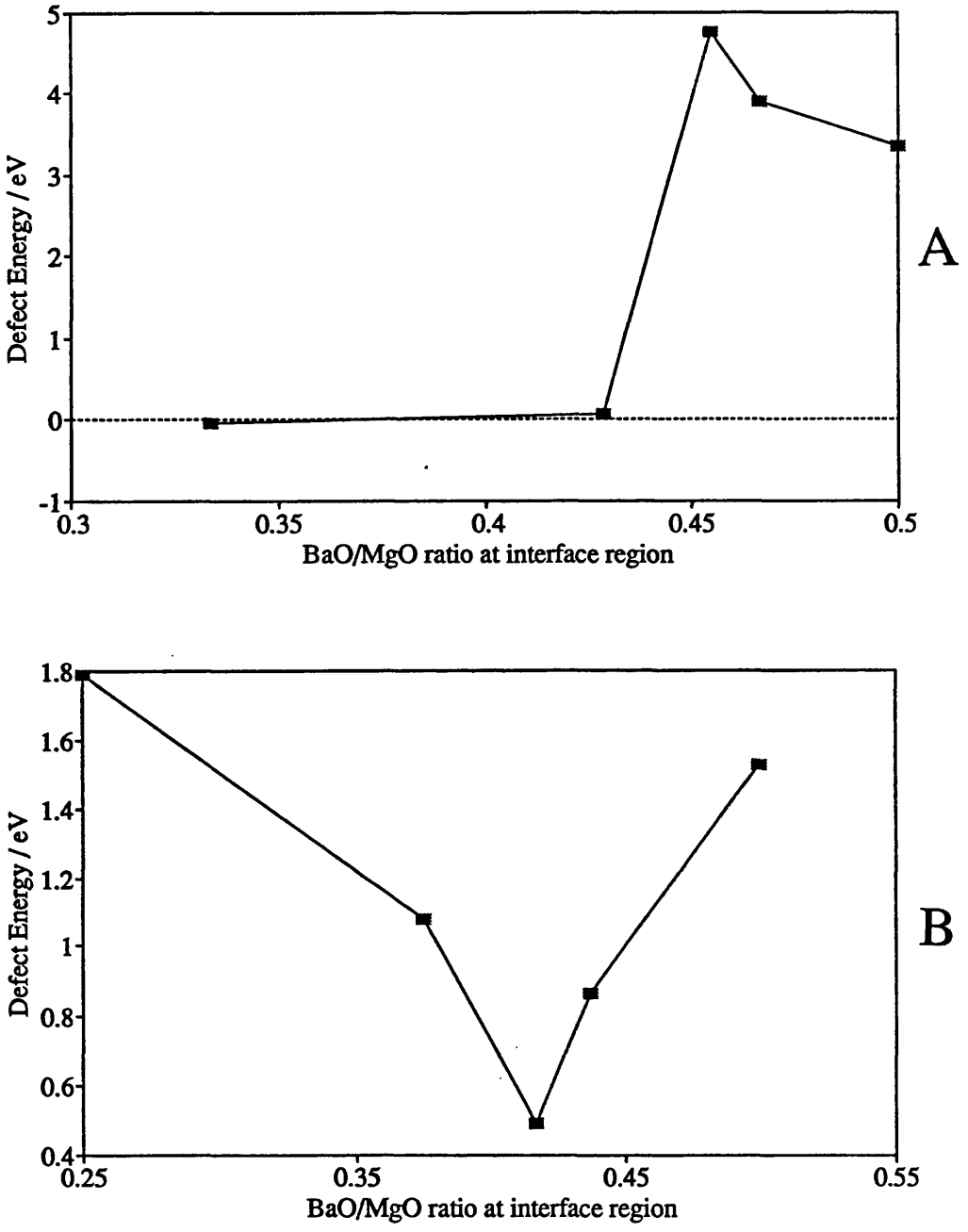

Figure 4.5 Calculated defect energies as a function of local BaO/MgO stoichiometry. (a) Defect type H1. (b) Defect type H2. The BaO is constrained to accommodate positions above the magnesium sublattice of the MgO substrate.

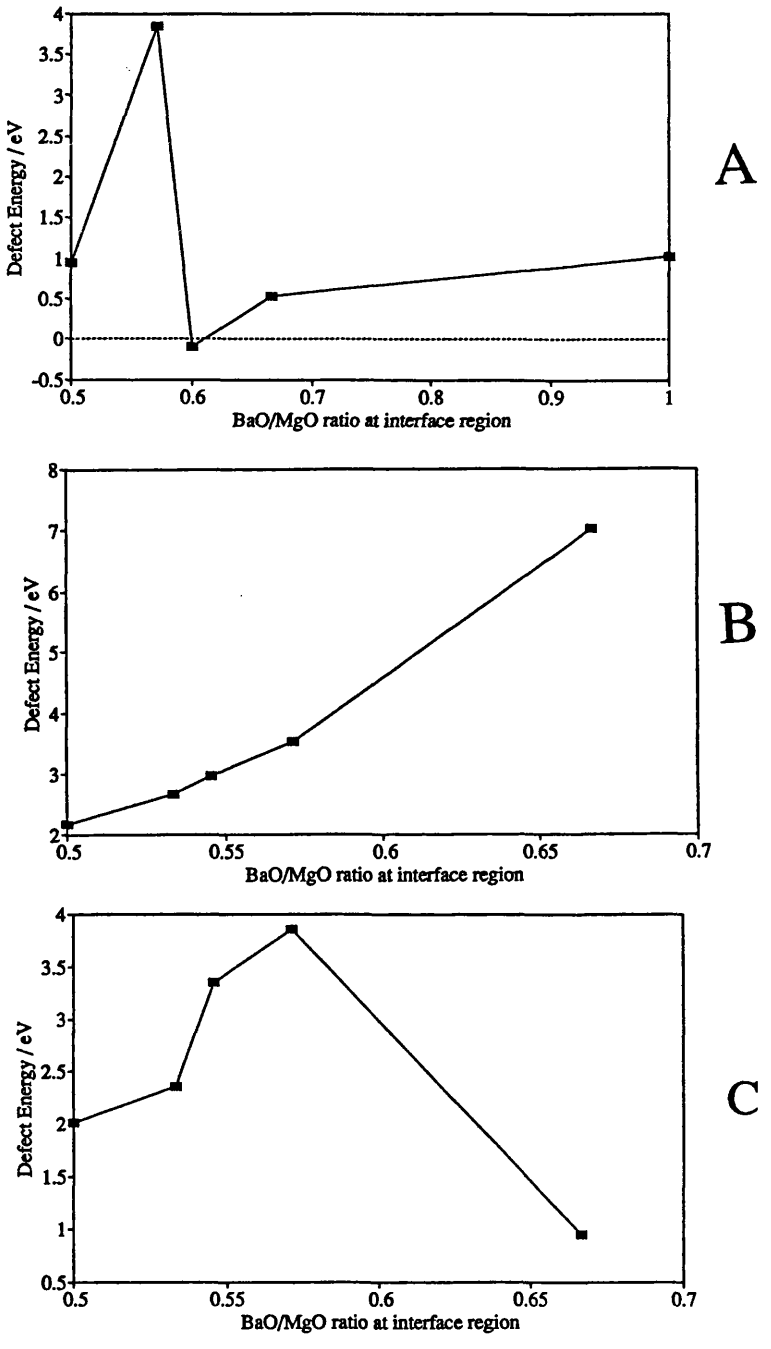

Figure 4.6 Calculated defect energies as a function of local BaO/MgO stoichiometry. (a) Defect type H3. (b) Defect type H4. (c) Defect type H5. The BaO is constrained to accommodate positions above the magnesium sublattice of the MgO substrate.

region). Figure 4.6a shows the calculated defect energies for defect type H3. A defect energy of -0.094 eV is calculated at a BaO/MgO stoichiometry of 0.6. The calculated structural configuration of this interface is dissimilar to the perfect interface structure (figure 4.7a represents the perfect interface structure and figure 4.7d, the reduced density interface with a local stoichiometry of 0.6) and therefore the minimisation has not located an alternative local energy configuration for the perfect lattice. A negative defect energy suggests that the existence of the defects will enhance the stability of the interface. We can therefore conclude that not only do these defects exist at the interface region but they must also be an intrinsic part of the low-temperature interface structure.

Figure 4.6b shows the calculated defect energies as a function of local BaO/MgO stoichiometry for defect type H4. The figure shows that the defect energy varies almost linearly with increasing defect concentration with a minimum defect energy of +2.17 eV at infinite dilution. Finally figure 4.6c shows the calculated defect energies for defect type H5. This figure shows a maximum defect energy at a BaO/MgO stoichiometry of 8:15 and an associated defect energy of +3.85 eV and a minimum at a higher defect concentration with a BaO/MgO stoichiometry of 1:3 and an associated defect energy of +0.94 eV. A defect energy of 2.01 eV is calculated at infinite dilution.

To ascertain the reasons by which the defect energy may be lowered we now consider the detailed relaxed structural configurations of three interfaces. Figure 4.7a shows the relaxed structure of the perfect interface i.e. with no defects. The minimisation of the perfect interface has resulted in the magnesiums relaxing towards the oxygen ions of the BaO lattice and away from the barium ions. Identical behaviour was observed from similar calculations performed by Cotter et al. (1988, 1989). The driving force underlying this behaviour is to maximise the contribution to the interfacial energy from

Figure 4.7 Diagrammatic representation of the calculated relaxed structures after relaxation of (a) The perfect full density interface. (b) Type H3 defects with a local BaO/MgO stoichiometry of 1:1. (c) type H5 defects with a local BaO/MgO stoichiometry of 1:3. (d) Type H3 defects with a local BaO/MgO stoichiometry of 3:5. Oxygens are coloured red, barium is white and magnesium is purple.

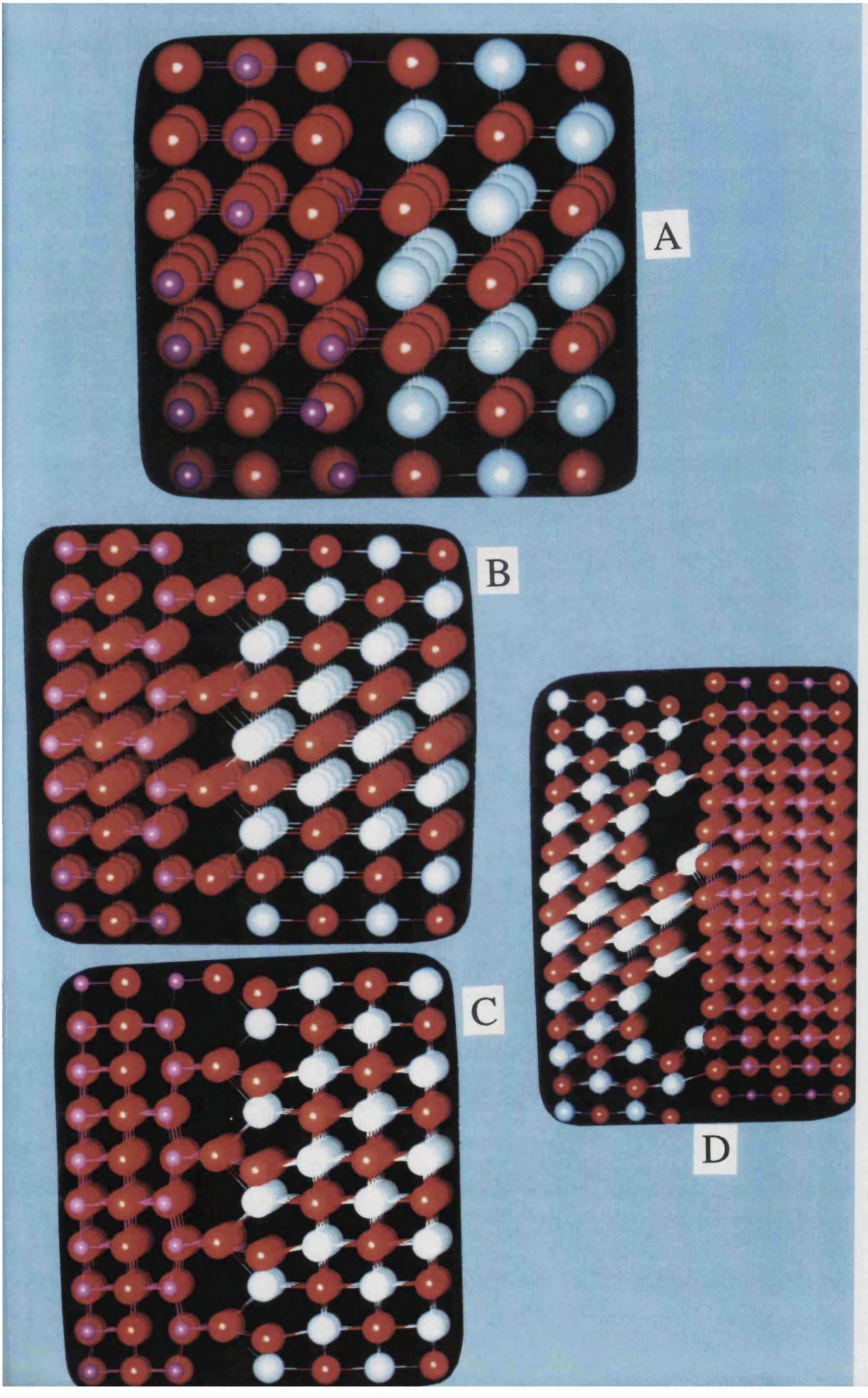
A
B
C
D

the attractive Ba^{2+}-O^{2-} interactions and minimise the contribution to the interfacial energy by the repulsive Mg^{2+}-Ba^{2+} interactions. Figure 4.7b shows the relaxed interface structure for the system containing type H3 defects with a BaO/MgO stoichiometry of 1:1. The removal of the atoms at the interface, which effectively reduces the density of ions at the interface region, has enabled good charge matching across the interface via removal of the unfavourable repulsive interaction between barium and magnesium ions. Figure 4.7c depicts the relaxed interface including type H5 defects with a BaO/MgO stoichiometry of 1:3. The removal of the ions together with the relaxation has again enabled good charge matching across the interface. The interface structures shown in figure 4.7b and figure 4.7c are however unstable with respect to the relaxed perfect interface structure implying that achieving good charge matching across the interface and decreasing ion density at the interface region will not necessarily stabilise the interface. Figure 4.7d is the relaxed interface structure with a BaO/MgO stoichiometry of 3:5. Again good charge matching and reduced ion density at the interface are observed. The interface in this case has been stabilised with respect to the perfect interface (as the defect energy is negative) and therefore this configuration is expected to be a part of the low temperature interface structure.

These calculations involved the BaO constrained to sit above the magnesium sublattice of the MgO structure. Further calculations were performed to identify any low energy reduced density interfaces, with the BaO above the oxygen sublattice. The reason attributed to the lower stability of this interface compared to BaO above the magnesium sublattice, is the oxygen-oxygen repulsion at the interface. The reduction of ion density at the interface is therefore expected to alleviate this unfavourable interaction by removal of one of the oxygens and may increase the interfacial stability. It is therefore justifiable in considering this interface further.

Four configurations were considered O1-O4 (Figure 4.4). The calculated stabilities are given in figure 4.8a-d respectively. In this case none of the reduced density interfaces are stabilised with respect to the interface with a full density of ions. For defect type O3 (figure 4.8c), the defect energy is calculated to be 0.0 eV at a BaO/MgO stoichiometry of 1:3. This is attributed to the minimisation again locating a local energy minima for the perfect (no defects) interface.

The work in this thesis is primarily to ascertain the factors conducive to the interfacial stability and therefore we have not exhaustively considered all possible configurations. An exhaustive treatment may indeed identify more reduced energy interfaces which are stabilised with respect to the perfect interface (for BaO above the oxygen sublattice of the MgO substrate).

4.5.2 Vacancy formation energies

In this section we examine the effect charged defects have on the interface. The justification for these calculations is that at temperatures other than absolute zero, the materials considered will be defective and the defect chemistry is likely to be modified by the presence of a surface or interface (Tasker et al. 1985).

Firstly we calculate oxygen vacancy formation energies in both MgO and BaO, as a function of depth relative to the interface. Second we calculate magnesium and barium vacancy formation energies as a function of depth from the interface.

The relaxed $\sqrt{2}\ a_o(MgO) = a_o(BaO)$ (BaO over Mg sublattice) interface structure is used as a reference state for the point defect formation energy calculations. The relaxation

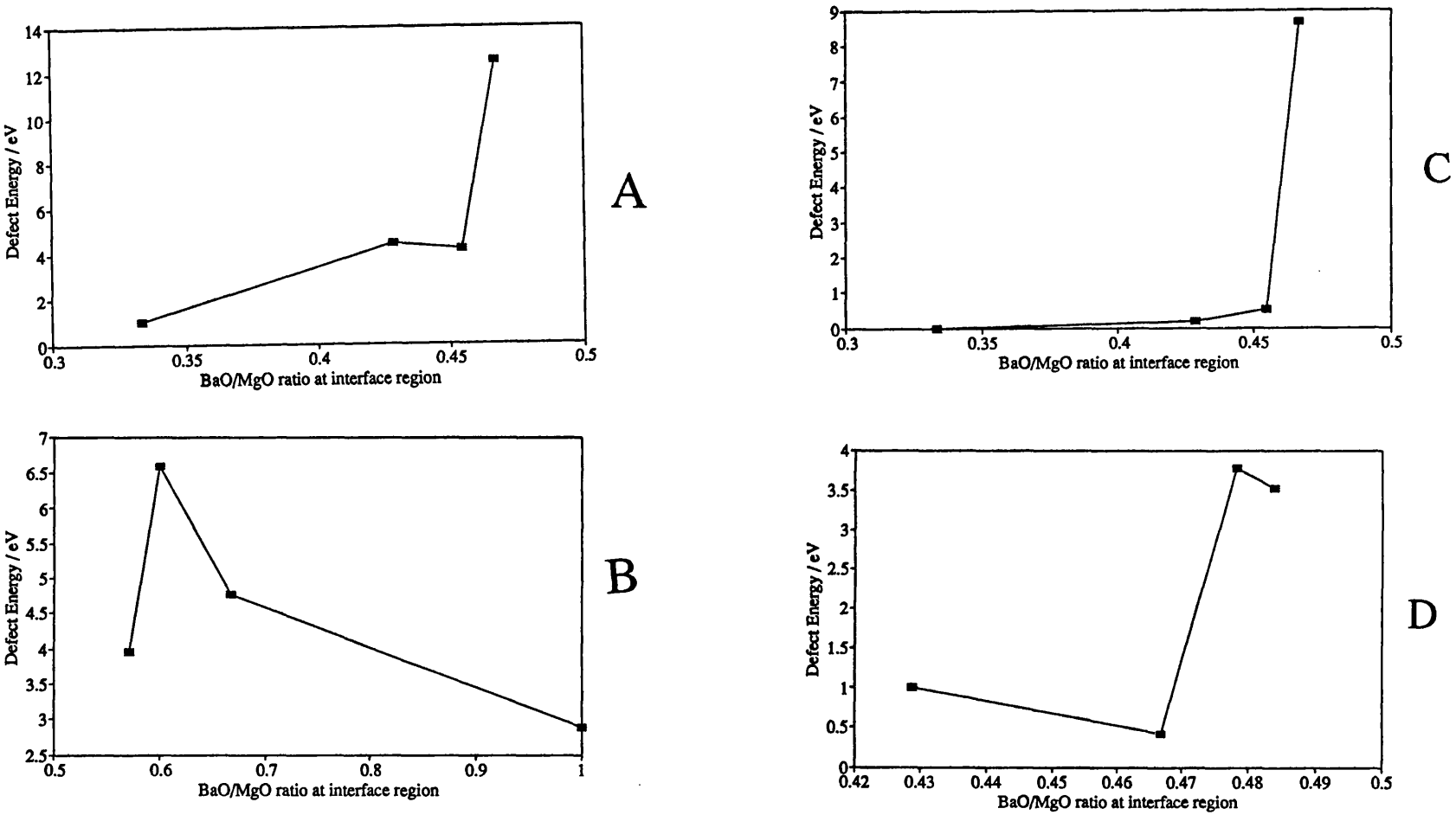

Figure 4.8 Calculated defect energies as a function of local BaO/MgO stoichiometry. (a) Defect type O1. (b) Defect type O2. (c) Defect type O3. (d) Defect type O4. The BaO is constrained to accommodate positions above the oxygen sublattice of the MgO substrate.

and rumpling at the interface, induces a long range electrostatic potential into the bulk of the crystal (Duffy et al. 1984). For a bulk defect, the outer region of the crystal is considered to be a polarisable dielectric continuum extending to infinity and the defect will be insensitive to this potential. The energies of charged defects calculated by the surface methods never tend to the values calculated by bulk methods as the potential is of infinite range (Mackrodt 1989a). This leads to a shift in the Madelung field in the near interface region, which can be quantified by the expression "qV", where q is the full ionic charge of the ion involved and V, the shift in potential. The shift V is dependent on the magnitude and displacement of the ions at the interface and hence will be unique to a given interface i.e. the shift in potential is the result of a dipole induced by relaxation of the surface ions. The calculated vacancy formation energies are therefore adjusted for the shift in the Madelung energy.

An extra feature that must be considered is that surfaces or interfaces are associated with a dielectric discontinuity at the surface or interface region. The dielectric discontinuity at an interface alters the polarisation of the oxide around a charged defect near the interface (Stoneham and Tasker 1987). From classical electrostatics, we can calculate the energy of a charge near a dielectric interface; For BaO//MgO with dielectric constants, ϵ_{MgO} and ϵ_{BaO}, then the presence of a charge, Q, in MgO, introduces an additional image term in the interfacial energy:

$$E_{image} = \frac{Q^2}{4z\epsilon_{MgO}} \left(\frac{(\epsilon_{MgO} - \epsilon_{BaO})}{(\epsilon_{MgO} + \epsilon_{BaO})} \right) \qquad (4.6)$$

Where z is the distance of the charge from the boundary. The effect of the image charge

is to stabilise charged defects approaching the interface from the material with lower dielectric constant. Thus from the dielectric constants, i.e. $\epsilon_{BaO} = 34$ and $\epsilon_{MgO} = 11$, we would expect charged defects approaching the interface from MgO to be stabilised. However, the detailed atomic structure may modify this result.

4.5.2a Anion Vacancy formation Energies

Figure 4.9 shows the oxygen vacancy formation energy in the BaO//MgO interface as a function of depth from the interface. The dotted lines represent oxygen vacancy formation energies in bulk BaO (17.3eV) and bulk MgO (25.1eV). MgO oxygen vacancies approaching the interface are destabilised by 1eV whilst BaO oxygen vacancies are stabilised by 4eV on approaching the interface. The continuum method therefore does not predict the general behaviour of vacancy formation energies as they approach the interface (the image charge effect stabilises charged defects approaching the interface from the material with lower dielectric constant). Furthermore, for the defect to pass through the interface, equation (4.6) gives a spurious divergence. When the defect approaches the interface from the material of higher dielectric constant, the energy (image charge) goes to plus infinity; when approaching from the material with lower dielectric constant, the energy goes to minus infinity. Although we would not expect good agreement of image theory at the interface. However, the image theory fails for all distances. The reason for the failure of the image theory can be attributed to the misfit strain energy and the effect that relaxation has on reducing this strain energy for the vacancy formation energies.

4.5.2b Cation Vacancy formation Energies

The vacancy formation energies for barium and magnesium in the BaO//MgO interface as a function of depth are given in figure 4.10. As with the oxygen vacancy formation

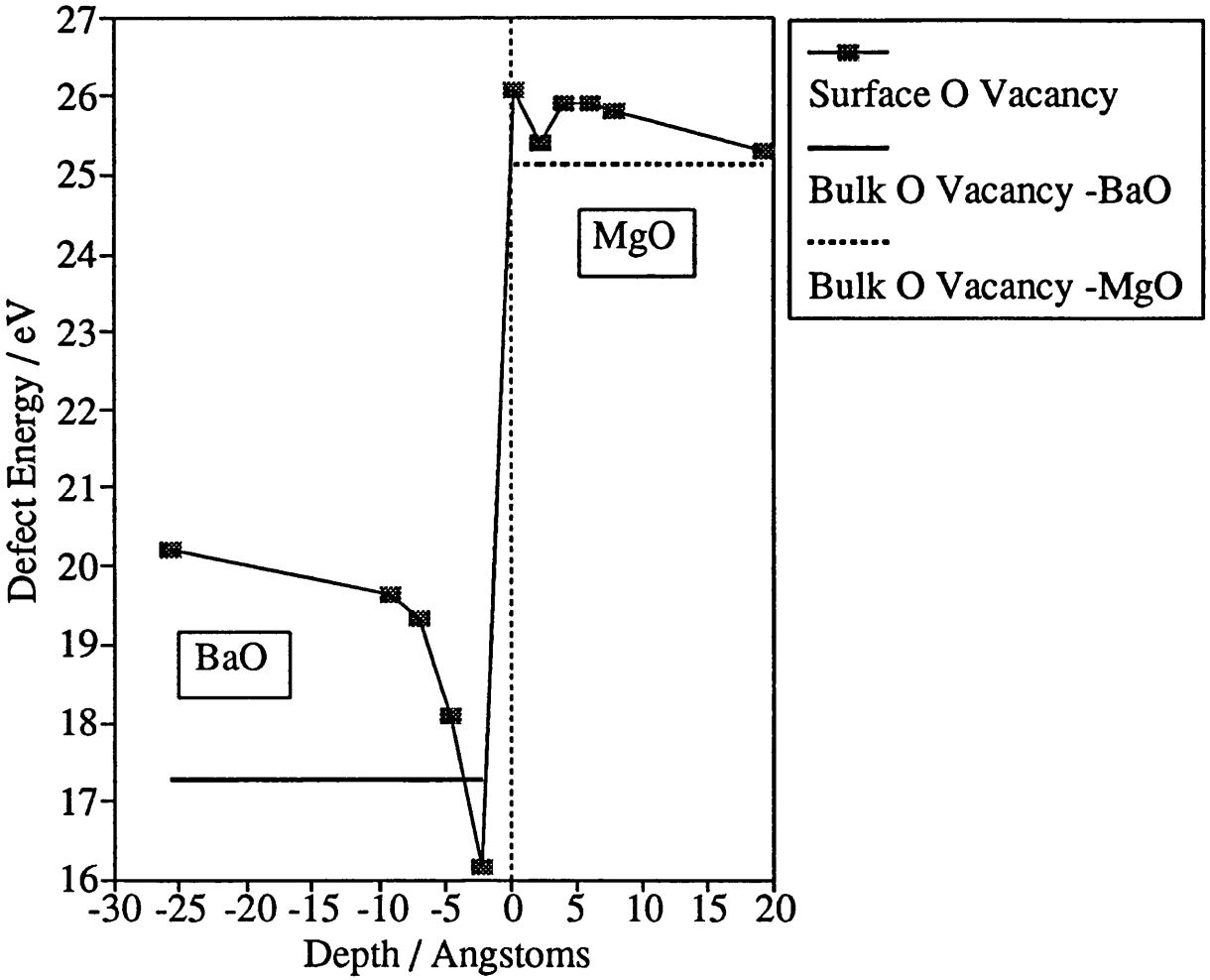

Figure 4.9 Oxygen vacancy formation energies as a function of depth in the near interface region of the BaO(100)//MgO(100) interface. A depth of 0 represents the interface. Positive depths represent MgO oxygen vacancies and negative depths represent BaO oxygen vacancies.

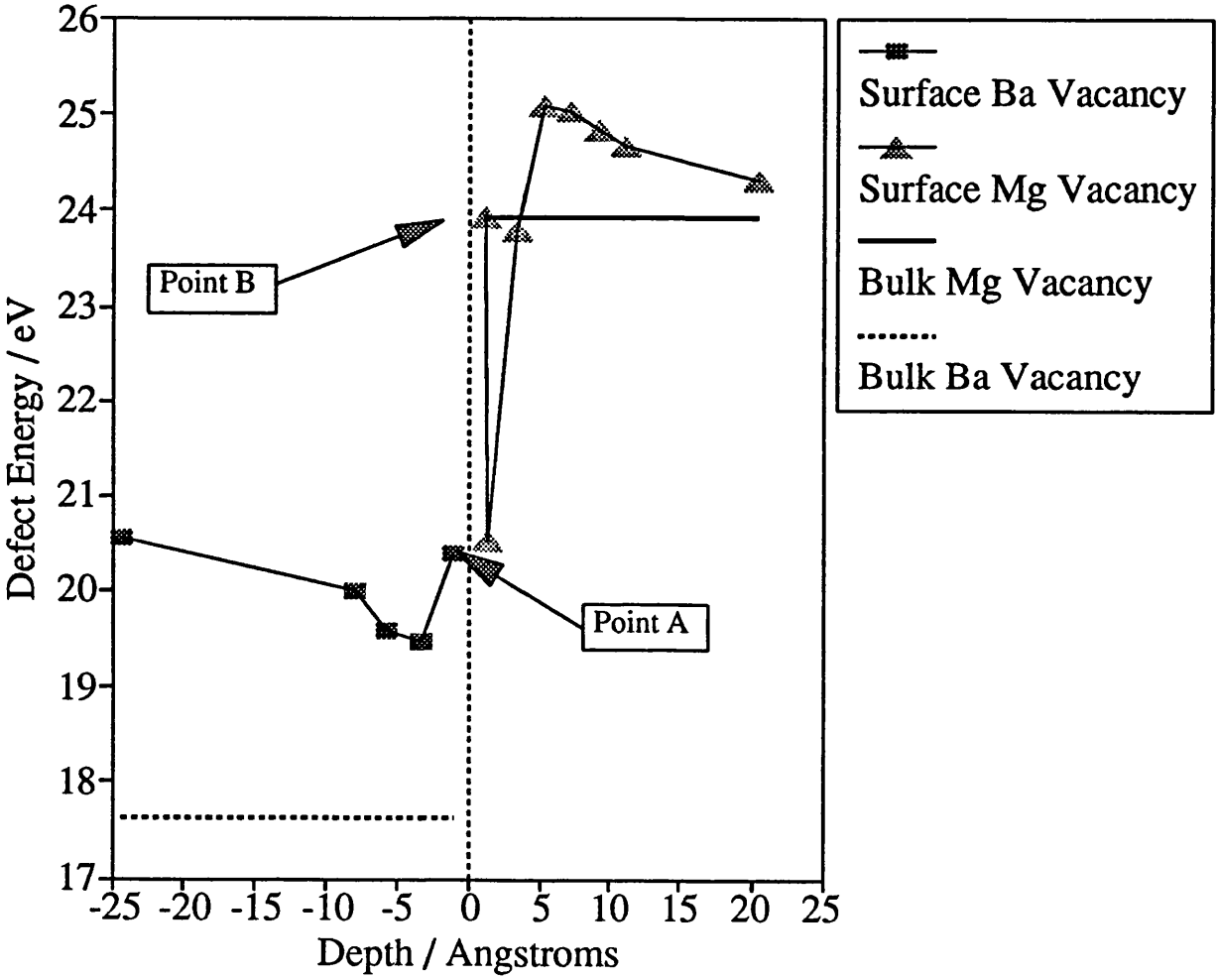

Figure 4.10 Barium and Magnesium vacancy formation energies as a function of depth in the near interface region of the BaO(100)//MgO(100) interface. A depth of 0 represents the interface.

energies, the cation vacancy formation energies do not exhibit the behaviour as predicted by image theory. Furthermore the figure shows a surprisingly low value for the magnesium vacancy formation energy for a magnesium ion 1.5Å from the interface (point A, figure 4.10). This represents a difference of 4eV compared to removing an adjacent magnesium ion (point B). This can be rationalised by considering that the removal of a magnesium ion (point A) which has the effect of reducing the unfavourable Ba-Mg interaction at the interface, whereas the removal of a magnesium ion (point B), in contrast, eliminates the favourable Mg-O interaction. This gives an insight into how the detailed atomic structure can substantially modify the behaviour as predicted by the continuum method.

Figure 4.11 shows a comparison of the variation of magnesium vacancy formation energies with depth for a pure MgO surface (Duffy et al. 1984) compared to the BaO//MgO interface. Close to the surface the calculated energies differ significantly from the continuum method for the MgO surface vacancy formation energies. However a few planes into the solid, the continuum approximation becomes very accurate (dielectric constant of a vacuum is 1). The calculated oxygen vacancy formation energies in MgO for the BaO//MgO interface appear to converge to the bulk value at a slower rate. This may be a consequence of the considerable relaxation at the interface causing a longer range modification of the MgO structure than a (100) MgO surface. Furthermore as the dielectric constant for BaO is higher than for MgO, the vacancies should be stabilised near the interface region and destabilised when in the bulk of the MgO. The calculated values however do not show this behaviour even though the continuum approximation correctly predicts the behaviour for the pure MgO. This reinforces our argument that the failure of the image theory is attributed to the misfit strain energy.

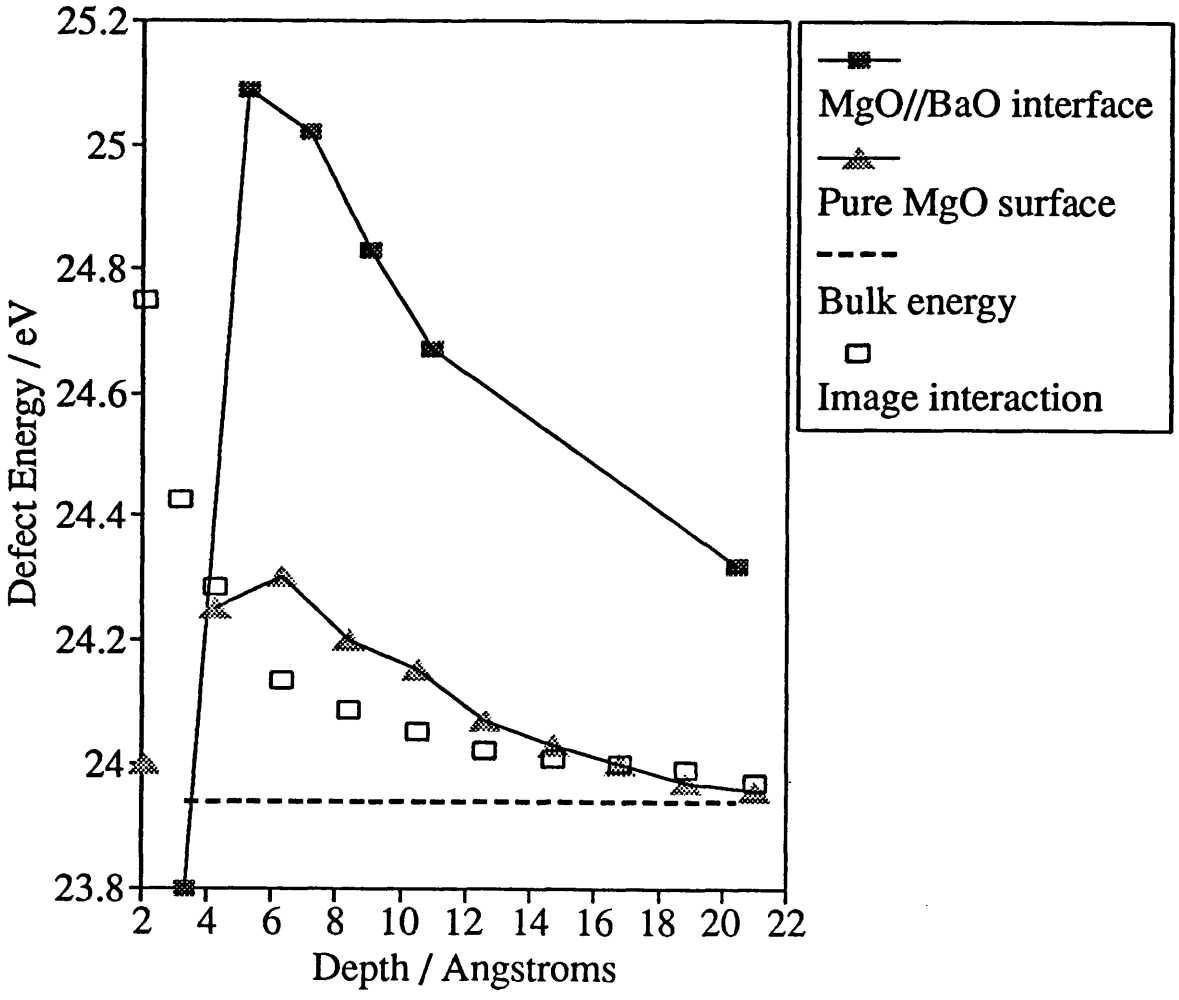

Figure 4.11 Comparison of the oxygen vacancy formation energies at a pure MgO surface and at the interface region of the BaO(100)//MgO(100) interface. The empty squares represents the image approximation.

4.6 BaO Monolayer Formation

The BaO//MgO interface formation has required the BaO to accommodate a 7% deviation from its natural lattice parameter. This requirement is imposed by the computer code to ensure periodicity in the interfacial lattice structure. To investigate the preferred configuration of a BaO monolayer on an MgO substrate we have allowed the monolayer to form from gradual additions of BaO units on the surface. The BaO may then adopt the most favourable configuration without being constrained to constant area. The BaO units are added to the MgO substrate at zero coverage and therefore simulate BaO island formation on the MgO substrate with no interaction from neighbouring islands.

Figure 4.12 shows the relaxed structures of one to eight BaO units added to the MgO substrate. The initial structures before relaxation were constructed by placing BaO units flat on the substrate adopting the $a_o(BaO) = \sqrt{2}a_o(MgO)$ configuration. For one BaO unit on the MgO substrate, the barium is seen to move away from the surface to reduce the unfavourable Ba-Mg interaction. The magnesium directly below the oxygen of the BaO unit has migrated out of the surface towards the oxygen resulting in an increased energy contribution to the system because of the close proximity of the oppositely charged ions. For two BaO units on the surface, the $a_o(BaO) = \sqrt{2}a_o(MgO)$ configuration is still apparent after relaxation. The magnesium ions directly below the oxygens of the BaO units are again seen to move out of the MgO surface decreasing the Mg-O distance. The barium ions are seen to move away from the magnesium ions over which they are constrained to sit driven by the unfavourable Ba-Mg interaction. The relaxational behaviour is essentially identical to the relaxation observed for the full coverage of the MgO surface by eight BaO layers in figure 4.7a. For three BaO layers the $a_o(BaO) =$

Figure 4.12 Relaxed structures of one to eight BaO units added to an MgO(100)substrate.

BaO on MgO

Chaos Calculation

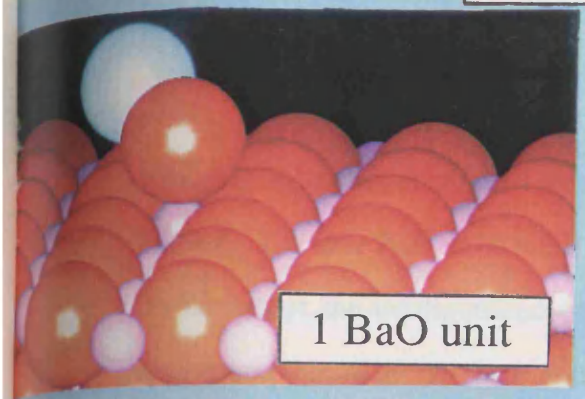

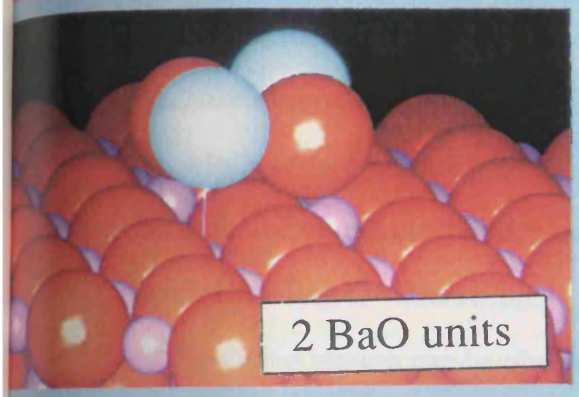

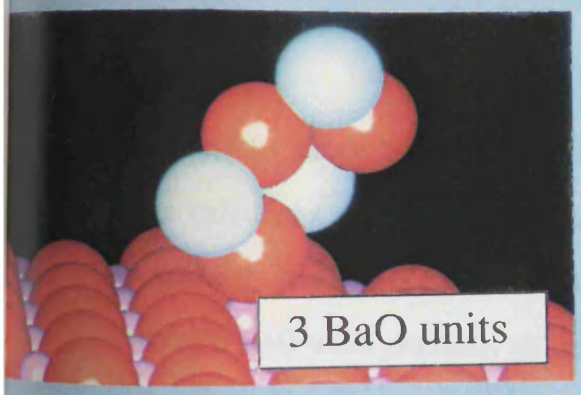

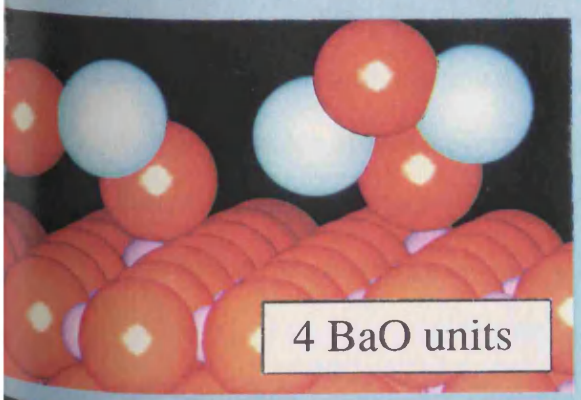

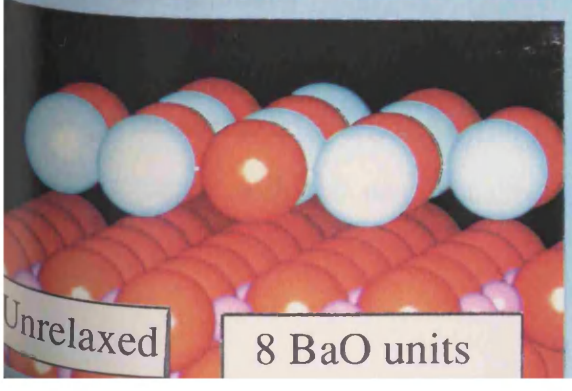

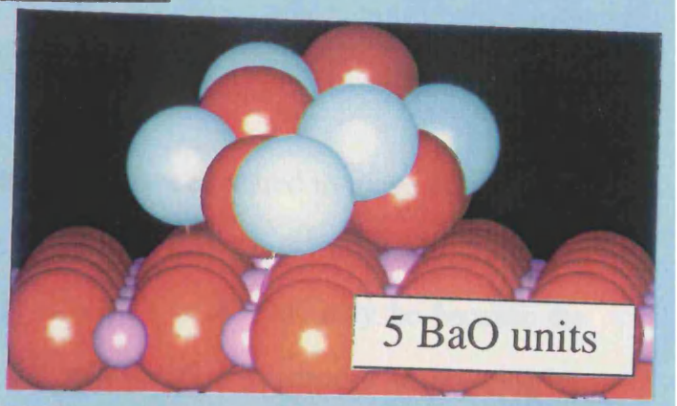

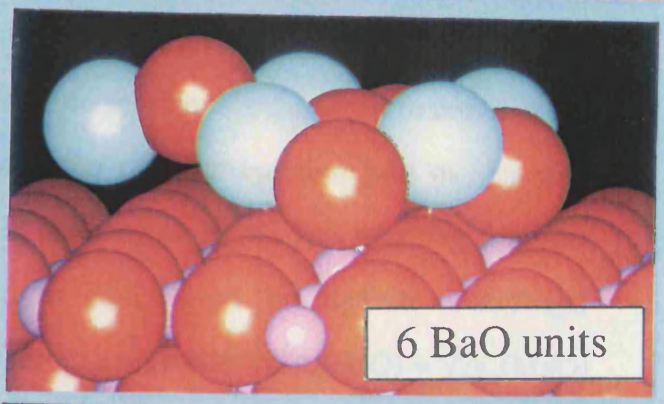

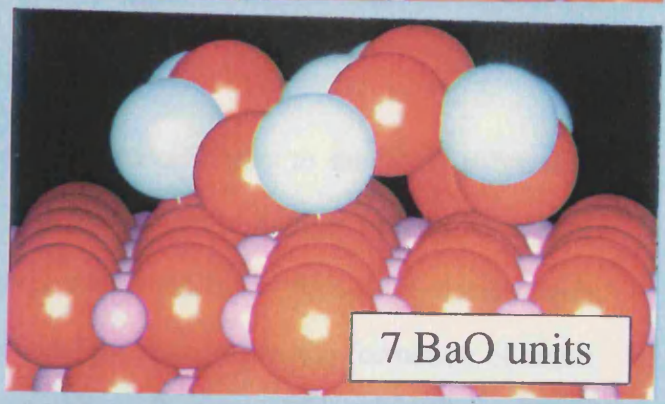

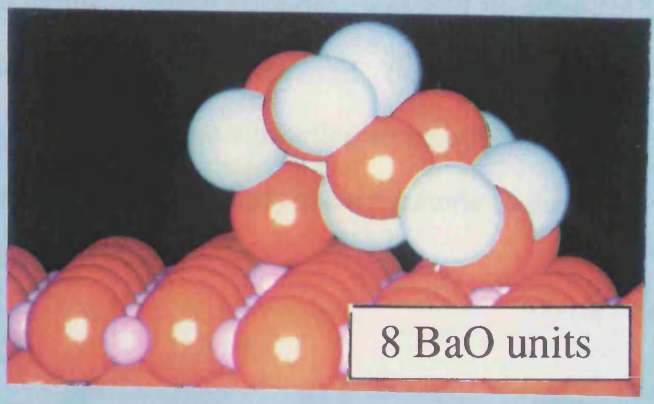

Purple - Magnesium

White - Barium

Red - Oxygen

$\sqrt{2}a_o$(MgO) relationship is not seen as the BaO units have appeared to move off the MgO surface. For four BaO units the BaO has split into two sets of two BaO units. The units do not adopt the configuration observed for two BaO units. This may be because the interaction between the two units direct the minimisation procedure in locating an alternative local energy configuration. With five or more BaO units cluster formation of BaO are observed on the MgO substrate. The magnesium is again seen to move out of the MgO surface resulting in the close proximity of the magnesium and oxygen ions again the driving force for this migration is the increase in stability resulting from the favourable Mg-O interaction. For five to eight layers no definite BaO//MgO configuration pattern can be observed from the structures also the a_o(BaO) = $\sqrt{2}a_o$(MgO) configuration is not conserved.

Figure 4.13 shows the calculated energy of adding BaO layers to the MgO substrate . The calculated energy of one BaO unit is lower than the energy of a BaO cluster containing many BaO units. This suggests than monolayer formation occurs with separate BaO units gradually filling the surface layer rather than the formation of small islands or clusters. This is based on purely thermodynamic considerations and therefore must be treated with caution as kinetic factors must also be considered. Furthermore the calculations are at zero coverage and therefore include no contribution from interactions from neighbouring BaO 'islands'. Further calculations to identify the magnitude of these interactions are therefore necessary.

4.7 Summary

In this chapter we have investigated the factors influencing the stability of a heteroepitaxial interface. The identification of stable (100) MgO and BaO surfaces together with the near equality a_o(BaO) : $\sqrt{2}a_o$(MgO) prompted us to consider the

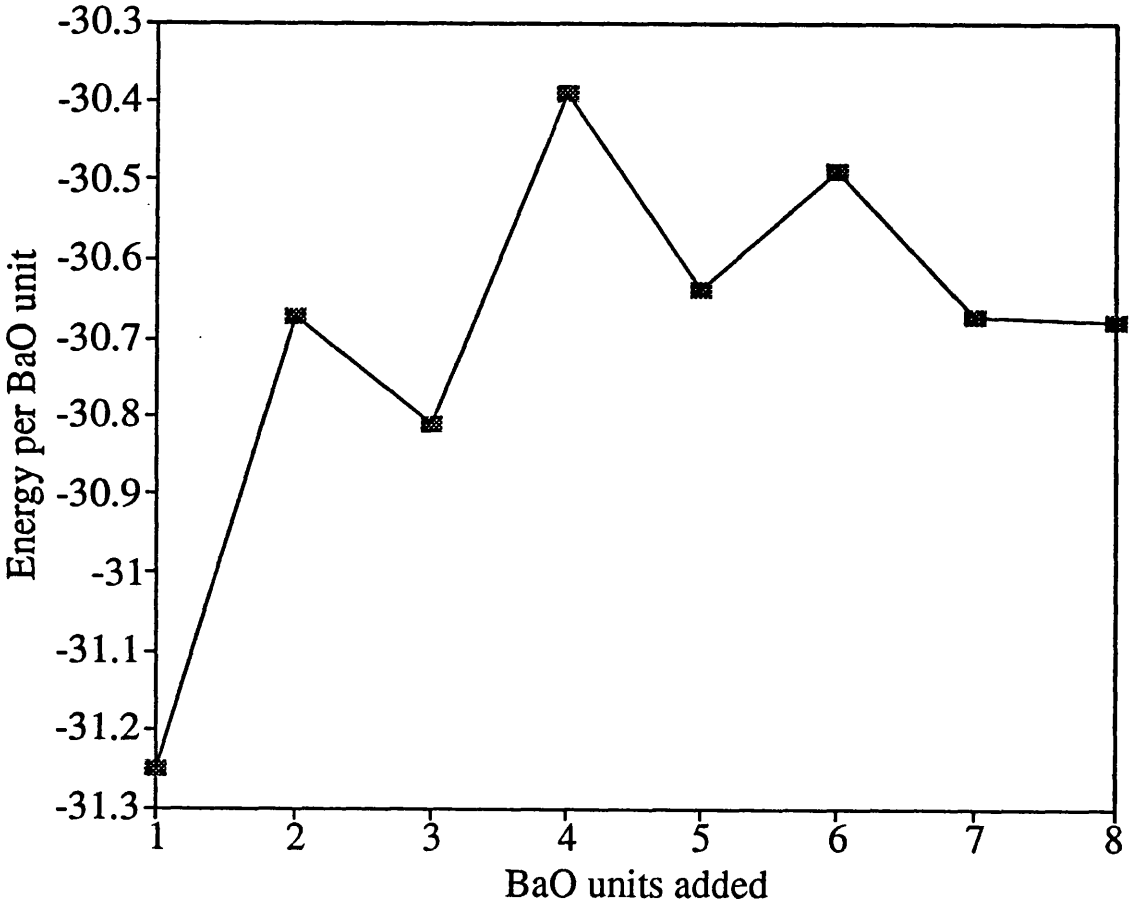

Figure 4.13 Calculated energies per BaO unit of each relaxed "cluster" of BaO on an MgO(100) substrate for one to eight units.

BaO(100)//$\sqrt{2}$ MgO(100) interface. Static simulation calculations predict that the interfacial stability will increase with BaO layers added to the MgO substrate reaching a maximum stability at 2 BaO monolayers. The epitaxial mismatch is accommodated entirely by the added BaO overlayers and therefore the interfacial stability with respect to isolated MgO and BaO surfaces is expected to fall with increasing BaO layers. From the reduced density calculations performed, we have identified one defect arrangement which adopts a lower energy (more stable) than the interface with a full density of ions. Therefore the vacancies are not defects in some ideal structure but are identified to be an intrinsic part of the low temperature interface configuration.

Vacancy formation energies at the interface reveal a poor correlation to defect energies predicted using the continuum method at near interface regions. For large distances from the interface the correlation improves but is never as good as for pure surfaces, this is attributed to the considerable relaxation at the interface as a result of the strain energy introduced into the system to accommodate the misfit between the two materials. The continuum method is therefore not a good approximation for interfaces where the relaxation at the interface is substantial resulting in a considerable long range modification of the BaO and MgO structures. The calculated vacancy formation energies of ions in close proximity to like charged ions are low and are therefore expected to be the major defects. Finally we have identified that BaO monolayer formation occurs on the MgO surface, by the addition of scattered BaO units as opposed to island formation assuming the interaction between neighbouring BaO units is not deleterious to the stability with increasing coverage.

In the next chapter we extend the range of materials considered to include $BaTiO_3$ and $SrTiO_3$ which are more technologically important and exhibit the perovskite structure.

Chapter 5

Heteroepitaxial Perovskite Interfaces

CHAPTER 5

5.1 Introduction

In this chapter we employ the methodology developed in chapter 4 to investigate the more commercially important materials $BaTiO_3$ and $SrTiO_3$. These materials adopt the perovskite type structure and will therefore increase the complexity of the problem because the (100) perovskite surfaces terminate with either an MO or a TiO_2 plane.

$SrTiO_3$ interfaces are useful systems to study because, as with MgO, single crystals of $SrTiO_3$ are available. Hence experiments similar to those performed by Cotter et al. (1988, 1989) on an MgO substrate could easily be reproduced using $SrTiO_3$. Thus we can provide predictions for tractable experimental studies. This would provide a test for the simulation and aid in the experimental interpretation.

We look at four interfaces; BaO interfaced with $SrTiO_3$ and $BaTiO_3$ and MgO interfaced with $SrTiO_3$ and $BaTiO_3$. The interfacial stability with increasing overlayer thickness on the substrate is calculated for all the interfaces. Vacancy formation energies of oxygen, barium, strontium and titanium are calculated at near interface regions for the $BaO(100)//SrTiO_3(100)$ interface. The effect of the vacancy formation energies on the interfacial stability is examined to elucidate the low temperature defect structure of the $BaO(100)//SrTiO_3(100)$ interface.

We next address the accommodation of misfit, as high values of the misfit were found in chapter 4 to be deleterious to the interfacial stability. First, by investigating the formation of BaO monolayers on $SrTiO_3$ by sequential additions of BaO units on the substrate surface. This allows the monolayer to form without any constraints on the BaO to accommodate a certain configuration to accommodate the misfit. Second, the

constant interfacial area boundary conditions imposed on interface calculations by the MIDAS code are removed. This allows for the interfaced material to adopt its natural lattice parameter away from the interface region.

Barium titanate and Strontium titanate are important materials with respect to both scientific and commercial applications. Polycrystalline samples of donor doped barium titanate may show a dramatic increase in resistivity in the vicinity of the Curie temperature, T_c. This behaviour is known as the positive temperature coefficient of resistance (PTCR) effect and has been the subject of many extensive experimental and theoretical investigations, primarily for its application to thermistor devices (Lewis et al. 1985a, Lewis and Catlow 1983). The effect of an interface on a barium titanate thin film may have severe implications to its PTCR effect as the relaxation expected at the interface region may modify the structural configuration of the $BaTiO_3$. Strontium titanate has been widely used as a substrate for superconducting $YBa_2Cu_3O_{6.5}$ thin films (Eibl et al. 1990a, Narayan et al. 1989, LeGoues 1988, Chen et al. 1988) as the mismatch between the $SrTiO_3$ substrate and the superconducting $YBa_2Cu_3O_{6.5}$ thin film is only ≈3% compared to the more commonly employed MgO substrate which is associated with an ≈8% misfit (Eibl et al. 1990b, Tanaka et al. 1990, Tong Lee et al. 1989, Ramesh et al. 1990). Understanding the behaviour of these materials as substrates for heteroepitaxial interfaces will provide a good starting point for further studies which may evaluate their behaviour in real applications.

5.2 Crystal Structure

Both barium titanate and strontium titanate exhibit the calcium titanate or perovskite type structure. The composition of a perovskite type structure is ABO_3, where A and B are different metal cations having formal valances of A^{2+} and B^{4+}. The size of the A cation is comparable to the O^{2-} ion and occupies a lattice site that is surrounded by a

regular array of twelve O^{2-} ions. The smaller B cation resides in an octahedral site, surrounded by six O^{2-} ions. The lattice parameter for $BaTiO_3$ is 3.89Å (Gronsky) and 3.90Å for $SrTiO_3$(Narayan et al. 1989). Calculated lattice parameters are 4.14Å for $SrTiO_3$ and 3.96Å for $BaTiO_3$.

Barium titanate becomes ferroelectric at temperatures below the Curie temperature, such a transition being accompanied by a distortion from cubic to a lattice with lower symmetry. The Ba^{2+} and Ti^{4+} are displaced relative to the oxygens, thereby developing a dipole moment. This does not drastically alter the ligand environment of the cations, however, the dipole moment associated with this distortion will cause the (100) surface to adopt a type 3 surface (chapter 4). The resulting surface energy will therefore be infinite without substantial reconstruction. The symmetry of the lattice will also increase the complexity of interfacing the material. Furthermore, as the calculations performed in this work are all at 0K which is below the Curie temperature of 120°C, the structural changes associated with this transition make interface calculations prohibitively difficult. The $BaTiO_3$ is therefore considered to be cubic at 0K. The relaxation and subsequent substantial structural modification of the $BaTiO_3$ at the interface region justifies this approach.

5.2.1 Surface Topography

$BaTiO_3$ and $SrTiO_3$ do not cleave well along any particular plane, but the most common surface is the (100). This gives rise to two surface structures, an AO plane and a BO_2 plane both of which are non polar and therefore to calculate the surface energy, the energy of two blocks, one terminating with the AO plane and the other terminating with a BO_2 plane must be considered. The calculated surface energy of $BaTiO_3$ is 1.44 Jm^{-2}, the surface terminating with BaO (100) being the more stable in accordance with the results of Lewis and Catlow (1985a). The calculated surface energy of $SrTiO_3$ is 1.32

Jm^{-2} with the surface terminating in SrO being more stable.

5.3 Interfacial Stability

From the arguments discussed in chapter 4, the substrate is allowed to exhibit its natural lattice parameter with the misfit accommodated entirely by the overlayer. To accommodate the misfit, the overlayer must ether be compressed or expanded relative to its natural lattice parameter. (If it is compressed a minus sign is designated to the percent misfit and a plus sign is designated if the overlayer is expanded).

5.3.1 BaO(100)//$SrTiO_3$(100) interface

The calculated lattice parameter of $SrTiO_3$ is similar to that of MgO, therefore epitaxial matching can be achieved by considering a 45° rotation of the BaO overlayer or $a_o(BaO) = \sqrt{2}a_o(SrTiO_3)$ resulting in a +6% lattice mismatch. The BaO overlayer can be considered as analogous to the SrO plane. The (100) $SrTiO_3$ offers two surfaces to interface with the MgO, one terminating with an SrO plane and the other terminating with a TiO_2 plane. Surface energy calculations suggest that the $SrTiO_3$ terminating with the SrO surface offers a more stable substrate to interface with MgO than the SrO terminated surface. However, the interface with BaO over the TiO_2 terminated $SrTiO_3$ is calculated to be more stable than over SrO terminated $SrTiO_3$. Figure 5.1 represents diagrammatically the configuration BaO is constrained to adopt when interfaced with the $SrTiO_3$ substrate. The BaO is arranged to ensure favourable charge matching across the interface i.e. the BaO oxygens are assigned to lay directly above the titanium sublattice. Calculations show this arrangement to be energetically more stable than barium occupying sites directly above the titanium sublattice.

The calculated energies of sequential additions of BaO to the $SrTiO_3$ substrate are given in figure 5.2 (types A and B are following equations 4.4 and 4.5, where type A indicates

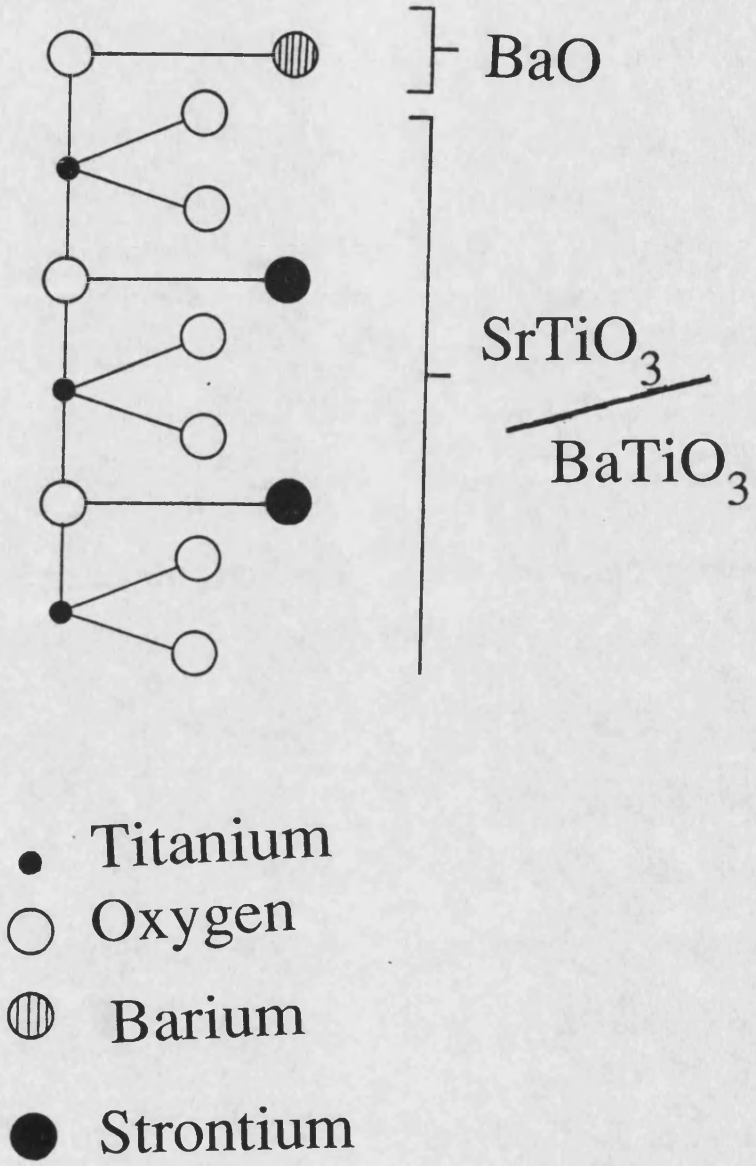

Figure 5.1 Diagrammatic representation of the interfacial configuration, BaO on $SrTiO_3$ or $BaTiO_3$ is constrained to accommodate.

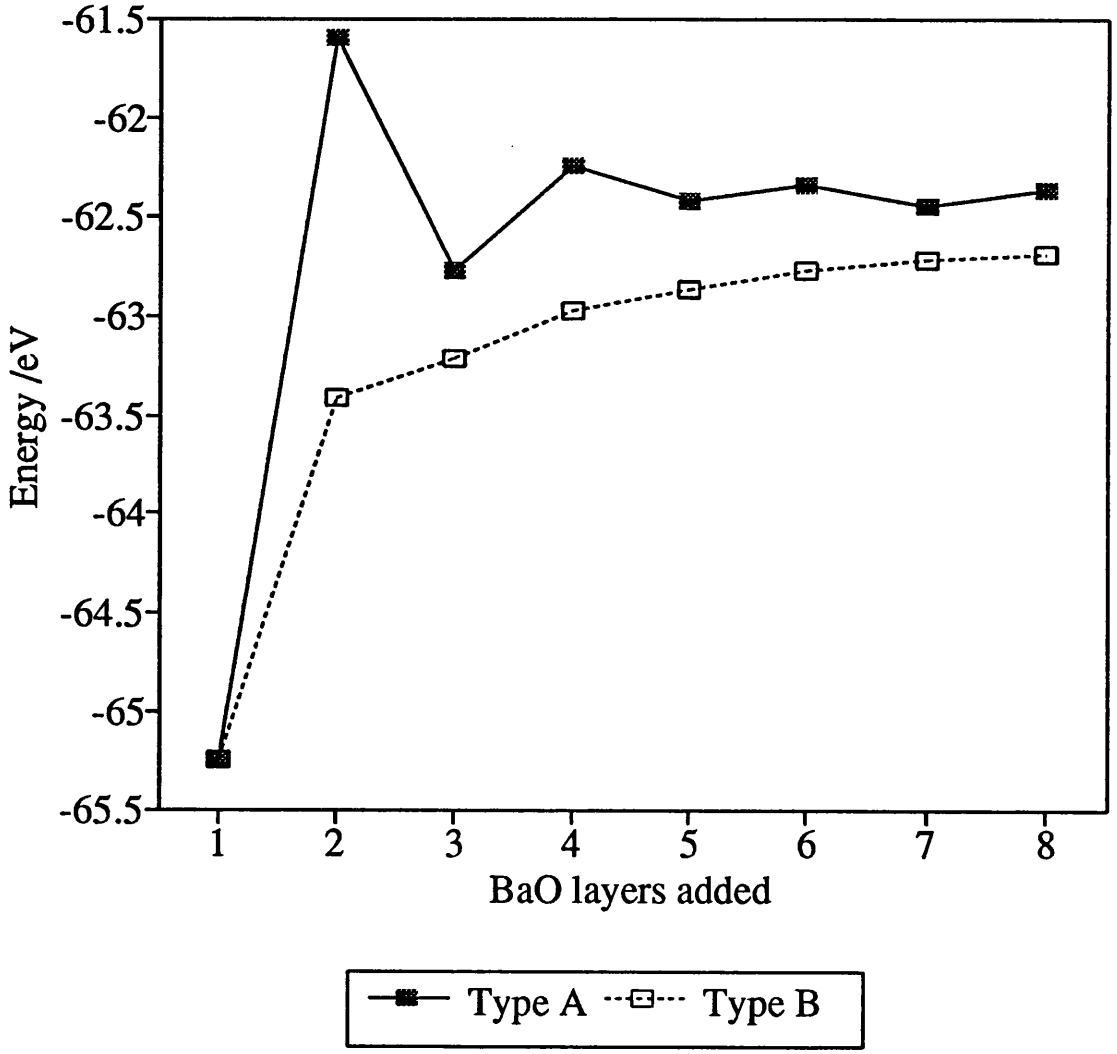

Figure 5.2 Calculated energies of sequential BaO layers added to a $SrTiO_3$ substrate. The energies are for two BaO units. The energy of 2 BaO units in a pure BaO crystal is calculated to be -62.52 eV.

the feasibility of adding further BaO layers to increase the thickness of the thin film and type B depicts how stable an interface with n BaO layers would be). Monolayer formation is seen to be the most stable interface and almost 2eV more stable with respect to bilayer formation. This may be a consequence of the first BaO layer extending the perovskite type structure as it is consistent with the perovskite "AO" plane. Further additions of BaO layers do not continue the "BO_2" plane arrangement.

5.3.2 BaO(100)//$BaTiO_3$(100)

The respective lattice parameters of BaO and $BaTiO_3$ conform to the $a_o(BaO) = \sqrt{2}a_o(BaTiO_3)$ relationship necessitating a +1% mismatch. Calculations predict the most stable interface structure to be analogous to BaO on $SrTiO_3$ (with BaO over the TiO_2 terminated $BaTiO_3$) and is shown in figure 5.1. Figure 5.3 represents the variation of interfacial stability with BaO overlayers added. The figure is qualitatively similar to figure 5.2. However, the stability of a BaO monolayer on $BaTiO_3$ is 0.83eV more stable than on $SrTiO_3$. This can be attributed to the lower mismatch between BaO and $BaTiO_3$ as the resulting loss in strain energy from the system required to accommodate the high +6% mismatch for BaO on $SrTiO_3$ will be much greater than the loss in strain energy resulting from a +1% mismatch for BaO on $BaTiO_3$. Relaxation effects should however reduce this strain energy especially for monolayer formation where the BaO has more relaxational freedom. Comparison of the energies at higher BaO additions, where the relief of mismatch strain energy cannot be easily removed by relaxation, should illustrate this argument more clearly.

Figure 5.4 shows the energies of successive BaO additions to $BaTiO_3$ and $SrTiO_3$ superimposed (figures 5.2 and 5.3 (Type B)) and figure 5.5 shows the difference in these values for one to eight layers. The energy difference at 8 layers should be greater than at monolayer coverage because the relaxational freedom of the BaO at the interface region

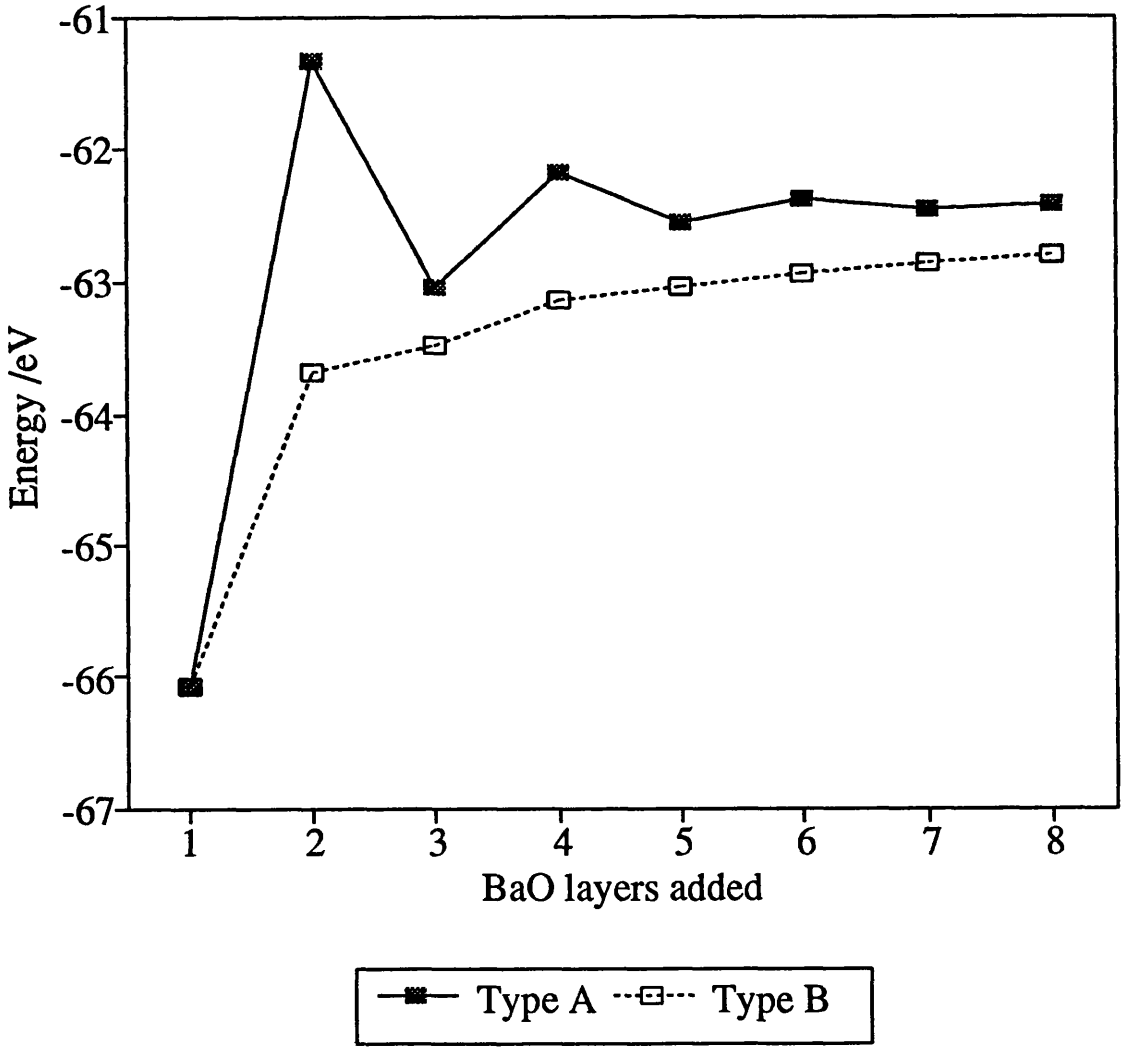

Figure 5.3 Calculated energies of sequential BaO layers added to an $BaTiO_3$ substrate. The energies are for two BaO units. The energy of 2 BaO units in a pure BaO crystal is calculated to be -62.52 eV.

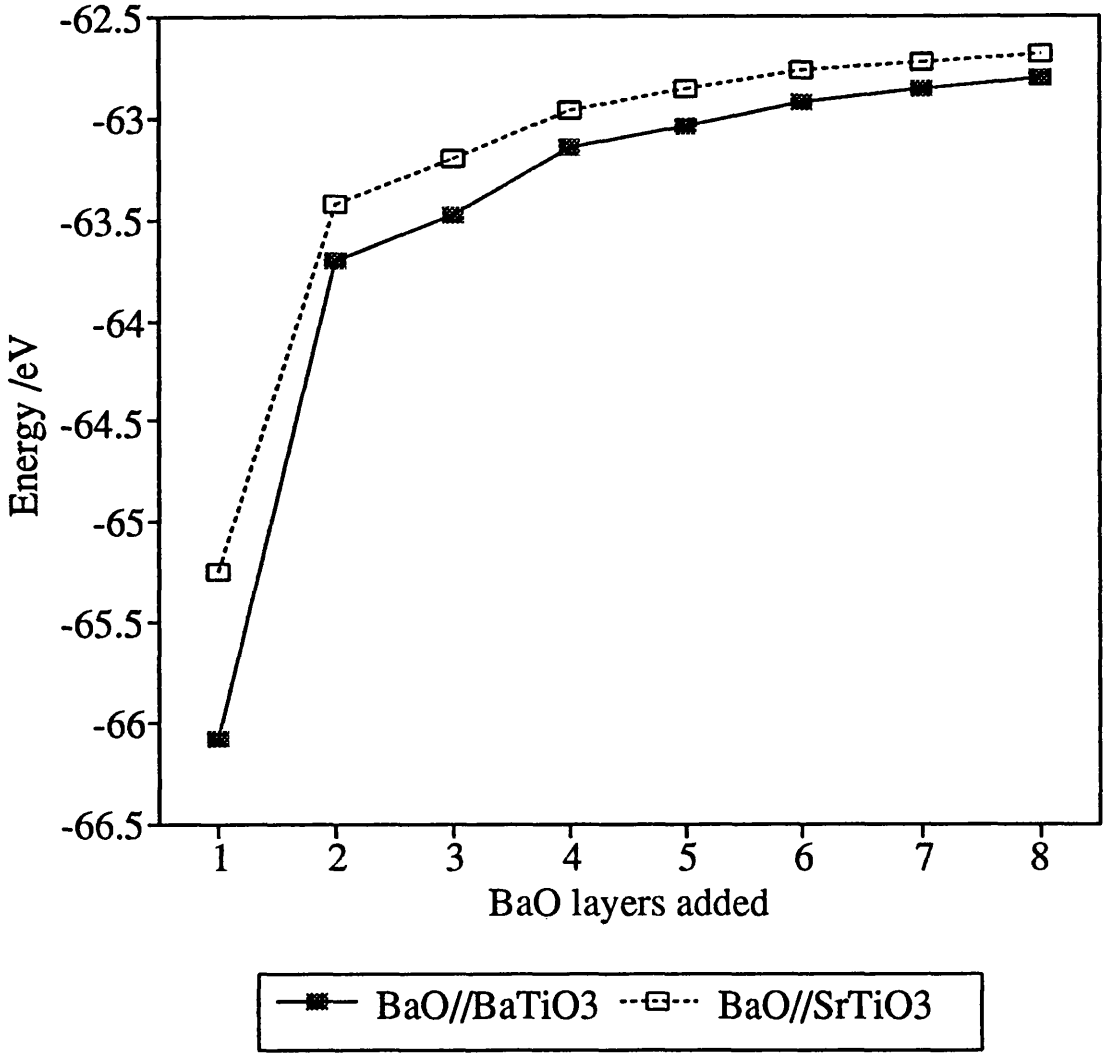

Figure 5.4 Figures 5.2 and 5.3 (type B) superimposed.

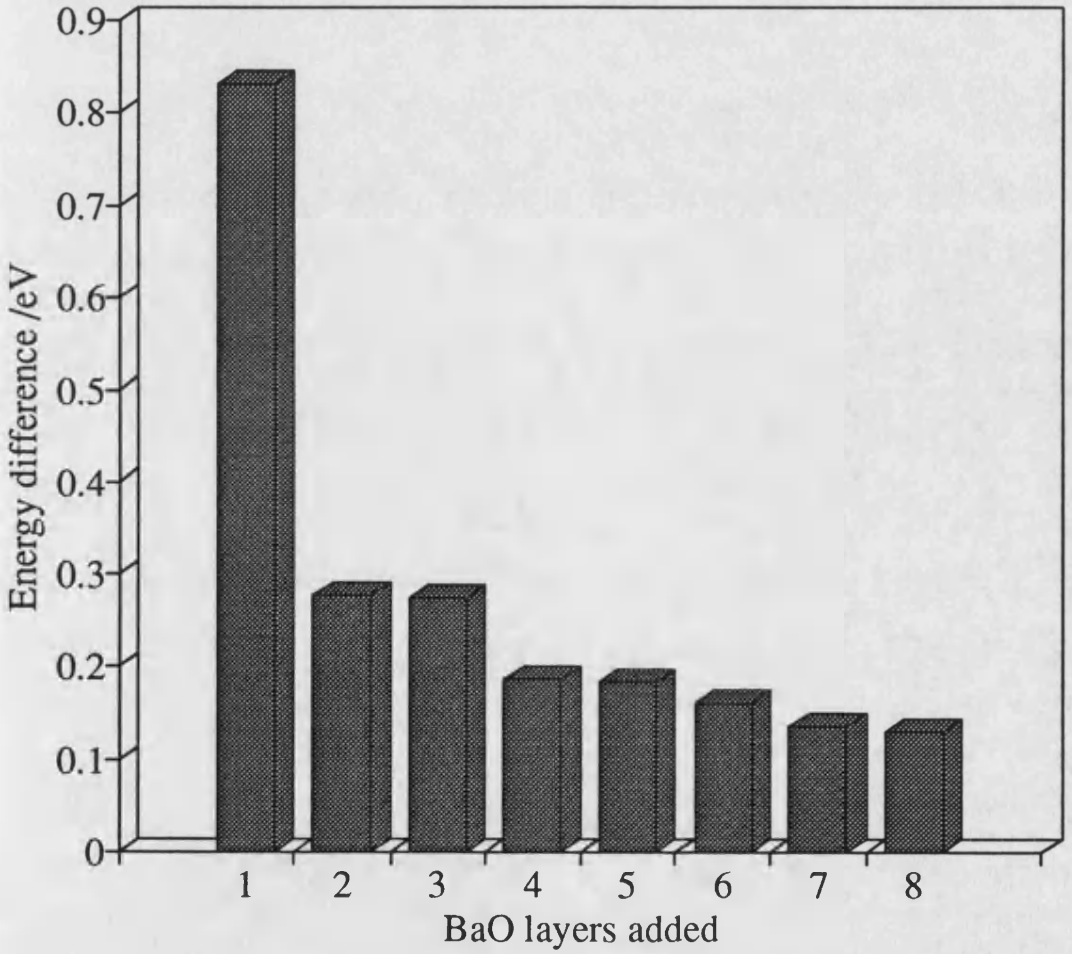

Figure 5.5 Difference in energy for BaO on $SrTiO_3$ and BaO on $BaTiO_3$ as a function of BaO layers added.

is hindered by the layers of BaO above it, or at worst, (no relaxation), a linear relationship of energy difference with layers should be observed. Clearly this is not evident from the graph where the energy difference is reduced for successive BaO layers. An explanation that can account for this observation is a variation of mismatch with BaO layers added. It seems apparent from these results that a hypothetical BaO monolayer has a lower lattice parameter than bulk BaO as the variation of strain energy with lattice parameter is not a linear function (figure 5.6). The variation of energy with lattice parameter for BaO (1,2,3 and 6 layers) is shown in figure 5.6. The graph shows the optimum lattice parameter of a hypothetical BaO monolayer "in space" to be reduced by as much as 7% compared to the bulk value. The energy of the BaO monolayer is also lower than the corresponding bulk value. The mismatch for a BaO monolayer on $SrTiO_3$ is therefore higher than initially predicted when considering the bulk BaO lattice parameter and the mismatch for monolayer coverage is calculated to be +13% for BaO on $SrTiO_3$ and +8% for BaO on $BaTiO_3$. The mismatch will reduce to +6% and +1% respectively for bulk BaO interfaces.

5.3.3 MgO(100)//$SrTiO_3$(100)

The calculated lattice parameters of MgO and $SrTiO_3$ are 4.2Å and 4.14Å respectively resulting in a -1.5% mismatch (assuming bulk MgO lattice parameter). The MgO can therefore lay directly on top of the $SrTiO_3$. The most stable configuration was calculated to be with the MgO laying above the $SrTiO_3$ terminating with the TiO_2 plane. Figure 5.7 shows diagrammatically the interface structure of an MgO monolayer on top of the $SrTiO_3$ substrate. Figure 5.8 shows the variation of energy with sequential MgO additions to the $SrTiO_3$ surface. The figure suggests that bilayer formation is least favourable, with further additions of MgO enhancing the stability of the interface.

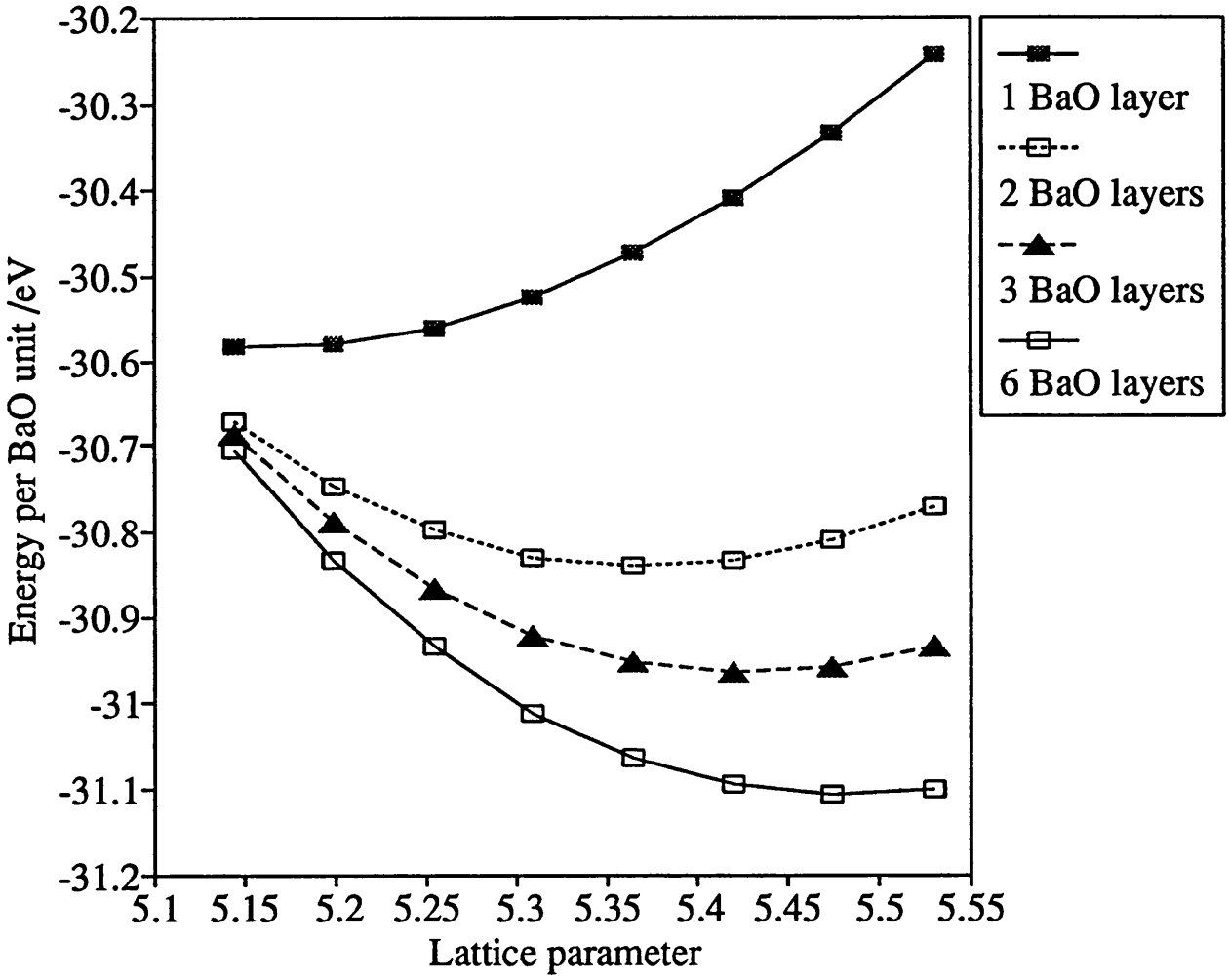

Figure 5.6 Energy of the BaO structural unit as a function of lattice parameter (Å) for 1,2,3 and 6 hypothetical BaO "monolayers in space".

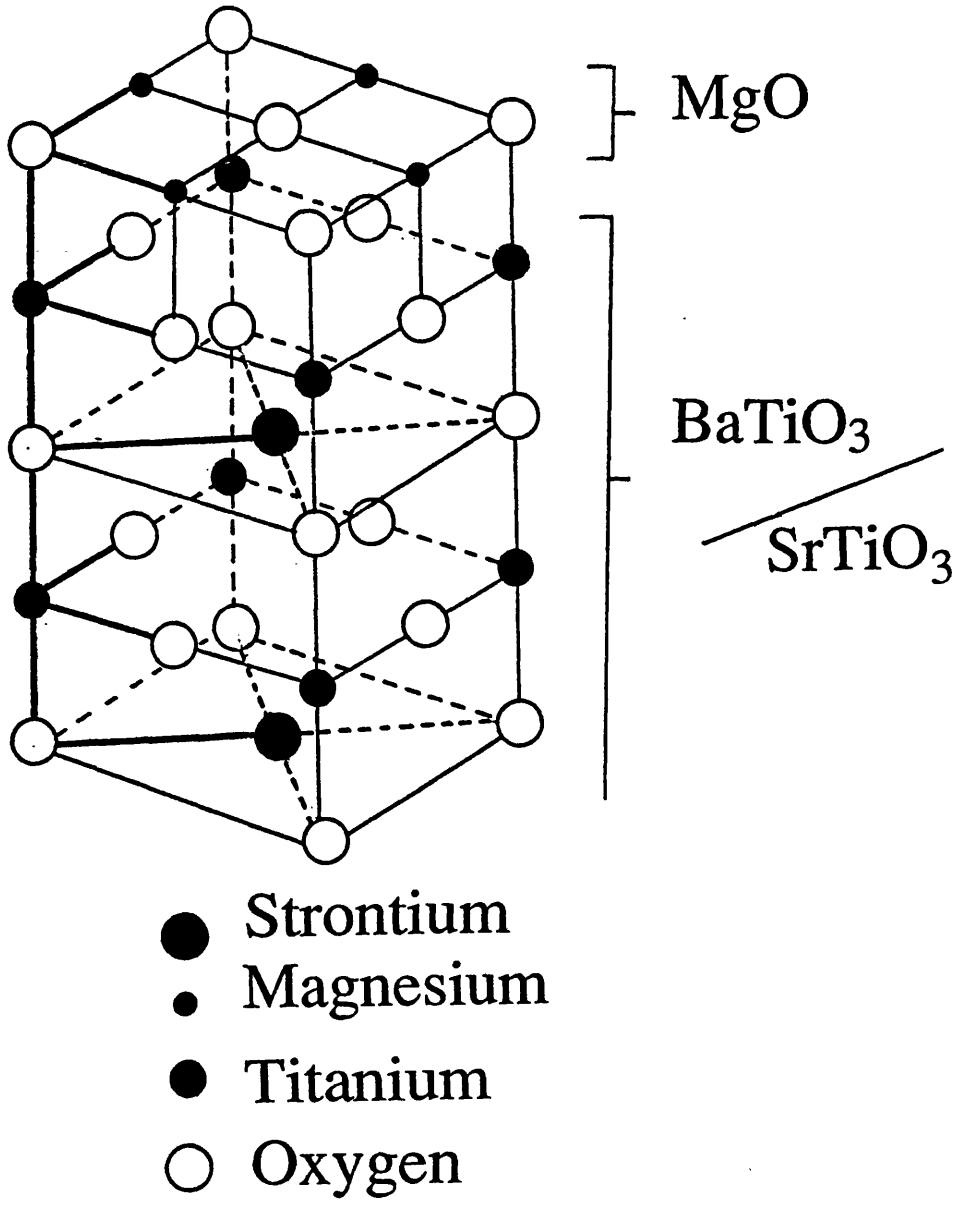

Figure 5.7 Diagrammatic representation of the interface configuration, MgO on $SrTiO_3$ or $BaTiO_3$ is constrained to accommodate.

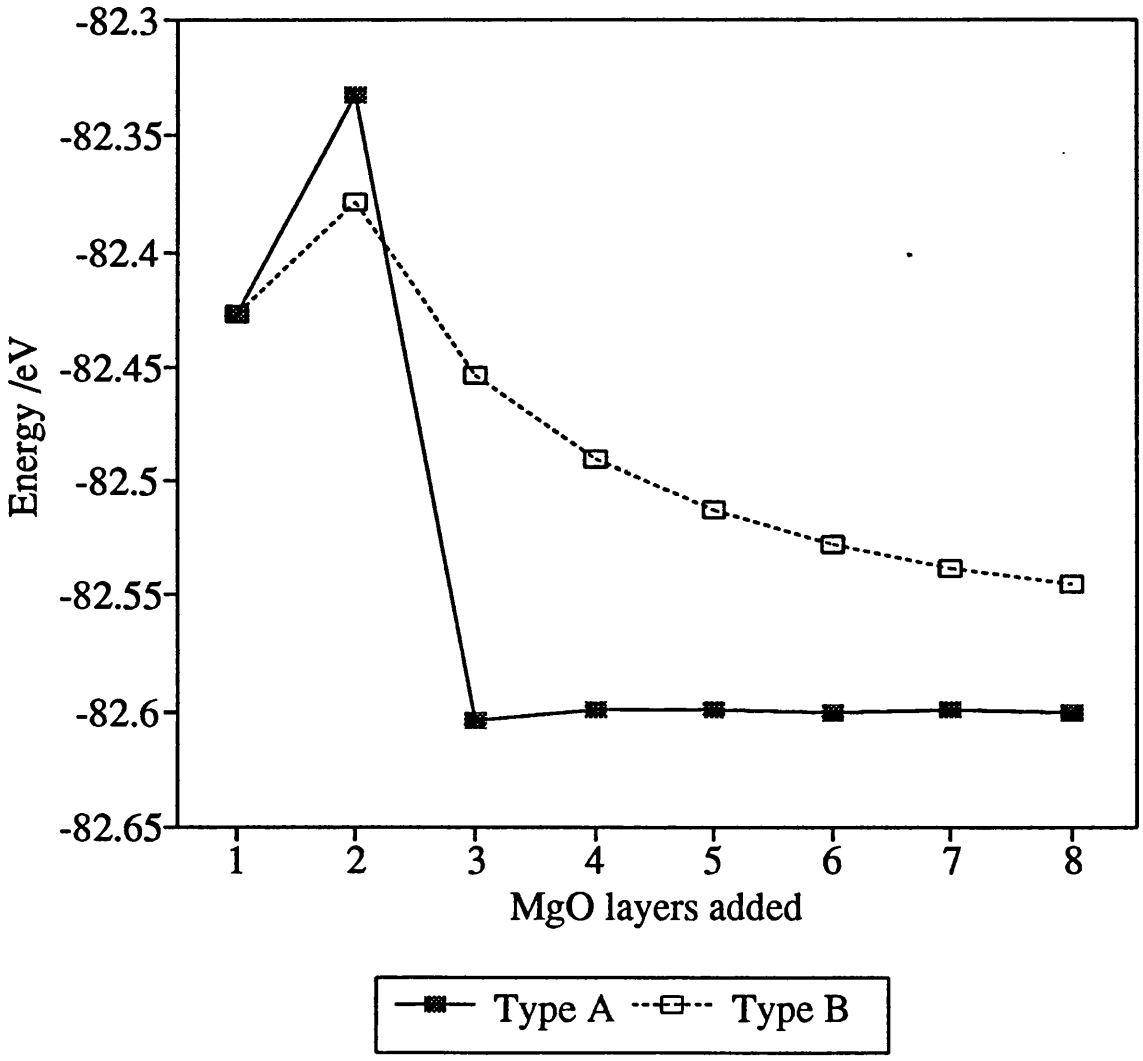

Figure 5.8 Calculated energies of sequential MgO layers added to a $SrTiO_3$ substrate. The energies are for two MgO units. The energy of 2 MgO units in an MgO crystal is calculated to be -82.64eV.

5.3.4 MgO(100)//$BaTiO_3$(100)

The MgO//$BaTiO_3$ interface is constructed in the same way as the MgO//$SrTiO_3$ interface, with the $BaTiO_3$ substrate terminating with the TiO_2 plane (figure 5.7). The resulting mismatch from this interface is about -6% (assuming bulk MgO lattice parameter). Figure 5.9 shows the variation of energy with MgO layers added. For this interface system the results suggest that MgO monolayer coverage presents the most stable interface and bilayer coverage the most unstable interface.

The variation of energy with lattice parameter for MgO (1,2,3 and 6 layers) is shown in figure 5.10. The figure shows the optimum lattice parameter for an MgO monolayer "in space" to be reduced by 6% of the bulk value. The mismatch for MgO on $BaTiO_3$ is therefore about 0% for monolayer coverage and increases to -6% for bulk coverage. For MgO on $SrTiO_3$ the initial +4.5% mismatch (monolayer coverage) changes to -1.5% mismatch for bulk MgO.

Figure 5.11 shows the energies of successive MgO additions to $BaTiO_3$ and $SrTiO_3$ superimposed (figures 5.8 and 5.9 (type B)). Clearly MgO monolayer formation on $BaTiO_3$ is more stable than on $SrTiO_3$. This is surprising considering the mismatch is higher for BaO on $BaTiO_3$ (assuming bulk MgO lattice parameters) however accounting for the "MgO monolayer contraction" the mismatch for MgO on $SrTiO_3$ is 4.5% higher than on $BaTiO_3$. At bilayer formation the stability reverses. Figure 5.10 indicates for 2 MgO layers the mismatch for MgO on $BaTiO_3$ is -3% whereas it is only +1.5% on $SrTiO_3$.

5.4 Vacancy Formation Energies at the BaO(100)//$SrTiO_3$(100) Interface Region

The inclusion of vacancies at the interface region enables good charge matching across the interface by removing the interactions between like charged ions at the interface

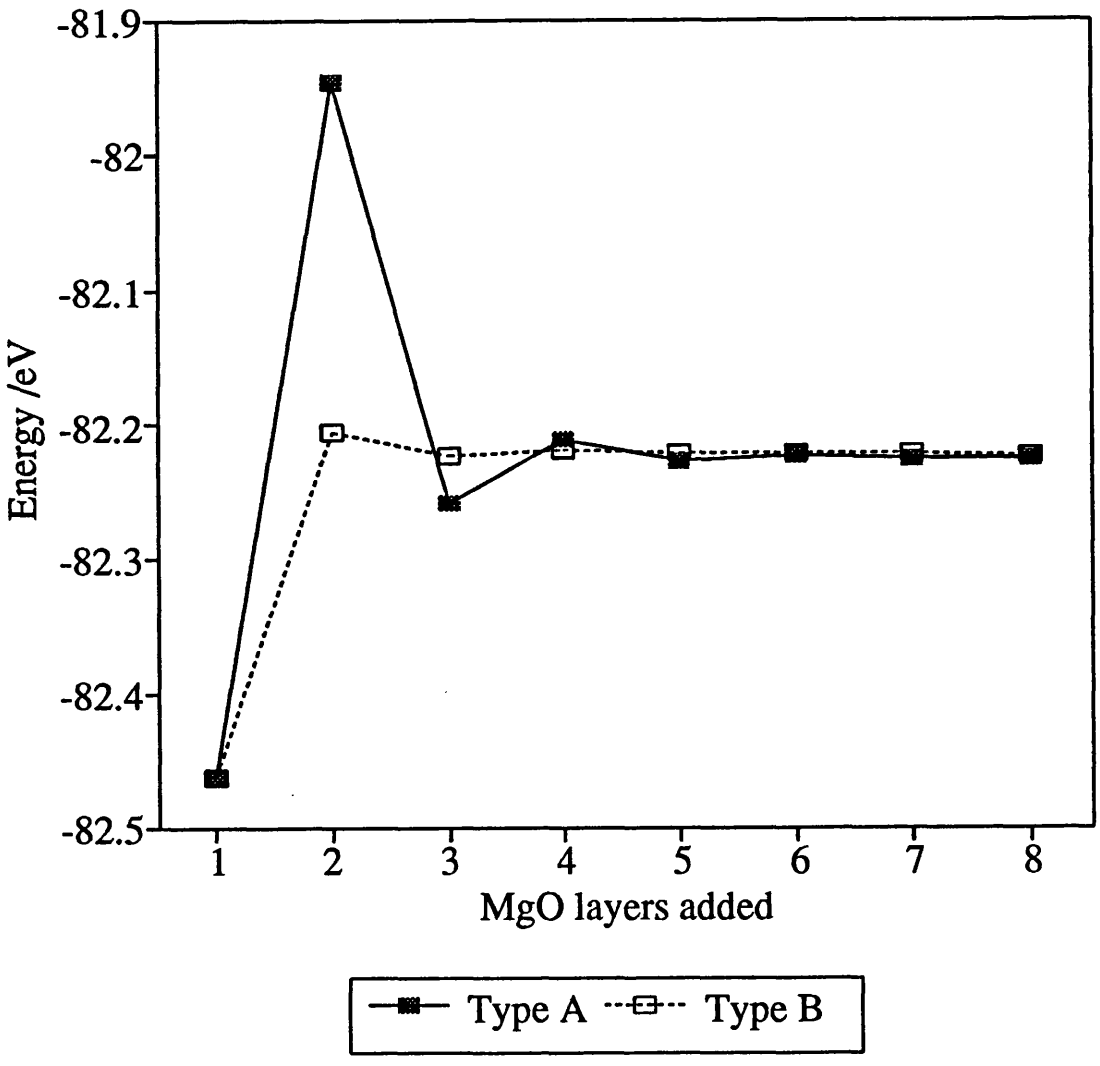

Figure 5.9 Calculated energies of sequential MgO layers added to a $BaTiO_3$ substrate. The energies are for two MgO units. The energy of 2 MgO units in an MgO crystal is calculated to be -82.64eV.

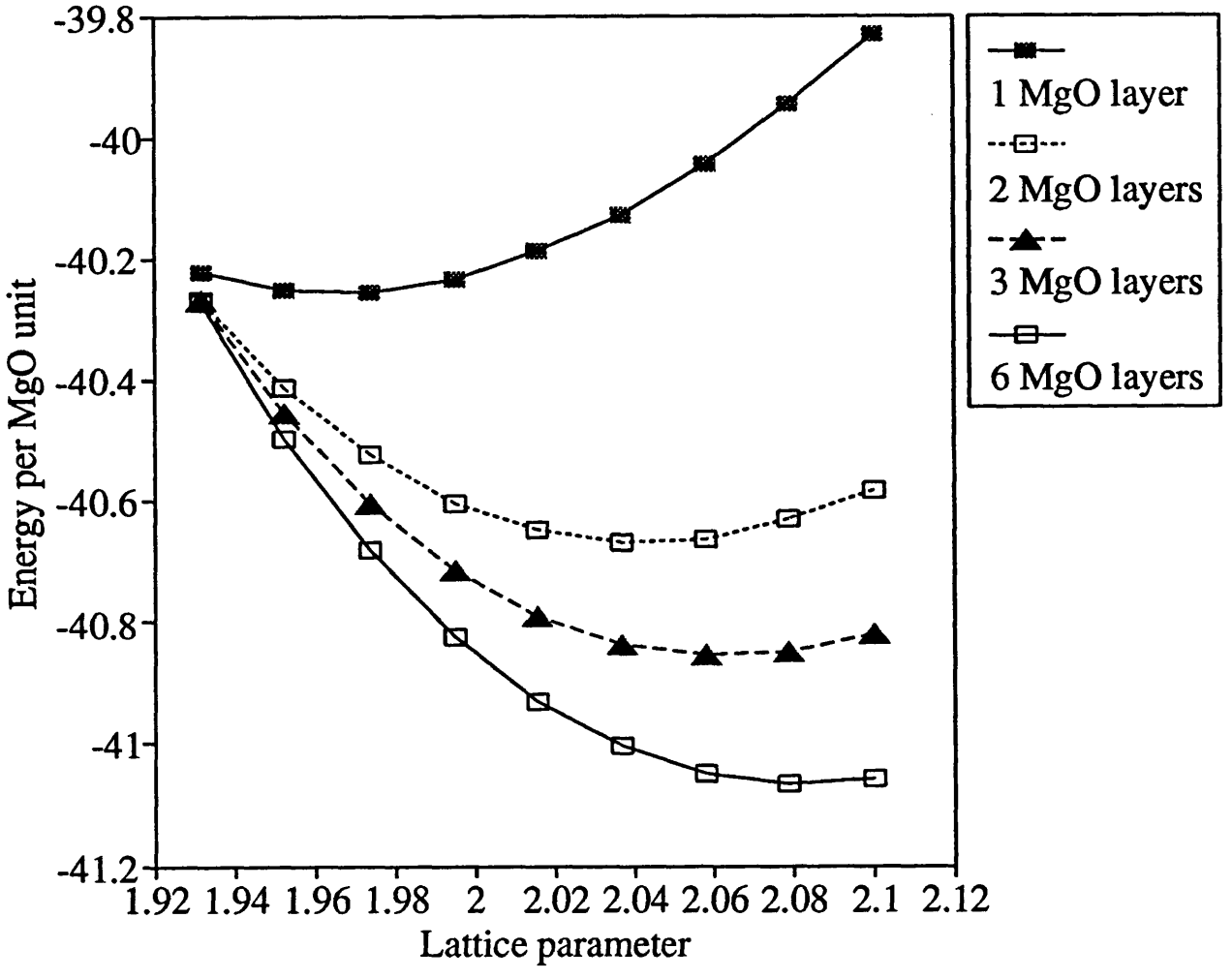

Figure 5.10 Energy of the MgO structural unit as a function of lattice parameter (Å) for 1,2,3 and 6 hypothetical MgO "monolayers in space".

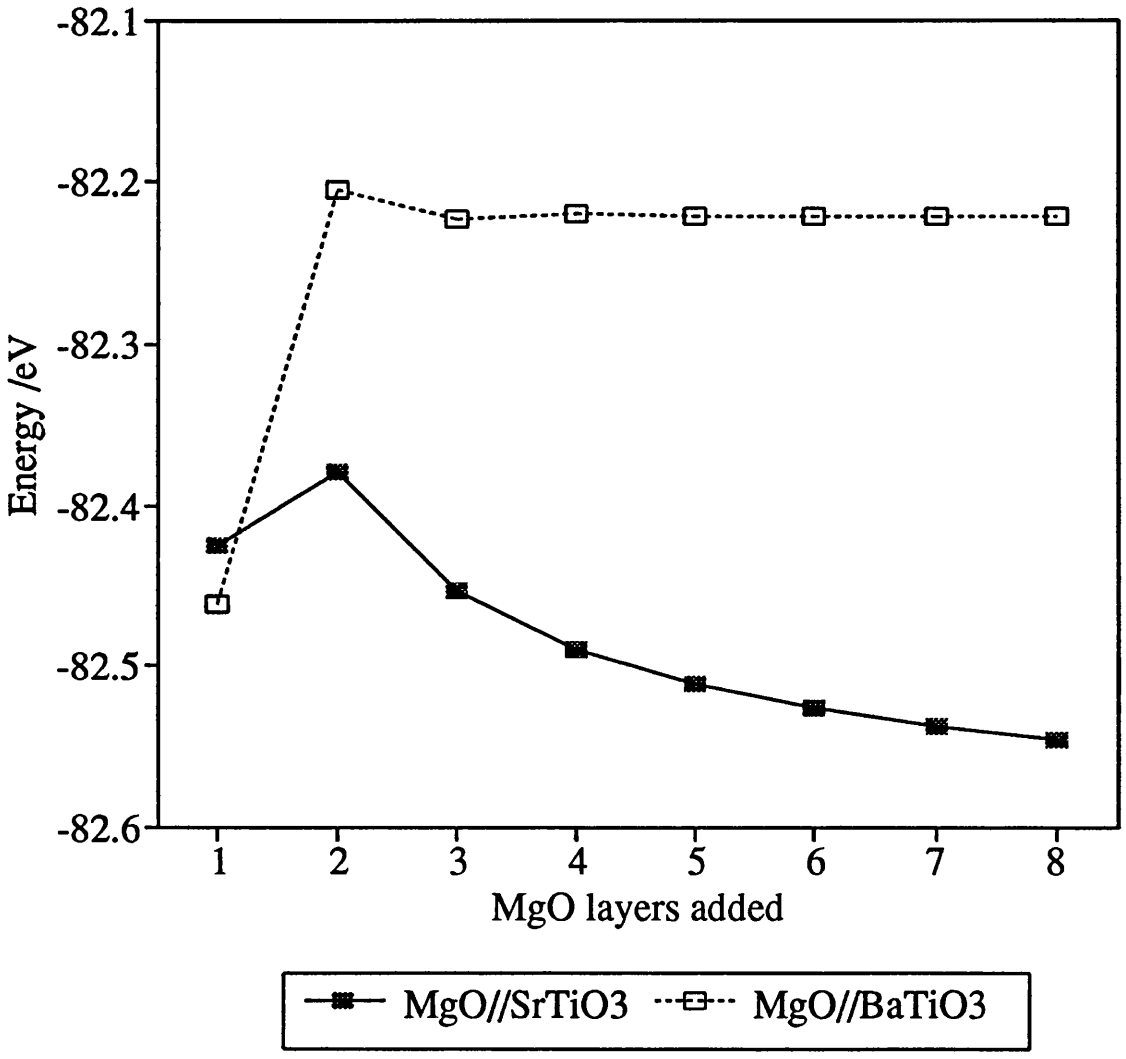

Figure 5.11 Figures 5.8 and 5.9 (type B) superimposed.

(which may be deleterious to the interfacial stability) and hence promote the stability of the interface. The calculation of vacancy formation energies across the interface region will therefore elucidate the low temperature defect structure of the BaO(100)//$SrTiO_3$ interface.

Figure 5.12 shows the oxygen vacancy formation energies plotted against distance from the interface. The dotted line represents oxygen formation energy in bulk BaO and the bold solid line, the oxygen vacancy formation energy in bulk $SrTiO_3$. The formation of an oxygen vacancy is more stable near the interface than in the bulk region for all distances for $SrTiO_3$ but convergence to the bulk value is very slow suggesting a long range structural modification because of the interfacial relaxation. Vacancy formation energy in BaO is more stable at short distances from the interface (less than 5Å) but at 7Å it reaches a maximum of 17.8eV before converging to the bulk value. The oxygen vacancy formation energies in the BaO block of the BaO//$SrTiO_3$ show a marked contrast to those in the BaO block in the BaO//MgO interface (figure 4.9).

Figure 5.13 shows barium and strontium vacancy formation energies in the BaO//$SrTiO_3$ near interface region. The strontium vacancy formation energy shows a minimum value for strontium removal at the first SrO plane; this may be attributed to the removal of the unfavourable Sr-Ba interaction. One may therefore predict that the removal of the first barium ion would also eliminate this unfavourable interaction and should be likewise reflected in a low vacancy formation energy. The figure shows however that this barium vacancy formation energy is a maximum. This result demonstrates the difficulty in predicting vacancy formation energies based on local environment as the energy is highly dependent on the detailed ionic relaxation around the defect. Furthermore the result demonstrates the power and versatility of atomistic simulation techniques.

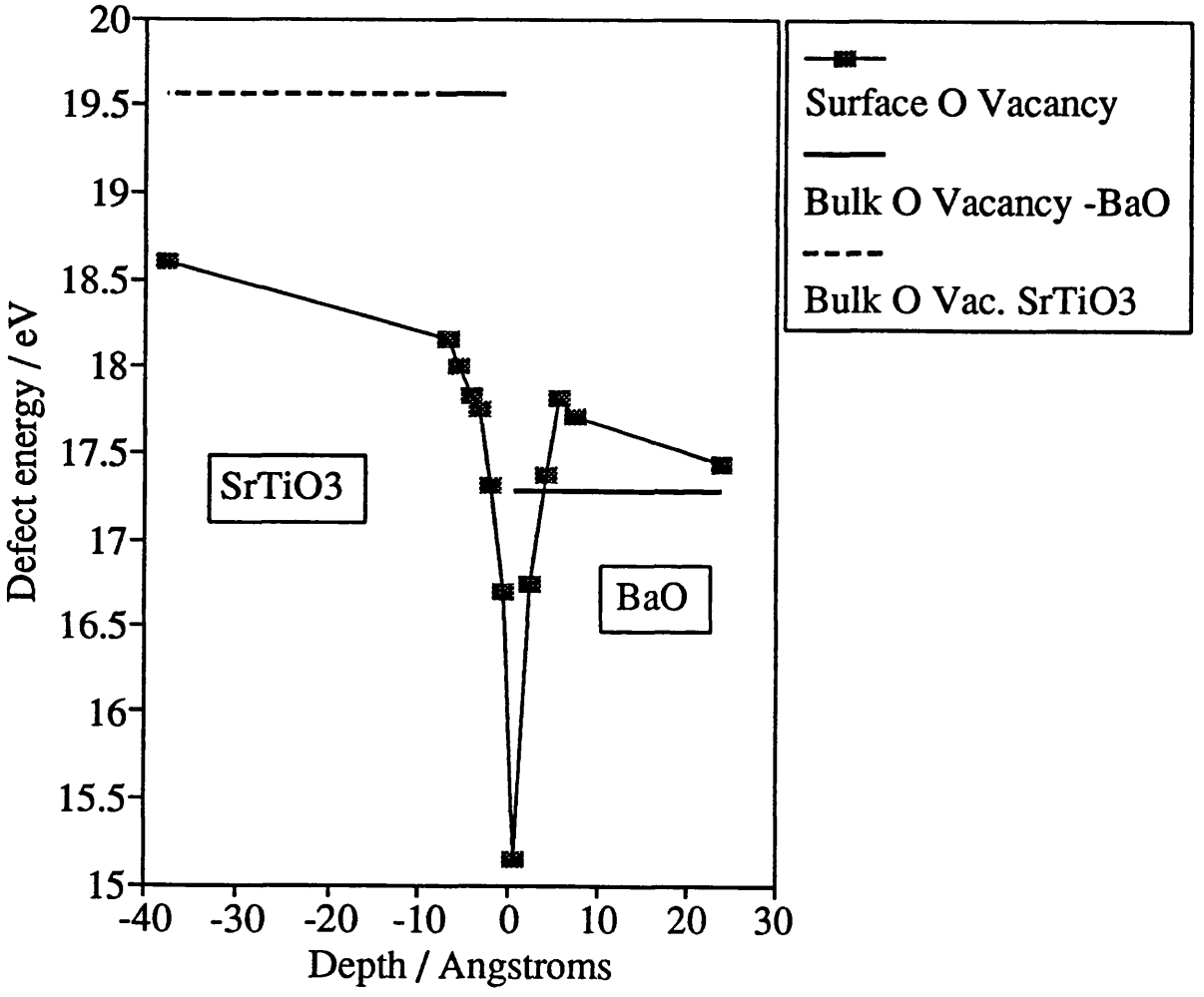

Figure 5.12 Oxygen vacancy formation energy in the near interface region of the BaO(100)//$SrTiO_3$(100) interface as a function of depth. A depth of 0 represents the interface. Positive depths represent BaO oxygen vacancies and negative depths represent $SrTiO_3$ oxygen vacancies. The bold dotted line indicates the bulk oxygen vacancy formation energy in $SrTiO_3$ and the bold continuous line represents the bulk oxygen vacancy formation energy in BaO. The dielectric constants of BaO and $SrTiO_3$ are calculated to be 35 and 11 respectively.

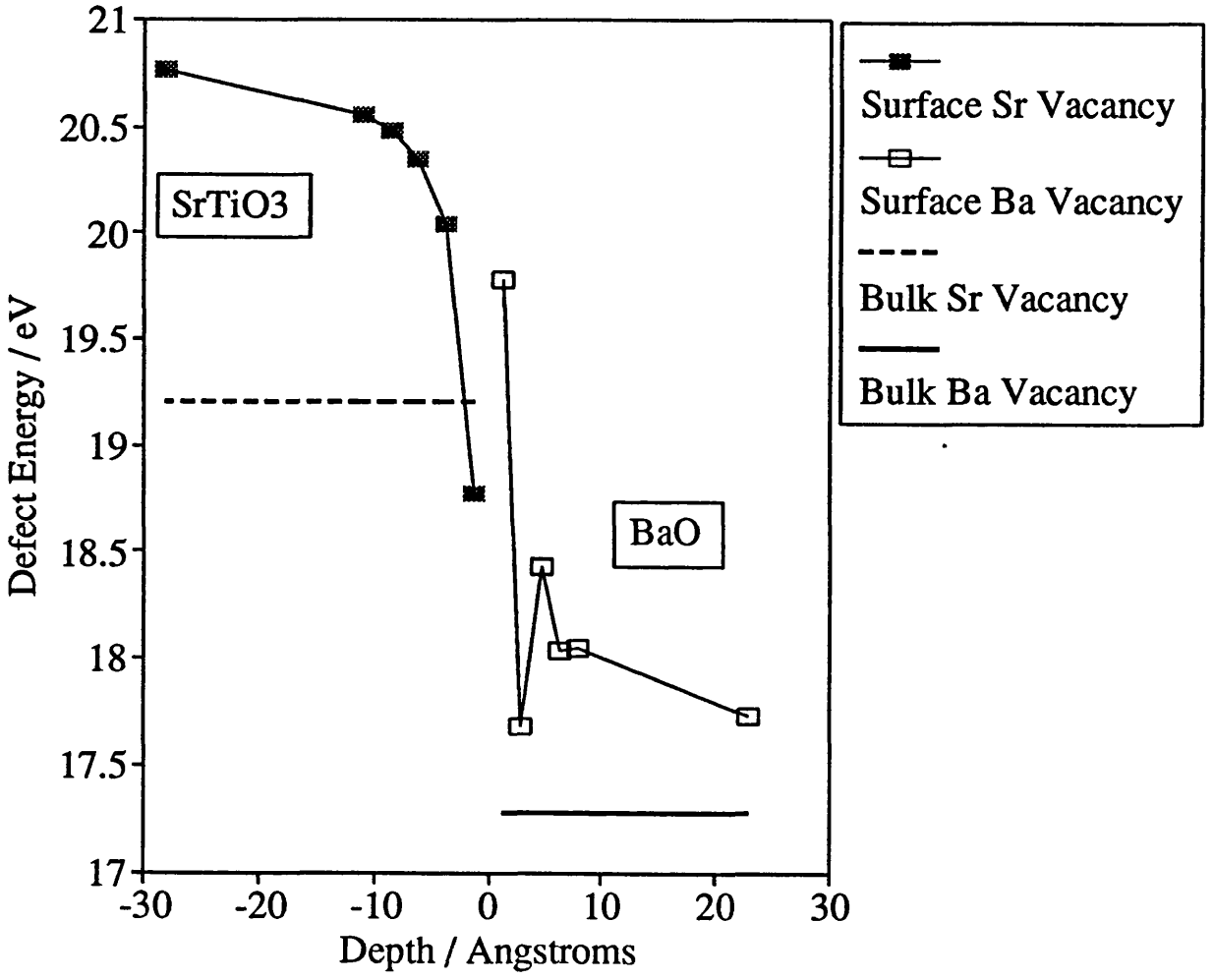

Figure 5.13 Strontium and Barium vacancy formation energies as a function of depth in the near interface region of the BaO(100)//$SrTiO_3$(100) interface. A depth of 0 represents the interface. The bold dotted line represents the strontium vacancy formation energy in bulk $SrTiO_3$ and the bold continuous line represents the barium vacancy formation energy in bulk BaO.

Figure 5.14 shows titanium vacancy formation energy at the near interface region. The formation of a titanium vacancy at the interface region is about 10eV more stable than the bulk value.

5.5 BaO Monolayer Formation on $SrTiO_3$

In this section, the mechanism by which a monolayer of BaO forms on a $SrTiO_3$ substrate is investigated. 1,2,3 and 4 BaO units are sequentially added to the $SrTiO_3$ surface and the system allowed to relax. The BaO is not constrained to accommodate any mismatch as only a maximum of 4 BaO units are added to an infinite $SrTiO_3$ surface. Only four systems were considered as the calculations are very cpu intensive.

The relaxed structures of 1,2,3 and 4 BaO units added to the surface of $SrTiO_3$ are illustrated diagrammatically in figure 5.15 and the variation of energy, per BaO unit, as a function of BaO units added to the $SrTiO_3$ surface is given in figure 5.16.

Substantial relaxation is observed for all the systems with the $SrTiO_3$ surface atoms relaxing out of the surface by more than a lattice spacing. For one BaO unit added, the $SrTiO_3$ surface oxygens can be observed to relax out of the surface and cluster around the added BaO unit. The energy of the system predicts this arrangement to be very stable compared to the other three systems (figure 5.16). This implies that monolayer formation occurs with the formation of individual BaO units on the surface as opposed to island or clusters of BaO. The relaxed structures of 2 and 4 BaO units added to the surface show strontium to have migrated from the second $SrTiO_3$ layer out above the surface!

Calculations involving ions undergoing large deviations from their natural lattice positions, such as surface relaxation and vacancy formation, can be modelled with

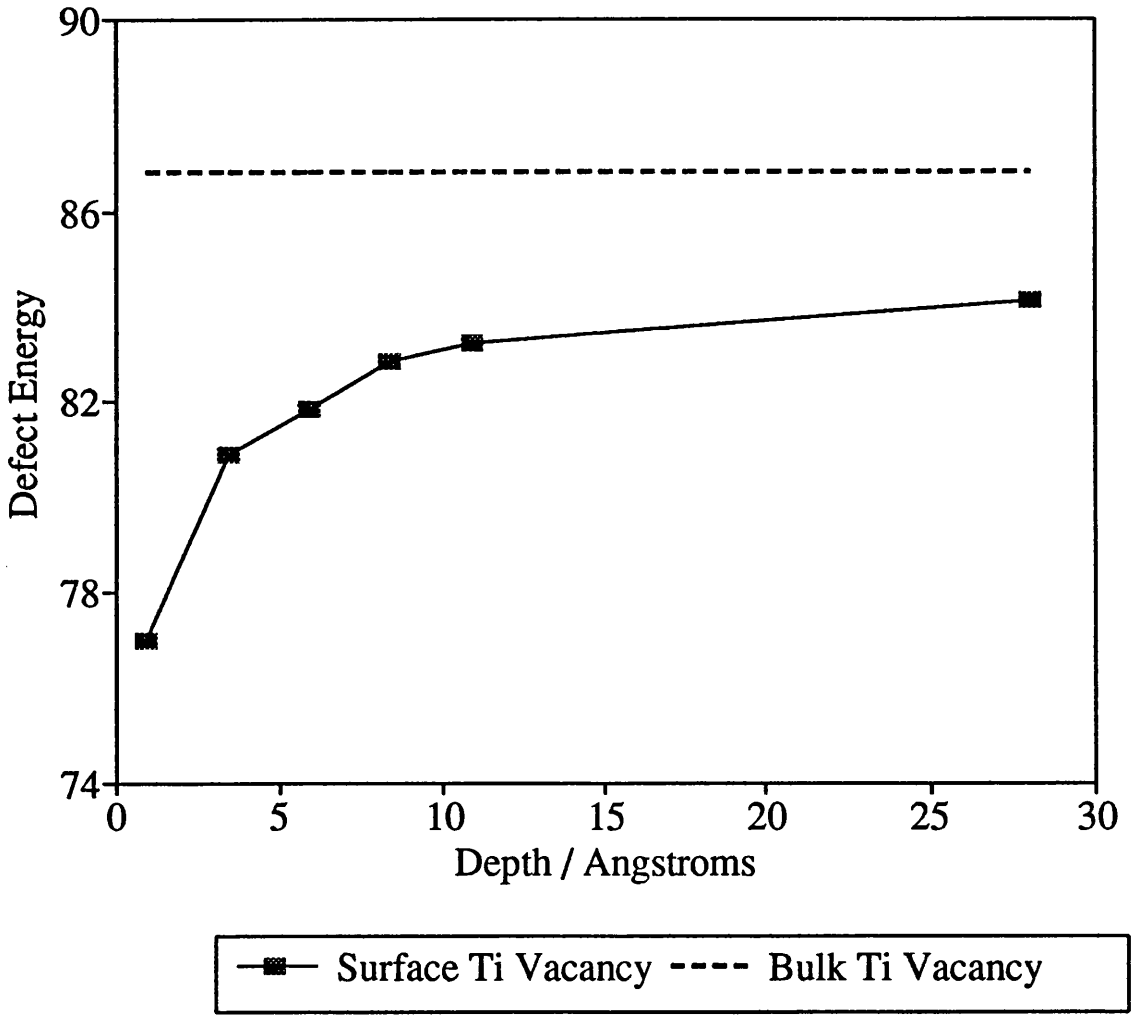

Figure 5.14 Titanium vacancy formation energy as a function of depth in the near interface region of the BaO(100)//$SrTiO_3$(100) interface. A depth of 0 represents the interface. The bold dotted line represents the titanium vacancy formation energy in bulk $SrTiO_3$.

Figure 5.15a Calculated relaxed structures of 1 and 2 BaO units added to a $SrTiO_3$ (100) surface.

BaO on SrTiO3

Chaos calculation

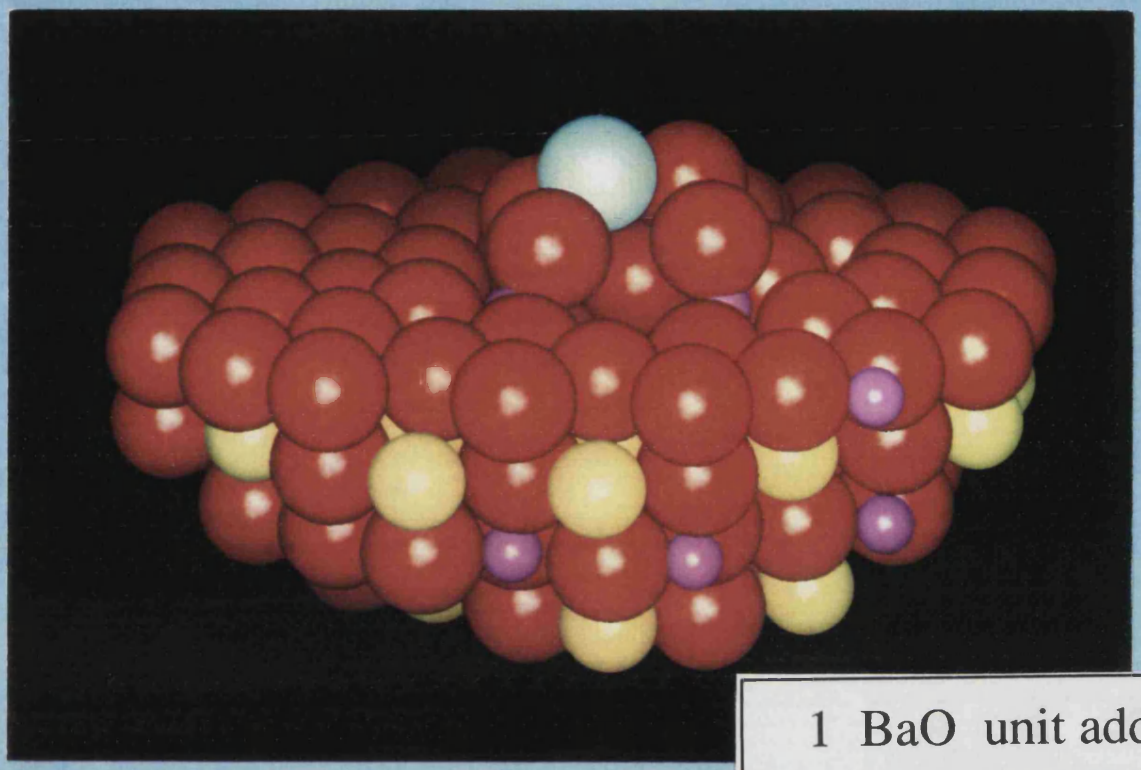

1 BaO unit added

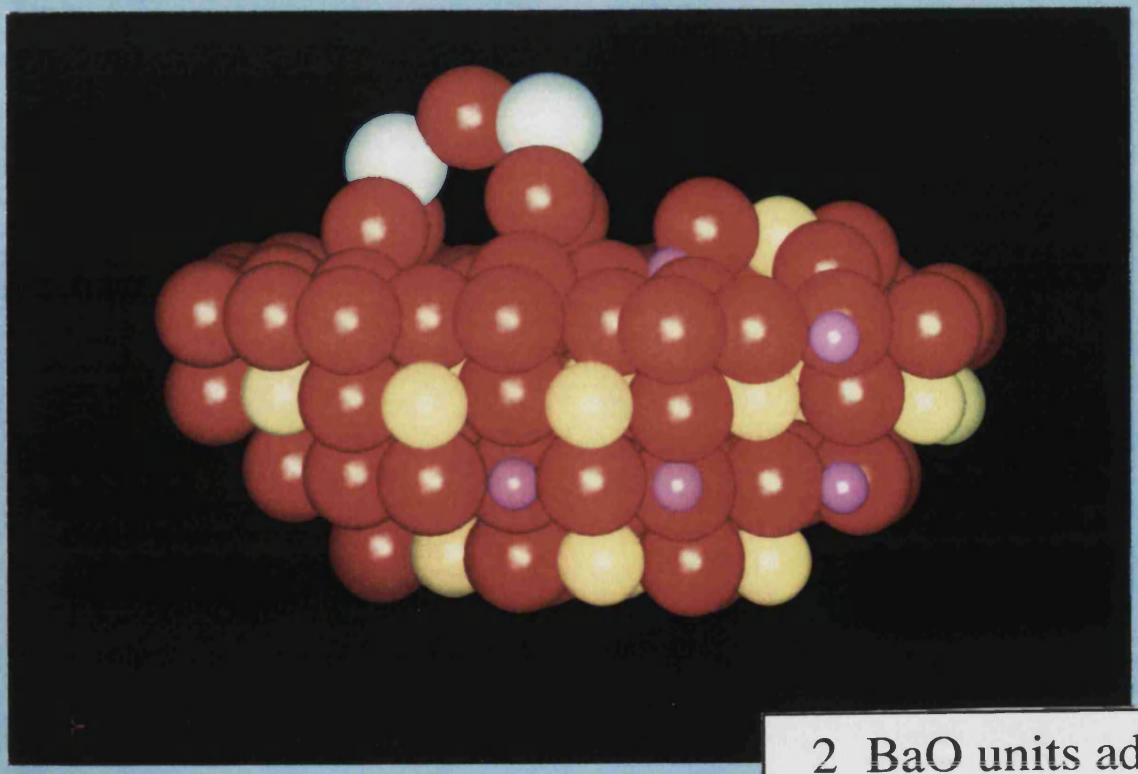

2 BaO units added

Figure 5.15b Calculated relaxed structures of 3 and 4 BaO units added to a $SrTiO_3(100)$ surface.

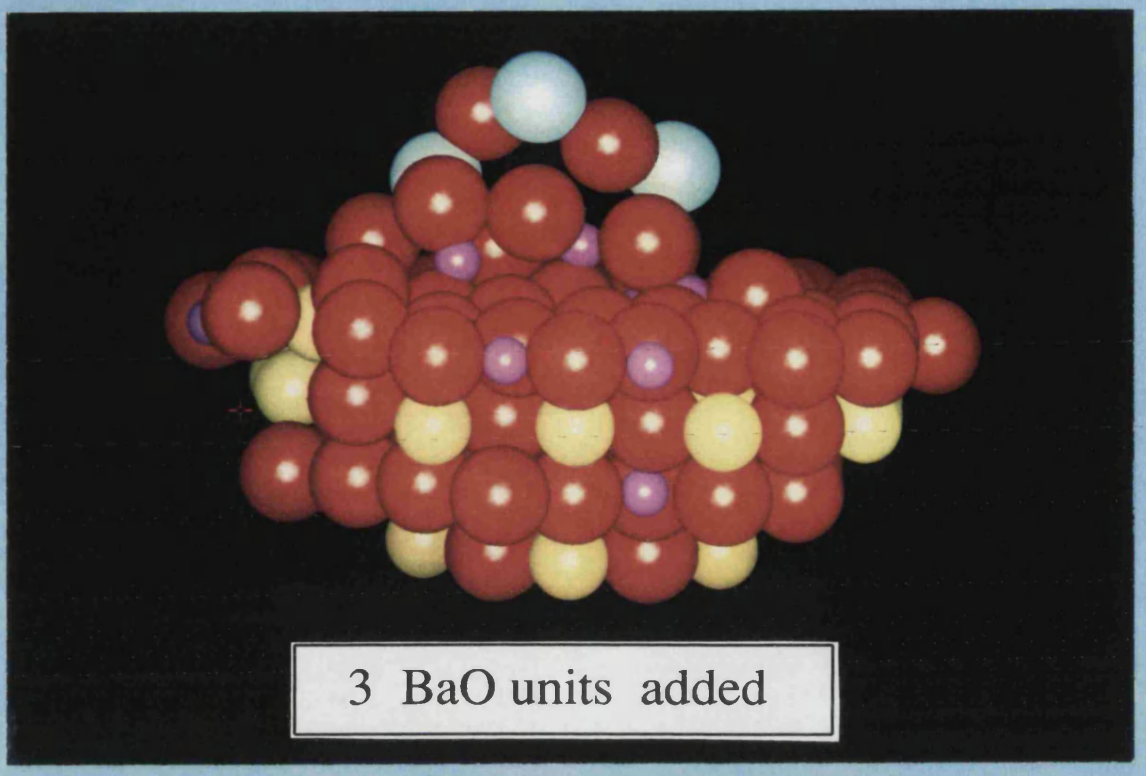

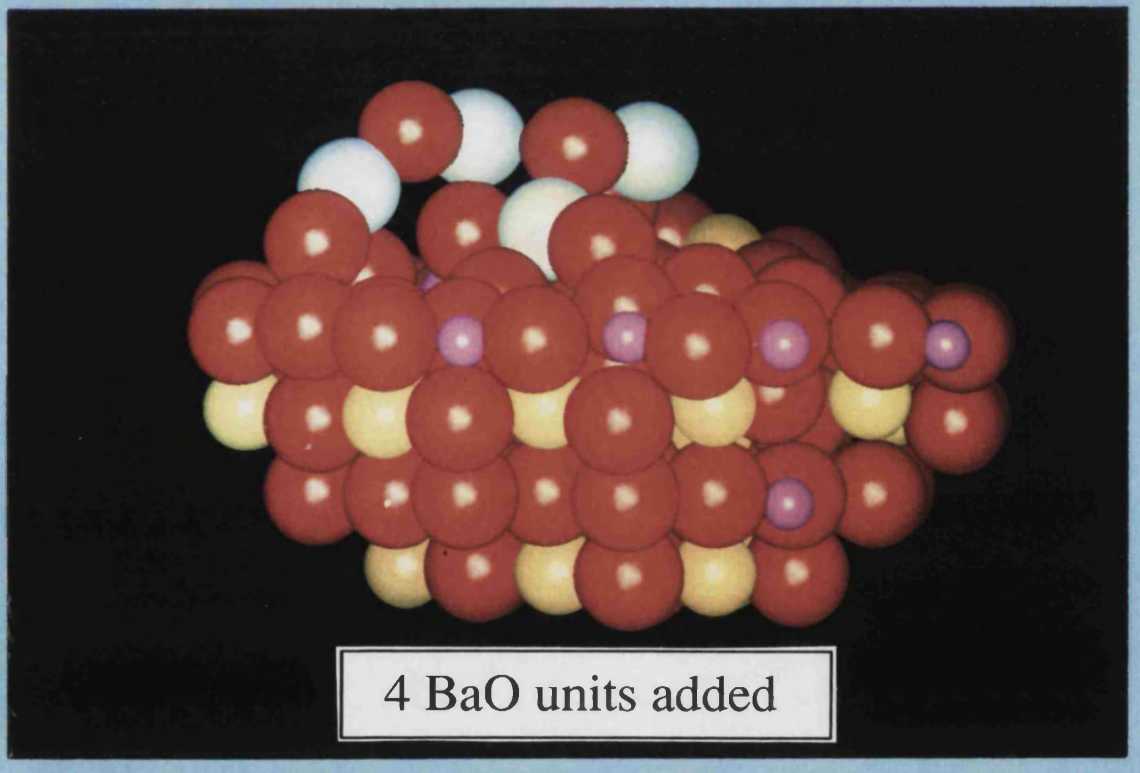

Titanium

Barium

Oxygen

Strontium

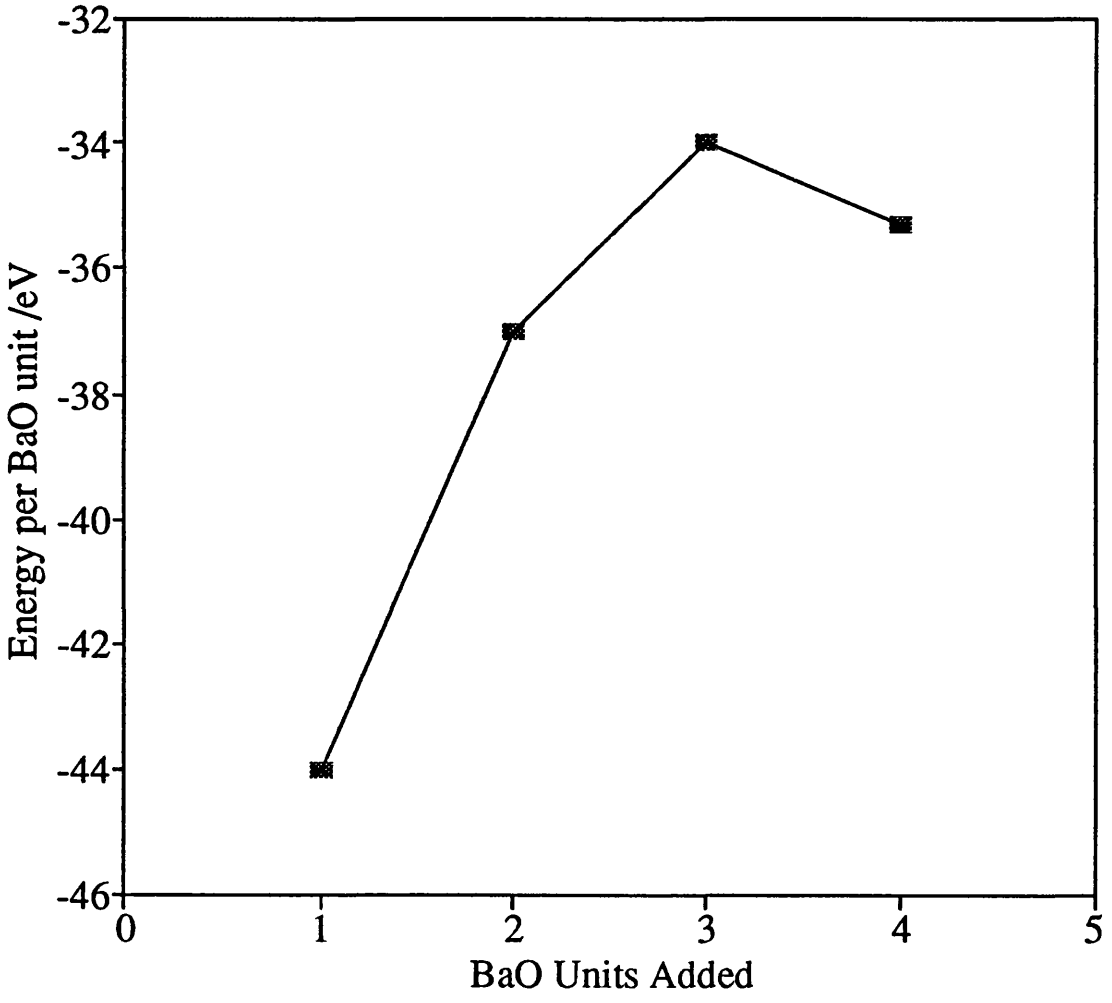

Figure 5.16 Calculated energies per BaO unit of each relaxed "cluster" of BaO on $SrTiO_3(100)$ for one to four units.

success using these types of potential (Lewis and Catlow 1985c). Indeed, the calculated results of the MgO surface energies relaxation and rumpling in chapter 4 gave excellent correlation to experimental results. The inaccuracies of these calculations are attributed to the changes in oxygen polarisability at the surface region because of the strong dependence of this parameter on crystal environment. The applications of these potentials and the result obtained with the systems described here, where clearly the BaO units are not in a BaO crystal environment, must therefore be treated with a degree of caution.

5.6 Removal of Constant Area Constraint

The interfaces simulated thus far, have indicated various factors responsible for interface stability such as good charge matching across the interface and reduced ion density at the interface, but most important is the deleterious effect straining the overlayer, to accommodate the mismatch, has on the interfacial stability.

The constant area constraint imposed by the simulation prevents the mismatch strain energy being alleviated by an expansion or contraction of the overlayers to exhibit their natural lattice spacings. This will obviously affect the charge matching across the interface, but interfacial relaxation and defect formation will optimise this. The problem in simulating this effect is the incommensurate lattices could lead to an infinitely large unit cell size (however experimental observations of symmetry at the interface suggest this is not the case). We can overcome this problem by constructing a (010) surface perpendicular to the interface (figure 5.17). The minimisations performed thus far have allowed relaxations in the [100] directions. Relaxations in the [010] and [001] directions are limited because of the constant area constraint imposed by the MIDAS code to ensure periodicity in neighbouring unit cells. The interfacial area can not change and the overlayer must accommodate this mismatch. The construction of a (010) surface will

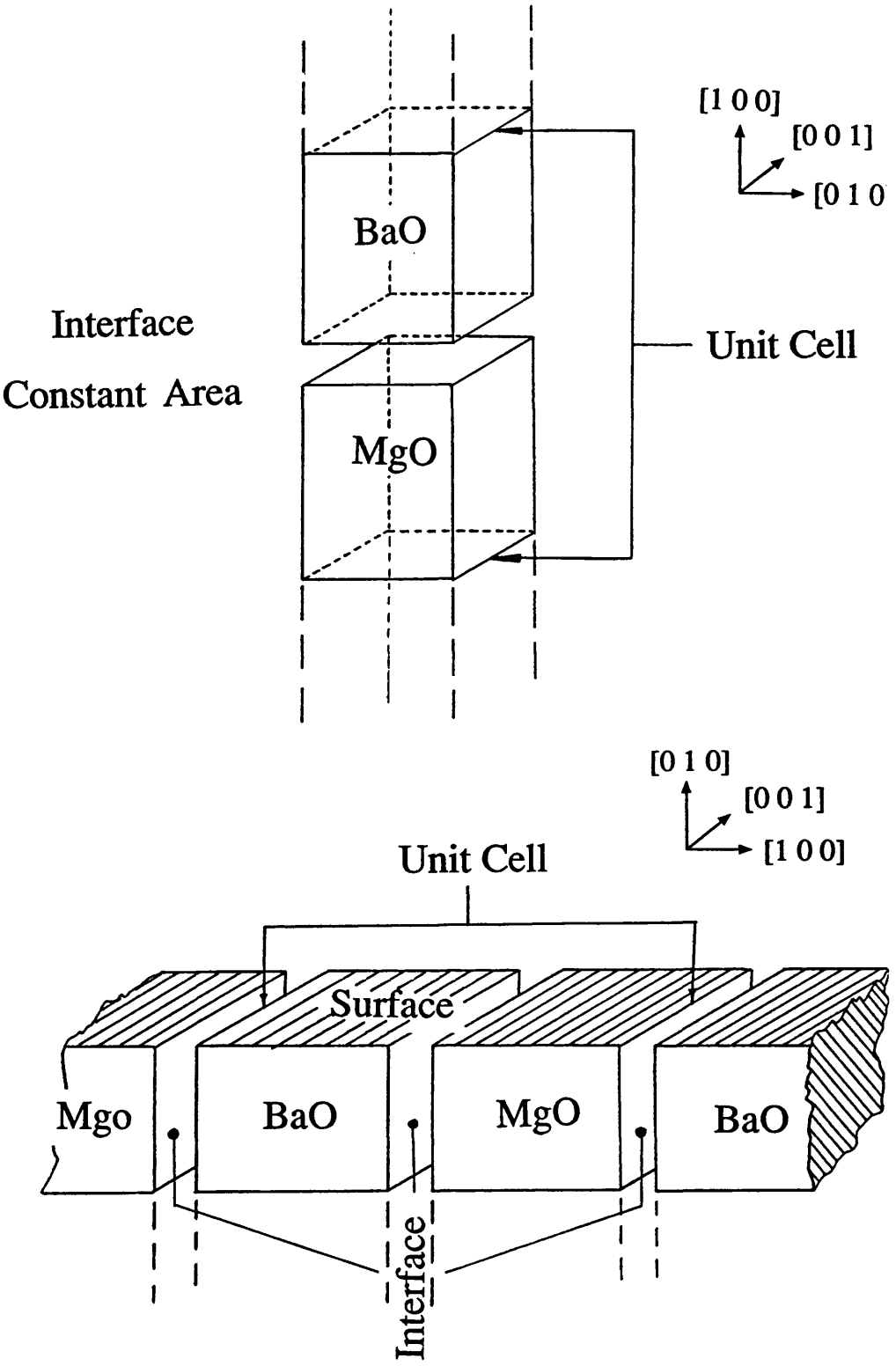

Figure 5.17 Top: original interface construction constrained to constant interfacial area in the [010] and [001] directions. Bottom: modified interface construction enabling relaxation in the [010] direction and hence allowing for an interfacial area change.

enable relaxation in the [010] direction. Since the interface is now perpendicular to this surface, relaxation into or out of the surface will also be associated with an *interfacial* area change. The constant area constrain must still be imposed and results in limited relaxation in the [100] and [001] directions. The [001] direction is in the plane of the interface and therefore relaxations in the plane of the interface are effectively restricted to one dimension. The construction of the new (010) surface also leads to the undesirable effect of having the interface region repeated every unit cell resulting in interface-interface interactions (for future calculations however this may be a useful parameter enabling us to examine edges). This effect will be more pronounced if the primitive unit cell is small thereby reducing the distance between neighbouring interfaces (figure 5.17). These calculations are therefore very intensive computationally and the small size of the primitive unit cell we can effectively model prevents any quantitative energy values from being produced especially as we have seen the relaxation effects at the interface to be of very long range into the crystals. We can however achieve a qualitative observation of how the strain energy induces the relaxation to reduce it and the resulting effect at the interface region. In these calculations, the accommodation of misfit strain is partitioned between the BaO and MgO on the basis of their respective bulk moduli so as to introduce as little strain energy into the system as possible. 1.7% of the 7% (bulk) mismatch is therefore assigned to be accommodated by the MgO and the remaining 5.3% to the BaO lattice. The MgO is constrained to accommodate a 1.7% expansion and the BaO a 5.3% contraction.

Figure 5.18a shows the individual ions within the new unit cell (region 2 is not shown for clarity). Figure 5.18b shows the behaviour of the ions at the interface region after partial relaxation and figure 5.18c after full relaxation. The relaxation of the magnesium ions (in the [100] direction) towards the BaO oxygens and away from the BaO bariums is consistent with previous calculations and in accordance with Cotter et al. (1988). This

Figure 5.18 (a) Pictorial representation of the modified interface construction with space filling atoms. (b) Behaviour of the ions at the interface region after the interface has been partially relaxed. (c) Behaviour of the ions at the interface after full relaxation. (d) Behaviour of the ions at the interface region after full relaxation with the number of planes explicitly relaxed in the [010] direction increased to 9. (e) As (d) with atom sizes reduced for clarity. Oxygen is coloured red, barium white and magnesium purple.

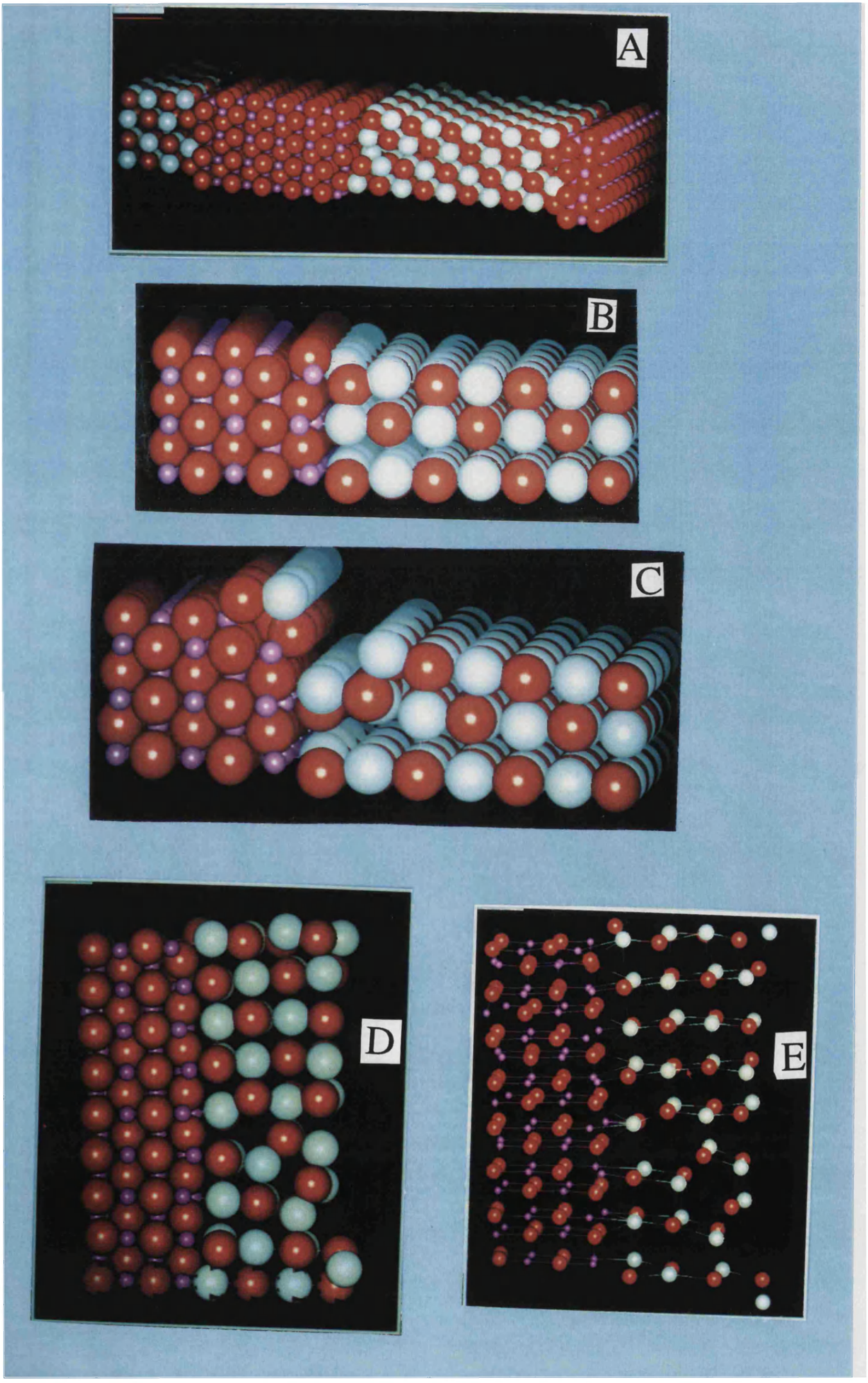
A
B
C
D
E

result shows the ions are indeed able to relax in the [100] direction, however the area must be conserved and the distance of the unit cell in the [100] direction remains fixed allowing little fluctuation in interplanar spacings.

Relieving the constant area constraint results in substantial reconstruction of the interface. The top barium ions at the interface region move towards the MgO crystal (figure 5.18b) and are finally associated with the MgO crystal together with the top layer of oxygens. It appears a "crack" is forming at the interface. The distance between the second and third BaO layers (in the [010] direction) is also artificially lengthened by approximately 1Å as a result of the relaxation. The BaO surface structure away from the interface predicts the BaO anions to relax into the bulk and the cations to relax out of the surface.

Figures 5.18d and 5.18e represent the same calculations as those above, with the depth ([010] direction) of the interface increased, enabling more ions in the [010] direction to relax explicitly. The figures show the behaviour of the ions at the interface region for nine BaO planes after full relaxation. The size of the ions in figure 5.18e have been reduced for clarity it is otherwise identical to figure 5.18d. The result of the relaxation is expected to reduce the imposed expansion of the BaO lattice and the imposed contraction of the MgO lattice as the imposed strain on the system will destabilise the interface. It appears however from figures 5.18d and 5.18e that the relaxation has resulted in the BaO expanding further as the BaO extends almost half a lattice unit higher than the MgO at the surface region. This unexpected result appears to result from a change in the BaO structure from plane five to seven from the surface. The structural modification appears to have resulted in a **local** expansion of the BaO crystal to accommodate the mismatch. A reduced ion density at the interface is also clearly visible from the figure.

The number of ions that can be accommodated within the computer is limited hence figures 5.18d and 5.18e are restricted to five planes perpendicular to the interface to maintain the depth of nine BaO planes. The interface-interface interaction is therefore more influential to the resulting relaxation behaviour than with 10 BaO planes in the [100] direction (as figures 5.18b and c). To accommodate more ions in the interface region the BaO and MgO were considered to be rigid ions and therefore allowing the number of ions to be doubled.

Figure 5.19a and 5.19b show the behaviour of the ions at the interface region after full relaxation for a system with 10 BaO and 10 MgO planes in the [100] direction. As these simulations give only qualitative information about the interfacial behaviour, employing a rigid ion model is justified. Figure 5.19a is a side view of the interface which is eight BaO planes deep, ten planes wide and two planes thick. The characteristic relaxation of the magnesium ions towards the BaO anions and away from the BaO cations is clearly seen. The "local" expansion of the BaO at the near interface region (observed in figures 5.18 d and e) is not apparent in this calculation. To accommodate the misfit strain energy, a reasonable contraction of the BaO lattice away from the interface is clearly evident. The BaO returns to its natural (bulk) lattice parameter five planes away from the interface region, whilst maintaining an artificially expanded lattice parameter at the interface. The contraction follows a smooth progression from a +5.3% mismatch at the interface (over 8 layers this corresponds to 0.42 of a lattice parameter) to adopting its natural lattice parameter. The fifth BaO plane is therefore about half a lattice parameter lower than the BaO plane at the interface. The MgO appears to exhibit the same behaviour with the MgO planes away from the interface region adopting their natural lattice parameter whilst MgO planes at the interface region remaining artificially compressed. This relaxation is more subtle than for the BaO and is barely visible in

Figure 5.19 (a) Behaviour of the ions at the interface region after full relaxation for a system with 10 BaO and 10 MgO planes in the [100] direction explicitly relaxed. (b) Side view of the interface. (c) Behaviour of the ions at the interface region after full relaxation for a system with 4 BaO planes explicitly relaxed in the [001] direction. Oxygen is coloured red, barium white and magnesium purple.

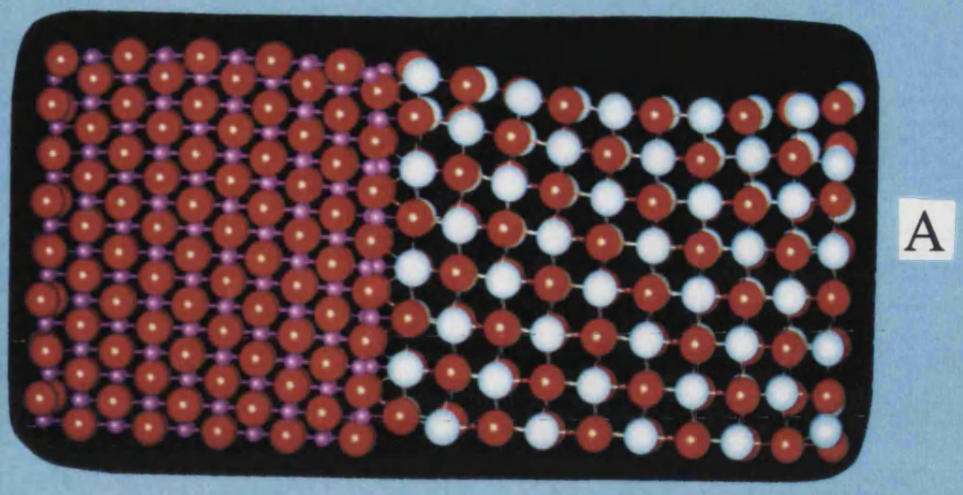

A

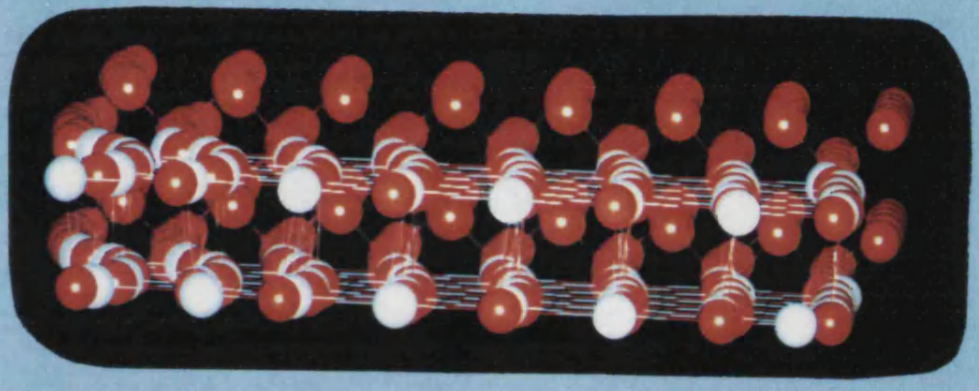

B

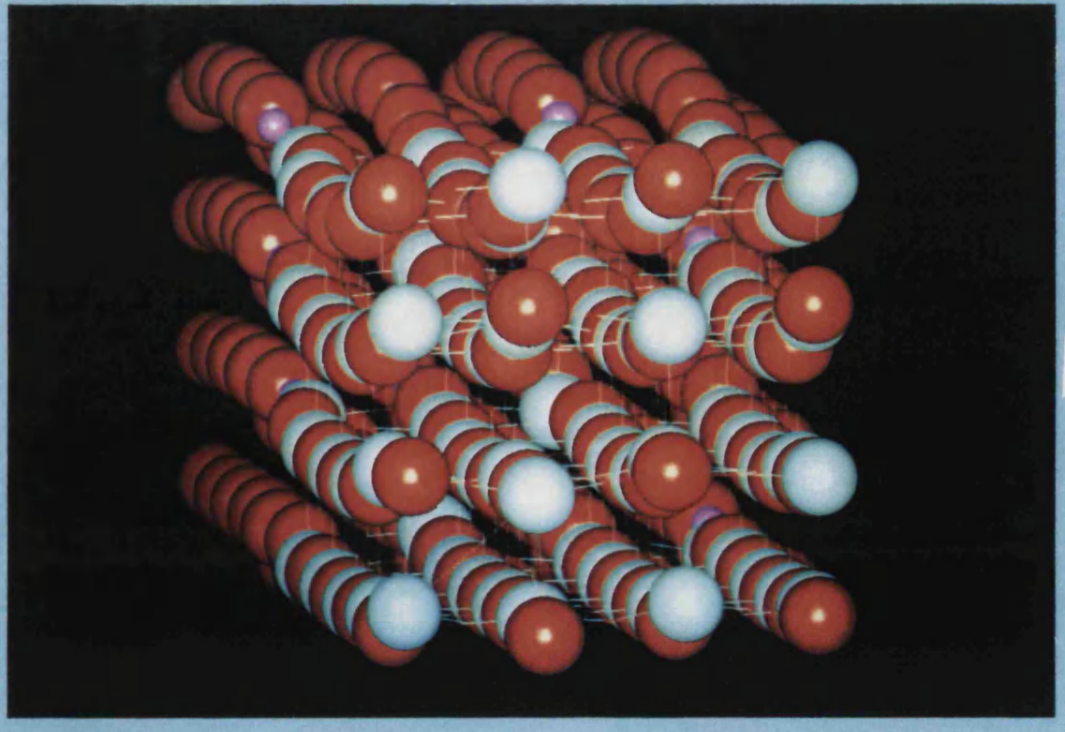

C

5.19a. Figure 5.19b shows a cross section of the interface. The relaxation is much more evident in this view and a "sine wave" like behaviour can be seen. The "amplitude" is high at the surface region and reduces to almost zero at the bottom layers (deeper into the bulk). A return to the natural lattice parameter away from the interface suggests a *strain gradient*; at the interface the lattice parameters of MgO and BaO are artificially lengthened or contracted, with the loss in energy, resulting from the strain in the lattices, compensated for by the favourable interactions across the interface. Strain gradients from interface regions, have also been observed experimentally by Dang and Veillet (1990) in epitaxial Co-Cu superlattices.

It must be noted that the surface relaxation of BaO and MgO are an intrinsic part of this type of calculation (albeit small compared to the interfacial relaxation) and will also contribute to the relaxational behaviour of the system.

Calculations performed thus far, have limited the thickness of the BaO crystal (relaxed explicitly) to two planes. To maintain a constant surface area only relaxations perpendicular to the surface ([010] direction) are allowed. Increasing the thickness to four BaO planes will enable more relaxation in the [001] direction (however conservation of surface area will greatly limit this relaxation). Figure 5.19c shows the interface with four BaO layers in the [001] direction. The depth of the interface has been reduced to four BaO planes to enable the number of ions to be accommodated by the computer. The wave-like behaviour of the interface is again clearly evident even with the limited depth of the interface. The relaxation parallel to the interface is (as predicted) very slight. Without the surface area restriction, the wave-like behaviour should be evident in two dimensions i.e. both perpendicular and parallel to the interface.

5.6.1 BaO Monolayer on MgO

The "removal" of the constant area constraint is now applied to investigate the relaxed structure of a BaO monolayer on the MgO substrate. Figure 5.20 shows diagrammatically the construction of the BaO monolayer on the MgO substrate with the existence of a surface perpendicular to the interface to allow for interfacial area variation in one dimension. The BaO monolayer is not constrained by further BaO layers and is therefore free to relax in both the [010] and [100] directions. The constant area condition continues to constrain the BaO to accommodate the mismatch in the [001] direction. Figures 5.21 show three projections (view A, view B, and view C) of the relaxed structure of the monolayer interface. Substantial reconstruction occurs at the interface region with ionic relaxation visibly extending seven lattice spacings into the bulk of the MgO substrate. View A shows the BaO overlayer to be "attached" to the top of the MgO substrate. Moving further from the top of the figure the MgO-BaO distance increases to 4.3Å suggesting the BaO has dissociated from the MgO. In view B, magnesium and oxygen ions have migrated from the MgO crystal to the top of the BaO monolayer. View C suggests a substantial modification of the BaO cubic structure after relaxation to an almost hexagonal symmetry. The relaxation perpendicular to the surface allows the BaO to accommodate its natural lattice parameter which is evident from figures 5.21 which show the BaO monolayer to have contracted perpendicular to the surface. The boundary conditions imposed on the BaO dictate that it accommodate the mismatch parallel to the interface. It appears to have achieved this by adopting a less dense configuration.

The removal of the constant area constraint was developed using the BaO(100)//MgO(100) system because both BaO and MgO are relatively simple structures. It may equally be applied to model more complex systems however this has not been considered as the size of the resulting system would be prohibitively large

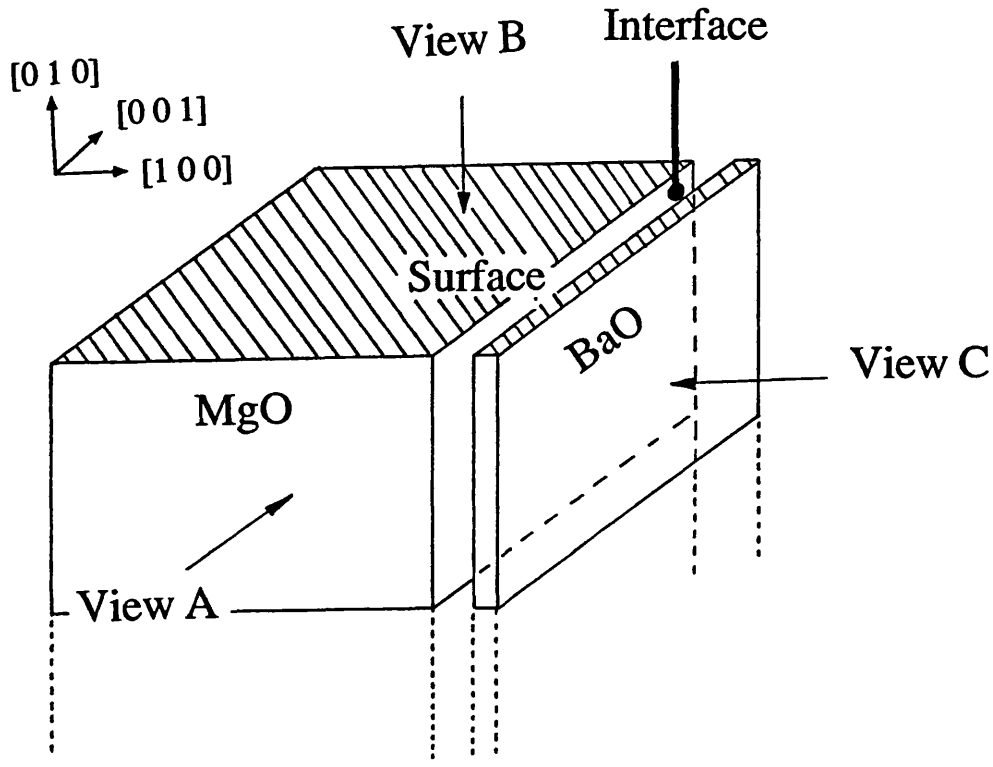

Figure 5.20 Construction of the interface allowing for relaxations in the plane of the interface [010] direction, for monolayer coverage.

Figure 5.21 Three projections of the BaO monolayer on MgO after relaxation. Oxygen is red, barium white and magnesium purple.

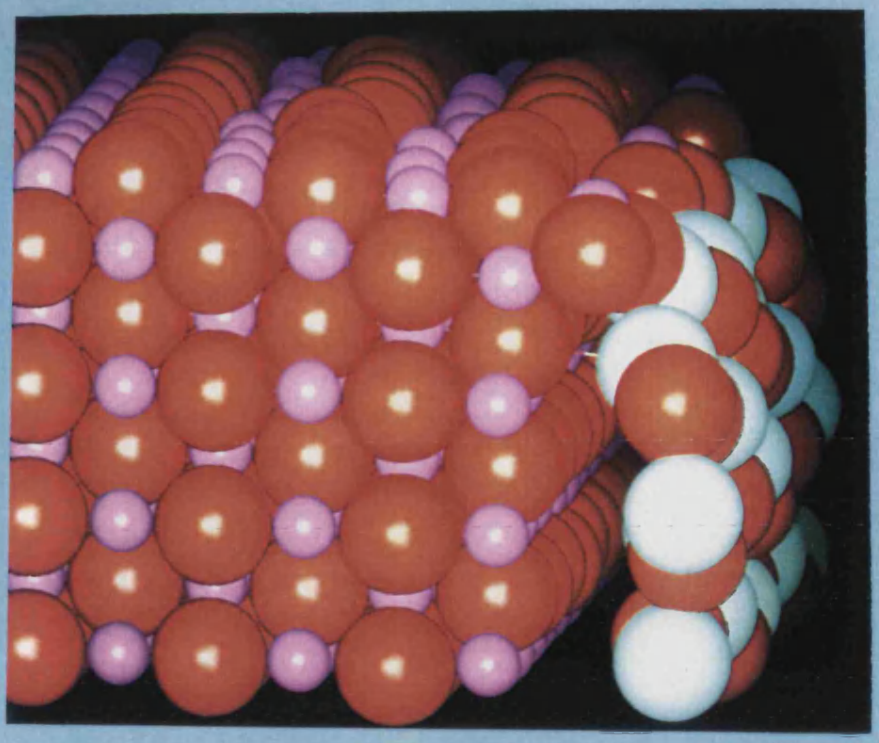

View A

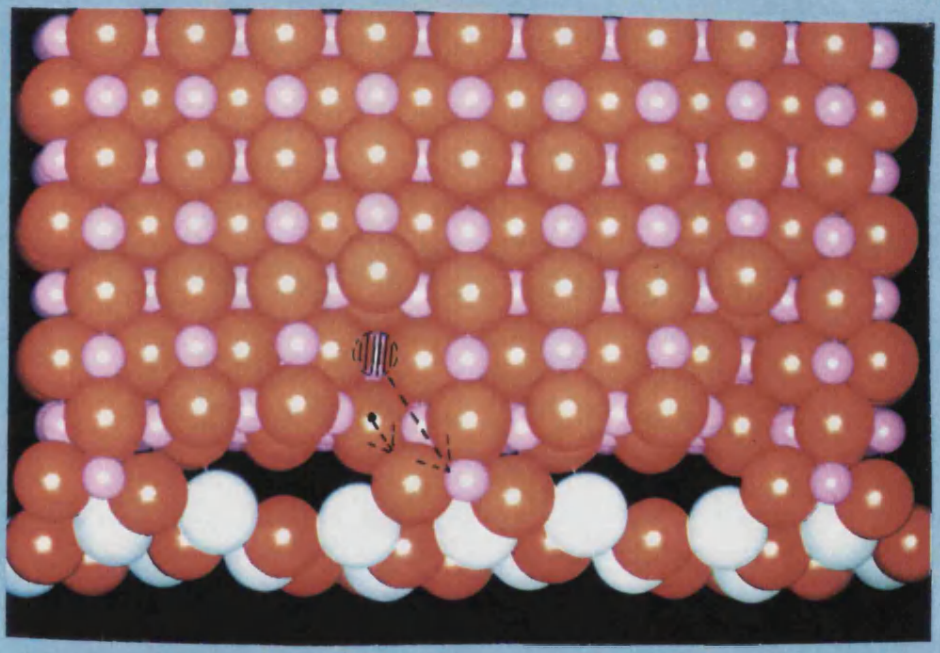

View B

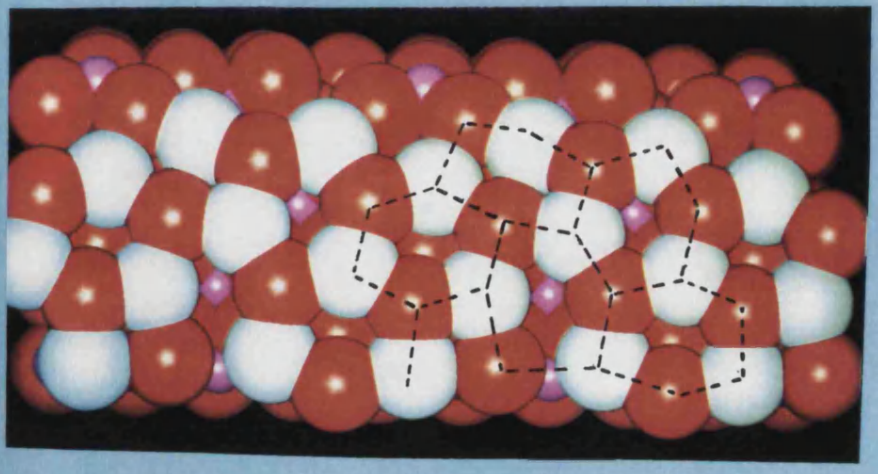

View C

computationally to consider even $SrTiO_3$ and $BaTiO_3$ interfaces. The application of this methodology must therefore wait for the inevitable increase in computer size and speed.

5.7 Summary

The most stable perovskite/rocksalt interfaces were those with the perovskite terminating with a TiO_2 plane at the interface region. From these results we have established that in determining the associated interfacial misfit for the substrate and thin film, the 'contracted' thin film lattice parameter must be considered.

For BaO on $SrTiO_3$ and $BaTiO_3$, the formation of the BaO monolayer was calculated to be the most stable. With further BaO additions the stability decreased until a constant energy was reached at about eight layers, with a maximum instability at two layers. For MgO on $SrTiO_3$ the interface was most stable for an MgO thin film of eight layers. For MgO on $BaTiO_3$, MgO monolayer formation was calculated to be the most stable. MgO on $SrTiO_3$ and $BaTiO_3$ showed maximum instabilities for two MgO layers added.

The methodology devised for the removal of the constant area constraint has enabled the strain energy imposed on the thin film and substrate to be dissipated by modifications of the interfacial area. The computational expense of these type of calculations has prevented the simulation of a large primitive unit cell in all three dimensions and therefore calculations were performed on a unit cell extended firstly in the [100] direction and next in the [010] direction at the expense of shortening the unit cell in the other two dimensions. Firstly the size of the cell explicitly relaxed in the [100] direction (figure 5.17) was extended. The results suggested the formation of a crack at the interface region. Second the size of the cell was increased in the [010] direction with 9 BaO planes in the [010] direction explicitly relaxed. This is at the expense of shortening the number of BaO and MgO planes in the [100] direction and thereby increasing the

detrimental interface-interface interaction. The relaxation reduced the strain in the system by lowering the density of the ions at the interface region with an associated **local** expansion of the BaO crystal. The results presented in this chapter verify that the reduction of ionic density at the interface region is a prerequisite for interfacial stability. The reduced density of ions at the interface has not been included explicitly in these calculations (unlike chapter 4) but are observed to be a consequence of reducing the strain energy, imposed by accommodating the mismatch.

Calculations employing the rigid ion model enabled the size of the unit cell to be effectively doubled. A unit cell extended in both the [100] and [010] directions was considered resulting in a wave-like pattern at the interface region where the BaO and MgO returned to their natural lattice spacings five planes away from the interface. The planes at the interface remained artificially lengthened (BaO) or compressed (MgO) to accommodate the mismatch.

It is undeniable that the misfit strain energy has a profound effect on the interface stability and its reduction is a major driving force to modifications of interfacial structure. Indeed, lowering the misfit strain energy imposed on the crystals to accommodate epitaxial matching, has been seen to increase the interfacial stability in all cases. The effects of factors such as relaxation, favourable interactions across the interface, formation of defects or dislocations has been seen to modify the stability but not to enable an interface of higher mimatch to become more stable than one of lower mismatch. If this were true in all cases the interfacial stability could be adjudged on purely geometrical grounds and the resulting interfacial misfit. This is investigated in the next chapter where interface structures of the same two materials with varying mismatch can be constructed using the Near Coincident Site Lattice theory (NCSL).

Chapter 6

BaO(1 0 0)//MgO(1 0 0) Twist Grain Boundaries

Using a Near Coincidence Site Lattice Theory

6.1 Introduction

In this chapter we use the near coincidence site lattice theory to construct interfaces with lower associated misfits. In conjunction with the minimisation techniques the relative stabilities of these interfaces can be calculated to find the most stable interfaces.

Interface structures investigated thus far have involved the overlayer constrained to adopt configurations conforming to a_o(substrate) = a_o(overlayer) or a_o(substrate) = $\sqrt{2}a_o$(overlayer) with an associated misfit of up to 7%. The resulting interfacial stability was found (in chapters four and five) to be heavily dependent on the magnitude of this mismatch. To increase the interfacial stability, configurations accommodating a much lower misfit are considered. The formation of a heteroepitaxial interface with configurations with a lower mismatch can be constructed using the Near Coincident Site Lattice Theory (NCSL) (Bollmann 1970, Smith and Pond 1976, Grimmer et al. 1974, Balluffi et al. 1982, Sutton and Balluffi 1987, Mykura et al. 1980, Gao et al. 1988). This theory, based on purely geometrical criteria, has also been applied with success to explain the existence of many experimentally observed interfaces (Mykura et al. 1980, Gao et al. 1988, Hwang et al. 1990).

We will first discuss the application of the near coincidence site lattice theory for a general two dimensional cubic (100) interphase boundary and show the special orientations with low associated misfits that can be constructed using this theory. This theory is then applied to construct various MgO(100)//MgO(100) twist grain boundaries and the relative stabilities of these interfaces are calculated using the minimisation techniques. The formation of coincident site lattice structures has been observed experimentally for these twist grain boundaries (Mykura et al. 1980, Gao et al. 1988,

Hwang et al. 1990). It is therefore a useful test of both the NCSL theory and the simulation techniques.

The near coincidence site lattice theory is next applied to the BaO(100)//MgO(100) system to investigate the variation of interfacial stability with percent misfit. This system is of little commercial importance. However it is a relatively simple system and is employed in this work as a model system representative of a heteroepitaxial interface with an incommensurate relationship. Furthermore the system has been investigated experimentally by Cotter et al. (1988, 1989) and therefore valuable comparisons with experimental observed interfaces can be made.

The methodology developed in this chapter can then be applied to more complex systems such as superconducting devices. This is addressed in chapter 7.

6.1.1 Near Coincident Site Lattice Theory (NCSL)

Near coincidence site lattice theory is a special case of the coincidence site lattice theory (CSL). For heteroepitaxial interfaces, the non-commensurate relationship between the lattice parameters of the two materials dictate that an exact coincidence cannot be found and hence a lattice misfit or near coincidence is introduced.

The full, three dimensional, CSL theory for cubic crystals is given by Grimmer et al. (1974). In this section we shall be concerned only with cubic {100} grain boundaries and heteroepitaxial interfaces.

We now outline the theory for these simple systems and apply it to the construction of new BaO(100)//MgO(100) interfaces with low associated misfits.

Cubic {100} interphase boundaries with lattice parameters a_1 and a_2, can be considered as two-dimensional square lattices. A two-dimensional coincidence site lattice is produced by rotating one square lattice with respect to the other about the common [100] axis (figure 6.1) until three lattice sites in the two materials are common. Exact coincidence, following Mykura et al. (1980), is given by;

$$(a_1/a_2)^2 = (m^2+n^2)/(k^2+l^2) \qquad (6.1)$$

Where k,l,m and n are integers. The rotational angle associated with this coincidence site lattice to bring the two crystals into exact coincidence is;

$$\Theta = \tan^{-1}(n/m) \pm \tan^{-1}(l/k) \qquad (6.2)$$

The four fold symmetry of the square lattices ensure positive and negative values of Θ give equivalent interfaces and therefore only values between 0 and 45° need be considered. The planar reciprocal coincidence density of crystal 1 and 2 are given by

$$\Sigma_1^p = m^2 + n^2 \qquad (6.3)$$

$$\Sigma_2^p = k^2 + l^2 \qquad (6.4)$$

The subscript p is used to denote a planar two dimensional coincidence (Gao et al. 1988). The coincidence density ($1/\Sigma_1^p$) is the fractional number of ions at the interface (of material 1) which are in coincidence with ions of material 2 (i.e. the ions have the same (010) and (001) coordinates for cubic {100} boundaries). Σ^p is also a measure of the primitive unit cell size. Exact coincidence only occurs when equation (6.1) is satisfied exactly (i.e. for grain boundaries where $a_1 = a_2$). However this relationship can never be

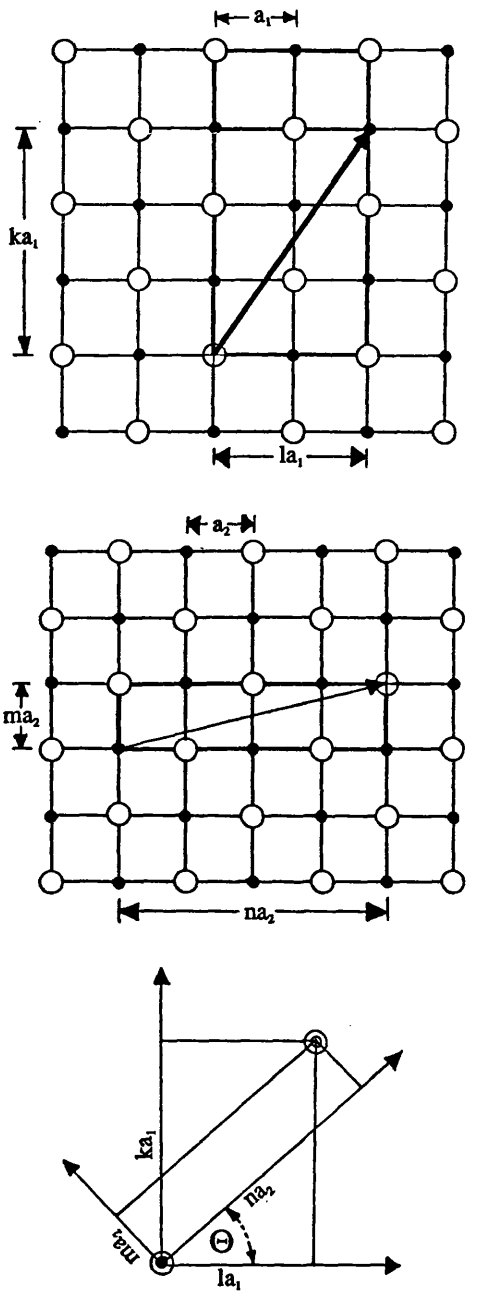

Figure 6.1 The geometry of two cubic lattices (with lattice parameters a_1 and a_2) forming a near coincident site lattice with associated angle of rotation Θ.

satisfied exactly for heteroepitaxial systems because the incommensurate relationship between the lattice parameters (for all known lattice parameters) ensures the left hand side of the equation is irrational whilst the right hand side is always rational. Equation (6.1) can be satisfied exactly if one or both of the lattice parameters are changed i.e. if the crystals are expanded or contracted with respect to their optimum lattice parameter.

The misfit, F, which must therefore be accommodated by this expansion or contraction is defined by the deviation from a coincidence condition, and designated a Near Coincidence Site Lattice (NCSL). This misfit is given by

$$F = 2(|a_1\sqrt{(\Sigma_1^p)} - a_2\sqrt{(\Sigma_2^p)}|) / (a_1\sqrt{(\Sigma_1^p)} + a_2(\sqrt{\Sigma_2^p})) \qquad (6.5)$$

A low value for the misfit resulting in a small loss in strain energy can always be achieved by increasing the size of Σ^p. The size of the resulting primitive unit cell however may become prohibitively large, even for modern supercomputers to accommodate, and the density of planar coincidence sites, Γ, (where $\Gamma = 1/\Sigma^p$) low. A low value of Γ is undesirable since it has been suggested by Brandan et al. (1964) that low values of Γ are conducive to low interfacial stability. The size of the unit cell which we are able to accommodate within the present simulation work is limited and therefore we are compelled to ensure the primitive cell size is suitably small ($\Sigma_p < 50$ assuming a simple rocksalt type structure). This would result in a high value of Γ but it is also likely to result in a high value for the misfit, F (Which we have shown in chapters four and five to be deleterious to the interfacial stability). A compromise between the value of the misfit and primitive unit cell size must therefore be sought.

For monatomic square lattices, all the solutions of equations (6.1) and (6.2) are coincidence site solutions. For diatomic square lattices with the NaCl (100) planar

structure, certain values of h,j,k and l will also give a coincidence between two positive or two negative ions. From Mykura et al. (1980) these are designated 'anti-coincidence orientations' and they occur when one of Σ_1^P, Σ_2^P is odd and the other is even. The NCSL primitive unit cell with anti-coincidence orientations will be assigned 'β' in this thesis. Mykura et al. also suggest these systems do not give minima in the interfacial energy. This can be explained by considering that a β type interface must accommodate a coincidence between either two positive or two negative ions and for two like charged ions in close proximity, this will inevitable destabilise the interface. However in this work we also include ionic relaxation which will enable the like charged ions to move away from each other and result in stable β-type interfaces. True coincidence site orientations occur when both Σ_1^P and Σ_2^P are odd and therefore will have one positive ion site and one negative ion site in coincidence per primitive unit cell. These will be assigned 'α' in this thesis.

The configuration for the BaO(100)//MgO interface considered in chapters 4 and 5 can be described using NCSL theory;

$\Sigma^P_{(BaO)} = (1^2+0^2) = 1$ $\Sigma^P_{(MgO)} = (1^2+1^2) = 2.$

$\Theta = \tan^{-1}(0) \pm \tan^{-1}(1) = 45^o$

The interface is designated anti-coincident and is therefore assigned a β. The NCSL description is therefore Σ^P 1/2 β, $\Theta = 45^o$ with F = 0.0714 (assuming lattice parameters $a_{MgO} = 4.2$, $a_{BaO} = 5.53$).

The discrepancy between the coefficients of linear expansion of the two materials may enable the materials to be in exact coincidence (i.e. misfit = 0) at a particular temperature

for a near coincidence site lattice of low misfit, F. The formation of the particular near coincidence site lattice at this temperature would (following the arguments of Balluffi et al. (1982)) contain less 'intrinsic' defects (i.e. defects which exist as an integral part of the low energy equilibrium boundary structure). This is of great importance to the application of these materials to electronic devices where the existence of defects may have deleterious effects on the material properties. Indeed in superconductors, defects may introduce local scattering potentials and also perturb phonon modes which may be crucial for coupling (Allan and Mackrodt 1989b). When the crystals are returned to room temperature however, the strain introduced at the interface region may cause the interface to crack. This has been observed in our calculations in chapter five (figures 5.18c) where the BaO and MgO were constrained to accommodate a 7% misfit and then allowed to relax to their natural lattice spacings.

6.2 Stability of MgO(100)//MgO(100) twist grain boundaries using CSL theory.

Mykura et al. (1980) have performed electron microscope measurements of the angular distribution of small, cubic MgO crystals deposited on an MgO (100) substrate and have found them to exhibit marked preferred orientations. These orientations conform well to those predicted using coincident site lattice theory. Mykura et al. measured the frequency of occurrence of MgO cubes as a function of disorientation angle Θ about the [100] direction in 1^{o} steps. A high occurrence at a particular disorientation angle is synonymous with a high stability of that particular coincident site lattice and associated disorientation angle. In this section we use CSL theory to construct various MgO(100)//MgO(100) twist grain boundaries (Sun and Balluffi 1982a, 1982b) and calculate their relative stabilities and relaxed interfacial structures using the minimisation techniques. The calculated results are then compared to MgO(100)//MgO(100) twist grain boundaries, experimentally observed by Mykura et al. (1980) This will provide a useful test of the computer simulation techniques combined

with CSL theory in reproducing the results of Mykura et al.

The size of the resulting primitive unit cell prohibits investigation of coincidence site lattices with $\Sigma^p > 25$. Three MgO planes were explicitly relaxed either side of the interface for coincidence site lattices of Σ^p= 1,5,13 and 17. Only one MgO plane either side of the interface was relaxed explicitly for the $\Sigma^p = 25$ as three planes exceeded the available size that could be accommodated within the computer. The results from the Σ^p=25 are therefore less reliable.

The calculated stability is the energy required to cleave the interface and form two perfect MgO(100) surfaces, per unit area. This is analogous to the calculation of surface energies.

6.2.1 Reduced density calculations

The action of placing an MgO(100) surface on MgO(100) at a specific orientation, inevitably results in two like charged ions being in close proximity (one almost directly above the other). Therefore, for the calculated MgO(100)//MgO(100) twist grain boundaries, the ionic density of the interface was reduced to remove these destabilising interactions. The procedure followed the results of Duffy (1986) whose calculations on NiO(100)//NiO(100) twist grain boundaries suggest that a reduction of ion density at the interface significantly enhances the stability.

The reduced density calculations involve the removal of a stoichiometric MgO unit from each surface unit cell to maintain charge neutrality. The ions to be removed were identified by considering the Madelung energies. The Madelung energies of all the ions at the interface region before relaxation were calculated and those ions with the most positive Madelung energies (i.e. the least stable) removed. The relaxation behaviour can

modify or even reverse this result as was observed for vacancy formation energies calculated at the near interface region for the $BaO(100)//SrTiO_3(100)$ in chapter 5 (figure 5.12 and 5.13). Thus the Madelung energies should be treated only as a guide and might not lead to the most stable interface.

The stabilities of the MgO(100)//MgO(100) twist grain boundaries after relaxation were calculated for all coincidence site lattices for Σ^P (type α) less than 29 and are given in table 6.1.

Table 6.1 shows that a reduced ion density at the interface stabilises the interface. As in all cases, increased stability is achieved by reducing the ion density, apart from the perfect crystal where $\Sigma^P = 1$. Moreover without the defects the interfaces would not exist and therefore defects are an integral part of the low temperature grain boundary structure. The relative ordering of stability for the various coincident site lattices observed experimentally are:

$$(\Sigma^P = 1) > (\Sigma^P = 5) > (\Sigma^P = 13) > (\Sigma^P = 25) > (\Sigma^P = 17)$$

These relative stabilities are identical to our calculated results.

6.2.2 Statistical Thermodynamic treatment of energies

The application of a simple statistical thermodynamical treatment of our results can provide relative occupational levels of the various coincidence site lattices at any temperature on the basis of their relative stabilities. Hence, a direct comparison of the occupational levels to the experimentally observed values can be made.

We consider the 'ground state energy' to be the perfect bulk MgO crystal i.e. the $\Sigma^P = 1$.

Table 6.1 Calculated stabilities of the MgO(1 0 0)//MgO(1 0 0) twist grain boundaries for Σ^p up to 25. With full and reduced densities of ions at the interface region.

Σ^p	k,l	Θ	Stability / Jm^{-2}	
			Full density	Reduced density
1	1,0	0°	+1.13	---
5	2,1	36.87°	Unstable	+0.45
13	3,2	22.62	Unstable	+0.44
17	4,1	28.07	Unstable	+0.09
25	4,3	16.25	Unstable	+0.43

The 'probability function' of the interfaces Σ^P = 5,13,17 and 25, with respect to their relative energies, is calculated using;

$$q_i = P_i \exp(-\Delta E/kT) \qquad (6.6)$$

P_i is the degeneracy of the interface (in this case, the same for each interface). ΔE is the energy with respect to the 'ground state' ($\Delta E = E(\Sigma^P = n) - E(\Sigma^P = 1)$). k is Boltzmanns constant and T is the temperature. The occupancy level of a particular interface can be calculated, for a given temperature, by dividing the probability function of the interface by the probability functions of all the interfaces considered.

$$\text{occupancy level} = (P_i \exp(-\Delta E/kT)/(\Sigma_i P_i \exp(-\Delta E/kT) \qquad (6.7)$$

The 'Σ' in equation (6.7) represents the summation of the probability functions for all the interface energies (not the planar reciprocal coincidence density). The occupancy level of the perfect bulk crystal is assigned the same level as the experimentally observed value. This automatically gives a value for the temperature and the occupancy levels of the other interfaces are calculated using the equations above. Fitting the occupational level of the perfect crystal to the results of Mykura et al. (1980) gave a temperature of 1500K. The occupational levels of the interfaces Σ^P = 1 to 25 are given in figure 6.2. The experimental results are included as a comparison. It is clear from the figure that there is an excellent correlation between the experimentally determined values and the calculated values. No comparison can be made with the interface calculations without defects as all of these interfaces were found to be unstable with respect to the pure MgO surfaces. The occupancy levels at higher temperatures can easily be calculated using equations 6.6 and 6.7. These calculations will be useful for assessing the occupational levels of the various interfaces after annealing. It has been proposed that the annealing

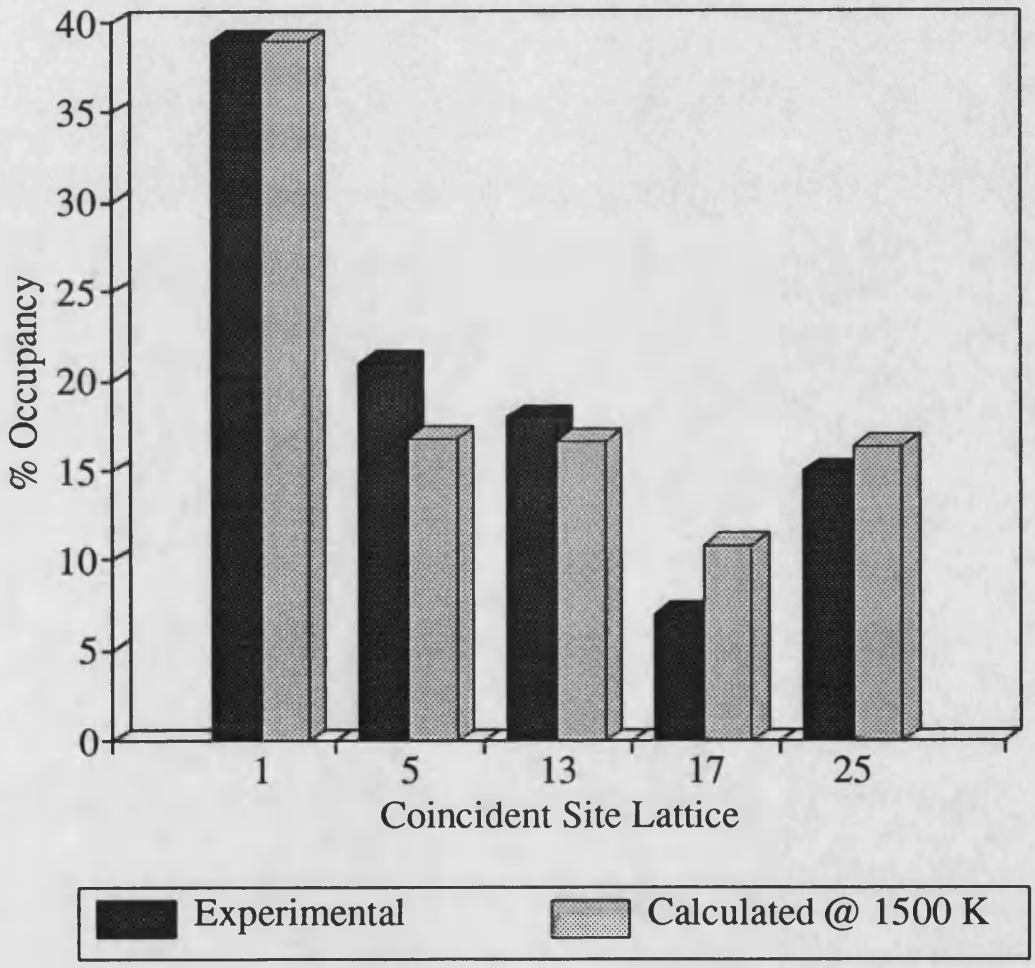

Figure 6.2 Comparison between the experimental and calculated occupation levels of the MgO(1 0 0)//MgO(1 0 0) twist grain boundaries for Σ^p up to 25.

process enables the crystals to rotate and adopt equilibrium orientations (Sautter et al. 1977). The occupational levels of the higher energy configurations will therefore increase with temperature. The application of statistical thermodynamics to obtain occupation levels at higher (annealing) temperatures from the calculated interface energies is ideally suited to predict this behaviour. The mechanism for rotation suggested by Pond and Smith(1977) involves the glide of screw dislocations out of the interface. This mechanism implies an 'activation energy' which will inevitably increase the inaccuracies of the calculated occupation levels, which is an equilibrium process.

6.2.3 Calculated relaxed structures of MgO(100)//MgO(100) twist grain boundaries

Figure 6.3 shows the relaxed structures of two of the interfaces including defects. Only one MgO layer either side of the interface is shown for clarity. Figure 6.3a is the $\Sigma^P = 5$ ($\Theta = 36.9°$)interface and figure 6.3b the $\Sigma^P = 13$ ($\Theta = 22.6°$) interface. The ions in the boundary plane restructure to form regular arrays of octagons (which surround the defects), hexagons and squares. The restructuring has enabled good charge matching across the interface resulting in a more stable structure than the interfaces with no defects. These structures have identical configurations to those calculated by Duffy (1986) for NiO(100)//NiO(100) twist grain boundaries.

Similar calculations were performed by Wolf (1985) on MgO twist grain boundaries. The relaxed grain boundary energies were calculated for $\Sigma^P = 1$ to 65 and no defects were included. The relaxed grain boundary energies were found to increase as a function of the twist angle for $\Theta \leq 20°$ (in accordance with the Read-Schottky model (1950)). For $\Theta > 20°$, the energy was found to be independent of Θ or Σ^P. He concluded that the properties of {100} twist boundaries are determined by the twist angle and not the value of Σ^P. In contrast to the work of Wolf, we find no correlation between the twist angle Θ and the grain boundary energy. The factors contributing to interfacial stability such as

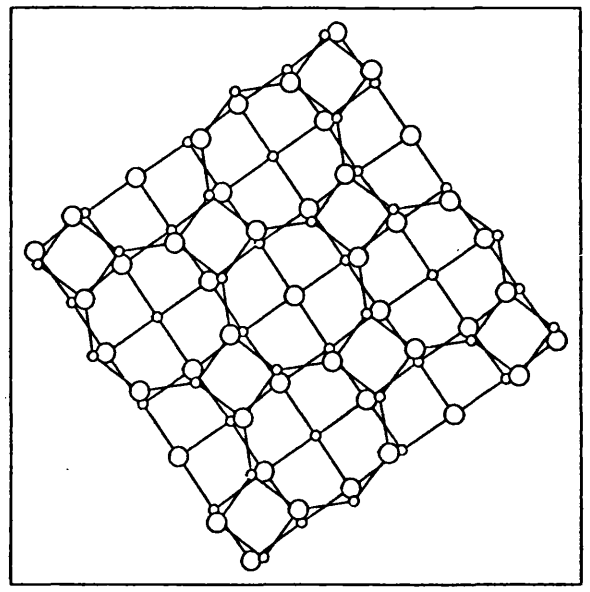

A

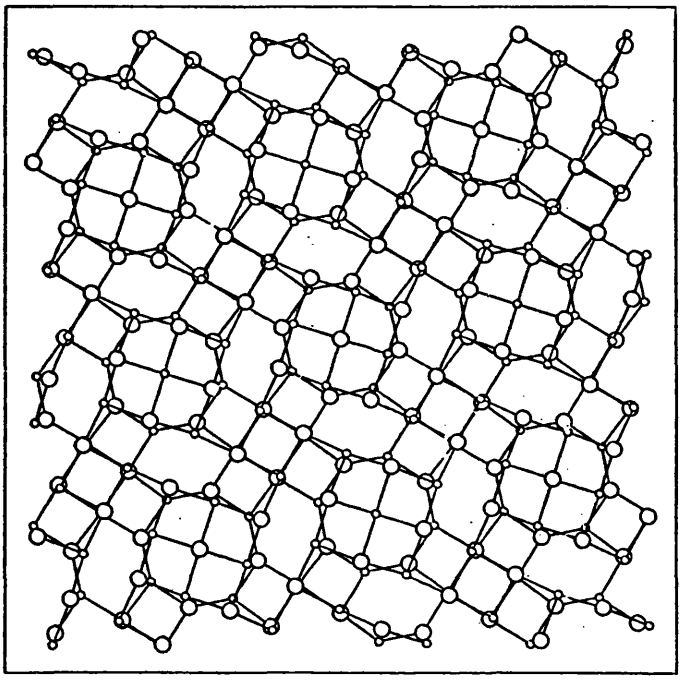

B

Figure 6.3 Graphical representation of the structure of the reduced density Σ^p = 5 and Σ^p = 17 MgO(1 0 0)//MgO(1 0 0) twist grain boundaries after relaxation. Only the two planes at the boundary plane are shown for clarity.

relaxation, charge matching across the interface, defects and dislocations and accommodation of misfit strain energy (for heteroepitaxial systems) show that stability of the grain boundaries can not be derived as a function of twist angle alone.

6.3 Stability of the BaO(100)//MgO(100) interfaces using NCSL theory

In this section we apply the near coincidence site lattice theory to construct various BaO(100)//MgO(100) heteroepitaxial interfaces and calculate their relative stabilities and relaxed structures using the minimisation techniques.

The interfaces predicted using the near coincidence site lattice theory for BaO(100) on MgO are given in table 6.2. These were calculated for a_o(BaO) = 5.53Å and a_o(MgO) = 4.20Å. Positive values of F indicate that the BaO overlayer must be expanded to accommodate the mismatch and negative values indicate that the BaO overlayer must be compressed to accommodate the mismatch.

For BaO monolayer and thin film coverage, the bulk BaO lattice parameter is not applicable to determine the near coincidence site lattice as the lattice parameter for a BaO monolayer is calculated to be about 7% smaller than for bulk BaO (figure 5.6). The 'contracted' lattice parameter must therefore be used. This obviously modifies the misfit F derived from using the NCSL theory and also introduces new NCSL's with low values of F. Table 6.3 shows the new NCSL's with their associated misfits adjusted for the changes in BaO lattice parameter for 1,2,3,6,8 and 20 BaO layers.

6.3.1 Potential Energy Surfaces

The initial configuration of the near coincidence site lattice can be constructed with the overlayer displaced in the plane of the interface ([010], [001] directions) such that one ion from the substrate and overlayer are in coincidence to ensure maximum interfacial

Table 6.2 Interfaces predicted for BaO(1 0 0) on MgO(1 0 0) using a near coincidence site lattice theory assuming a bulk value for the BaO lattice parameter.

$\Sigma^P_{BaO}/\Sigma^P_{MgO}$		k l m n	Θ	Misfit F
1/2	β	1 0 1 1	45	+0.0714
5/8	β	1 2 2 2	18.435	+0.0401
5/9	α	2 1 3 0	26.565	+0.0188
8/13	β	2 2 3 2	11.310	+0.0324
9/13	α	3 0 3 2	33.690	-0.0880
9/16	β	3 0 4 0	0	+0.0126
10/17	β	3 1 4 1	4.399, 32.471	-0.0098
16/29	β	4 0 5 2	21.801	+0.0223
17/29	α	4 1 5 2	7.765, 35.838	-0.0081
25/41	α	4 3 5 4	1.790, 14.470	-0.0278
26/45	β	5 1 6 3	15.255, 37.875	-0.0008
29/50	β	5 2 7 1	13.671, 29.932	-0.0027

Table 6.3 Predicted %misfit for the BaO(1 0 0)//MgO(1 0 0) interface using a near coincidence site lattice theory for 1,2,3,6,8 and 20 BaO layers on the MgO substrate. These values were calculated by incorporating the optimum BaO lattice parameter for "n" BaO layers 'in space'.

$\Sigma^P_{BaO}/\Sigma^P_{MgO}$		% Misfit for n Layers					
		n = 1	= 2	n = 3	n = 6	n = 8	n = 20
1/2	β	+14.3	+10.2	+9.1	+8.1	+7.9	+7.5
5/9	α	+9.1	+5.0	+3.9	+2.8	+2.6	+2.2
9/16	β	+8.5	+4.3	+3.2	+2.2	+2.0	+1.6
10/17	β	+6.2	+2.1	+1.0	-0.03	-0.3	-0.7
8/13	β	+4.0	-0.2	-1.3	-2.3	-2.5	-2.9
5/8	β	+3.2	-0.9	-2.0	-3.1	-3.3	-3.7
13/20	β	+1.2	-2.9	-4.0	-5.0	-5.2	-5.6
17/26	β	+0.9	-3.2	-4.3	-5.3	-5.5	-5.9
9/13	α	-1.9	-6.0	-7.1	-8.2	-8.4	-8.8
13/18	β	-4.0					
13/17	α	-6.9					

stability. This approach assumes that the interfacial energy is controlled by the ions which are in coincidence. As the distance between the two ions in coincidence is smaller than non-coincident ions they will contribute more to the interfacial stability than any other ionic interaction. For type β interfaces, some ions are in coincidence with like charged ions i.e. anti-coincidence orientation (type β). This results in a destabilisation of the interface. This can be further complicated because the coincidence of oppositely charged ions may contribute less to the interfacial stability than the sum of the contributions of all the ions across the interface. This is particularly important for interfaces with large primitive unit cell areas (NCSL's with high Σ^P) as the ratio of coincidence sites to non-coincidence sites (Γ) decreases. This argument also implies that low values of Γ, are conducive to interfacial stability (assuming a purely geometric consideration) as suggested by Brandon et al.(1964). However, Sutton and Balluffi (1987) find experimental results which violate this proposal. In addition Sutton and Balluffi found low Γ at constant interplanar spacing as proposed by Wolf (1985) is conducive to interfacial stability for a limited number of cases involving metal/metal and oxide/oxide. For metal/oxide interfaces the model fails.

Further effects include the relaxation at the interface which will modify the ion positions at the interface to reduce the unfavourable like-charged ion interactions. However, a method for reducing the possible starting positions for a minimisation is essential. This is achieved by noting that the calculated relaxation remains dependent on the initial configuration of the interface primitive unit cell. The most energetically favourable initial (unrelaxed) configuration can then be predicted using a '*potential energy surface*'. This involves calculating the unrelaxed energy of the primitive unit cell with the overlayer displaced in the [010] and [001] directions and the unrelaxed energies calculated for all displacements. A particular displacement will result in all the interactions across the interface being a minimum and therefore locating the most stable

unrelaxed interface energy. This method essentially calculates and presents graphically all the local minima configurations for the unrelaxed interface. It is assumed that initiating the relaxation with the primitive unit cell adopting the global unrelaxed energy minimum configuration will result in a lower relaxed interface energy than at an alternative configuration.

The calculated potential energy surfaces for the Σ^P = 10/17 β, Θ = 4.399° and Θ = 32.471° are shown in figure 6.4a and 6.4b respectively. The figure appears to represent the profile of the MgO substrate at the atomic level as it is 'probed' by the BaO. Figure 6.4a shows a clearly defined pattern with cubic symmetry whereas figure 6.4b (Θ = 32.471°) the pattern is somewhat distorted. This is attributed to the higher rotational angle associated with this interface. The rotational angles are clearly evident from the potential energy surfaces. If a line were drawn connecting the 'circles' in each of the figures, the line would be for figure 6.4a, +4.399° from the horizontal and for figure 6.4b, -32.471° from the horizontal. The patterns observed in the potential energy surfaces are very similar to images obtained using the atomic force microscope (Kotomin et al. 1990, Binnig and Quate 1986, Binnig et al. 1987) which can be used to measure forces as small as 10^{-18}N resulting in the ability to 'map' the surface of a crystal with a resolution of 2.5Å. These calculations are essentially analogous to the probing of surfaces by the atomic force microscope.

Figures 6.4a and 6.4b clearly show minimum energy configurations with vector displacements in the [010] and [001] directions from which to start the full minimisation. The variation of unrelaxed energy with interfacial distance (vector displacement in the [100] direction for the Σ^P = 10/17 β, Θ = 4.399°) is given in figure 6.5 and suggests the relaxation should be initiated with the BaO 2.09 Å away from the MgO substrate. The two atomic planes either side of the interface are also shown in the bottom left of the

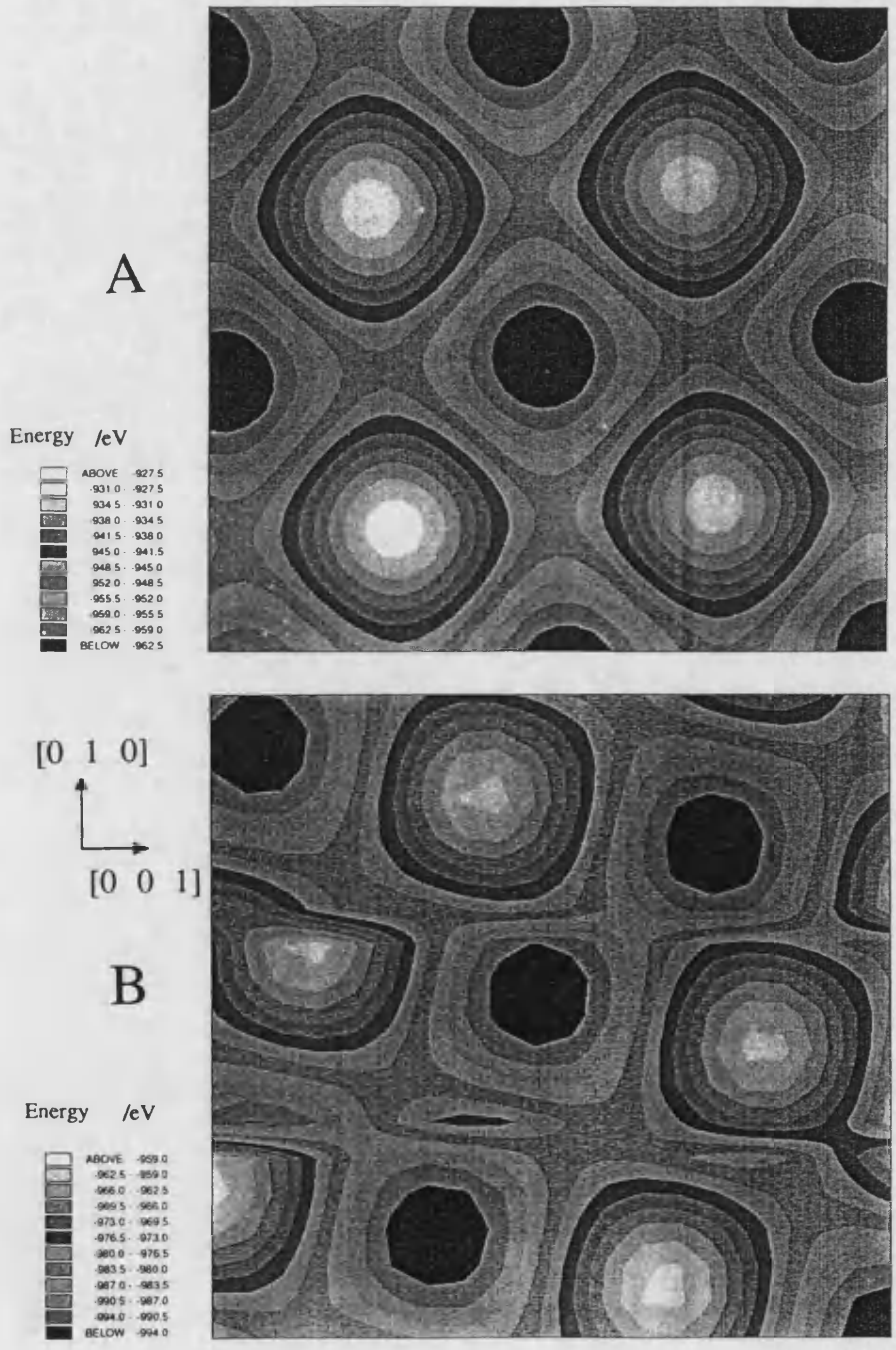

Figure 6.4 Calculated potential energy surfaces of the BaO(1 0 0)//MgO(1 0 0) $\Sigma^p = 10/17$ β interfaces. (a) $\Theta = 4.399^o$. (b) $\Theta = 32.471^o$.

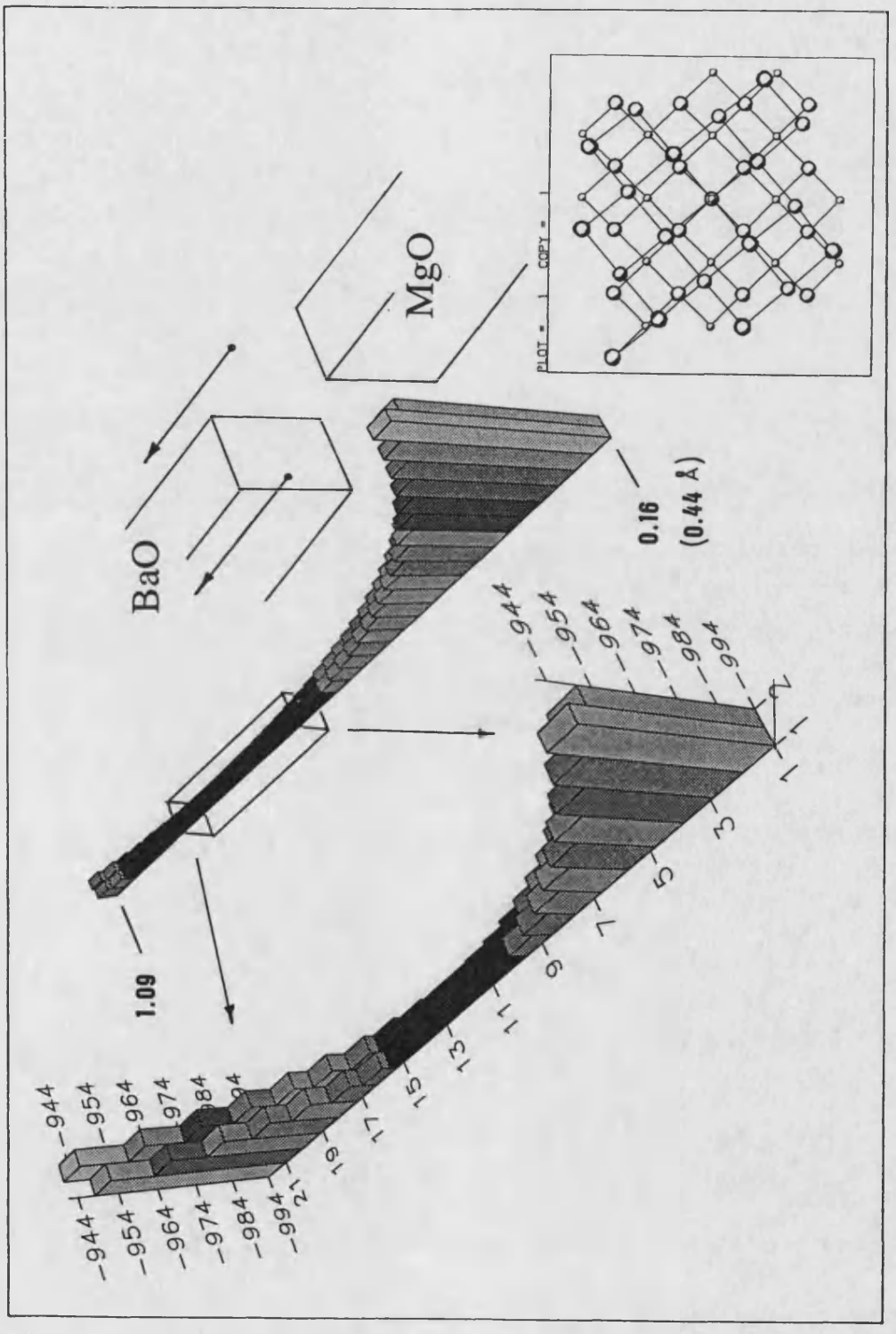

Figure 6.5 Variation of interfacial energy with BaO(1 0 0)//MgO(1 0 0) interfacial distance for the $\Sigma^p = 10/17\ \beta\ \Theta = 4.399^o$ interface.

figure. From these calculations the initial configuration of the BaO with respect to the MgO substrate with vector displacements in the [100], [010] and [001] directions is obtained.

6.3.2 Results

The calculated relaxed interfacial stabilities for the NCSL's given in table 6.3 for one to six BaO overlayers are presented in table 6.4 (the percent misfit is accommodated entirely by the BaO overlayer). The interfacial stability is the energy required to cleave the interface to form an MgO surface and a BaO thin film (with its natural 'in space' lattice parameter) per unit interfacial area (equation 6.8 and figure 6.6).

$$\Delta E = [(E_{BaO} + E_{MgO}) - E_{BaO//MgO}] / Area_{(interface)} \qquad (6.8)$$

where ΔE is the interfacial stability. Negative stabilities indicate that the interface is unstable with respect to the pure BaO 'thin film' and MgO surface.

Figures 6.7 a-d show the interfacial stabilities of the various NCSL's as a function of % mismatch. For BaO monolayer coverage (figure 6.7a), none of the interfaces are stable with a mismatch greater than +3.2 %. It is expected that the interfacial stability should increase with decreasing mismatch. The strain energy required to accommodate the mismatch will destabilise the interface resulting in a maximum stability at the lowest value for the mismatch. Figure 6.7a shows this as the BaO must be expanded (positive mismatch) to accommodate the mismatch. However when the BaO overlayer must be compressed (negative mismatch), the interfacial stability continues to increase with increasing mismatch. The $\Sigma^P = 13/17\alpha$ (19.65°) is constrained to accommodate a -6.9% mismatch yet the interfacial stability after relaxation is +0.132 Jm^{-2}. This rather unexpectedly high result may be explained by considering the effect of the relaxation of

Table 6.4 Calculated stabilities after relaxation, for the BaO(1 0 0)//MgO(1 0 0) interfaces predicted using a near coincidence site lattice theory for one to six BaO layers on the MgO substrate.

$\Sigma^p_{BaO}/\Sigma^p_{MgO}$		Interfacial Stability for n BaO layers /Jm^{-2}					
		n=1	n=2	n=3	n=4	n=5	n=6
1/2	β	-0.46	-0.098	-0.351	-0.349	-0.428	-0.469
5/9	α	-0.134	-----	-0.051	-0.006	-0.104	-0.108
9/16	β	-0.067	-0.025	-0.028	-0.005	-0.009	**+0.003**
10/17	β 4.399°	-0.040	**+0.104**	**+0.078**	**+0.117**	**+0.108**	**+0.117**
10/17	β 32.471°	-0.048	**+0.110**	**+0.057**	**+0.093**	**+0.087**	**+0.095**
8/13	β	-0.026	**+0.126**	**+0.069**	**+0.079**	**+0.090**	**+0.049**
5/8	β	-0.025	**+0.189**	**+0.116**	**+0.132**	**+0.094**	**+0.075**
13/20	β 7.125°	**+0.038**	**+0.146**	-0.030			
13/20	β 29.745°	-0.009	**+0.114**	----			
17/26	β 2.726°	**+0.051**					
17/26	β 25.346°	**+0.037**					
9/13	α	**+0.068**	-0.018	-0.027			
13/18	β	**+0.068**	+0.004				
13/17	α 19.65°	**+0.132**					

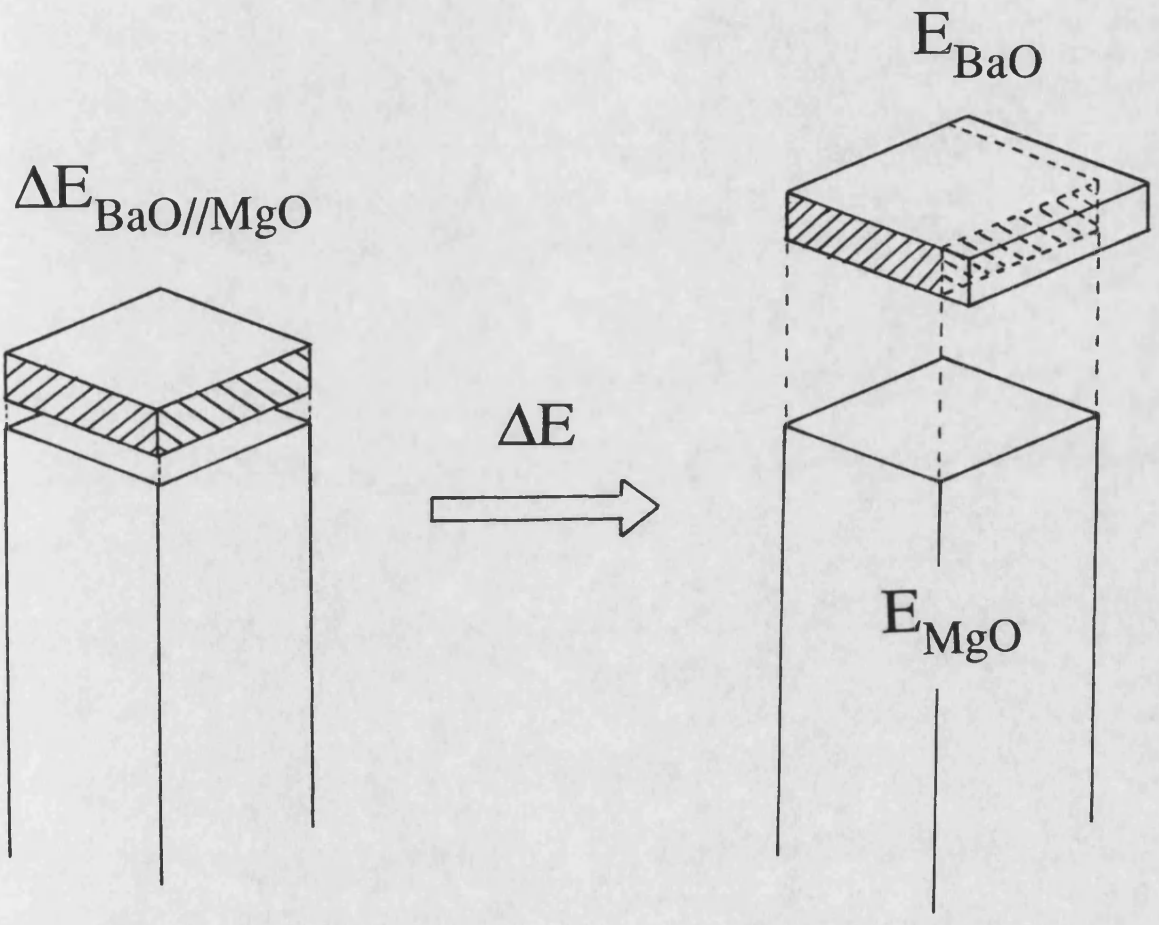

Figure 6.6 Schematic diagram of the way the interfacial stability is calculated.

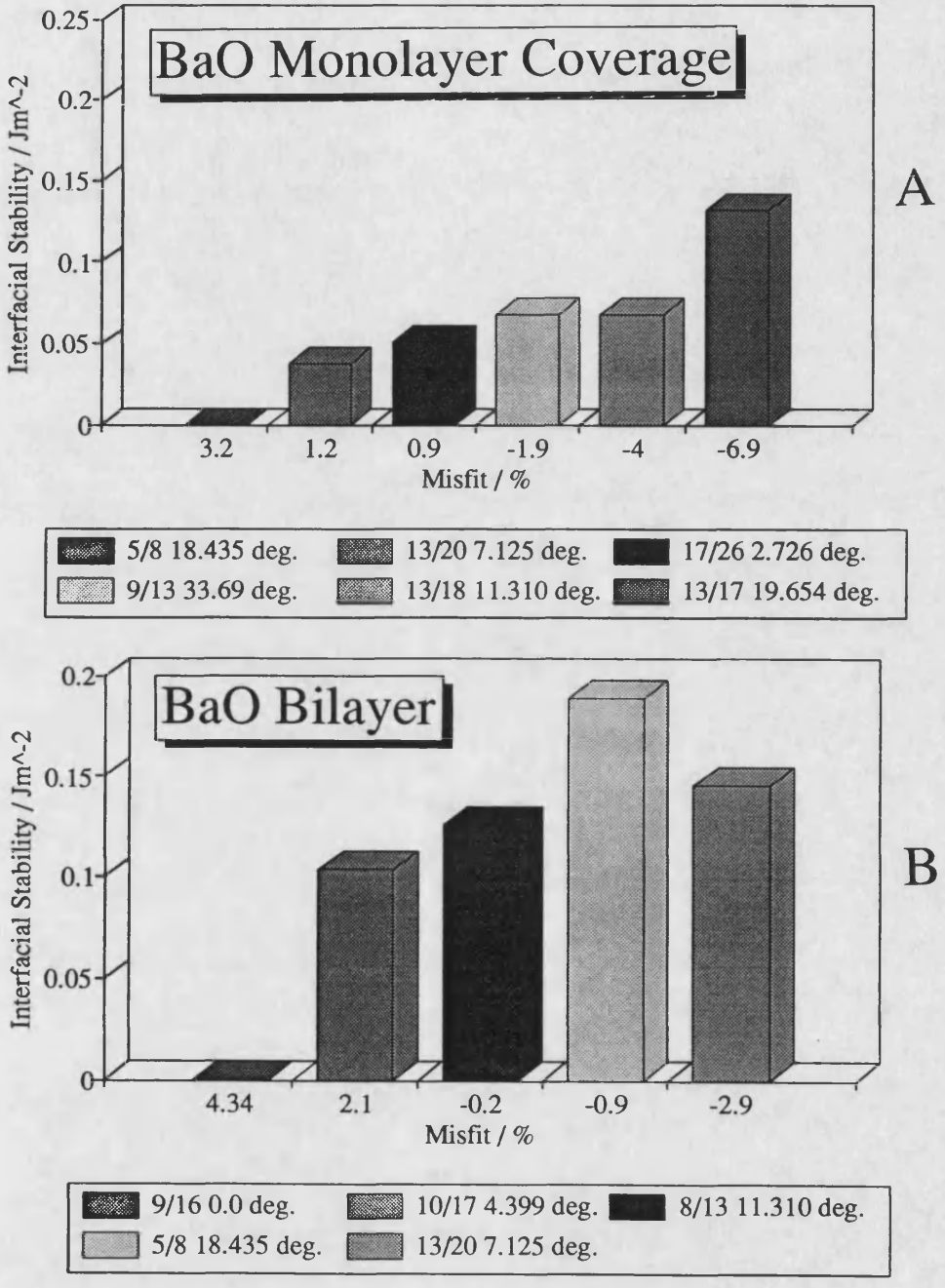

Figure 6.7 Variation of interfacial stability with %misfit for various BaO(100)//MgO(100) interfaces. (a) one BaO overlayer, (b) two BaO overlayers.

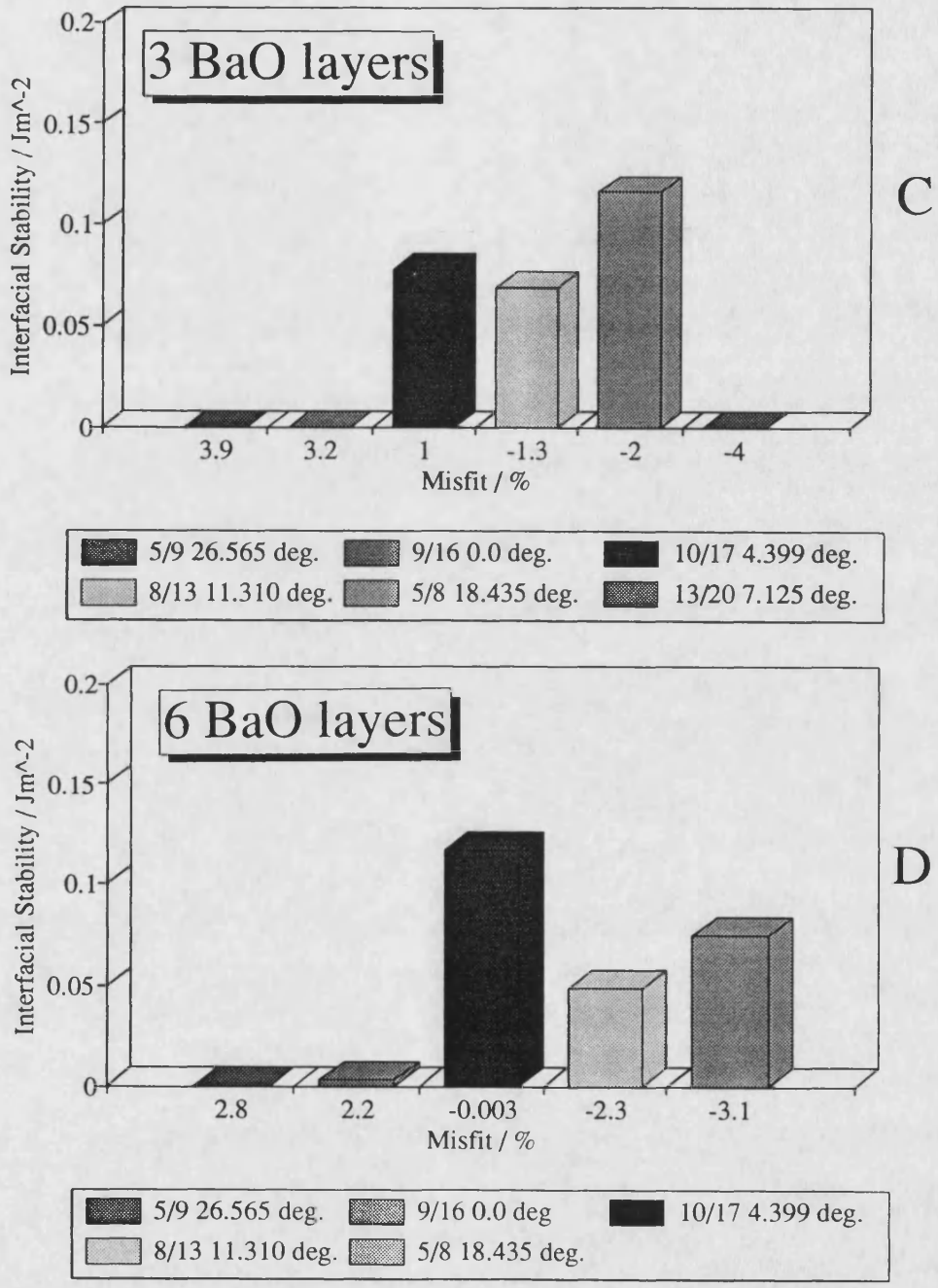

Figure 6.7 Variation of interfacial stability with %misfit for various BaO(100)//MgO(100) interfaces. (c) three BaO overlayers, (d) six BaO overlayers.

the interface. The relaxation reduces the strain energy in the system by allowing the BaO to relax in the [100] direction (perpendicular to the interface). The BaO has initially been compressed to accommodate the mismatch and the 'excess' BaO relaxes to form a 'partial' second BaO layer on top of the first layer. This type of behaviour is very pronounced for one BaO layer on the MgO substrate but for higher layer coverage, the reduced freedom of relaxational movement will prevent the BaO from relaxing out of the interface region because of BaO layers above.

Figure 6.7b shows two BaO overlayers on the MgO substrate. The most stable interface is the $\Sigma^P = 5/8\ \beta$ ($\Theta = 18.435°$) which accommodates a -0.9% misfit. The $\Sigma^P = 13/20\ \beta$ ($\Theta = 7.125°$) has a higher mismatch at -2.9% but is less stable by 0.043 Jm^{-2}. With one BaO layer the stability continues to increase with increasing 'negative' mismatch. However for two layers, the additional BaO layer has restricted the relaxation in the [100] direction. For two layers the $\Sigma^P = 8/13\ \beta(11.310°)$ has the lowest mismatch at -0.2% however it is less stable than the $\Sigma^P = 5/8\ \beta$ ($\Theta = 18.435°$) by 0.079 Jm^{-2}. The stability cannot therefore be determined purely by considering the percent misfit as other factors must contribute to the interfacial stability. The $\Sigma^P = 5/8\ \beta$ ($\Theta = 18.435°$) has a higher planar density of coincidence sites (Γ) at constant interplanar spacing than the $\Sigma^P = 8/13\ \beta$ ($\Theta = 11.310°$). This has been suggested by Sutton and Balluffi (1987) to be conducive to increased interfacial stability and may, in part, be responsible for the increased stability for the $\Sigma^P = 5/8\ \beta$ ($\Theta = 18.435°$) interface because of the high density of favourable interactions across the interface.

Figure 6.7c shows three BaO layers on the MgO substrate. The $\Sigma^P = 5/8\ \beta$ ($\Theta = 18.435°$) is again the most stable interface and of the three interfaces found to be stable it must also accommodate the highest misfit of the three. This behaviour may still be attributed to the high planar density of coincidence sites at constant interplanar spacing associated

with this interface as the it is higher than the $\Sigma^P = 8/13\ \beta$ ($\Theta = 11.310°$) and $\Sigma^P = 10/17\ \beta$ ($\Theta = 4.399°$) interfaces even considering the high -2% misfit. For three BaO layers a clear stability maximum can be observed for interfaces with an associated low misfit. Interfaces with a misfit of more than -4% or more than +3.2% are found to be unstable with respect to pure BaO and MgO surface and are therefore not expected to be observed experimentally.

Figure 6.7d shows the stability of interfaces with six BaO layers on the MgO substrate. The most stable interface is now the $\Sigma^P = 10/17\ \beta$ ($\Theta = 4.399°$) which has the lowest associated misfit. This interface is now 0.042 Jm^{-2} more stable than the $\Sigma^P = 5/8\ \beta$ ($\Theta = 18.435°$).

The only interface of type α is the $\Sigma^P = 5/9\ \alpha$ ($\Theta = 26.565$). This interface is not found to be stable at any BaO coverage yet it has a relatively low value of Γ. The reason for the instability of this interface must therefore be the high misfit.

Figure 6.8 shows the variation of interfacial stability of the $\Sigma^P = 5/8\ \beta$ ($\Theta = 18.435°$) for 1-14 BaO layers added. The figure shows a clear maximum at 2 BaO layers added (the interface also has the lowest associated mismatch for 2 BaO layers). The interfacial stability then decreases with increasing mismatch. The stability can be seen to be directly related to the interfacial mismatch (assuming the reduced BaO lattice parameter for thin BaO films 'in space') apart from one spurious divergence at three BaO layers. The interfacial stability of three BaO layers is somewhat surprising considering the interface is 0.016 Jm^{-2} less stable than with four BaO layers even though with four BaO layers the misfit is 1.3% higher. The stability of BaO monolayer coverage is unstable for the $\Sigma^P = 5/8\ \beta$ ($\Theta = 18.435°$) system and is associated with a +3.2% misfit. For six BaO overlayers the misfit is -3.1% and the interface is stable. This is because the strain

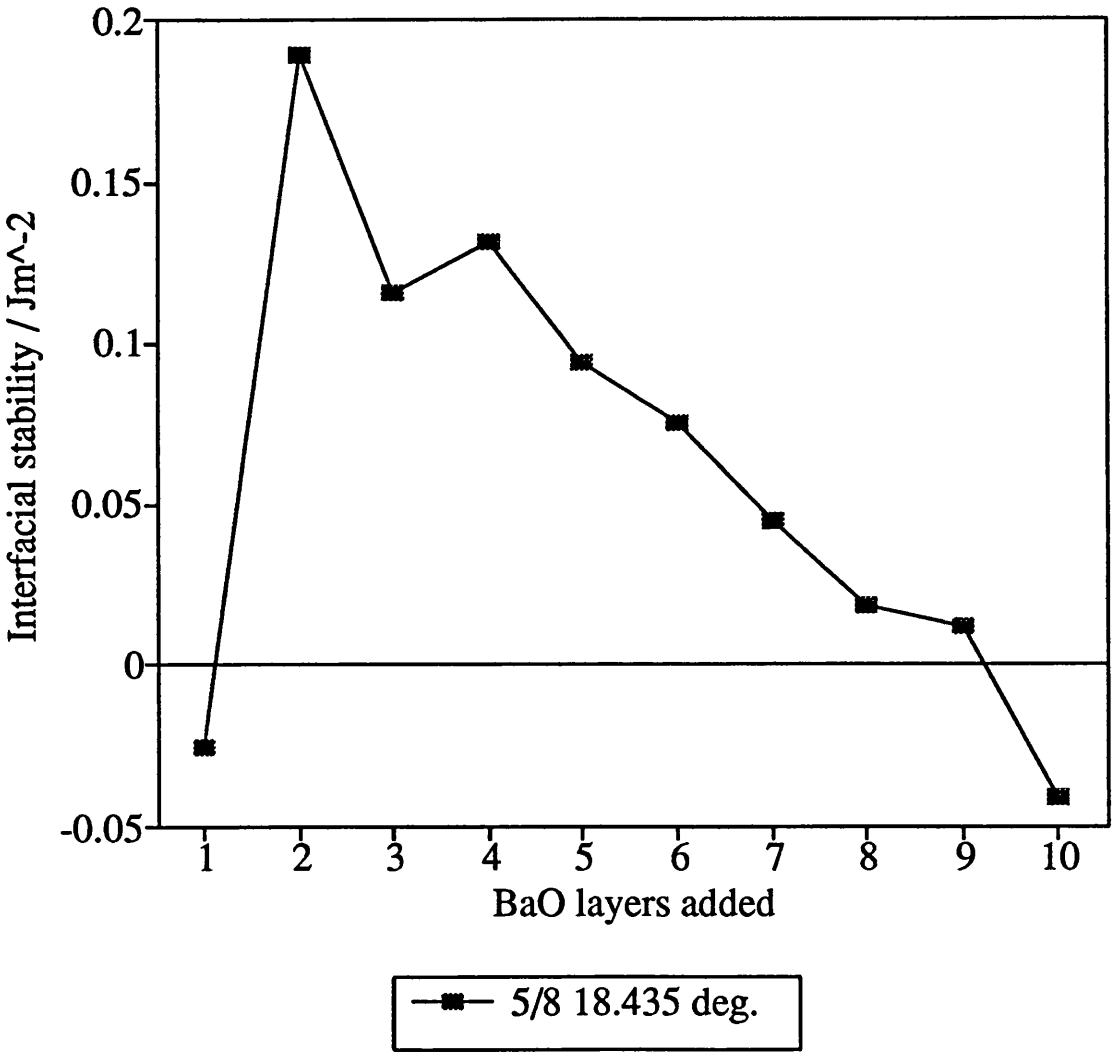

Figure 6.8 Stability of the $\Sigma^{p} = 5/8\ \beta$ ($\Theta = 18.435^{o}$) interface as a function of BaO layers added to the MgO substrate

energy lost in expanding the BaO crystal cannot be removed by the relaxation when the BaO is expanded. Furthermore the strain energy lost in expanding the crystal is greater than the energy lost in compressing it (for a few percent of the BaO equilibrium separation the energy gradient is steeper for compression than expansion (figure 5.6)).

Figure 6.9 shows the variation of interfacial stability of the $\Sigma^P = 10/17\ \beta$ ($\Theta = 4.399°$) and ($\Theta = 32.471°$). The stability of the lower angle NCSL is more stable for all BaO layers added to the MgO apart from the two BaO layers added, where the 32.471° NCSL is more stable by 0.006 Jm^{-2}. Likewise for the $\Sigma^P = 13/20\ \beta$ ($\Theta = 7.125°$, $\Theta = 29.745°$) and $\Sigma^P = 17/26\ \beta$ ($\Theta = 2.726°$, $\Theta = 25.346°$), for monolayer coverage, the lower angle NCSL is the more stable interface. The results of Mykura et al. (1980) for CdO on MgO suggest that the frequency of occurrence of a NCSL with two associated angles is higher for the higher angle NCSL. It is therefore assumed that the higher angle NCSL is more stable than the lower angle NCSL in contrast to our predictions. The resolution of the experimental results however may prevent two similar angle NCSL's from being adequately resolved and therefore attributing a higher frequency to an incorrectly assigned NCSL.

The results presented here are mainly β-type NCSL i.e. anti-coincident orientations. Experimental work by Mykura et al. (1980) has shown these interfaces to be unstable (i.e. the β-type interfaces were not observed). In contrast to the work of Mykura et al., the computer simulation results presented in this thesis suggest these interfaces are indeed stable. The explanation given by Mykura et al. as to why these interfaces should be unstable is the instability introduced via like charged ions coming into close proximity. However the interfacial energy is comprised of contributions from all ion-ion interactions across the interface. The close proximity of two like charges is unlikely to dominate the interfacial energy especially for large primitive unit cells. Indeed the

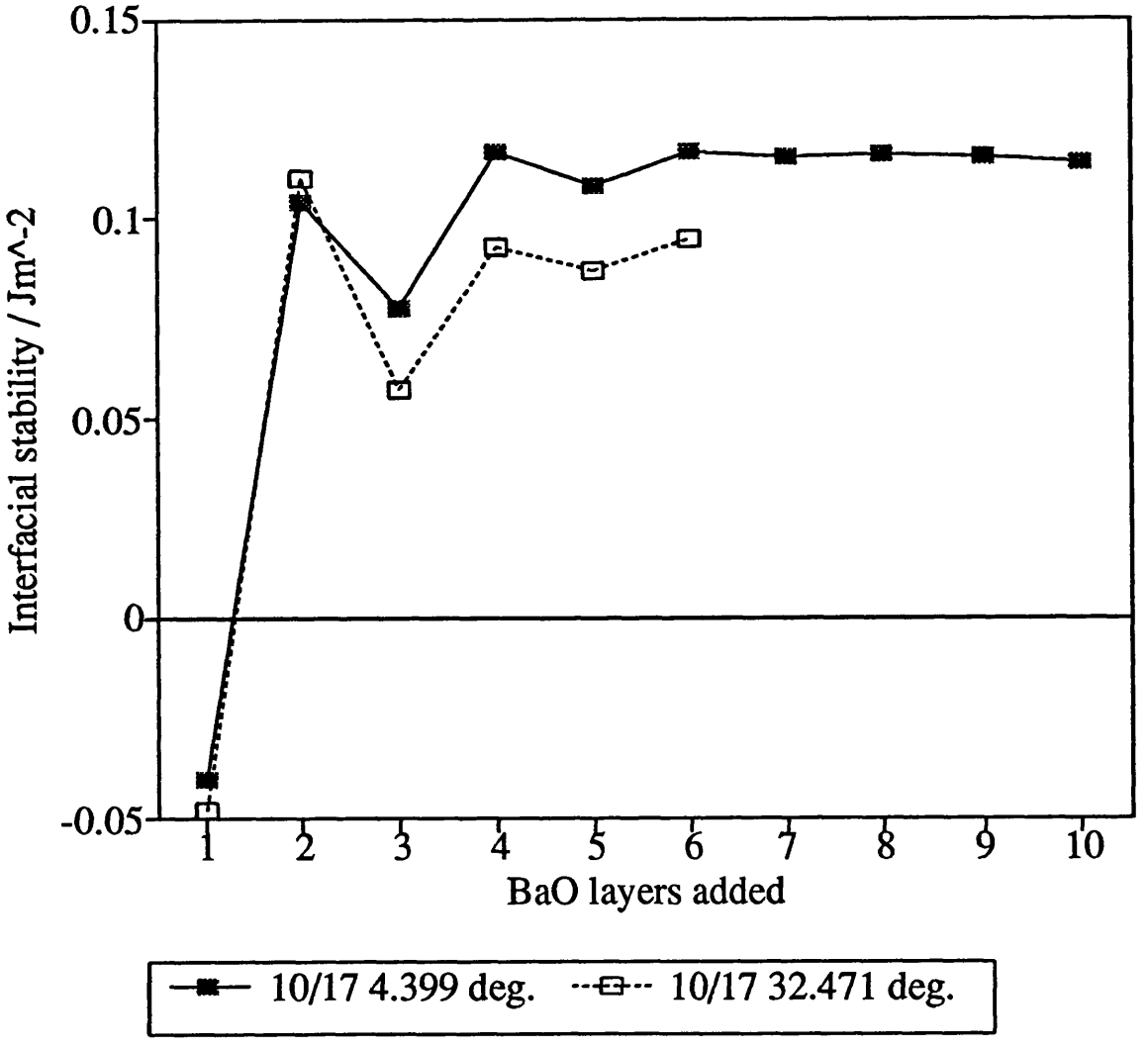

Figure 6.9 Stability of the Σ^{p} = 10/17 β (Θ = 4.399° and Θ = 32.471°) interfaces as a function of BaO layers added to the MgO substrate.

relaxation will adjust the positions of the individual ions to reduce these unfavourable interactions.

From all the interfaces considered, it appears the interfaces with two BaO overlayers are the most stable and the Σ^P = 5/8 β (Θ = 18.435°) with two layers the most stable interface identified for BaO(100)//MgO(100) (up to six layers) at +0.189 Jm^{-2}. If this is true, then the interface becomes more unstable with increasing BaO thickness. This may be a consequence of the small size of primitive unit cell the computer can accommodate and larger NCSL's (with lower associated misfits) may result in the identification of a more stable interface. Another factor we were not able to address because of the computational limitations is the formation of defects at the interface region, which, as was shown for MgO(100)//MgO(100) twist grain boundaries, are an integral part of the low temperature interface structure.

For the MgO(100)//MgO(100) twist grain boundaries the occupational levels of the various interfaces were calculated using a statistical thermodynamics approach. This approach may also be applied for the BaO(100)//MgO(100) heteroepitaxial interface to ascertain the occupational levels of the various NCSL's at different annealing temperatures. However the variation in misfit associated with a particular NCSL changes with increased thin film thickness. The occupation levels thus derived from the interfacial stabilities must also be dependent on the number of BaO overlayers the interface contains.

6.3.3 Relaxed interface structures

Figure 6.10 shows the structures of the Σ^P = 13/20 β (Θ = 29.745°) and Σ^P = 8/13 β (Θ = 11.310°) for BaO monolayer coverage after relaxation. The figures show a projection viewing the BaO overlayer with the MgO substrate hidden underneath. The structure of

Figure 6.10 Representations of the $\Sigma^P = 13/20\ \beta$ ($\Theta = 29.745°$) and $\Sigma^P = 8/13\ \beta$ ($\Theta = 11.310°$) interfaces after relaxation for a BaO(1 0 0) monolayer on an MgO(1 0 0) substrate. Oxygen is coloured red and barium is white.

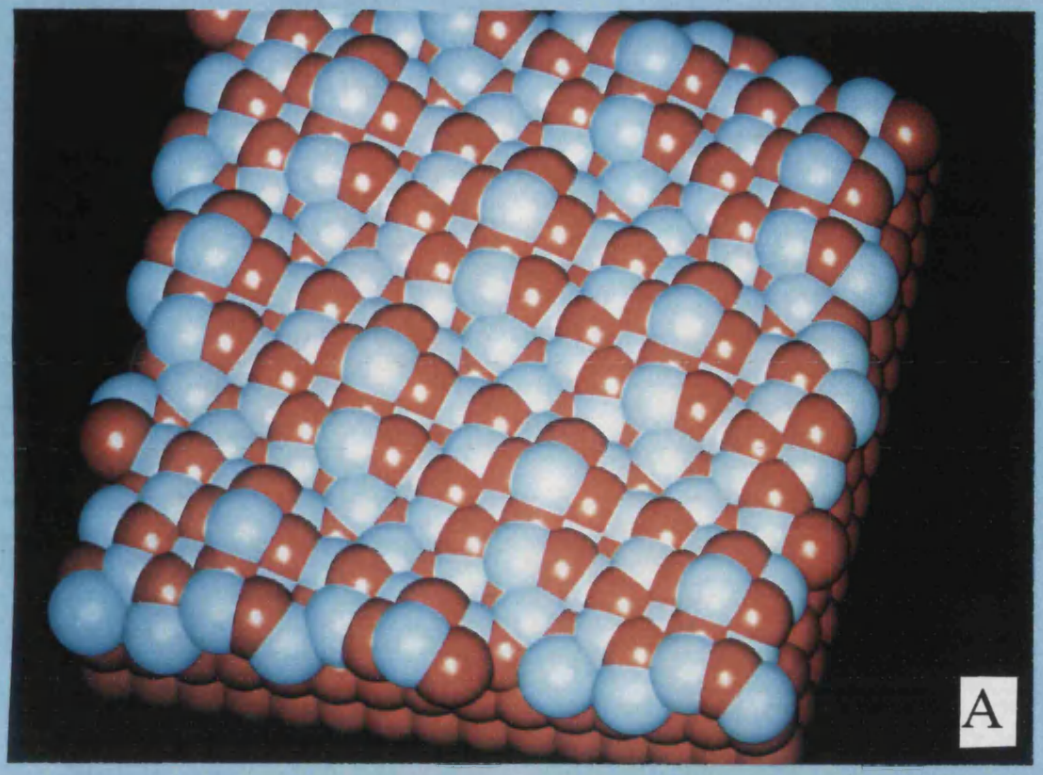

$\Sigma^{p} = 13/20\ \beta\ (\Theta = 29.745^{o})$

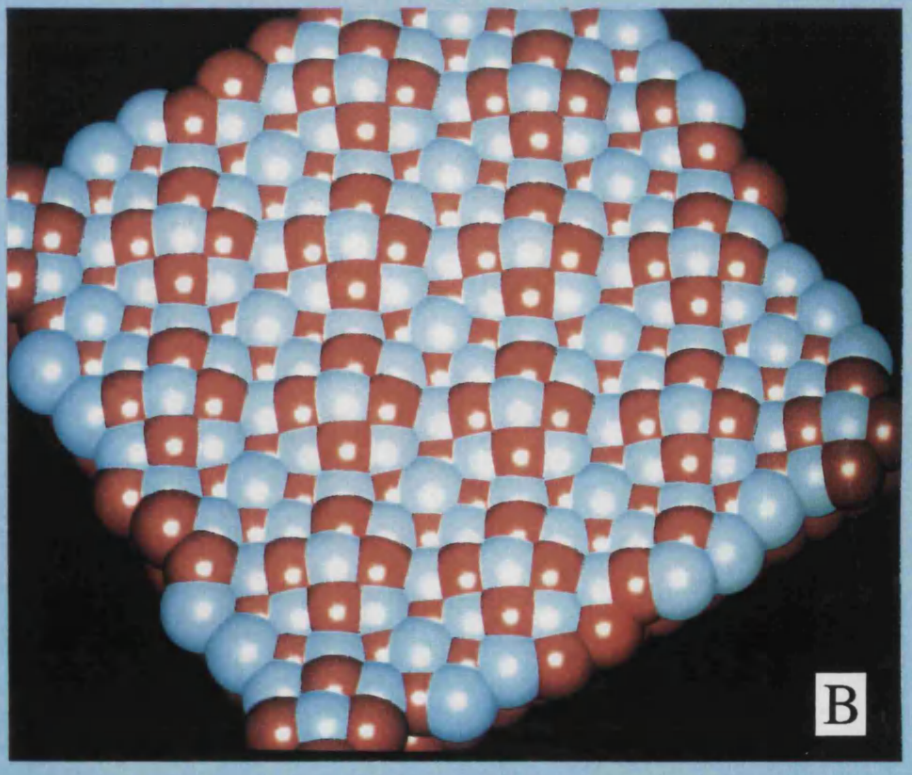

$\Sigma^{p} = 8/13\ \beta\ (\Theta = 11.310^{o})$

the Σ^P = 13/20 β (Θ = 29.745°) exhibits substantial relaxation of the BaO overlayer, resulting in a structure considerably different to the original unrelaxed structure. The two-dimensional periodicity is maintained with a short periodic wavelength as determined by the NCSL however it is difficult to observe this from the structure. The Σ^P = 8/13 β (Θ = 11.310°) exhibits the primitive unit cell periodicity more clearly. Most of the relaxation is in the [100] direction, however relaxation in the [010] and [001] directions are also observed resulting in a wave-like behaviour in the plane of the interface with the wavelength equal the size of the NCSL considered.

Figure 6.11 shows the relaxed structures of the Σ^P = 17/26 β (Θ = 25.346° and Θ = 2.726°). The two interfaces are identified by the same NCSL but have different angles associated with them. The resulting relaxed structures also bear little resemblance to each other.

The BaO overlayers in figures 6.10 and 6.11 are not flat but exhibit a wave-like pattern in the [100] direction. To accommodate epitaxial matching the BaO must be expanded. For the BaO to exhibit this wave like pattern the Ba-O bond distance must further deviate from its equilibrium distance which further reduces the stability. The driving force for this relaxation behaviour must therefore be to optimise the interactions across the interface region. The interfaces with high planar densities of coincidence sites therefore retain an energy advantage over interfaces with low values and are accordingly more stable even when accommodating high misfit values.

Figure 6.12 shows the relaxed structure of the Σ^P = 5/9 α (Θ = 26.565°). The same projection of the interface is shown but the ions in the top figure are represented by smaller balls. The BaO overlayer appears to form small islands (within the primitive unit cell size). These are a consequence of the large (+9.1%) mismatch between the BaO

Figure 6.11 Representations of the $\Sigma^{P} = 17/26\ \beta$ ($\Theta = 25.346°$) and $\Sigma^{P} = 17/26\ \beta$ ($\Theta = 2.726°$) interfaces after relaxation for a BaO(1 0 0) monolayer on an MgO(1 0 0) substrate. Oxygen is coloured red and barium is white.

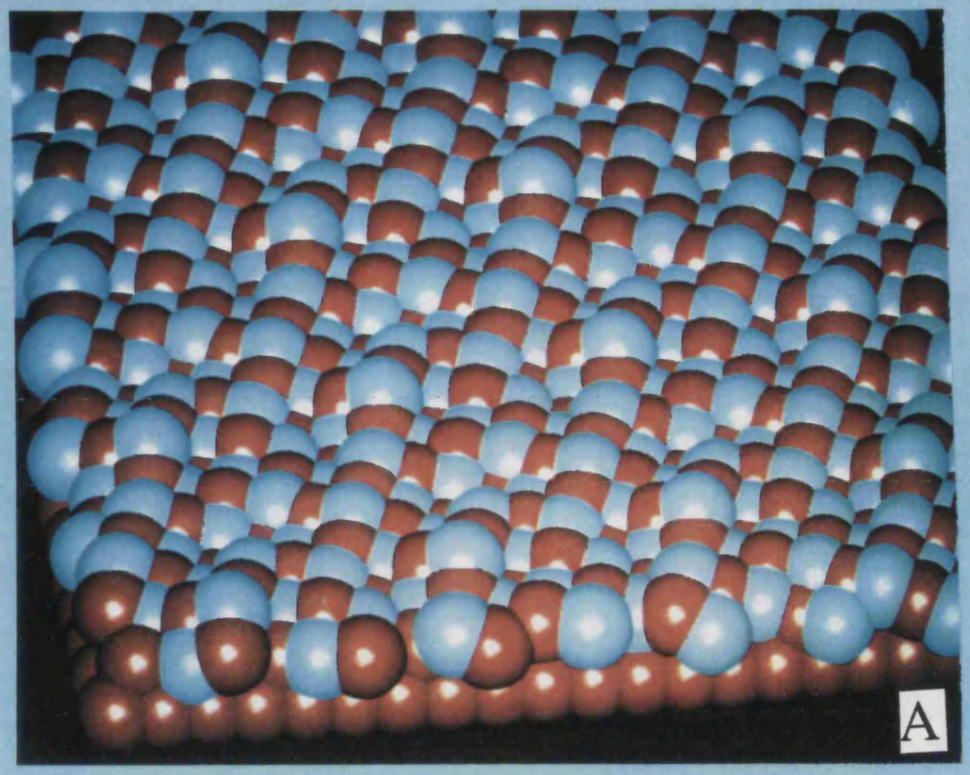

$\Sigma^{p} = 17/26\ \beta\ (\Theta = 25.346^{o})$

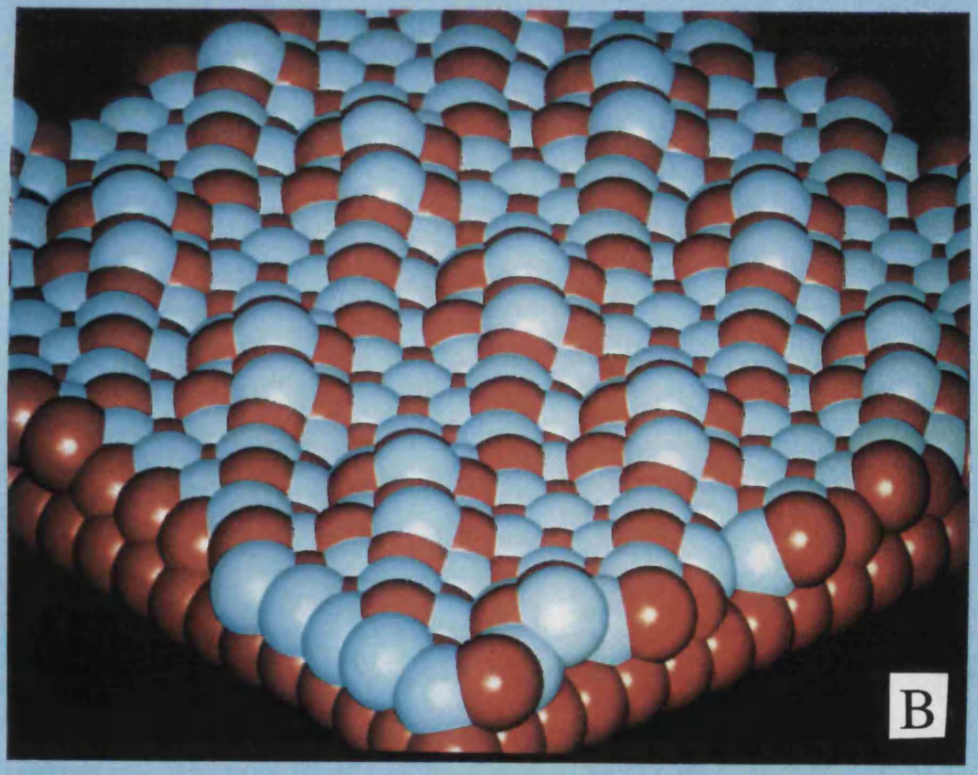

$\Sigma^{p} = 17/26\ \beta\ (\Theta = 2.726^{o})$

Figure 6.12 Diagrammatic representation of the Σ^{p} = 5/9 α (Θ = 26.565°) interface after relaxation for a BaO(1 0 0) monolayer on an MgO(1 0 0) substrate. Oxygen is coloured red barium white and magnesium purple. The size of the coloured ball representing the ionic radii is reduced in the top figure for clarity.

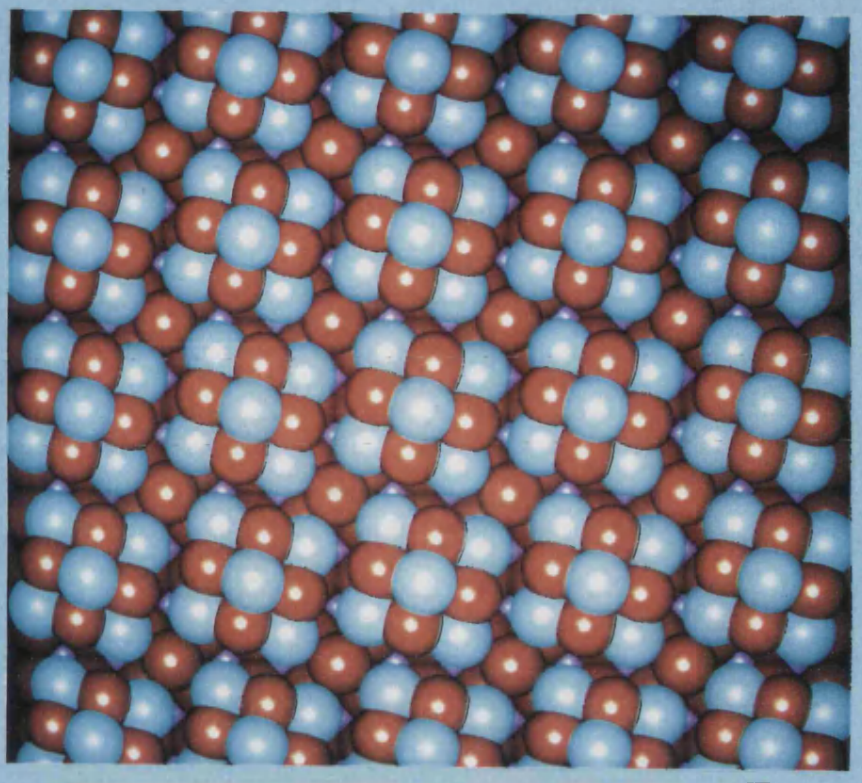

A

$\Sigma^{p} = 5/9\ \alpha\ (\Theta = 26.565^{o})$

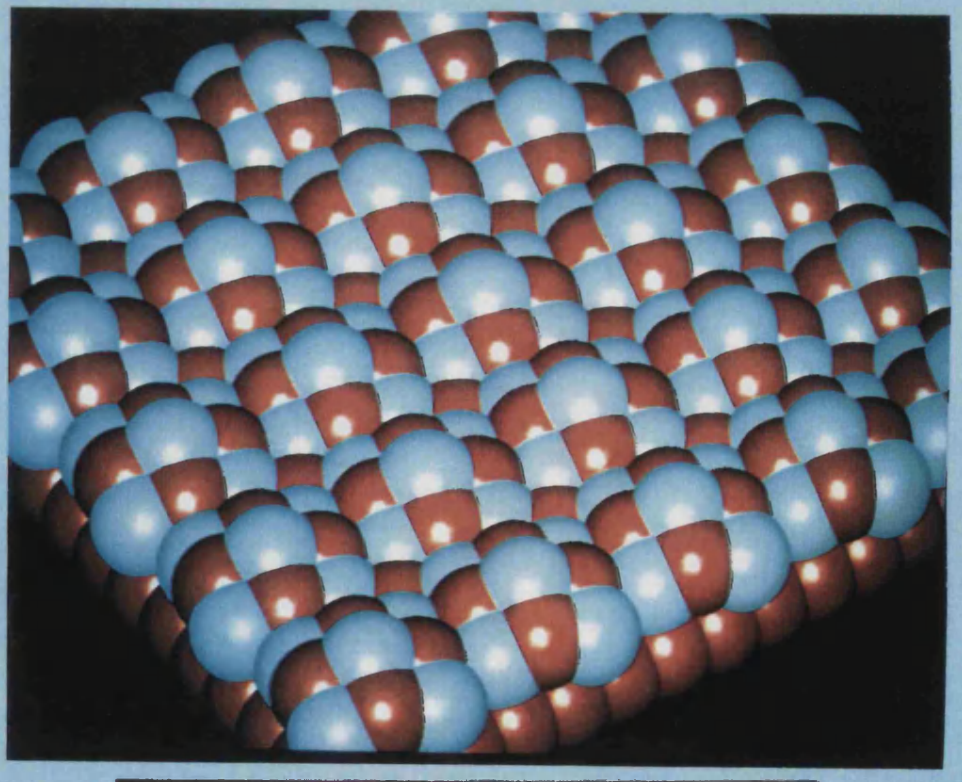

B

$\Sigma^{p} = 5/9\ \alpha\ (\Theta = 26.565^{o})$

and MgO in this NCSL and the BaO adopts its optimum lattice spacings within these islands to increase the interfacial stability. It is expected that the Σ^P 1/2 β ($\Theta = 45°$) with a 14.3% associated mismatch would behave in a similar manner. In fact almost no relaxation is observed in the [010] or [001] directions. This is attributed to the high number of favourable interactions across the interface (i.e. high planar density of coincidence sites) dominating the relaxation. It must also be noted however that this interface is calculated to be unstable with respect to a pure MgO surface and a BaO monolayer 'in space'.

Figure 6.13 shows BaO bilayer coverage on the MgO substrate for the $\Sigma^P = 10/17$ β ($\Theta = 4.399°$) and $\Sigma^P = 9/13$ α ($\Theta = 33.690°$). The top right hand of each figure shows a side projection of the primitive unit cell of the interface with reduced 'ion size' (for reasons of clarity). The BaO bilayer in the $\Sigma^P = 10/17$ β ($\Theta = 4.399°$) appears to have deviated little from the natural BaO cubic structure. This behaviour is typical of all the stable NCSL's with 2 BaO layers (table 6.4). The $\Sigma^P = 9/13$ α ($\Theta = 33.690°$) however shows considerable relaxation and rumpling and this interface is unstable. The $\Sigma^P = 9/13$ α ($\Theta = 33.690°$) is associated with a +6% misfit. To relieve the strain energy imposed on the system, the BaO appears to have corrugated in one dimension to reduce the two dimensional surface area and accommodate the misfit. The relaxational freedom for many layers of BaO however would restrict this behaviour.

6.4 Summary

Throughout the history of research on interfaces, workers have looked for a simple geometric criterion for high interfacial stability. This work has shown that a simple geometrical argument such as near coincidence site lattice theory together with the resulting misfit to accommodate epitaxial matching can predict whether an interface is likely to be stable or not but the method has very little quantitative predictive power.

Figure 6.13 Diagrammatic representations of the $\Sigma^P = 10/17\ \beta$ ($\Theta = 4.399°$) and $\Sigma^P = 9/13\ \alpha$ ($\Theta = 33.690°$) interfaces after relaxation for a BaO(1 0 0) bilayer on an MgO(1 0 0) substrate. Oxygen is coloured red barium white and magnesium purple. The small figures in the top right hand side show the relaxed primitive unit cell. The sizes of the balls representing the ionic radii are reduced for clarity.

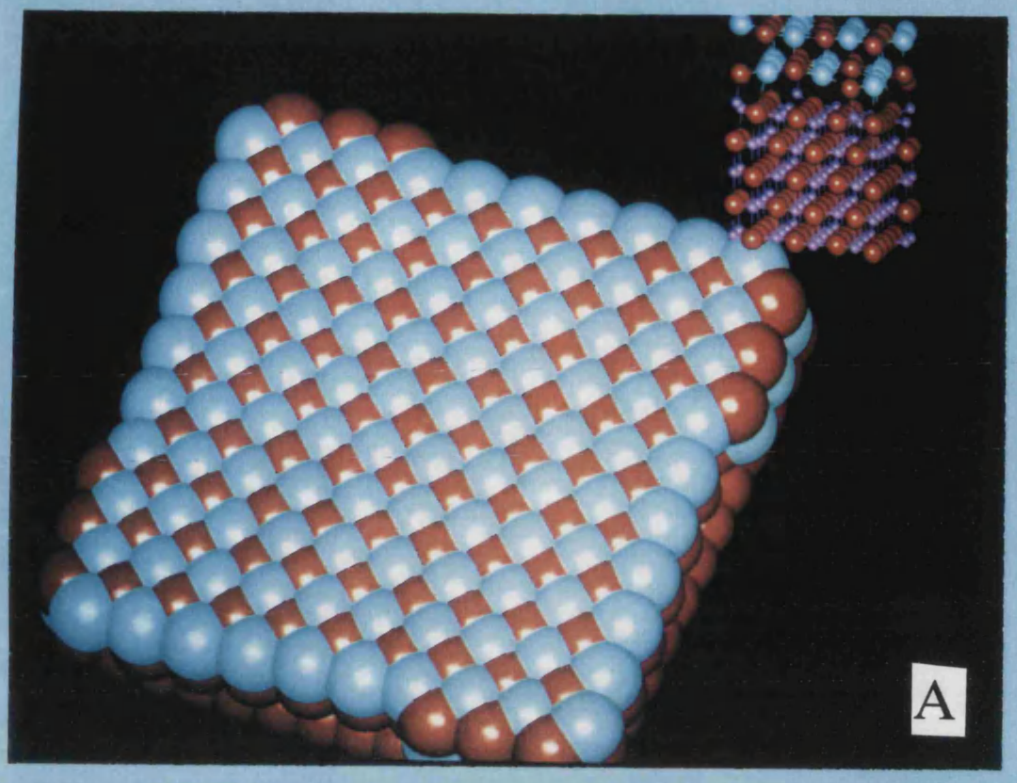

$\Sigma^{p} = 10/17\ \beta\ (\Theta = 4.399^{o})$

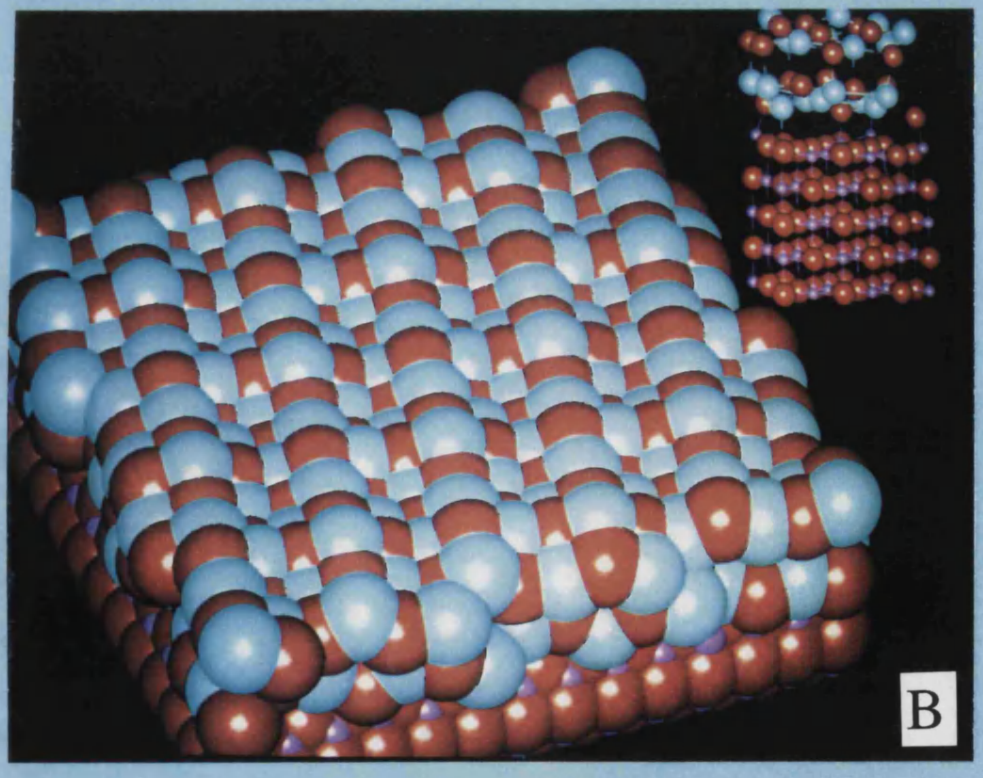

$\Sigma^{p} = 9/13\ \alpha\ (\Theta = 33.690^{o})$

Coupled with the computer simulations, this method has yielded good quantitative information about the interface stability, structure and mechanisms by which the interface is stabilised or destabilised.

This has been prompted by the many complex factors contributing to interfacial stability such as charge matching across the interface, accuracy and transferability of interatomic potentials, defect formation, reduced ion density at the near interface regions and relaxation. These factors can all be examined using the simulation techniques presented in this work.

For the MgO(100)//MgO(100) twist grain boundaries it accurately predicted the occupational levels of the coincidence site lattices in good agreement with experimental observations and suggests that defects are an integral part of the low temperature twist grain boundary structure.

For the BaO(100)//MgO(100) we have found that the interfacial stability is heavily dependent on the %mismatch. For positive misfits the relaxation has led to the formation of small BaO islands (however these can only be as large as the primitive unit cell size) with Ba-O bond distances adopting their natural lattice spacings within the islands. For negative misfits, the BaO overlayer 'corrugates' to reduce the two dimensional surface area to accommodate the misfit. Other factors also contribute to the interfacial stability. The $\Sigma^{P} = 5/8\ \beta$ ($\Theta = 18.435$) was calculated to be more stable than an interface with a lower misfit. This is attributed to the high planar density of coincidence lattice sites.

The near coincidence site lattice theory cannot predict an interface with zero misfit for a reasonable primitive unit cell size. The relaxational behaviour of thin films enables this strain energy to be significantly reduced resulting in a stable interface. For many BaO

overlayers on an MgO substrate however the resulting strain energy contribution from each BaO overlayer will destabilise the interface and the relaxation to reduce this strain is inhibited by the many BaO layers. It has been suggested by Balluffi et al. (1982) that the misfit at the interface is accommodated by the presence of defects or misfit dislocations. A useful extension to this work therefore would be to examine the effect misfit dislocations have on the interfacial stability and extend the work to include 'bulk' interfaces.

In the next chapter we extend our investigation to include the superconductor $YBa_2Cu_3O_{6.5}$ interfaced to an MgO substrate using the methodology developed in this chapter.

Chapter 7

YBa2Cu3O6.5//MgO Interfaces

7.1 Introduction

The formation of superconducting thin films is fundamental to their application in electronic devices (Simon 1991, Larbalestier 1991). Simulation techniques have the potential to elucidate the factors which may ultimately be responsible for the superconducting properties at the atomic level (Allan et al. 1989). Therefore, these techniques may be used to model the effects a substrate will have on the superconducting properties. This, in turn, may lead to the identification of the optimum conditions required to produce a stable thin film on a suitable substrate, with the superconducting properties retained or even enhanced. Although this position has not yet been realised, many workers have focused their attentions in deriving potentials for high T_c superconductors with much success (Baetzold 1988, Mackrodt 1989b, Zhang and Catlow 1992). Indeed the calculations have resulted in modelling bond lengths to within 0.03Å.

The aim of the work in this chapter is to employ the methodologies developed in chapters 4,5 and 6 to investigate the formation of $YBa_2Cu_3O_{6.5}$ thin films on MgO. The high T_c superconductor $YBa_2Cu_3O_{6.5}$ was chosen for our interface studies for various reasons. Firstly it represents a more complex oxide than the ceramics considered thus far with many $YBa_2Cu_3O_{6.5}$(001) planes with which to terminate the $YBa_2Cu_3O_{6.5}$ at the interface. Secondly the literature on the interfaces considered thus far is scarce whereas the literature on this material is extensive and finally several $YBa_2Cu_3O_{6.5}$ surfaces have been observed to terminate the $YBa_2Cu_3O_{6.5}$ at the interface such as the (001), (100), (010) and (110) surfaces. The theoretical studies on this material should therefore elucidate many more factors which must be considered in examining interfaces of a complex material. We first employ the near coincidence lattice theory to simulate the various orientations of the $YBa_2Cu_3O_{6.5}$ (001)//MgO(100) twist boundaries (c-axis of the $YBa_2Cu_3O_{6.5}$ normal to the MgO(100) surface) observed experimentally (Hwang et al.

1990) which will provide a useful test of the simulation techniques and may also aid in the interpretation of the experimental results. We next examine the $YBa_2Cu_3O_{6.5}$(100)//MgO(100) and the $YBa_2Cu_3O_{6.5}$(010)//MgO(100) interfaces (c-axis of the $YBa_2Cu_3O_{6.5}$ perpendicular to the MgO(100) surface) for one to six layers.

These calculations will enable us to compare and contrast the relative stabilities and ionic behaviour at the interface region of the $YBa_2Cu_3O_{6.5}$ thin film when interfaced to MgO. Furthermore, $YBa_2Cu_3O_{6.5}$ offers six planes which may terminate the $YBa_2Cu_3O_{6.5}$ at the $YBa_2Cu_3O_{6.5}$(001)//MgO(100) interface and the simulation techniques are employed to elucidate which $YBa_2Cu_3O_{6.5}$ plane will result in the most stable interface.

7.1.1 Review

The electrical resistivity of many metals and alloys drops suddenly to zero when the material is cooled to a sufficiently low temperature. This phenomenon, called superconductivity, was first observed by Onnes (1911). At a critical temperature, T_c, the specimen undergoes a transition from a state of normal electrical resistivity to a superconducting state.

Superconductivity occurs in many metallic elements of the periodic system and has also been observed in alloys and intermetallic compounds. The important development of recent years has been the identification of superconductivity in doped ceramic oxides. The range of transition temperatures now extends from 0.001K for Rh, to 125K for $Tl_2Ba_2Ca_2Cu_3O_{10}$. The new high temperature superconductors can therefore be operated at the temperatures of liquid nitrogen, a cheap and plentiful cryogen, with radical implications to the engineering constraints on applications.

The practical applications of superconductors however, requires not only zero resistivity at high temperatures but also that the transport of current is high. The critical current, J_c, associated with the superconductor is defined as the maximum current the device may carry per unit area of the device.

Many factors can be correlated to the superconducting transition temperature, T_c(Allan et al. 1989). However, the limits or even the fundamental interactions that give rise to it are, as yet, unknown, although we can identify the molecular features that may enhance or inhibit superconductivity. One key component is that the crystal lattices of all (known) high T_c superconductors contain planes of a late first row transition metal (usually copper) and oxygen atoms sandwiched between layers of other elements (Jorgensen 1991). When the material is cooled to below the transition temperature, the Cu-O planes provide perfect highways for the electrons to travel. The other elements in the crystal lattice can be chosen and arranged to increase or decrease T_c(Allan 1989b) often by modifying the electron and hole distributions (Hasegawa et al. 1987).

7.1.1a Experimental Studies

In this review the experimental studies of $YBa_2Cu_3O_{7-x}$ on $SrTiO_3$ and MgO are examined to identify the observed structural configurations which can then be constructed and examined computationally. The behaviour of the ions at the interface region together with the calculated interfacial stabilities may aid the interpretation of the experimental results.

The application of the superconductor for electronic devices involves the fabrication of high quality thin films. Much interest, both experimental and theoretical, has been directed towards the high T_c superconductor $YBa_2Cu_3O_{7-x}$ or YBCO and the formation of high quality YBCO thin films on a suitable substrate resulting in the retention of the

superconducting YBCO properties (i.e. T_c above 77K (liquid nitrogen temperatures) and J_c of the order 10^7 Acm^{-2} at 77K). The ideal substrate for this material would presumably be a closely lattice matched substrate such as $SrTiO_3$ giving a 3% mismatch (for $YBa_2Cu_3O_{7-x}$ a=3.884, b=3.822, c=11.675 (LeGoules 1988) and for $SrTiO_3$ a=3.90 (Narayan et al. 1989)) as the results in chapters 3-6 suggest a low interfacial misfit is conducive to the stability. The close lattice matching should result in high crystallinity and low defect concentration at the interface and hence lead to exemplary superconducting properties. This has led many workers to investigate this interface(Olsson et al. 1991, Kramer et al. 1988, Bakunin et al. 1989, LeGoules 1988, Kwo et al. 1987, Chen et al. 1988, Eibl 1990a, Narayan et al. 1989). Most of these groups have also investigated the $YBa_2Cu_3O_{7-x}(100)//SrTiO_3(100)$ and $YBa_2Cu_3O_{7-x}(010)//SrTiO_3(100)$ interfaces (with the $YBa_2Cu_3O_{7-x}$ c-axis parallel to the interface). This interface necessitates a much lower misfit and increases the coherence length of the thin film. The mismatch is aggravated considerably for $YBa_2Cu_3O_{7-x}$ deposition at higher temperatures owing to the addition of thermal misfit resulting from the differences in coefficients of thermal expansions (Narayan et al. 1989) ($\alpha_{YBCO} = 1.5 \times 10^{-5}$ K^{-1} and $\alpha_{SrTiO3} = 1.1 \times 10^{-5}$ K^{-1}). Narayan et al. (1989) found that the dislocations due to the combined effects of misfit and thermal strains propagate into the $SrTiO_3$ substrate. Furthermore Olsson et al. (1991) found low deposition temperatures resulted in lower transition temperatures, broader superconducting transitions and lower critical currents. Olsson et al. solved this problem by growing a $PrBa_2Cu_3O_{7-x}$ template and subsequently depositing the $YBa_2Cu_3O_{7-x}$ at the higher temperature (as there is negligible mismatch between $PrBa_2Cu_3O_{7-x}$ and $YBa_2Cu_3O_{7-x}$ for 0 - 800K (Olsson et al. 1991)). This led to reproducible, good quality films, with the superconducting properties retained. The mismatch was removed solely by the $PrBa_2Cu_3O_{7-x}//SrTiO_3$ interface with the $PrBa_2Cu_3O_{7-x}$ accommodating the defects, dislocations and induced low crystallinity which is so damaging to the $YBa_2Cu_3O_{7-x}$ superconducting properties. There are

however disadvantages with $SrTiO_3$ as a substrate for YBCO thin films. Firstly it is quite expensive and is available only as small wafers. Some of the substrates are twinned at room temperature which may result in inhomogeneous YBCO films. Another disadvantage with $SrTiO_3$ is the high dielectric constant and high dielectric loss. Hence $SrTiO_3$ is not a useful substrate for microwave applications (Ravi et al. 1990).

MgO as an alternative substrate does not suffer from the disadvantages of preparation and high dielectric constant. However, it is less well lattice matched to $YBa_2Cu_3O_{7-x}$ than $SrTiO_3$. Therefore MgO is expected to be a worse candidate for a substrate for superconducting thin film formation (Eibl et al. 1990a, Ramesh et al. 1990, Hwang et al., 1990, Tanaka et al. 1990, Matsui et al. 1992) than $SrTiO_3$. Many workers have suggested that the resulting thin film would be less crystalline (Ramesh et al. 1990) and hence harder to reproduce than employing a $SrTiO_3$ substrate. Indeed Dimos et al. (1988, 1990) proposed that all high angle grain boundaries (resulting from the poor misfit and subsequent polycrystalline nature of the $YBa_2Cu_3O_{7-x}$ on MgO (Hwang et al. 1990)) would result in many weak links for supercurrents, with the intergrain J_c dropping by a factor of 250 across the boundary and an intrinsic limit of 10^4 A/cm^2 at 77K. Yet despite these arguments, many authors for example (Berezin et al. 1990, Talvacchio et al. 1989) have shown MgO to be a good substrate for the YBCO thin film. Furthermore Hwang et al. (1990) have showed $YBa_2Cu_3O_{7-x}$ thin films on MgO to exhibit good superconducting transport properties with T_c = 89K and $J_{c,77K} = 10^6$ A/cm^2 comparable to using a $SrTiO_3$ substrate. Hwang et al. investigated all possible orientational relationships between $YBa_2Cu_3O_{7-x}$ and MgO and compared the experimental results with those predicted from a simplified near coincidence site lattice theory. The comparison yielded an excellent correlation, with only one predicted orientation which was not observed. Hwang et al. suggested that the $YBa_2Cu_3O_{7-x}$ grains locked into the preferred orientations with respect to the substrate have a high probability of forming

special low energy boundaries among themselves. These special boundaries are free from extraneous phases and have a high connectivity of Cu-O-Cu planes and are therefore not catastrophic to Tc and J_c. This argument supports the assumption that these chains are an integral part of the superconductivity behaviour in accordance with Allan and Mackrodt (1989b) who suggest superconductivity may be exhibited by one-dimensional Cu-O networks.

The $YBa_2Cu_3O_{7-x}$ thin film may grow with the c-axis either normal or perpendicular to the surface of the MgO substrate. Work by Moeckly et al. (1990) has shown $YBa_2Cu_3O_7$ thin films to grow predominantly with the c-axis normal to the plane of the MgO substrate. For polycrystalline MgO substrates T_c was measured to be 78K (10-12K below that generally obtained with $YBa_2Cu_3O_7$ films grown on single MgO crystals (Hwang et al. 1990)). Work by Ravi et al. (1990) has shown $YBa_2Cu_3O_{7-x}$ thin films to grow with the c-axis parallel to the surface of the MgO substrate with orientational relationships $YBa_2Cu_3O_{7-x}(100)//MgO(100)$, $YBa_2Cu_3O_{7-x}(010)//MgO(100)$ and $YBa_2Cu_3O_{7-x}(110)//MgO(100)$. The relative stabilities of the interfaces with either the c-axis of the $YBa_2Cu_3O_{7-x}$ parallel or normal to the interface can not be deduced from the experimental observations of the interfaces. However computer simulation can be employed to ascertain the relative stabilities of the $YBa_2Cu_3O_{7-x}//MgO$ interfaces and therefore provides a powerful tool to compliment the experimental observations.

Experimental observations of $YBa_2Cu_3O_7$ thin films grown on single MgO crystals have suggested the misfit to be accommodated by the formation of dislocations (Q. Li et al. 1989) defects (Eibl et al. 1990b, Fujiwara et al. 1990) and polycrystalline mosaic structures (Ramesh et al. 1990). These factors may contribute to the deterioration of the superconducting properties. However Ramesh observed the formation of a periodic array of interfacial dislocations (to accommodate the misfit) was not observed to extend

beyond the first unit cell along the c-direction ($YBa_2Cu_3O_{7-x}$(001)//MgO(100) interface).

In summary, high quality $YBa_2Cu_3O_{7-x}$ thin films may be grown on both $SrTiO_3$ and MgO substrates with the c-axis of the $YBa_2Cu_3O_{7-x}$ either parallel or perpendicular to the substrate. The misfit is accommodated by interfacial dislocations extending no further than the first $YBa_2Cu_3O_{7-x}$ unit cell resulting in the retention of the $YBa_2Cu_3O_{7-x}$ superconducting properties

7.1.1b Theoretical Studies

The interest in high-T_c superconductors has prompted many workers to focus their attentions in researching these materials using atomistic simulation (Allan and Mackrodt 1989b, Allan et al. 1989a, Baetzold 1988, Baetzold 1990, Baetzold 1991, Kenway et al. 1991, Islam and Baetzold 1989, Islam 1990, Islam and Ananthamohan 1991, Mackrodt 1989b, Zhang and Catlow 1992). The simulation techniques offer an approach to investigate some of the important features of the high T_c superconductors that is highly specific, versatile and predictive. This section illustrates this by reviewing some of the simulation work that has been carried out on high T_c materials.

The calculations on the superconductors using atomistic simulation have mostly been performed at 0K. At this temperature the superconductor is metallic. The application of metal potentials would therefore seem more appropriate, yet the excellent correlation between calculated and theoretically determined structural configurations advocate continuing with these potentials. Indeed empirical two body potentials together with the available codes have fitted the $YBa_2Cu_3O_7$ to within 0.03Å for the major bonds (Baetzold 1988). The excellent correlation may be attributed to the material properties of the superconductor being continuous through the transition temperature.

Most of the atomistic simulation work has been directed towards bulk properties. Baetzold (1988, 1990, 1991) investigated ionic and electronic defects in $YBa_2Cu_3O_7$ and $YBa_2Cu_3O_{6.5}$ concluded that oxygen O(1) ions (figure 7.1) are most easily removed from the crystal in accordance with neutron diffraction studies (Beno et al. 1987, Jorgensen et al. 1990) on oxygen deficient samples. The removal of this oxygen results in a shortening of the Cu(1)-O(4) bond length which is associated with a decrease in the superconducting transition temperature. The variation of T_c with oxygen stoichiometry in various high T_c superconductors has been measured experimentally by many authors (Shafer et al. 1987, Cava et al. 1990, Veal et al. 1989). Work by Jorgensen et al. (1990) on the variation of T_c with δ for $YBa_2Cu_3O_{7-\delta}$ suggests that various structural parameters that vary with δ can be correlated to T_c in the $YBa_2Cu_3O_{7-\delta}$ system. Moreover, some authors have attempted to establish similar correlations for chemically substituted systems. Miceli et al. (1988), for example, have postulated that T_c is a simple function of the Cu(1)-O(4) bond length for oxygen deficient and Co-doped (Cu(1) site) $YBa_2Cu_3O_{7-\delta}$. Atomistic simulation studies by Islam and Baetzold (1989) has also shown a trend towards decreasing T_c with increasing M^{2+}-O(4) (where M=Fe, Co, Ni, Cu and Zn) and decreasing Cu(1)-O(4) bond distances. This suggests a critical Cu(1)-O(4) bond length for superconducting behaviour. However, Jorgensen et al. (1990) argue that the number of systems that have been reported is too small to suggest that the Cu(1)-O(4) bond distance can be exploited as a probe for T_c. Furthermore, data for $Nd_{1+x}Ba_{2-x}Cu_3O_{7-\delta}$ suggest (Jorgensen et al. 1990) that Cu-O bond lengths are not suitable probes of T_c in this system. This may be a consequence of 'average' as opposed to 'local' identification of bond lengths; In many compounds of the type $Y_{1-x}M_xBa_2Cu_3O_{7-\delta}$, $YBa_{2-x}M_xCu_3O_{7-\delta}$, and $YBa_2Cu_{3-x}M_xO_{7-\delta}$ increased doping, M, leads to a transition to average tetragonal symmetry (superconductivity is observed to disappear at the orthorhombic-tetragonal transition (Jorgensen et al. 1990)). However superconductivity, often with a reduced T_c, persists into the tetragonal phase (Tokura et

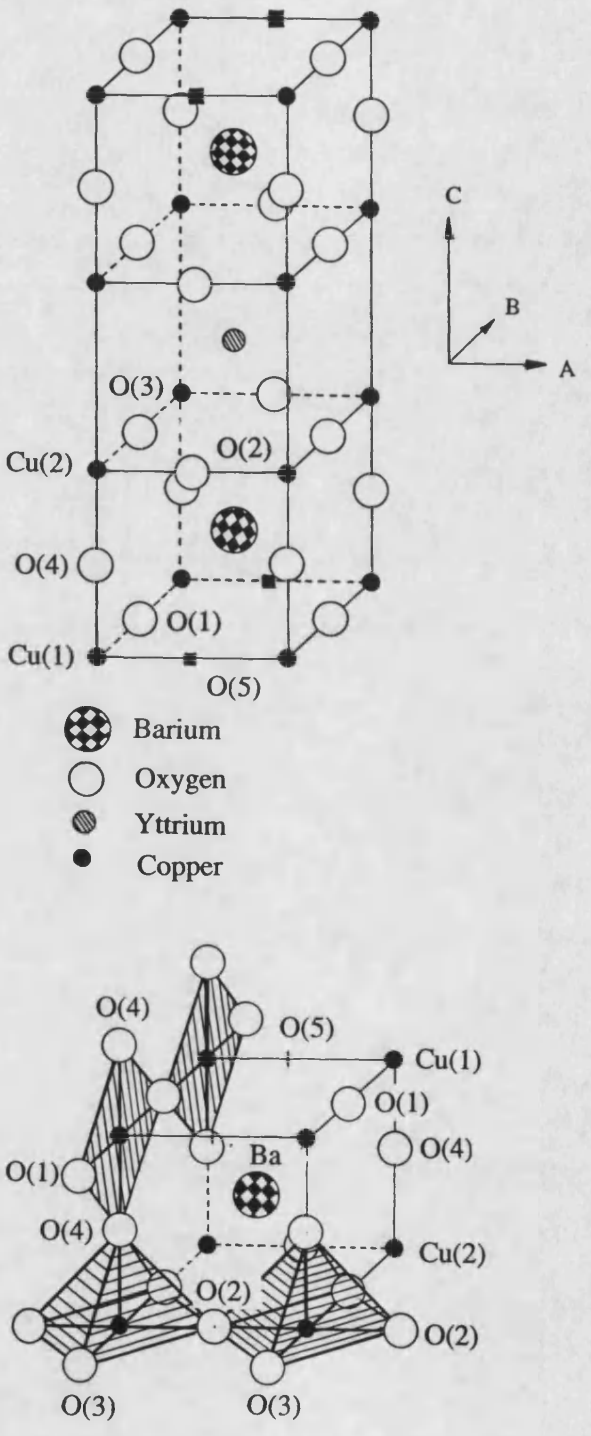

Figure 7.1 Diagrammatic representation of the $YBa_2Cu_3O_7$ structure indicating ion site notation.

al. 1988). This suggests that no correlation exists between symmetry and superconductivity. However, more detailed studies have elucidated the 'local' symmetry to be orthorhombic (Hiroi et al. 1988) and the tetragonal symmetry observed is the 'average' structure. Recent atomistic simulation work by Zhang and Catlow (1992) on $YBa_2Cu_4O_8$ link T_c with the Cu(2)-Cu(2) separation, and furthermore, they suggest correlations with other structural parameters may also be valid.

To establish whether certain structural parameters may be employed as T_c probes, local structural determinations are more suitable to investigate this effect, such as atomistic simulation. Moreover, atomistic simulation provides an excellent tool to investigate the 'local' symmetry of the system and also provides a relatively easy and inexpensive method by which the defect and dopant ion concentrations may be adjusted to optimise T_c. This is provided that the link between defect concentrations and T_c can be clearly established.

7.2 Crystal Structure of Orthorhombic $YBa_2Cu_3O_{6.5}$

The structure of $YBa_2Cu_3O_{6.5}$ has been determined to be orthorhombic with space group symmetry Pmmm by neutron diffraction (Miraglia et al. 1987, Jorgensen et al. 1990). The structure is essentially identical to that of $YBa_2Cu_3O_7$ (figure 7.1) with a 50% depletion of oxygen from the O(1) positions (Blumberg et al. 1989, Baetzold 1991, Kondo 1990). The 50% depletion of the O(1) oxygen positions gives rise to many oxygen filling permutations suggesting supercell formation with the thermodynamically more stable configuration predominating (Zhang et al. 1990, Muller et al. 1990, Shaked et al. 1989). This has been shown by Nakazawa and Ishikawa (1989) to occur for $YBa_2Cu_3O_{6+\delta}$ by careful heat treatment. Electron diffraction and high resolution electron microscopy studies by Zandbergen et al. (1987) on $YBa_2Cu_3O_{6.5}$ showed the [1 0 0] zone diffraction pattern exhibits weak extra spots at positions 1/2 0 0 and 0 1/2 0,

suggesting a doubling of the a_o and/or b_o lattice parameters in one or two directions. For specimens made under more carefully controlled conditions, the $YBa_2Cu_3O_{6.5}$ oxygen superstructure is much better ordered (Takabatake et al. 1988, Amelinckx et al. 1990) and exhibits a $2a_o$ or "orthorhombic II" structure. Kondo (1990) has shown that the ordering of the O(1) oxygens, resulting in the orthorhombic II $YBa_2Cu_3O_{6.5}$ structure, can be explained in terms of the long range Coulomb interaction between the oxygen ions, the ionization potential of the copper and the electron affinity of oxygen. Figure 7.2 shows diagrammatically the structure of the $YBa_2Cu_3O_{6.5}$ orthorhombic II structure, the copper CuO_2 planes, and CuO_2 chains are shown at the bottom of figure 7.1. The CuO_2 planes are considered to be the conduction layers and the CuO_2 chains, charge reservoir layers (Jorgensen 1991).

7.2.1 Calculated Orthorhombic II $YBa_2Cu_3O_{6.5}$ Crystal Structure

The structure of $YBa_2Cu_3O_{6.5}$ was calculated using the potentials of Baetzold (1988) derived for $YBa_2Cu_3O_7$. The $YBa_2Cu_3O_{6.5}$ structure was constructed considering a basis of 25 ions with one oxygen removed from the O(1) position in accordance with the experimental results (figure 7.3) to reproduce the orthorhombic II structure. Assigning formal charges to $YBa_2Cu_3O_7$, does not result in electroneutrality and therefore Baetzold assigned partial charges to the O(1) and O(4) sites. For $YBa_2Cu_3O_{6.5}$, the unit cell maintains electroneutrality with formal charges. The calculated bond lengths for $YBa_2Cu_3O_{6.5}$ are given in table 7.1. Experimentally determined bond lengths (Miraglia et al. 1987, Jorgensen et al. 1990) are given as a comparison together with recent work by Baetzold (1991) showing calculated $YBa_2Cu_3O_{6.5}$ bond lengths using potentials derived specifically for this structure.

The fit to the experimental data is less accurate for $YBa_2Cu_3O_{6.5}$ than for $YBa_2Cu_3O_7$ (Baetzold 1988). This is expected because of the nonequivalent Cu(1) ions resulting in

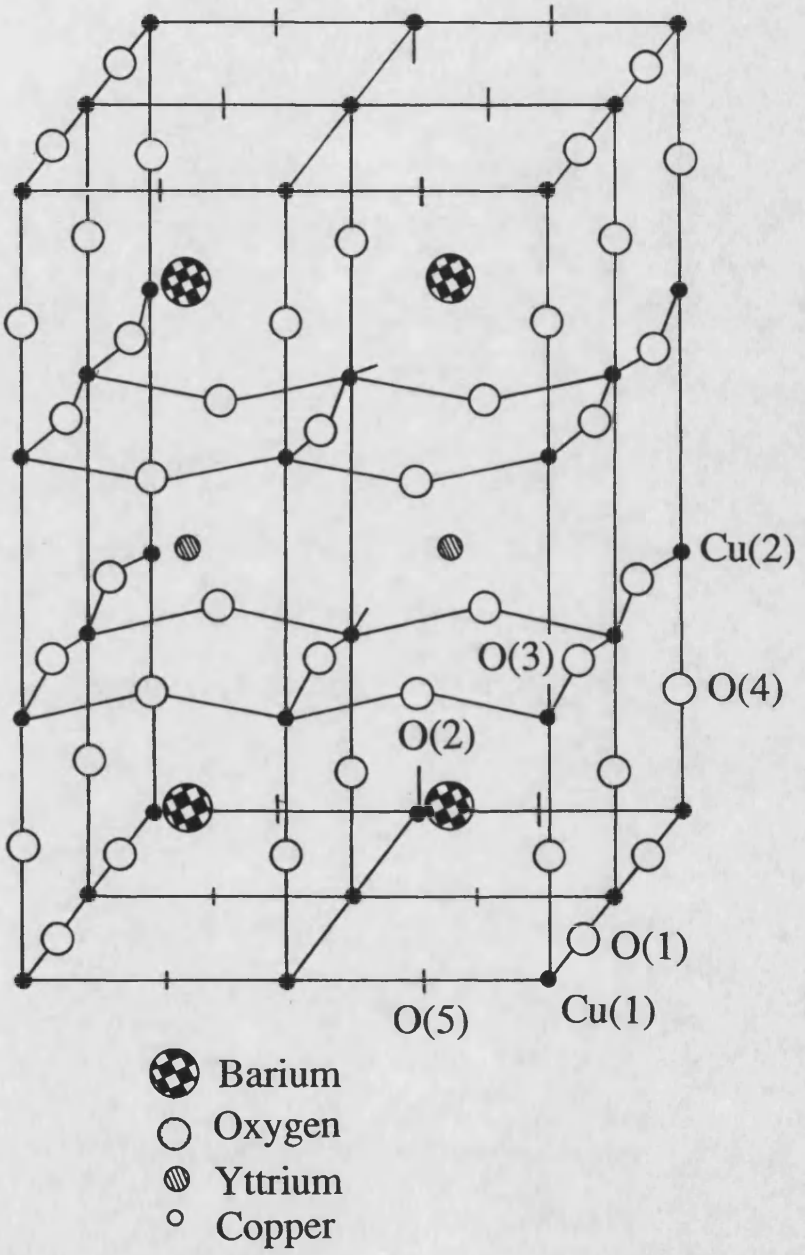

Figure 7.2 Diagrammatic representation of the orthorhombic II $YBa_2Cu_3O_{6.5}$ structure indicating ion site notation.

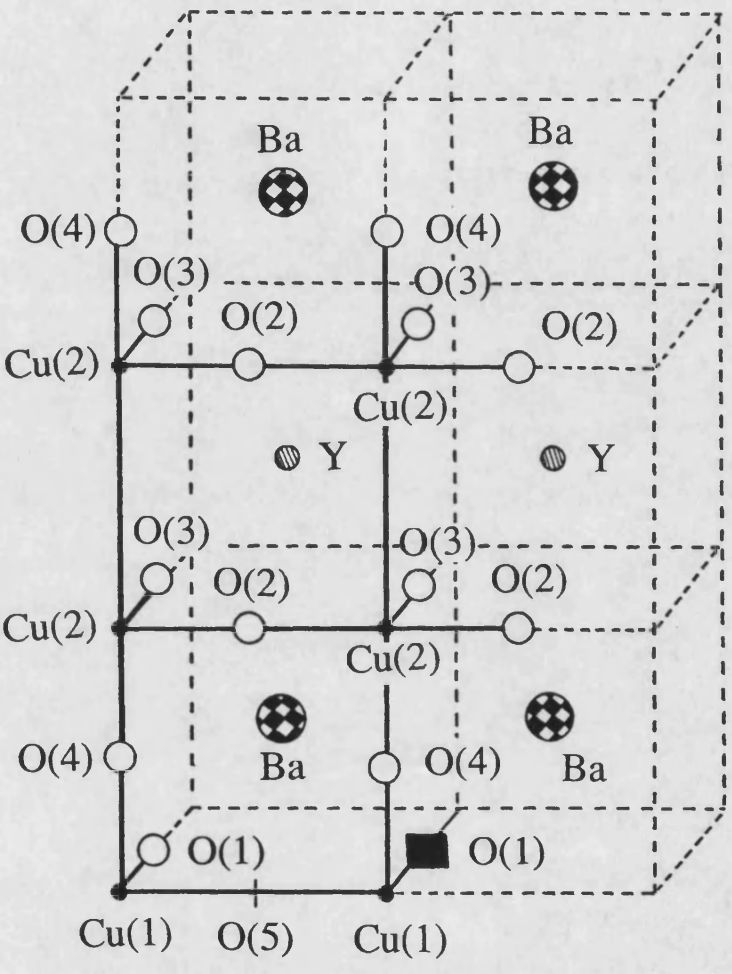

Figure 7.3 Representation of the $YBa_2Cu_3O_{6.5}$ unit cell structure employed for the calculations in this thesis.

BOND	Calc.		Average	Exp.	Baetzold		Average
Ba-O(4)	2.70	2.83	2.77	**2.77**	2.68	2.78	2.73
Ba-O(2)	2.99	2.99	2.99	**2.93**	2.91	2.91	2.91
Ba-O(3)	2.93	3.02	2.98	**2.90**	2.85	2.91	2.88
Ba-O(1)	3.03		3.03	**2.96**	2.92		2.92
Y-O(2)	2.40	2.40	2.40	**2.40**	2.39	2.41	2.40
Y-O(3)	2.39	2.41	2.40	**2.41**	2.44	2.29	2.37
Cu(1)-O(4)	2.04	1.79	1.91	**1.80**	1.89	2.06	1.98
Cu(1)-O(1)	1.93		1.93	**1.94**	1.93		1.93
Cu(2)-O(4)	2.34	2.73	2.54	**2.43**	2.50	2.14	2.32
Cu(2)-O(2)	1.95	1.92	1.94	**1.94**	1.90	1.92	1.91
Cu(2)-O(3)	1.95	1.94	1.95	**1.95**	1.94	1.95	1.95
a/2	3.84			**3.85**	3.80		
b	3.86			**3.87**	3.87		
c	12.21			**11.75**	11.71		

Table 7.1 Calculated $YBa_2Cu_3O_{6.5}$ bond lengths employing potentials derived for $YBa_2Cu_3O_7$ by Baetzold (1988) and including full ionic charges, compared to experimentally determined values (Miraglia et al. 1987). $YBa_2Cu_3O_{6.5}$ bond lengths calculated by Baetzold (1991) are also given as a comparison. These bond lengths were calculated using potentials derived specifically for $YBa_2Cu_3O_{6.5}$ and include partial charges. Bond lengths are in Angstroms.

two calculated lengths for all bonds except Ba-O(4) and Cu(1)-O(1). The calculated bond lengths agree well with experimentally determined values. The poorest structural agreement comes from the c parameter which is overestimated by 4%. The calculations by Baetzold however achieve a much higher accuracy (0.3%). This may be a consequence of the partial charges assigned by Baetzold, to the oxygen ions to provide 0.2 holes per CuO_2 unit in the plane, in accordance with experimental studies for $YBa_2Cu_3O_7$ (Wang 1987).

Figure 7.4(a) shows the calculated structure of $YBa_2Cu_3O_{6.5}$. Figure 7.4(b) shows the $YBa_2Cu_3O_{6.5}$ structure depicted by a stick model. The CuO_2 planes, with copper coordinated to five oxygens, and the CuO_2 chains with copper coordinated to four oxygens are clearly visible in the figure. The two CuO_2 planes are separated by an yttrium plane and are connected to the CuO_2 chains by the apical oxygen of the five coordinated copper Cu(2). Unlike the $YBa_2Cu_3O_7$ structure, the CuO_2 chains alternate between adjacent Cu(1) ions because of the 50% filling of the O(1) positions. A most striking feature is the 0.8Å displacement of the barium ions towards the CuO_2 planes. Furthermore, the Ba-O(1-4) bond distances are calculated to be higher than the experimentally determined values suggesting that we have identified an alternative 'local minima' structure.

7.3 Surface Topography

The $YBa_2Cu_3O_{6.5}$(001) surface can be cut six ways resulting in either BaO, CuO_2, yttrium, CuO_2, BaO or CuO_x planes terminating the surface (figure 7.5). However all these surfaces are, following Tasker (1979), type 3 surfaces and are therefore, unstable (see chapter 4.2). A stable type 2 surface may be constructed if the $YBa_2Cu_3O_{6.5}$ is cut at the yttrium plane and 50% of the yttrium removed from the surface and repositioned at the bottom of the crystal to form a neutral repeat unit (figure 7.6). This is the only (001)

Figure 7.4a Diagrammatic representation of the calculated relaxed structure of orthorhombic II $YBa_2Cu_3O_{6.5}$. Oxygen is coloured red, barium is white, yttrium is yellow and copper, blue.

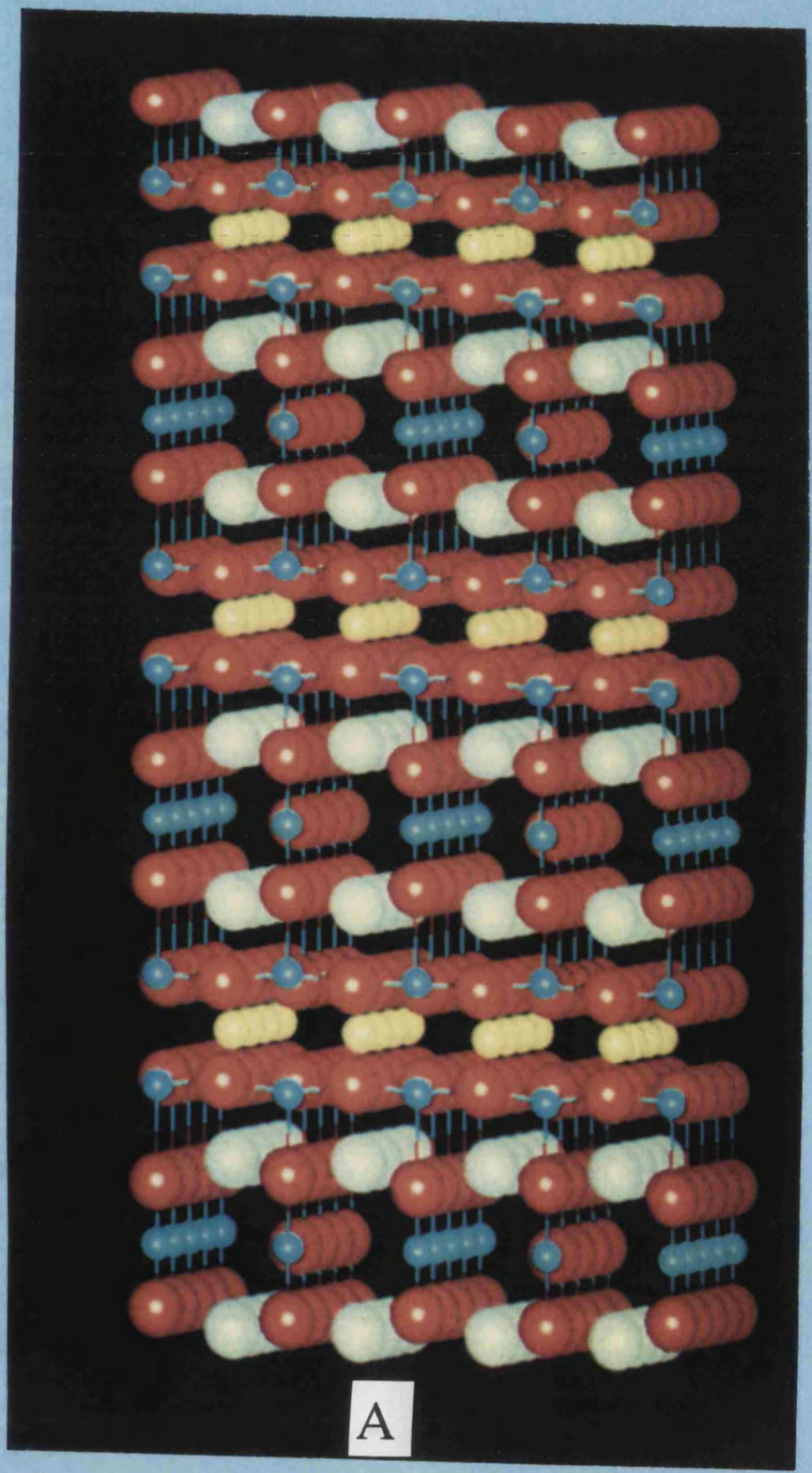
A

Figure 7.4b Diagrammatic representation of the calculated relaxed structure of orthorhombic II $YBa_2Cu_3O_{6.5}$ indicating the CuO_2 chains and CuO_2 planes (coloured blue).

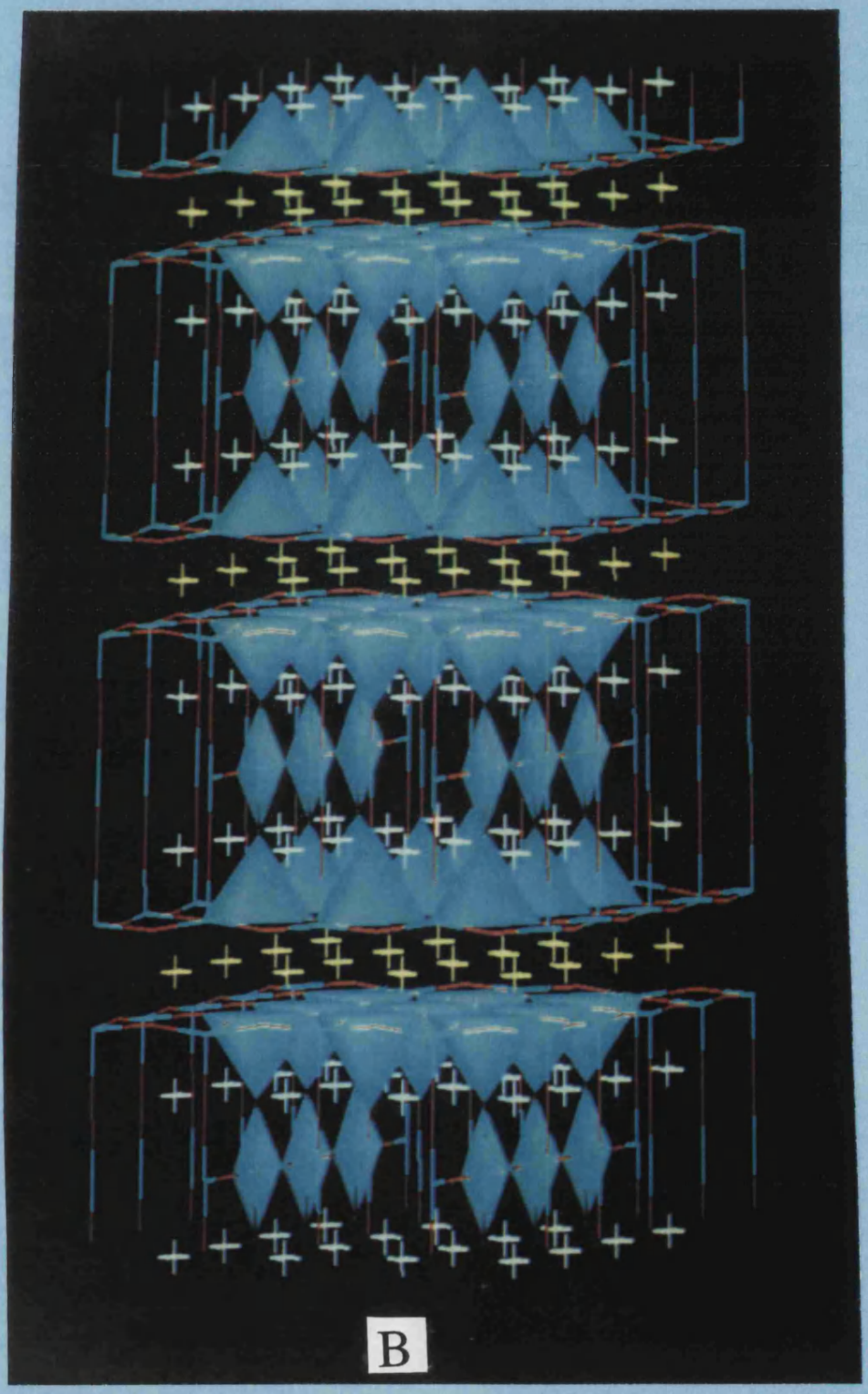
B

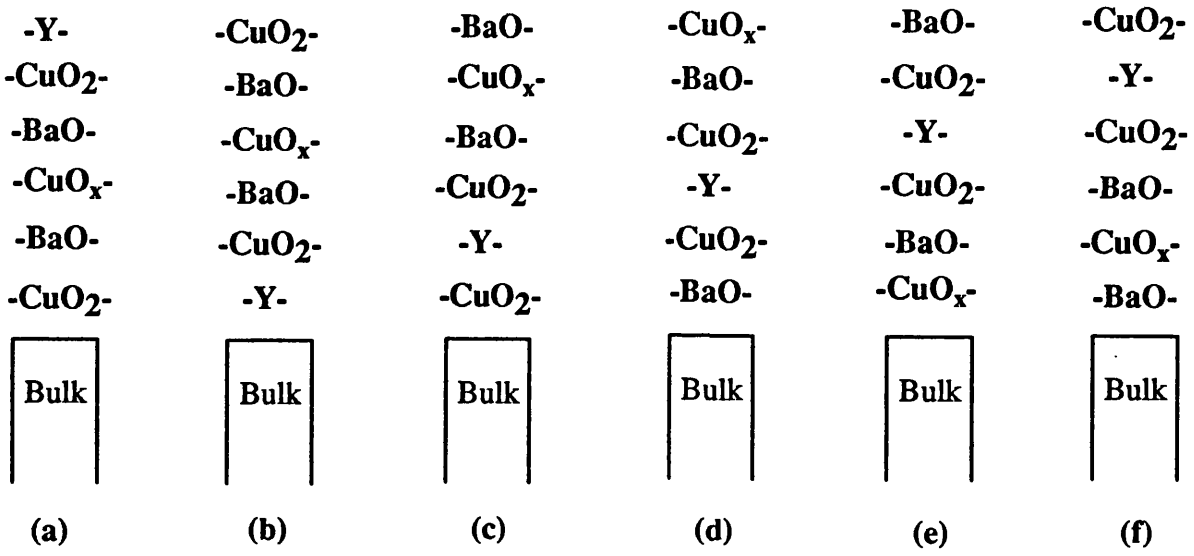

Figure 7.5 Diagrammatic representation of the six possible $YBa_2Cu_3O_{6.5}$ (001) atomic surface terminations.

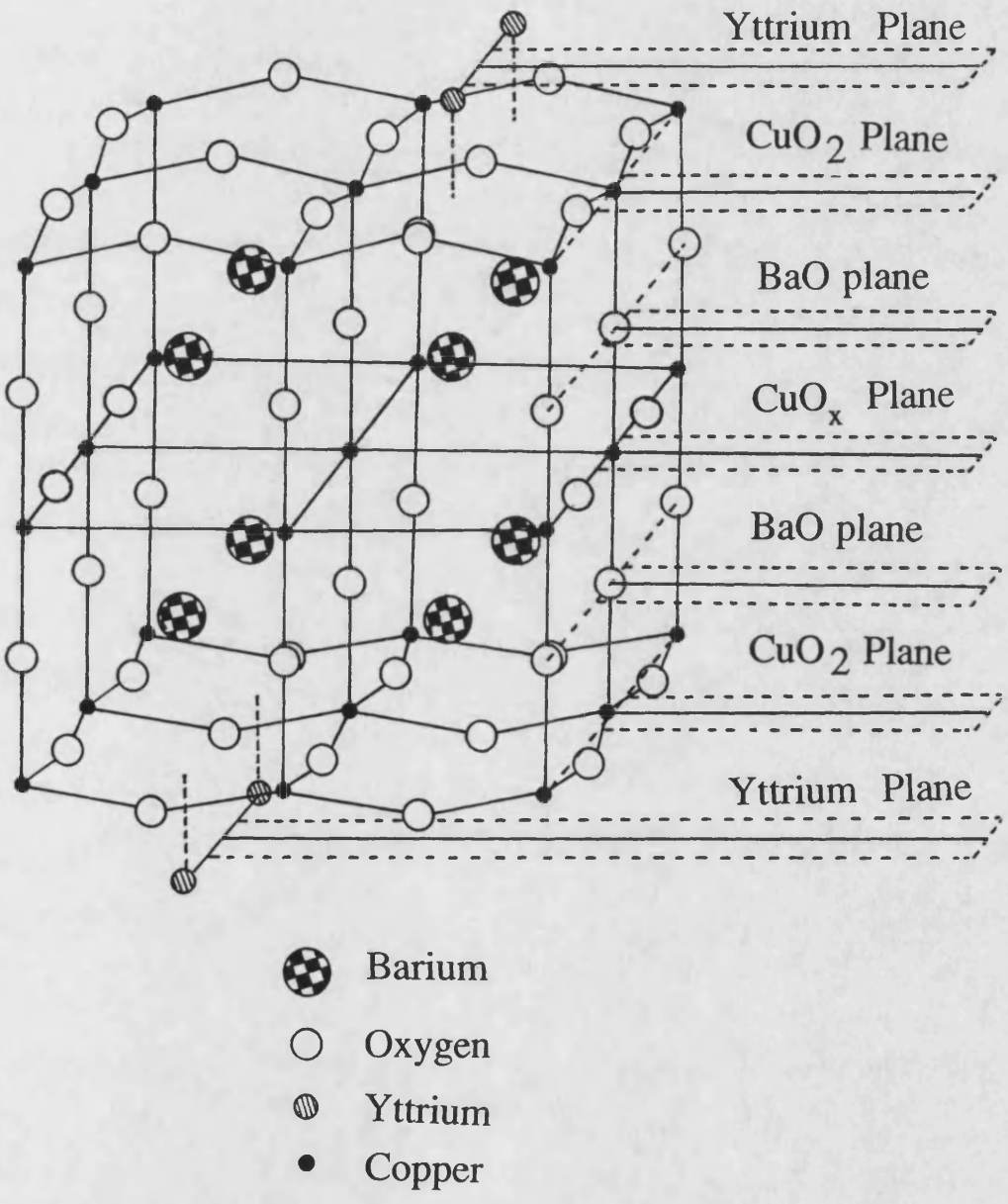

Figure 7.6 Diagrammatic representation of the $YBa_2Cu_3O_{6.5}$ (001) surface, constructed to give a type II surface (Tasker 1979).

surface which could be identified to be constructed of neutral repeat units and therefore stable. The calculated surface energy of the yttrium terminated surface is 10.51 Jm^{-2} before relaxation and 1.54 Jm^{-2} after relaxation. The surface energy after relaxation is expected to be lower than this value as the calculated surface energy had not converged with the size of cell explicitly relaxed. This value however represents the largest cell that could be accommodated within our available computer resources and required 27,000 Cray XMP cpu seconds to minimise. A difference of 8.97 Jm^{-2} between the relaxed and unrelaxed $YBa_2Cu_3O_{6.5}$ surface energies clearly demonstrates an enormous surface relaxation required to minimise the forces in the system. This is a consequence of the $YBa_2Cu_3O_{6.5}$ unrelaxed surface being terminated by Y^{3+} ions.

Figure 7.7 shows the unrelaxed (top) and relaxed (bottom) structures of the $YBa_2Cu_3O_{6.5}$ (001) surface, terminated at yttrium. The substantial relaxation is, primarily, to reduce the effect of terminating the $YBa_2Cu_3O_{6.5}$ surface with a highly charged plane. The copper Cu(2) and oxygens O(2) and O(3) from the CuO_2 plane have migrated from the second plane to terminate the $YBa_2Cu_3O_{6.5}$ with a neutral CuO_2 plane instead of the original, highly charged, Y^{3+} plane resulting in substantial stabilisation of the surface. The Y^{3+} ions are, after the surface relaxation, more than 2Å below the top copper oxygen plane. Oxygen ions from as far as the fifth $YBa_2Cu_3O_{6.5}$ plane have migrated over 2Å towards the surface. However, the CuO_2 plane 6 appears to exhibit little relaxation compared to the unrelaxed structure and by plane 7 the structure is consistent with the bulk $YBa_2Cu_3O_{6.5}$ structure.

The first experimental study on the surface of $YBa_2Cu_3O_7$ was performed by Van De Leemput et al. (1988) who, examined the (001) surface of an $YBa_2Cu_3O_7$ single crystal, with a scanning tunnelling electron microscope in air. On this surface they found that the orthorhombic crystal structure extends to the surface. The microscopic structure at

Figure 7.7 Calculated $YBa_2Cu_3O_{6.5}$ surface structures; (a) before relaxation; (b) after relaxation. Oxygen is coloured red, yttrium is yellow, copper is blue and barium, white.

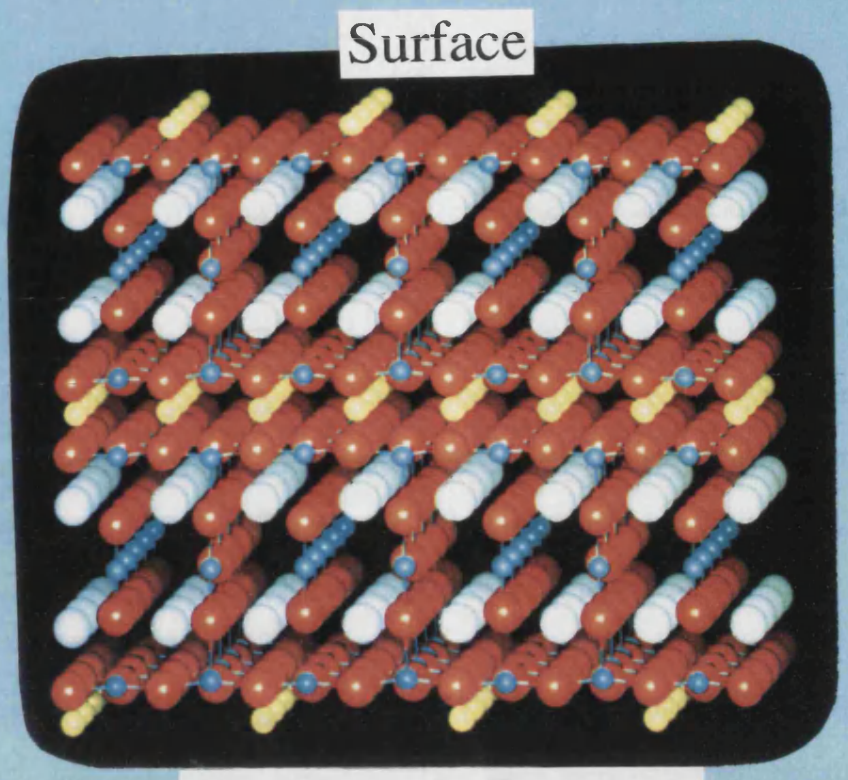

Unrelaxed Structure

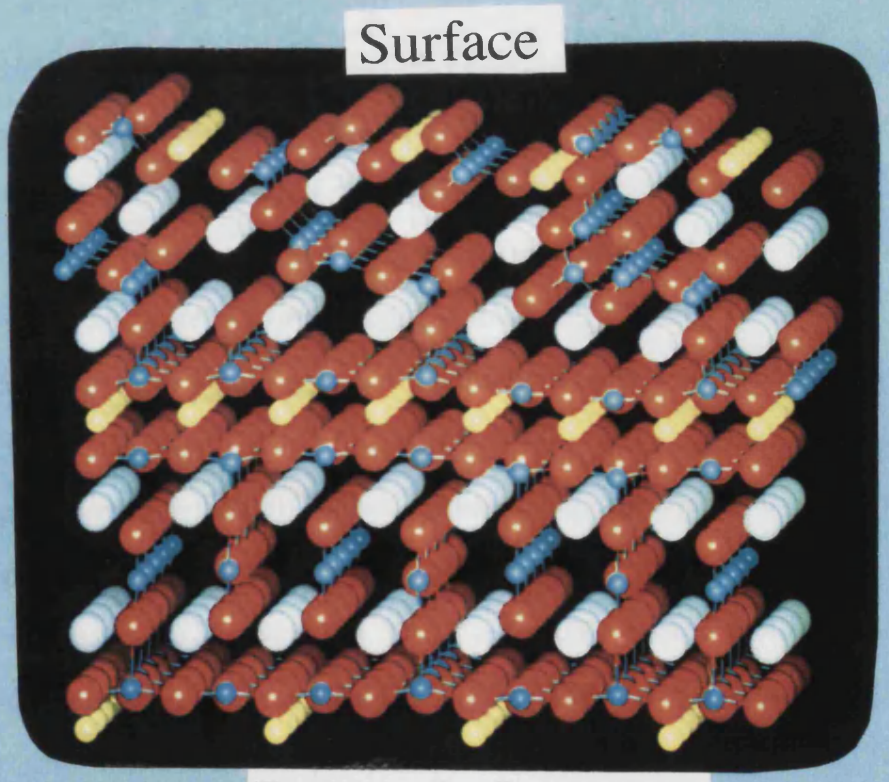

Relaxed Structure

Figure 7.8 shows diagrammatically $YBa_2Cu_3O_7$ cleaved at three places to give six distinct surfaces. The repeat unit of each surface is shown in the figure. This is assuming the copper ions are all in the Cu^{2+} charge state and that the hole is uniformly distributed on the oxygen ions sites O(1) and O(4). This assignment, employed by Baetzold (1988) to model $YBa_2Cu_3O_7$, is consistent with photoemission experiments which show no Cu^{3+} ground state ions (Horn et al. 1987) and quantum-mechanical cluster calculations (Baetzold 1988) which show equivalent Cu site populations and more hole population on O sites 1 and 4 than 2 and 3 in the ground state. The two stable (type 2) surfaces are terminated with BaO and CuO. This may perhaps explain the barium plane terminating the $YBa_2Cu_3O_7$ found experimentally (Bursill and Fan 1988) as cleavage of the $YBa_2Cu_3O_7$ crystal to form a type 2 surface must result in the formation of a BaO surface. An $YBa_2Cu_3O_7$ (001) surface terminating with an yttrium or CuO_2 plane results in a type 3 surface and such surfaces are therefore not expected to be observed experimentally. Alternative assignations of ionic charges may result in $YBa_2Cu_3O_7$ surfaces being assigned either 'stable' type 2 or 'unstable' type 3 incorrectly and therefore the assignation of ionic charges for theoretical calculations is critical to surface calculations. The same argument can also be applied to the theoretical treatment of interfaces.

7.4 Alternative $YBa_2Cu_3O_{6.5}$ Structures

The structure of $YBa_2Cu_3O_{6.5}$ has been elucidated to be orthorhombic II with space group symmetry Pmmm. Near coincidence site lattice theory can predict interface construction for orthorhombic systems grown on a cubic substrate (Kern 1989, Lamagna et al. 1992). However, the size of the cell required to accommodate this interface is, as yet, too large to consider computationally. The main aim of this chapter is to attempt to simulate the $YBa_2Cu_3O_{6.5}$(001)//MgO(100) interface using near coincidence site lattice

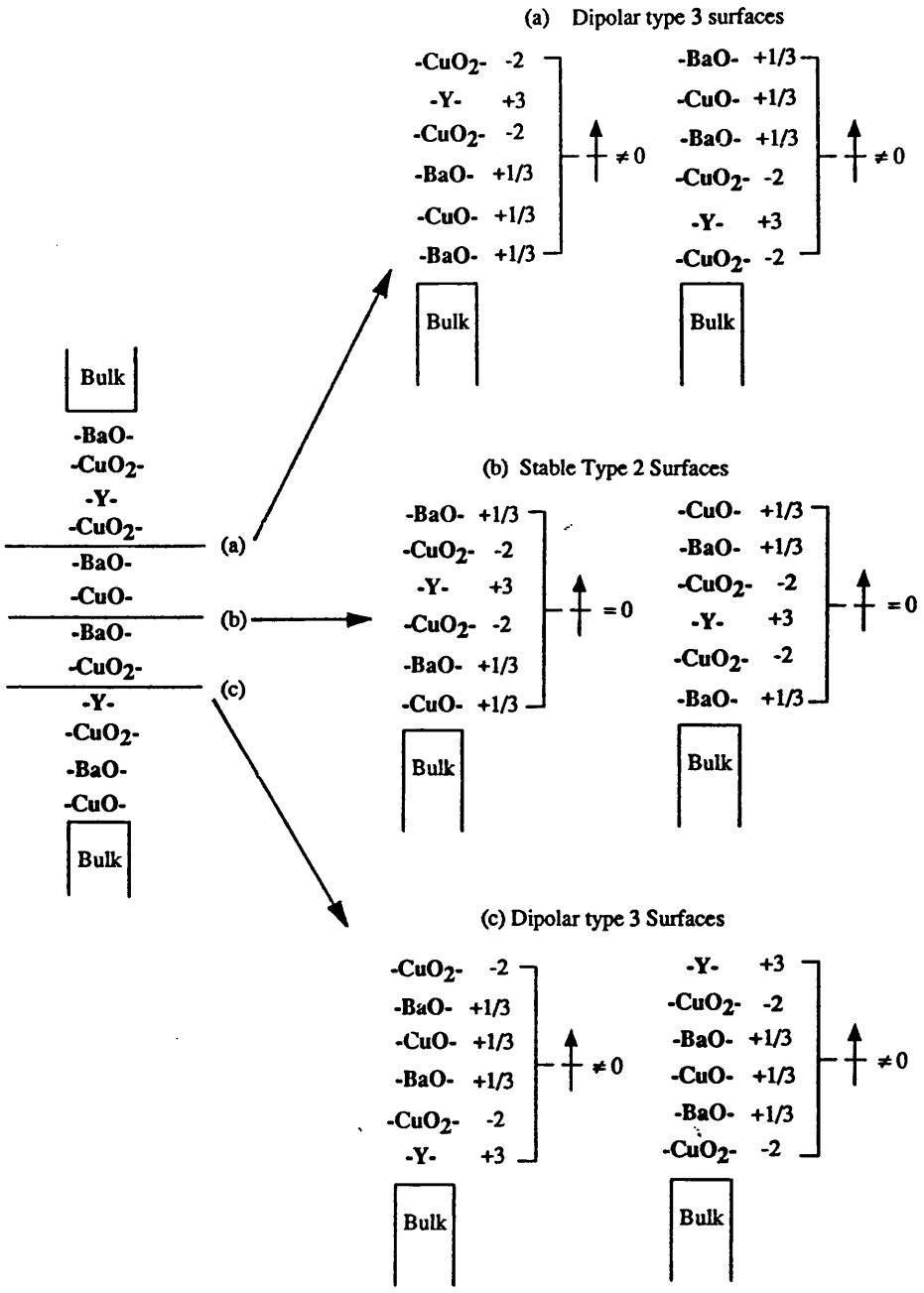

Figure 7.8 Diagrammatic representation of the two possible type II surfaces (Tasker 1979) of $YBa_2Cu_3O_7$. To the left of the figure the bulk $YBa_2Cu_3O_7$ planes are shown with three possible cleavage planes to give six different $YBa_2Cu_3O_7$ surface terminations. Cleavage along "(a)" results in two dipolar type 3 surfaces which terminate with CuO_2 and BaO. The number to the right of each plane represents the effective charge on each plane following the assignation of Baetzold (1988). Cleavage along "(b)" gives the two stable type 2 surfaces which terminate with a BaO and a CuO plane. Finally cleavage along "(c)" results in the formation of two further dipolar (type 3) surfaces which terminate with a CuO_2 and an yttrium plane.

theory. To enable the accommodation of the primitive unit cell within the computer resources we have available, the $YBa_2Cu_3O_{6.5}$ must exhibit tetragonal, rather than orthorhombic II symmetry. Extensive work by Kenway (1991) shows that the material properties of tetragonal and orthorhombic symmetries are similar and therefore provides some justification for this approach.

Two alternative $YBa_2Cu_3O_{6.5}$ structures have been constructed which adopt a tetragonal symmetry, these are designated type A and type B. The structure of the hypothetical $YBa_2Cu_3O_{6.5}$ structure, types A and B, are shown in figure 7.9 and 7.10 respectively. Type A is constructed with the oxygen O(1) positions from alternate Cu(1)O(1) planes empty or full (figure 7.9) as opposed to 50% O(1) coverage on every Cu(1)O(1) plane. Type B is constructed with the type A O(4) oxygens used to fill the O(1) and O(5) positions (figure 7.10).

The same potentials, used to derive the crystal structure of orthorhombic II $YBa_2Cu_3O_{6.5}$, were employed for $YBa_2Cu_3O_{6.5}$ structural types A and B, again using full ionic charges. The calculated energy of the unit cell of the $YBa_2Cu_3O_{6.5}$ type A structure is -523.78 eV and type B, -523.83 eV. This compares to -524.82 eV for the $YBa_2Cu_3O_{6.5}$ orthorhombic II structure. The 0.02% difference is fairly low and therefore it may be possible to synthesise these structures. Furthermore, the structure of the $YBa_2Cu_3O_{6.5}$ was elucidated by neutron diffraction (Miraglia et al. 1987, Jorgensen et al. 1990), which generally, only determines the average structure and may therefore exhibit local structural deviations from the average orthorhombic II structure. Indeed, several workers have identified deviations from the materials average structural configurations; a few are outlined below.

The presence of vacancy ordered superstructures in $YBa_2Cu_3O_{6.5}$ was first discovered by

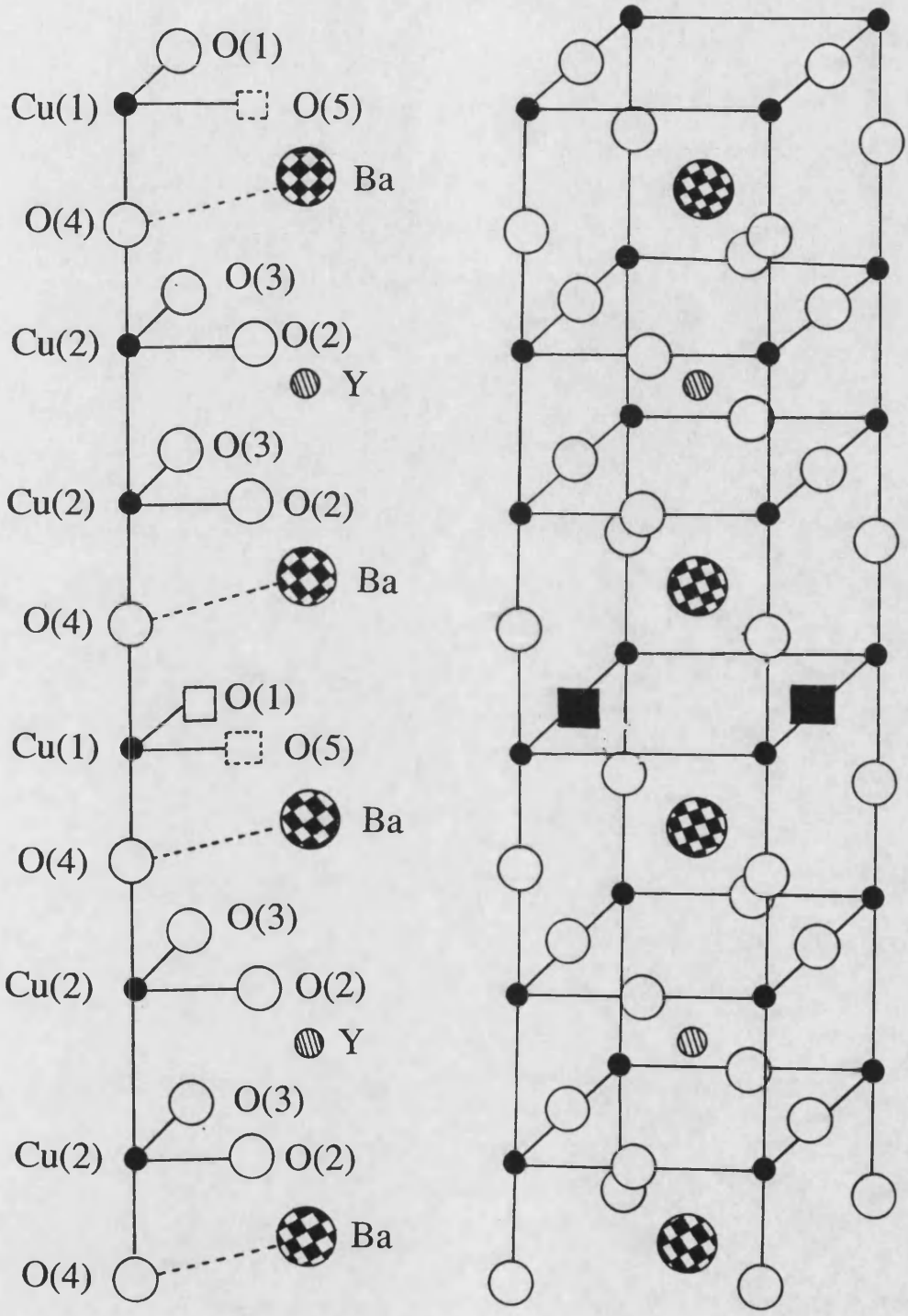

Figure 7.9 Diagrammatic representation of $YBa_2Cu_3O_{6.5}$ type A structure indicating ion site notation. To the left of the figure is the primitive unit cell. Note nonequivalent ions may be similarly labelled to ensure consistency with most experimental work which ascertains only the average structural configuration as opposed to local structural variation and therefore does not allow for the identification of these nonequivalent ions.

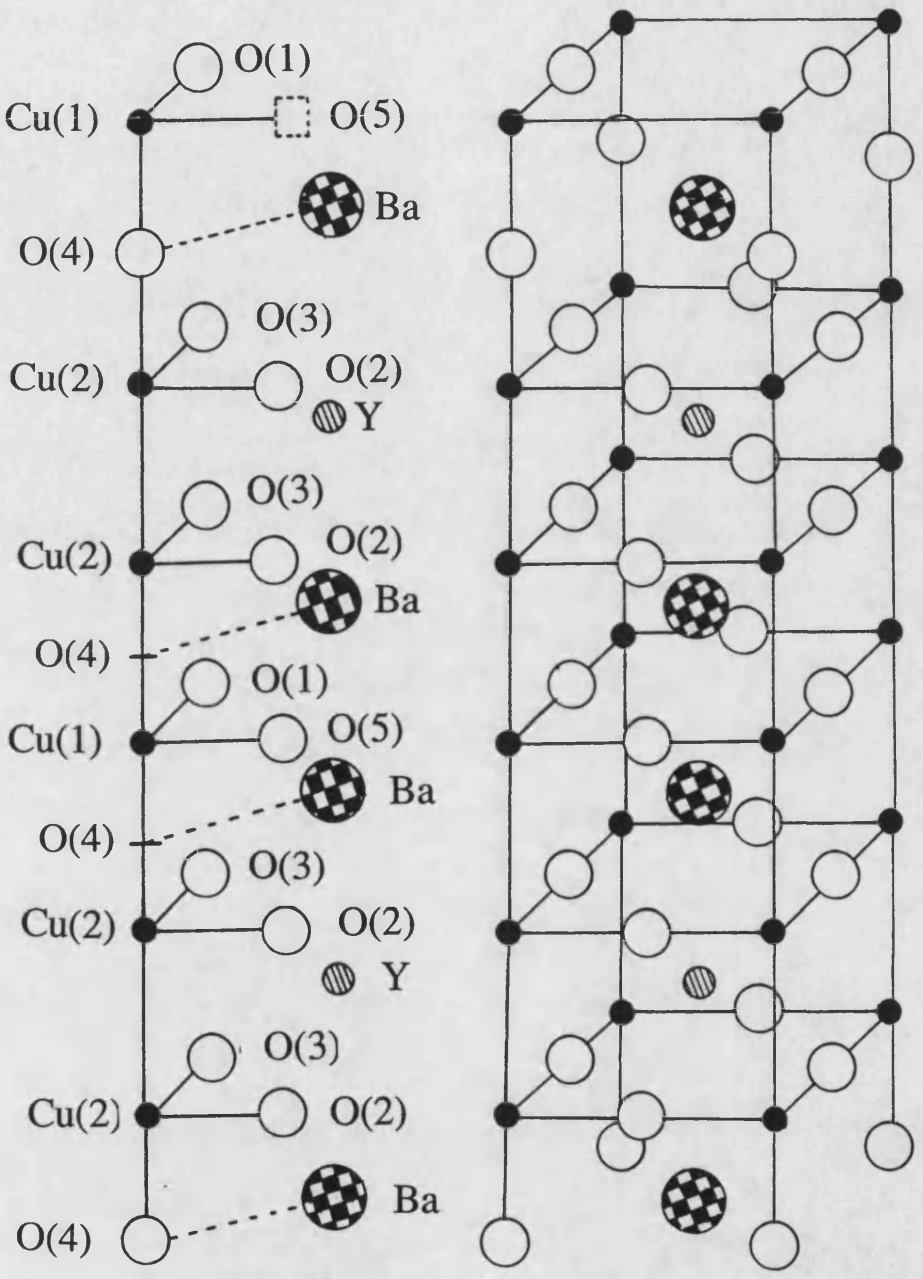

Figure 7.10 Diagrammatic representation of $YBa_2Cu_3O_{6.5}$ type B structure indicating ion site notation. To the left of the figure the primitive unit cell is shown.

means of electron diffraction and high resolution electron microscopy (Zandbergen et al. 1987). This work by Zandbergen et al. also led to the identification of the orthorhombic II structure of $YBa_2Cu_3O_{6.5}$. High resolution electron microscopy has also been used to identify stacking defects such as double CuO layers in $YBa_2Cu_3O_{7-\delta}$ (Zandbergen et al. 1988). Indeed Fischer et al. (1989) have prepared crystals in which systematically all CuO layers are doubled, leading to an ideal composition $YBa_2Cu_4O_8$ (this material has also been studied theoretically by Zhang and Catlow (1992)). It has also been possible to produce crystals in which single and double CuO layers alternate regularly corresponding to an ideal composition $Y_2Ba_4Cu_7O_{15}$ (Hewat et al. 1990) or $1\text{-}2\text{-}3^{1/2}$. A recent review by Amelinckx et al. (1991) examines the electron microscopy work that has been performed to identify local rather than average structural configurations in elucidating various superstructures, stacking defects and growth twins. This work further suggests that it may indeed be possible to synthesise the type A and B $YBa_2Cu_3O_{6.5}$ structures.

The calculated relaxed structures of type A and type B are shown in figures 7.11 and 7.12 respectively. Figure 7.11a shows three representations of the $YBa_2Cu_3O_{6.5}$ type A structure. The left structure is a stick representation with the CuO_2 chains and CuO_2 planes outlined in blue. The CuO_2 chains do not alternate between adjacent Cu(1) ions (as in orthorhombic II $YBa_2Cu_3O_{6.5}$) as all the O(1) positions are full. This results in a plane of copper Cu(1) ions with the Cu(1) ions coordinated to two oxygens. This is clearly evident from the ball and stick representation in the centre figure 7.11(a). To the right of figure 7.11(a) only the copper coordination is represented with the atom positions removed. From this figure it can be seen that the copper planes are comprised of Cu(2) ions coordinated to five oxygens, and Cu(2) ions coordinated to four oxygens to give the characteristic CuO_2 planes observed in the $YBa_2Cu_3O_{6.5}$ orthorhombic II structure. The four coordinated Cu(2), is a consequence of the large Cu(2)-O(4) distance

Figure 7.11 Calculated relaxed structural configuration of type A, $YBa_2Cu_3O_{6.5}$. A(i) Stick representation of the structure showing the CuO_2 planes and CuO_2 chains (coloured blue). A(ii) Ball and stick representation of the structure, oxygen is coloured red, barium is white yttrium is yellow and copper, blue. A(iii) CuO_2 chains and planes only, including additional CuO_2 planes resulting from the original modification of the orthorhombic II structure to give the hypothetical type A $YBa_2Cu_3O_{6.5}$ structure. (B) Enlarged view of the CuO_2 planes connected to the CuO_2 chains.

Type A

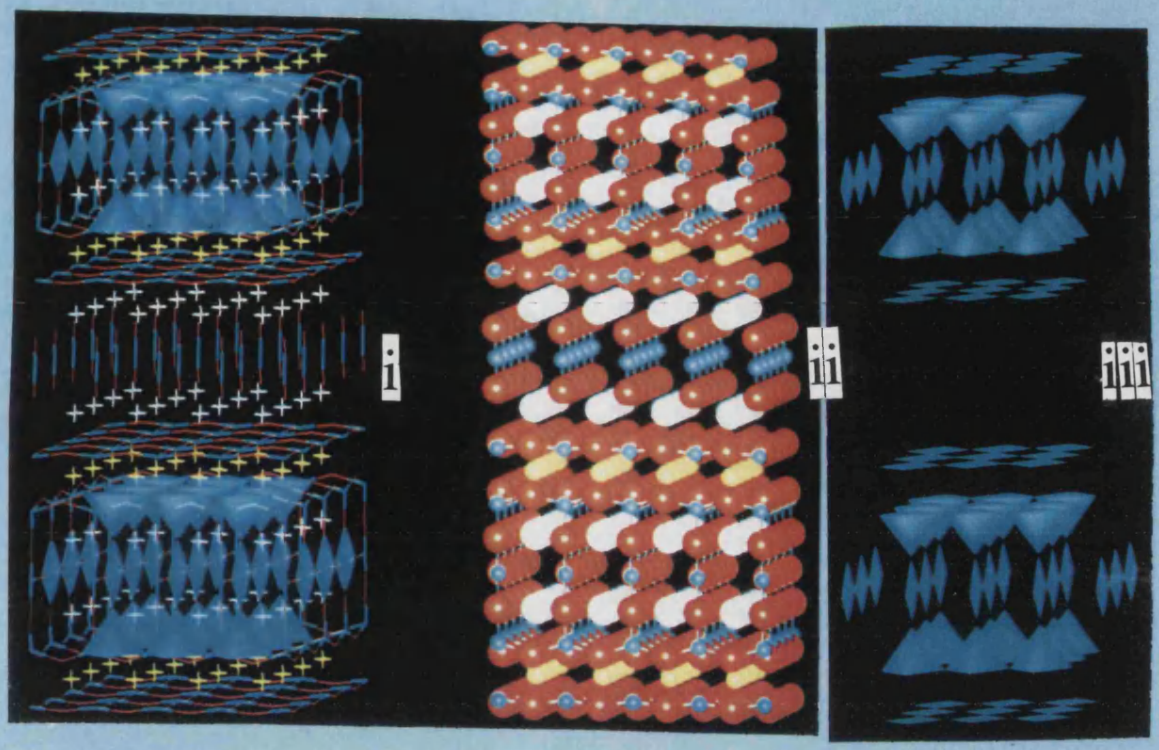

A

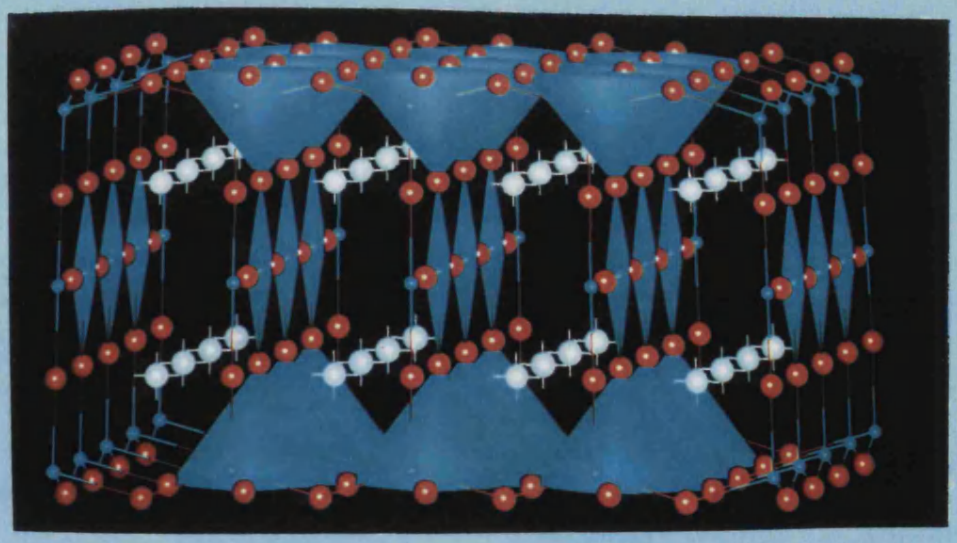

B

Figure 7.12 Calculated relaxed structural configuration of type B, $YBa_2Cu_3O_{6.5}$. A(i) stick representation of the structure showing the CuO_2 planes and CuO_2 chains (coloured blue). A(ii) ball and stick representation of the structure. Oxygen is coloured red, barium is white, yttrium is yellow and copper, blue. A(iii) CuO_2 chains and planes only including additional CuO_2 planes resulting from the original modification of the orthorhombic II structure to give the hypothetical type B $YBa_2Cu_3O_{6.5}$ structure.

Type B

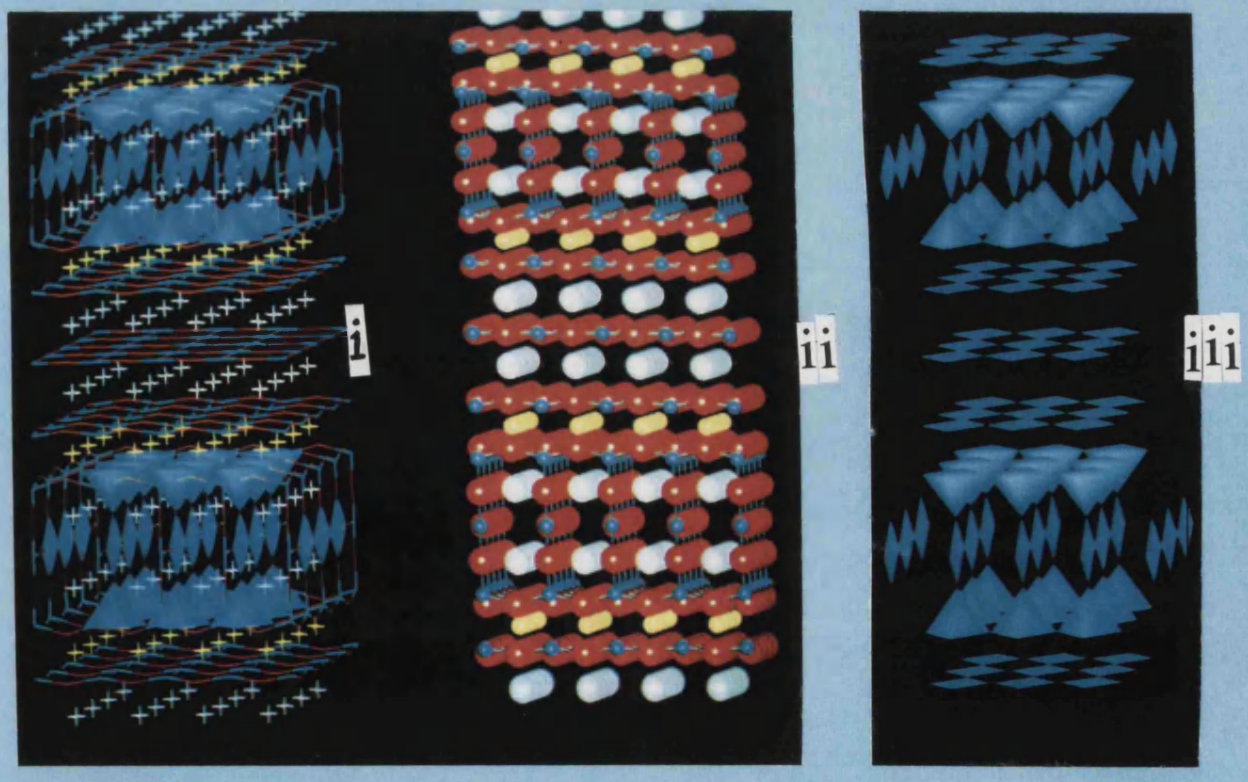

resulting from the minimisation procedure. Figure 7.11b shows an enlarged section of the structure with the size of the ions reduced to ensure clarity of the CuO_2 chains and CuO_2 planes.

Figure 7.12 shows three representations of the $YBa_2Cu_3O_{6.5}$ type B structure. Again the CuO_2 chains do not alternate as the O(1) positions are full. In this structure the five coordinated copper CuO_2 planes are separated by three CuO_2 planes where the copper is coordinated to only four oxygens. Other variations in structural details from the $YBa_2Cu_3O_{6.5}$ orthorhombic II structure include CuO_2 planes sandwiched between a plane of yttrium and a plane of barium and a further CuO_2 plane sandwiched between two barium planes. In each of these planes the copper is coordinated to four oxygens.

Table 7.2 gives the bond lengths of the ions in the type A and B structures compared to experimentally determined values for orthorhombic II $YBa_2Cu_3O_{6.5}$ (Miraglia et al. 1987). The calculated bond lengths for type A and type B are still in good agreement with the experimental results. The Cu(2)-O(1) bond length, however, is higher than the experimentally determined value for the type A structure and lower for type B. Similarly the c parameter is larger than the experimental studies suggest for type A and lower for type B. This is to be expected for the type B structure because the O(4) oxygens were used to accommodate the O(4) and O(5) sites.

The structures A and B do not exhibit the doubling of the a_o parameter (as the orthorhombic II structure) to accommodate the 50% O(1) depletion in the primitive unit cell and therefore the size of the interface primitive unit cell predicted using the near coincidence site lattice theory for structures A and B will be smaller and more easily accommodated within the computer resources available.

BOND	Type A		Average	Exp.	Type B		Average
Ba-O(4)	2.74	2.97	2.90	**2.77**	2.76		2.76
Ba-O(2)	3.09	2.84	2.97	**2.93**	3.09	2.83	2.96
Ba-O(3)	3.10	2.84	2.97	**2.90**	3.11	2.83	2.97
Ba-O(1)	2.85		2.85	**2.96**	2.85	2.81	2.83
Y-O(2)	2.31	2.49	2.40	**2.40**	2.32	2.48	2.40
Y-O(3)	2.31	2.50	2.41	**2.41**	2.31	2.49	2.40
Cu(1)-O(4)	1.99	1.80 1.80	1.86	**1.80**	1.98		1.98
Cu(1)-O(1)	1.94		1.94	**1.94**	1.94	1.95	1.95
Cu(2)-O(4)	3.43	1.96	2.70	**2.43**	1.95		1.95
Cu(2)-O(2)	2.02	1.95	1.99	**1.94**	2.03	1.97	2.00
Cu(2)-O(3)	2.02	1.95	1.99	**1.95**	2.03	1.97	2.00
a	3.88			**3.85**	3.92		
b	3.87			**3.87**	3.91		
c	12.36 (c/2)			**11.75**	11.40 (c/2)		

Table 7.2 Calculated $YBa_2Cu_3O_{6.5}$ bond lengths for the hypothetical $YBa_2Cu_3O_{6.5}$ structural types A and B compared to experimentally determined values for orthorhombic II $YBa_2Cu_3O_{6.5}$ (Miraglia et al. 1987). All bond lengths are in Angstroms.

7.4.1 Surface Topography

The $YBa_2Cu_3O_{6.5}$ type A structure can be cleaved along the (001) plane to give two surfaces. One terminating with a CuO plane, and the other terminating with a BaO plane. The repeat unit contains no dipole moment and therefore the surfaces are expected to be stable. An $YBa_2Cu_3O_{6.5}$ type A surface, cleaved along the (001) plane, terminating with an yttrium plane will have a dipole in the repeat unit and is therefore expected to be unstable Similarly the $YBa_2Cu_3O_{6.5}$ type B structure can be cleaved along the (001) plane to form two surfaces, one terminating with a BaO plane and the other, a CuO plane. Surfaces terminating with yttrium are expected to be unstable.

The surface energy of the BaO/CuO terminated $YBa_2Cu_3O_{6.5}$ type A (001) surfaces is calculated to be 1.25 Jm^{-2} before relaxation and 0.69 Jm^{-2} after relaxation. For BaO/CuO terminated $YBa_2Cu_3O_{6.5}$ type B (001) surfaces an unrelaxed value of 1.25 Jm^{-2} and relaxed value of 0.93 Jm^{-2} is calculated. The unrelaxed surface energies of $YBa_2Cu_3O_{6.5}$ types A and B, are much lower than the yttrium terminated $YBa_2Cu_3O_{6.5}$ orthorhombic II (001) surface energy (10.51 Jm^{-2}). This is attributed to the lone Y^{3+} ions terminating the $YBa_2Cu_3O_{6.5}$ orthorhombic II surface. The orthorhombic II relaxed surface energy is also higher than the $YBa_2Cu_3O_{6.5}$ type A and B structures. This may, however, be a consequence of the non-convergence of region size for the orthorhombic II surface energy calculation.

7.5 Near Coincidence Site Lattice Theory of the $YBa_2Cu_3O_{6.5}$(001)//MgO(100) interfaces.

Various orientations of $YBa_2Cu_3O_{7-x}$ grains in polycrystalline films prepared on (001) MgO substrates have been observed to agree well with the prediction of a simplified theory of near coincidence site lattice between $YBa_2Cu_3O_{7-x}$ and MgO (Ravi et al. 1990, Ramesh et al. 1990). In this section we employ a near coincidence site lattice theory to

construct $YBa_2Cu_3O_{6.5}$(001)//MgO(100) interfaces and the simulation techniques are then employed to calculate the relaxed interface structures and stabilities to compare with the experimentally determined values.

The a and b lattice parameters of $YBa_2Cu_3O_{6.5}$, type A structure are 3.88Å and 3.89Å respectively. For the $YBa_2Cu_3O_{6.5}$(001)//MgO(100) interfaces predicted using a near coincidence site lattice theory, $YBa_2Cu_3O_{6.5}$ was considered to have a two dimensional square lattice of parameter 3.885Å. Similarly for $YBa_2Cu_3O_{6.5}$, type B, the a and b lattice parameters are calculated to be 3.92Å and 3.91Å respectively and therefore, a two dimensional square lattice of parameter 3.915Å was chosen. Table 7.3 shows the interfaces predicted for $YBa_2Cu_3O_{6.5}$(001)//MgO(100) (type A and B) using near coincidence site lattice theory. The bulk lattice parameters of types A and B are employed as the unit cells of the type A and B structures are many layers thick and therefore the contraction of one unit cell 'in space' is expected to be negligible. Table 7.3 lists all the near coincidence site lattices for $YBa_2Cu_3O_{7-x}$//MgO observed experimentally and is therefore not a complete list.

Three $YBa_2Cu_3O_{6.5}$(001)//MgO(100) systems were investigated computationally: $\Sigma^P_{YBCO}\Sigma^P_{MgO}$ = 1/1 α (Θ = 0°), $\Sigma^P_{YBCO}\Sigma^P_{MgO}$ = 5/4 β (Θ = 26.565°) and $\Sigma^P_{YBCO}\Sigma^P_{MgO}$ = 20/17 β (Θ = 12.529°). The MgO substrate is constrained to accommodate its natural lattice parameter and the $YBa_2Cu_3O_{6.5}$ is therefore required to accommodate the full misfit. The interfaces were considered with one $YBa_2Cu_3O_{6.5}$ unit cell on the MgO(100) surface. We first consider the $\Sigma^P_{YBCO\ (type\ A)}\Sigma^P_{MgO}$ = 1/1 α (Θ = 0°) interface. This interface can be constructed with the $YBa_2Cu_3O_{6.5}$(001) plane terminating with either CuO, CuO_2, Y, BaO, or Cu at the $YBa_2Cu_3O_{6.5}$//MgO interface. Construction of the system with Y, Cu or CuO_2 at the interface results in a dipole moment in the $YBa_2Cu_3O_{6.5}$ which is expected to destabilise the interface and therefore only interfaces

$\Sigma^P_{YBCO}\Sigma^P_{MgO}$		k	l	m	n	Θ	Misfit / % Type A	Type B
1/1	α	1	0	1	0	0	+8.05	+7.02
5/4	β	2	1	2	0	26.565	-3.10	-4.13
9/8	β	3	0	2	2	45	+2.16	+1.14
10/9	β	3	1	3	0	18.435	+2.79	+1.76
16/13	β	4	0	3	2	33.690	-2.33	-3.35
20/17	β	2	4	1	4	12.529, 40.601*	-0.07	-1.10
25/20	β	3	4	2	4	10.305	-3.10	-4.13
29/25	α	2	5	3	4	15.068*, 31.329	+0.63	+0.39
29/25	α	5	2	5	0	21.801	+0.63	+0.39

* Denotes not observed experimentally so far.

Table 7.3 Near coincidence site lattices (NCSL) for the $YBa_2Cu_3O_{6.5}$ (001)//MgO(100) interfaces calculated for $YBa_2Cu_3O_{6.5}$ structural types A and B assuming lattice parameters of 3.875Å and 3.915Å respectively.

with BaO or CuO at the interface were considered. For BaO at the interface, two arrangements can be envisaged. Firstly, with the BaO over the magnesium sublattice of the MgO, or alternatively, with the BaO over the oxygen sublattice of the MgO. Calculations suggest the interface is more stable with the BaO over the magnesium sublattice in accordance with the BaO//MgO interface calculations in chapter 4. Similarly when CuO terminates $YBa_2Cu_3O_{6.5}$ at the $YBa_2Cu_3O_{6.5}$//MgO interface, the copper can adopt positions above the oxygens of the MgO substrate with the oxygens of the CuO plane directly above the magnesiums of the MgO substrate. Alternatively, the copper may be positioned above the magnesiums and the oxygen of the CuO plane adopt positions above the oxygen of the MgO substrate. The latter configuration results in unfavourable cation-cation and anion-anion interactions and is therefore expected to be unstable. Similarly for the $YBa_2Cu_3O_{6.5}$ type B structure, the $YBa_2Cu_3O_{6.5}$ BaO and CuO planes at the interface enable the interface to be constructed with no dipole perpendicular to the interface. Again the interface is calculated to be more stable with the BaO accommodating sites above the magnesium sublattice, or for CuO at the interface, a greater stability is attained with the copper above the oxygen sublattice of the MgO. Table 7.4 shows the interfacial energies, in Jm^{-2}, of the $YBa_2Cu_3O_{6.5}(001)$//MgO(100), $\Sigma^{P}_{YBCO}/\Sigma_{MgO} = 1/1\alpha$ ($\Theta = 0^{o}$), type A and B interfaces with CuO and BaO planes terminating the $YBa_2Cu_3O_{6.5}$ at the interface. The interfacial energies represent the energy required to cleave the interface to form a pure MgO surface and an $YBa_2Cu_3O_{6.5}$ monolayer thin film 'in space' per unit interfacial area (see equation 6.8 and figure 6.6).

The calculated stabilities for these interfaces (table 7.4) are all negative indicating that the interface is unstable with respect to an MgO(100) surface and an $YBa_2Cu_3O_{6.5}$ thin film 'in space'. The results do not however imply that the interface can not exist. Indeed $YBa_2Cu_3O_{6.5}$ is not thermodynamically stable with respect to its constituents as

$YBa_2Cu_3O_{6.5}$ Structural Type	Interfacial Stability /Jm^{-2}		Interfacial $YBa_2Cu_3O_{6.5}$ Plane
	Initial	Final	
Type A	-4.00	-2.21	BaO
Type A	-2.73	-0.71	CuO
Type B	-3.59	-2.02	BaO
Type B	-2.28	-0.51	CuO

Table 7.4 Calculated interfacial energies of the $YBa_2Cu_3O_{6.5}$ (001)//MgO(100), $\Sigma^p = 1/1\ \alpha$ ($\Theta = 0°$) interfaces for $YBa_2Cu_3O_{6.5}$ structural types A and B with CuO and BaO planes terminating the $YBa_2Cu_3O_{6.5}$ at the interface region.

the reaction

$$2\ YBa_2Cu_3O_{6.5} = Y_2BaCuO_5 + 3BaCuO_2 + 2CuO \qquad (7.1)$$

becomes favourable (Garzon and Raistrick 1991, Lazarev et al. 1991) below 1073K. Indeed, Sleight (1991) suggests there to be adequate data to conclude that any $RBa_2Cu_3O_7$ superconductors are not thermodynamically stable at any temperature or pressure. The calculated results therefore provide a useful comparison between various interfacial structural configurations. The configuration with a CuO plane terminating the $YBa_2Cu_3O_{6.5}$ at the interface region is calculated to be more stable than with a BaO termination, for both structural types A and B. For $YBa_2Cu_3O_{6.5}$ structure type A, the interface is 1.50 Jm^{-2} more stable with a CuO plane terminating the $YBa_2Cu_3O_{6.5}$ at the interface as opposed to a BaO plane and for type B, the interface is 1.51 Jm^{-2} more stable with a CuO plane terminating the $YBa_2Cu_3O_{6.5}$ at the interface as opposed to a BaO plane.

Figure 7.13 shows the relaxed structures of the Σ^P = 1/1 α (Θ = 0°) (type A) $YBa_2Cu_3O_{6.5}$(001)//MgO(100) interfaces. Figure 7.13a shows the relaxed interface structure with the BaO plane terminating the $YBa_2Cu_3O_{6.5}$ at the interface. The barium and oxygen ions from the BaO plane are constrained to accommodate positions directly above the magnesium sublattice of the MgO substrate. Figure 7.13b shows the relaxed interface structure with the CuO plane terminating the $YBa_2Cu_3O_{6.5}$ at the interface. The copper ions of the CuO plane are constrained to accommodate positions directly above oxygen ions from the MgO substrate and the oxygen ions of the CuO plane are constrained to accommodate positions directly above the magnesium ions of the MgO substrate. To the left of each figure (7.13(a) and (b)), the unit cell is displayed.

Figure 7.13 Calculated relaxed $YBa_2Cu_3O_{6.5}(001)//MgO(100)$, $\Sigma^P = 1/1$ α (Θ = 0_o) type A interface structures. (a) BaO plane terminating the $YBa_2Cu_3O_{6.5}$ at the interface region. (b) CuO plane terminating the $YBa_2Cu_3O_{6.5}$ at the interface region. Oxygen is coloured red, barium is white, yttrium is yellow, copper is blue and magnesium is purple.

$\Sigma^{p} = 1/1\ \alpha\ (\Theta = 0^{o})$ BaO (Type A)

A

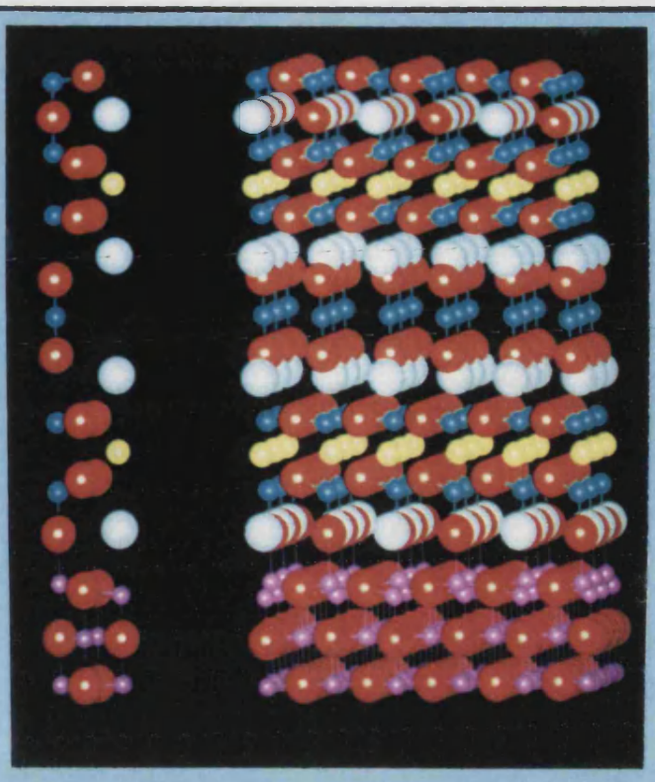

$\Sigma^{p} = 1/1\ \alpha\ (\Theta = 0^{o})$ CuO (Type A)

B

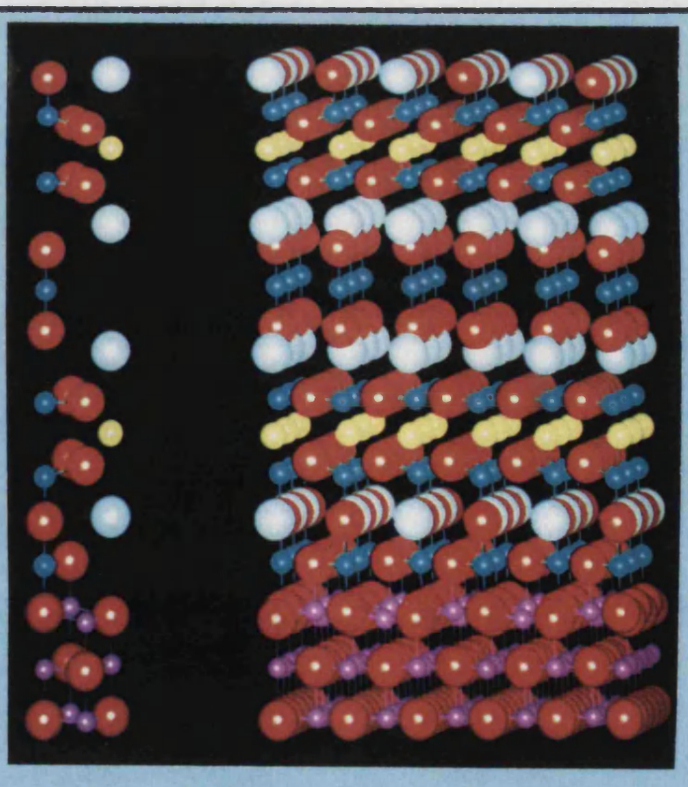

For both interfaces, there is little observable relaxation within the $YBa_2Cu_3O_{6.5}$ thin film however figure 7.13a shows substantial relaxation of the top MgO layer, with the magnesium ions directly below the oxygens from the $YBa_2Cu_3O_{6.5}$ BaO plane, displaced 0.3Å, perpendicular to the interface, towards the oxygen and therefore decreasing the magnesium-oxygen distance across the interface. The magnesium ions directly below the bariums from the $YBa_2Cu_3O_{6.5}$ BaO plane, are displaced 0.16Å, perpendicular to the interface, away from the barium ions resulting in an increase in the magnesium-barium distance. This relaxational behaviour is qualitatively similar to the behaviour observed for the BaO//MgO interface in chapter 4 and is a consequence of the minimisation procedure, maximising the favourable cation-anion interactions (magnesium-oxygen) and minimising the unfavourable cation-cation interactions (barium-magnesium) across the interface region. A similar type of behaviour is observed for the system with $YBa_2Cu_3O_{6.5}$ terminated with CuO at the interface (figure 7.13b). In this figure the MgO oxygens at the interface region directly below the copper ions from the $YBa_2Cu_3O_{6.5}$ are displaced 0.48Å towards the copper ions and the magnesium ions directly below the $YBa_2Cu_3O_{6.5}$ oxygens are displaced 0.29Å towards the oxygens enhancing the favourable cation-anion interactions.

Figure 7.14a,b shows the relaxed structures of the Σ^P = 1/1 α (Θ = 0°) (type B) $YBa_2Cu_3O_{6.5}$(001)//MgO(100) interfaces. Figure 7.14a shows the $YBa_2Cu_3O_{6.5}$ thin film terminating with the CuO plane at the interface and figure 7.14b shows the $YBa_2Cu_3O_{6.5}$ thin film terminating with the BaO plane at the interface. Similar relaxational behaviour to figures 7.13a,b is observed with substantial ion displacements at the interface region resulting in the enhancement of the favourable cation-anion interactions. In both figures 7.13a,b and 7.14a,b the relaxation is observed to extend to the third MgO layer from the interface.

Figure 7.14 Calculated relaxed $YBa_2Cu_3O_{6.5}(001)//MgO(100)$, $\Sigma^p = 1/1$ α (Θ = 0°) type B interface structures. (a) CuO plane terminating the $YBa_2Cu_3O_{6.5}$ at the interface region. (b) BaO plane terminating the $YBa_2Cu_3O_{6.5}$ at the interface region. Oxygen is coloured red, barium is white, yttrium is yellow, copper is blue and magnesium is purple.

$\Sigma^{p} = 1/1\ \alpha\ (\Theta = 0^{o})$ CuO (Type B)

A

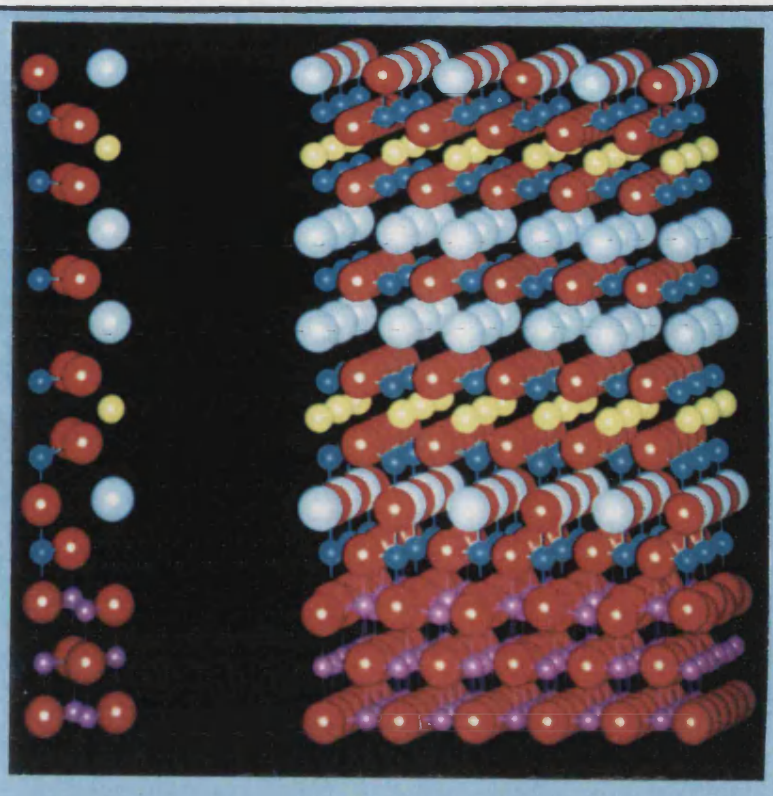

$\Sigma^{p} = 1/1\ \alpha\ (\Theta = 0^{o})$ BaO (Type B)

B

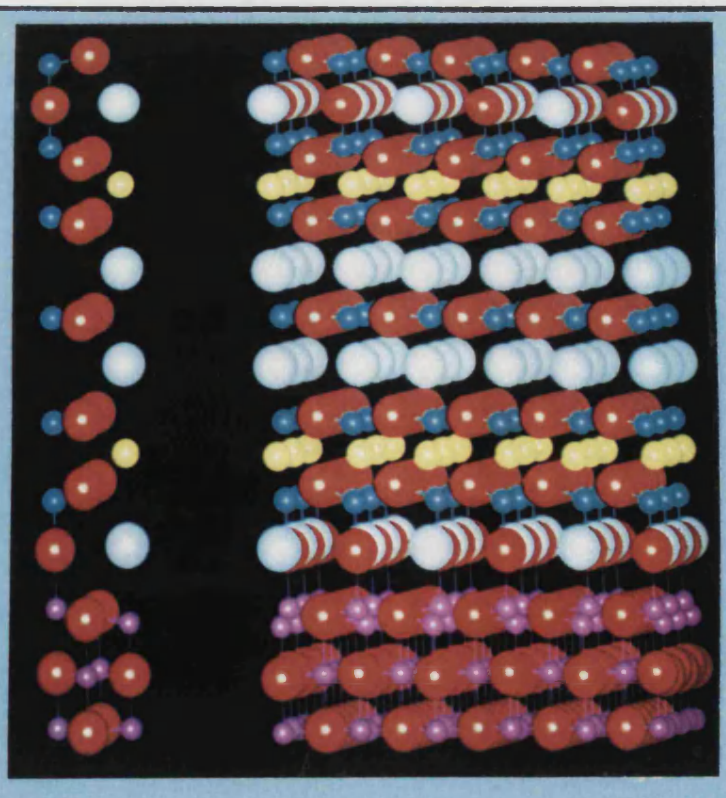

Thus far we have only considered the relaxational behaviour of the MgO substrate yet the modification of the $YBa_2Cu_3O_{6.5}$ structure as a result of interfacing with the MgO substrate is of paramount importance to the superconducting properties of the material. Indeed, small changes in bond lengths have serious implications to the T_c of the material (Miceli et al. 1988, Islam and Baetzold 1989, Zhang and Catlow 1992). The structural modifications of the $YBa_2Cu_3O_{6.5}$ as a result of the relaxation are not apparent from inspection of the structure and therefore the relaxation of the $YBa_2Cu_3O_{6.5}$ is monitored by inspection of the bond lengths. Table 7.5 shows the calculated $YBa_2Cu_3O_{6.5}$ (type A) bond lengths for the pure structure, compared to bond lengths calculated for the structure when interfaced to MgO (for both the BaO and CuO planes terminating the $YBa_2Cu_3O_{6.5}$ at the interface). From table 7.5 it can be seen that the largest modification in bond length is +10% for the Ba-O(4) bond (the bond length has increased) with the $YBa_2Cu_3O_{6.5}$ terminated with CuO at the interface. This result is somewhat surprising since the largest change in Ba-O(4) bond length was expected to be the Ba-O(4) bond at the interface when the $YBa_2Cu_3O_{6.5}$ is terminated with BaO at the interface. However this bond length has been modified by only 5%. Furthermore the 10% change in Ba-O(4) bond length is not from the first BaO plane adjacent to the interface, but the second BaO plane i.e. 6 planes from the interface (figure 7.13b). The Cu(1)-O(4) bond length (suggested to be an indication of T_c associated with the material (Miceli et al. 1988, Islam and Baetzold 1989, Zhang and Catlow 1992)) has been reduced by 8.7% as a consequence of the interface. This reduction is exactly the same for the $YBa_2Cu_3O_{6.5}$ terminated with either BaO or CuO at the interface. This again is a surprising result since the Cu(1)-O(4) bond is observed at the surface for the BaO terminated interface (figure 7.13a) and directly at the interface for the CuO terminated interface (figure 7.13b). Furthermore the changes in bond lengths for most of the bonds appear to be independent of whether the interface was constructed with the CuO or BaO plane terminating the $YBa_2Cu_3O_{6.5}$ at the interface region. This result suggests the reduction

BOND	Pure $YBa_2Cu_3O_{6.5}$		Interfaced $YBa_2Cu_3O_{6.5}$ CuO Plane		BaO Plane	
Ba-O(4)	2.74	2.97	2.93	3.27	2.93	3.11
Ba-O(2)	3.09	2.84	3.17	2.91	3.14	2.88
Ba-O(3)	3.10	2.84	3.18	2.87	3.14	2.88
Ba-O(1)	2.85		2.90		2.90	
Y-O(2)	2.31	2.49	2.38	2.60	2.37	2.58
Y-O(3)	2.31	2.50	2.37	2.59	2.37	2.58
Cu(1)-O(4)	1.99	1.80 1.80	1.83	1.80 1.80	1.83	1.80 1.80
Cu(1)-O(1)	1.94		2.08		2.08	
Cu(2)-O(4)	3.43	1.96	3.16	1.86	3.15	1.89
Cu(2)-O(2)	2.02	1.95	2.13	2.07	2.15	2.07
Cu(2)-O(3)	2.02	1.95	2.14	2.01	2.15	2.07

Table 7.5 Calculated $YBa_2Cu_3O_{6.5}$ structural type A bond lengths in the $YBa_2Cu_3O_{6.5}$(001)//MgO(100), Σ^P = 1/1 α (Θ = 0°) interface with CuO and BaO planes terminating the $YBa_2Cu_3O_{6.5}$ at the interface region. The calculated bond lengths for pure $YBa_2Cu_3O_{6.5}$ type A are also given as a comparison. Bond lengths are in Angstroms.

of the strain energy introduced into the $YBa_2Cu_3O_{6.5}$ is the major driving force in the relaxational behaviour as each plane, whether terminating the $YBa_2Cu_3O_{6.5}$ at the interface or surface plane, is associated with the same strain to accommodate the misfit. Furthermore the ionic relaxation attributed to the interface would result in the modification of ions near the interface region. This suggests that a modification of the structural configuration of the $YBa_2Cu_3O_{6.5}$, such as changes in bond lengths, may be induced by choosing a suitable substrate and interfacial configuration with associated misfit. Furthermore it may be possible to predict a structural configuration which maximises T_c. This argument is however very speculative and much more work is required to monitor the effect of the misfit on T_c.

The second system studied is the $\Sigma^P = 5/4\ \beta$ ($\Theta = 26.565°$). Two interfaces were considered for both structural types A and B, firstly with the CuO plane terminating the $YBa_2Cu_3O_{6.5}$ at the interface and second with the BaO plane terminating the $YBa_2Cu_3O_{6.5}$ at the interface. Table 7.6 gives the energies of the relaxed interfaces relative to the relaxed surface energy of the MgO surface and the $YBa_2Cu_3O_{6.5}$ thin film 'in space'. An energy of +0.16 Jm^{-2} is calculated for the $\Sigma^P = 5/4\ \beta$ ($\Theta = 26.565°$) CuO (type A) suggesting that the interface is stable with respect to a pure MgO surface and $YBa_2Cu_3O_{6.5}$ thin film 'in space'. Again the interfaces with the CuO planes terminating the $YBa_2Cu_3O_{6.5}$ are calculated to be more stable than with BaO terminating the $YBa_2Cu_3O_{6.5}$ at the interface. Figure 7.15 a shows the relaxed $\Sigma^P = 5/4\ \beta$ ($\Theta = 26.565°$) CuO (type B) interface structure, to the left of the figure is the interface primitive unit cell and the right of the figure shows an extended portion of the interface. The interfacial relaxation has resulted in substantial modification of both the MgO substrate and the $YBa_2Cu_3O_{6.5}$ thin film structures. Rumpling of the CuO and BaO planes at the interface is clearly evident from the figure. The CuO plane sandwiched between two barium planes exhibits a rumpling of the oxygen ions with amplitude 0.9Å. This is a

$YBa_2Cu_3O_{6.5}$ Structural Type	Interfacial Stability /Jm^{-2} Initial	Final	Interfacial $YBa_2Cu_3O_{6.5}$ Plane
Type A	-2.31	-0.82	BaO
Type A	-2.31	**+0.16**	CuO
Type B	-2.95	-1.29	BaO
Type B	-2.88	-0.14	CuO

Table 7.6 Calculated interfacial energies of the $YBa_2Cu_3O_{6.5}(001)//MgO(100)$, $\Sigma^P = 5/4\ \beta$ ($\Theta = 26.565°$) interfaces for $YBa_2Cu_3O_{6.5}$ structural types A and B with CuO and BaO planes terminating the $YBa_2Cu_3O_{6.5}$ at the interface region.

Figure 7.15 Calculated relaxed $YBa_2Cu_3O_{6.5}(001)//MgO(100)$, $\Sigma^P = 5/4\ \beta$ (Θ = 26.565°) interfaces. (a) $YBa_2Cu_3O_{6.5}$ type B structure with CuO terminating the $YBa_2Cu_3O_{6.5}$ at the interface region. (b) $YBa_2Cu_3O_{6.5}$ type A structure with BaO terminating the $YBa_2Cu_3O_{6.5}$ at the interface region.

$\Sigma^p = 5/4$ ($\Theta = 26.565°$) CuO (Type B)

A

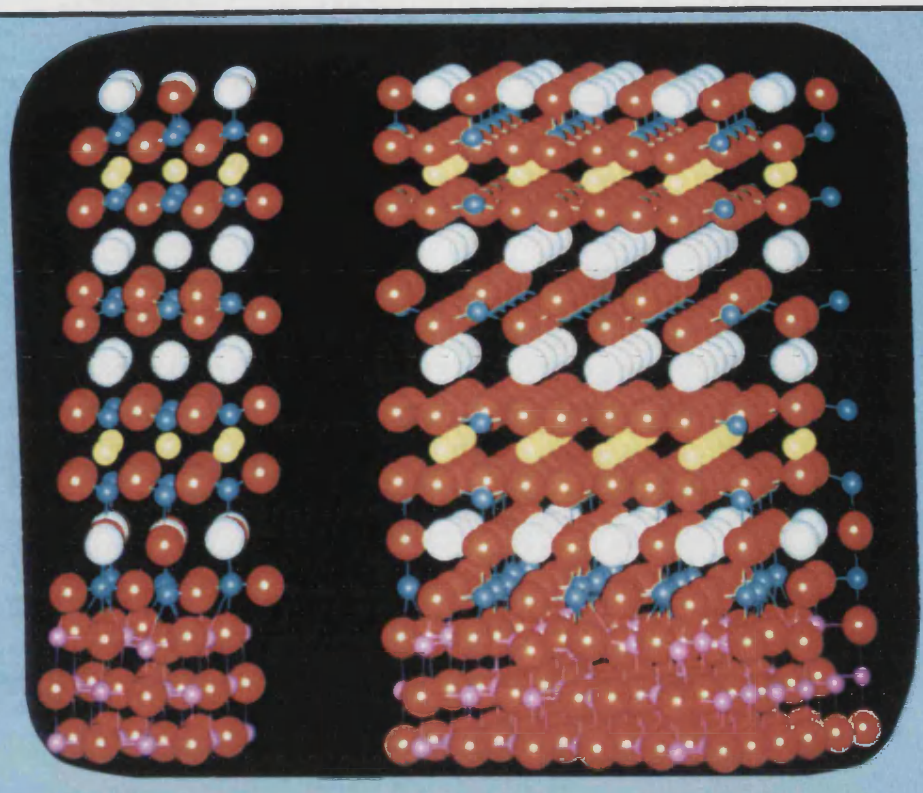

$\Sigma^p = 5/4$ ($\Theta = 26.565°$) BaO (Type A)

B

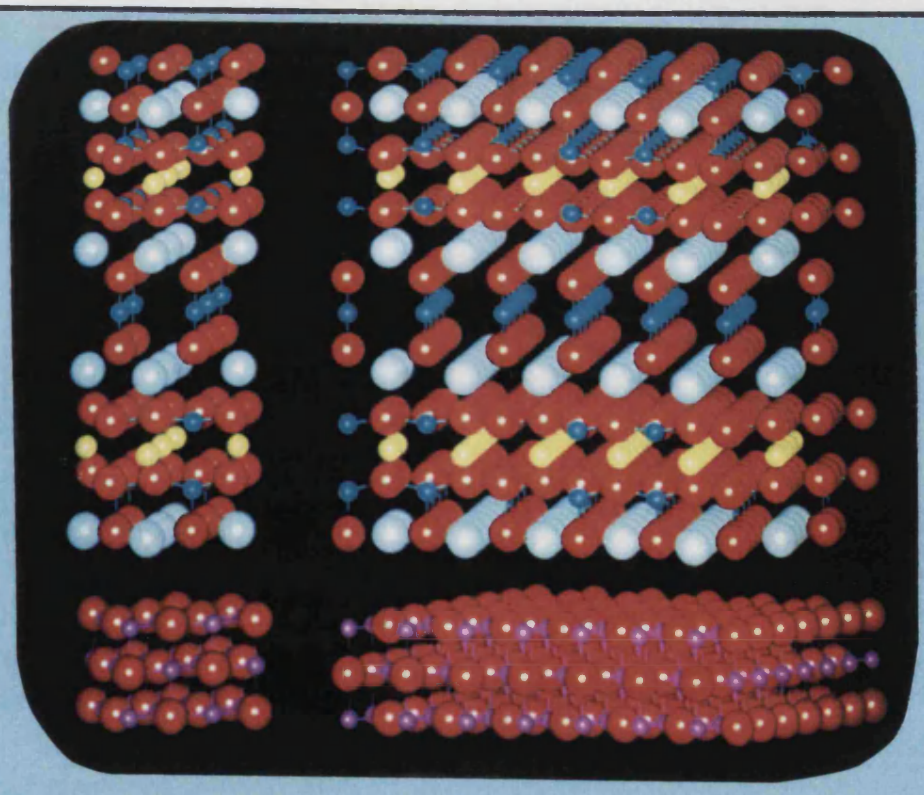

rather surprising observation since the CuO plane is the seventh plane from the interface and no other plane further than two planes from the interface appears to have deviated far from the pure relaxed $YBa_2Cu_3O_{6.5}$ (type B) structure.

Figure 7.15b shows the relaxed structure of the $\Sigma^P = 5/4\ \beta$ ($\Theta = 26.565°$) BaO (type A) interface. The stability of this interfacial configuration is -0.82 Jm^{-2} and the figure shows that the $YBa_2Cu_3O_{6.5}$ thin film has moved about 2Å away from the MgO surface. This observation strengthens the argument that the CuO plane offers the best surface with which to interface to the MgO.

The $YBa_2Cu_3O_{6.5}(001)//MgO(100)$ interfaces investigated thus far have required the $YBa_2Cu_3O_{6.5}$ thin film to be expanded by 8.05 and 7.02% for the $\Sigma^P = 1/1\alpha$ configuration for $YBa_2Cu_3O_{6.5}$ structural types A and B respectively, and compressed by 3.10 and 4.13% for the $\Sigma^P = 5/4\beta$ configuration. From the work in chapter 6, these high values of the misfit are expected to severely destabilise the interface compared to an interface of much lower misfit. The next interface considered is the $\Sigma^P = 20/17\beta$ ($\Theta = 12.529°$) CuO (type A) which has a very low associated misfit of -0.07%. Only one calculation on this interface has been performed because of the enormous size of the primitive unit cell resulting from this configuration. Following the results of chapter 6, the lower angle associated with the near coincidence site lattice was chosen on the basis that the lower angle near coincidence site lattices are more stable. Furthermore the $\Sigma^P = 20/17\beta$ ($\Theta = 40.601°$) system has not yet been observed experimentally (Hwang et al. 1990, Ravi et al. 1990) which may imply that the interface is more unstable than alternative configurations. The CuO plane was chosen to terminate the $YBa_2Cu_3O_{6.5}$ at the interface as the results of the $\Sigma^P = 1/1$ and $\Sigma^P = 5/4$ interfaces suggest termination with this plane to be more stable than terminating the $YBa_2Cu_3O_{6.5}$ with the BaO plane at the interface. Finally the MgO and $YBa_2Cu_3O_{6.5}$ structures were considered

employing the rigid ion model to further reduce the resulting primitive cell size and therefore enabling the system to be adequately accommodated by the computer resources available.

The calculated unrelaxed and relaxed interfacial energies of the Σ^P = 20/17β (Θ = 12.529°) CuO (type A) interface are -0.40 Jm^{-2} and +0.55 Jm^{-2} respectively. This is 0.39 Jm^{-2} more stable than the Σ^P = 5/4β (Θ = 26.565°) CuO (type A) interface, furthermore the stability is expected to be increased with the inclusion of ionic polarisability into the calculation. In accordance with the results of chapter 6, the calculated energies of the $YBa_2Cu_3O_{6.5}$(001)//MgO(100) interfaces are more stable for low associated misfits.

Figure 7.16a-c shows the relaxed structure of the $YBa_2Cu_3O_{6.5}$(001)//MgO(100), Σ^P = 20/17 β (Θ = 12.529°) interface with the CuO plane terminating the $YBa_2Cu_3O_{6.5}$ at the interface. Figure 7.16a shows the primitive unit cell, figure 7.16b shows the $YBa_2Cu_3O_{6.5}$ (CuO) plane on the MgO substrate with the rest of the $YBa_2Cu_3O_{6.5}$ structure removed for clarity. The oxygens from the CuO plane are coloured light brown as opposed to red. Figure 7.16c is a view of the interface looking down the c-axis of the $YBa_2Cu_3O_{6.5}$, again the oxygens of the CuO plane are coloured light brown and the rest of the $YBa_2Cu_3O_{6.5}$ removed for clarity. The relaxational behaviour has resulted in an alignment of the CuO chains with the MgO enabling excellent charge matching across the interface, indeed every copper ion is almost directly aligned with an oxygen from the MgO substrate and every oxygen from the CuO chains is aligned with a magnesium ion from the MgO substrate. Figure 7.16a shows for each unit cell one copper is directly above a magnesium ion. The removal of this unfavourable cation-cation interaction is therefore expected to further stabilise the interface. The MgO surface in figure 7.16a also appears to corrugate on relaxation. The magnesium and oxygen ions below the CuO chains are displaced, relative to the MgO substrate, by 0.15Å perpendicular towards the

Figure 7.16 Calculated relaxed $YBa_2Cu_3O_{6.5}(001)//MgO(100)$, $\Sigma^P = 20/17\beta$ ($\Theta = 12.529^o$) type A interface with CuO terminating the $YBa_2Cu_3O_{6.5}$ at the interface region. (a) Primitive unit cell of the interface. (b) View looking down at the interface with only the CuO plane shown. (c) View normal to the interface with only the CuO plane shown. For clarity the size of the balls representing the ions has been reduced. Oxygen is coloured red, barium is white, yttrium is yellow, copper, blue and magnesium purple.

A

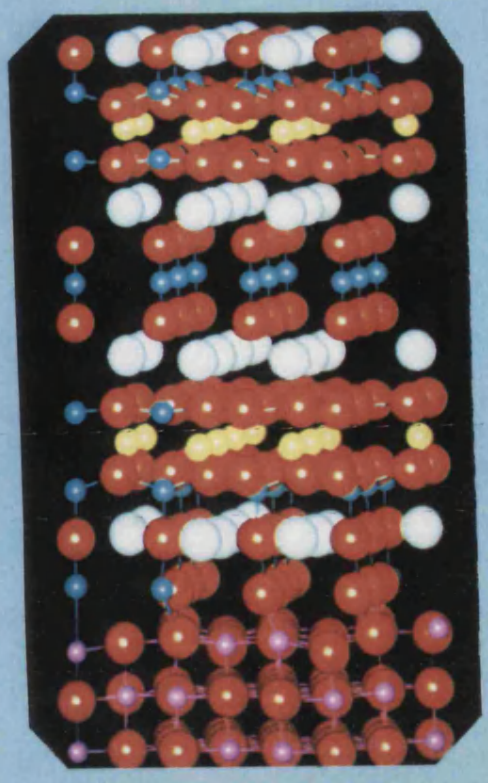

$\Sigma^{p} = 20/17\ \beta$

$(\Theta = 12.529^{o})$

CuO (Type A)

B

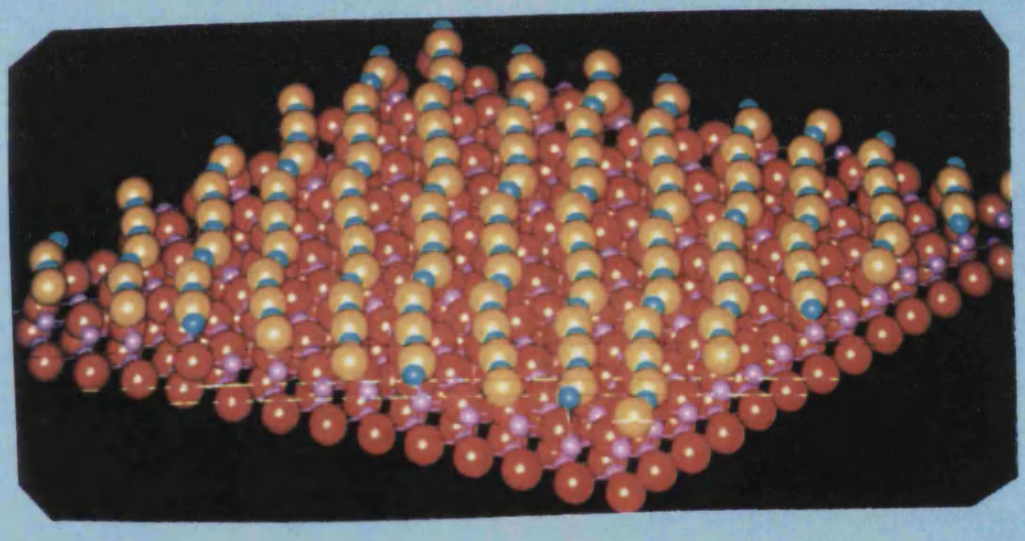

C

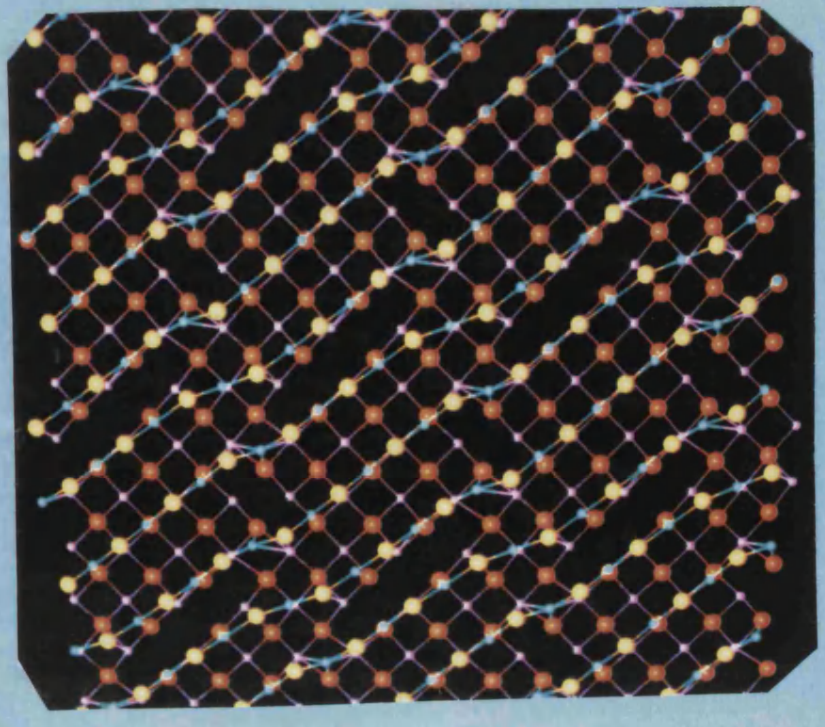

interface whereas those MgO ions not directly below a CuO chain are displaced by 0.15Å into the MgO crystal. However, the relaxation is not limited to displacements of ions perpendicular to the interface as figure 7.16c exhibits relaxation of magnesium and oxygen ions parallel to the interface. The surface MgO bond distances vary by up to 50% to enhance the charge matching across the interface region, giving the appearance of small MgO 'islands' at the top of the MgO substrate. Figure 7.17 includes a schematic representation of this behaviour showing the virtually isolated islands of MgO.

7.6 $YBa_2Cu_3O_{6.5}$(100)//MgO(100) and $YBa_2Cu_3O_{7-x}$(010)//MgO(100) Interfaces.

The $YBa_2Cu_3O_{6.5}$//MgO interfaces considered thus far have maintained the c-axis of the $YBa_2Cu_3O_{6.5}$ thin film perpendicular to the MgO(100) surface. This interface has been observed experimentally by Ramesh et al. (1990) with the 8% misfit (assuming the Σ^P = 1/1 configuration) accommodated by the formation of a periodic array of interfacial dislocations. The large misfit between the two lattices has prompted workers to investigate the $YBa_2Cu_3O_{7-x}$(100)//MgO(100) or $YBa_2Cu_3O_{7-x}$(010)//MgO(100) interfaces which are associated with a much lower misfit (Hwang et al. 1990, Ravi et al. 1990) with the c-axis of the $YBa_2Cu_3O_{6.5}$ parallel to the MgO(100) surface.

In this section we consider the $YBa_2Cu_3O_{6.5}$//MgO interface, constructed with the c-axis of the $YBa_2Cu_3O_{6.5}$ parallel to the MgO(100) surface; specifically the $YBa_2Cu_3O_{7-x}$(100)//MgO(100) and $YBa_2Cu_3O_{7-x}$(010)//MgO(100) interfaces for $YBa_2Cu_3O_{6.5}$ type A structures.

$YBa_2Cu_3O_{6.5}$ (type A) is calculated to have lattice parameters a = 3.88 Å, b = 3.87 Å, c = 24.72 Å and MgO a = b = c = 4.2Å. The interface can be constructed with the $YBa_2Cu_3O_{6.5}$ (100) on the MgO(100) surface with the near coincidence vectors being $YBa_2Cu_3O_{6.5}$[1 0 0] and MgO[6 0 0] i.e. 1 $YBa_2Cu_3O_{6.5}$ unit matches with 6 MgO units

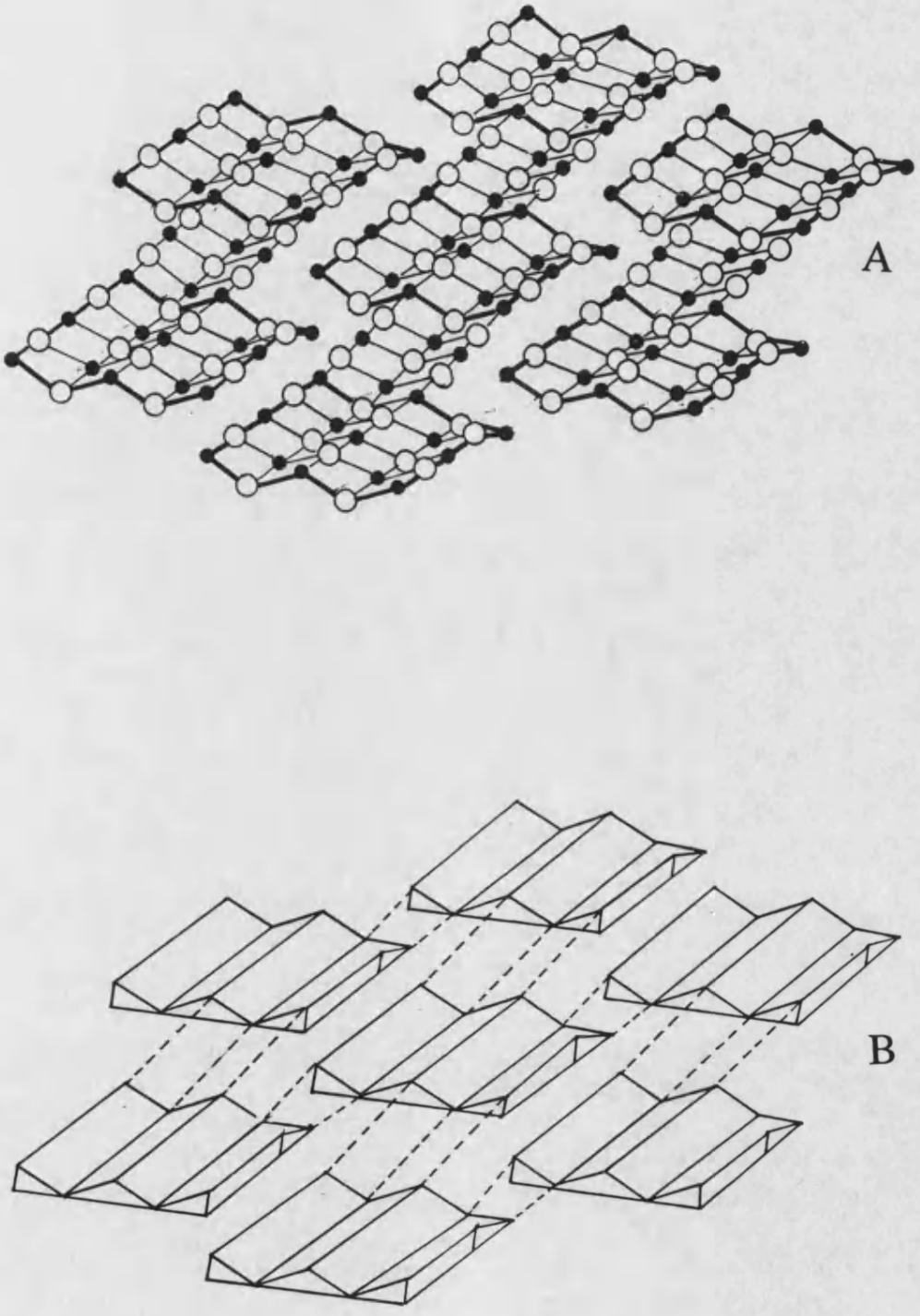

Figure 7.17 Representation of the top MgO layer terminating the MgO at the $YBa_2Cu_3O_{6.5}(001)//MgO(100)$ Σ^p = 20/17 β (Θ = 12.529°) interface. (a) shows the individual ions of the MgO plane and (b) idealised representation of the MgO "islands".

resulting in a lattice misfit of +8.05% in the $YBa_2Cu_3O_{6.5}$ a-axis ([1 0 0] direction) and +1.92% in the $YBa_2Cu_3O_{6.5}$ c-axis([0 0 1] direction). The $YBa_2Cu_3O_{6.5}$ (100) may terminate with (Cu, O) or (Y, Ba, O) ions at the interface which are hereafter referred to as the CuO plane and the YBaO plane respectively. Figure 7.18a shows diagrammatically, the $YBa_2Cu_3O_{6.5}$(100)//MgO(6 0 0) arrangement with CuO ions terminating the $YBa_2Cu_3O_{6.5}$ at the interface.

The $YBa_2Cu_3O_{6.5}$(010)//MgO(100) interface is also investigated; the construction of this interface is identical to the $YBa_2Cu_3O_{6.5}$(100)//MgO(100) interface. Figure 7.18b shows the $YBa_2Cu_3O_{6.5}$(010)//MgO(100) interface with the CuO plane terminating the $YBa_2Cu_3O_{6.5}$ at the interface. The relaxation may be initiated with the $YBa_2Cu_3O_{6.5}$ positioned with vector displacement (x,0,z) relative to the MgO(100) surface for the $YBa_2Cu_3O_{6.5}$(010)//MgO(100) interface and vector displacement (0,y,z) for the $YBa_2Cu_3O_{6.5}$(100)//MgO(100) interface. If these initial configurations lead to different interfacial structures and energies (resulting from local energy minima) this interface then presents the simulator with a formidable task. One solution is to calculate a potential energy surface (chapter 6) to elucidate the minimum unrelaxed energy and initiate the relaxation from that point. The $YBa_2Cu_3O_{6.5}$ may also be displaced perpendicular to the interface requiring several potential energy surfaces to be calculated. The calculation of a potential energy surface is very expensive computationally. Furthermore the identification of an unrelaxed global minima does not necessarily ensure the identification of a relaxed global minima and, therefore, the $YBa_2Cu_3O_{6.5}$ was positioned by inspection ensuring good charge matching i.e. optimising cation-anion interactions across the interface. A further point to note is the $YBa_2Cu_3O_{6.5}$(100) or $YBa_2Cu_3O_{6.5}$(010) thin film on the MgO(100) surface is dipolar. However because the film, for 1 $YBa_2Cu_3O_{6.5}$ layer (1 $YBa_2Cu_3O_{6.5}$ unit cell) is only 2 atomic layers thick, the relaxation is expected to reduce this dipole resulting in a stable

A

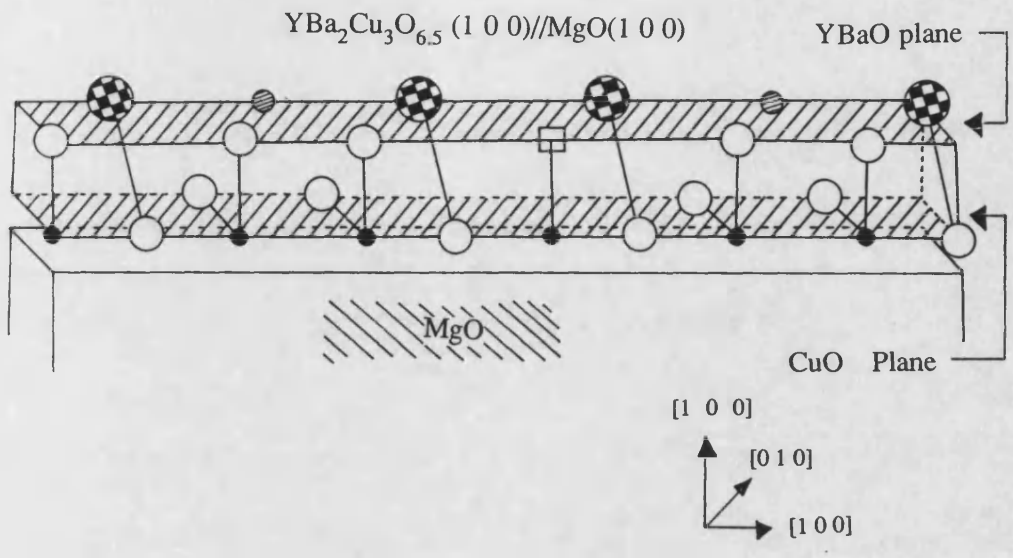

B

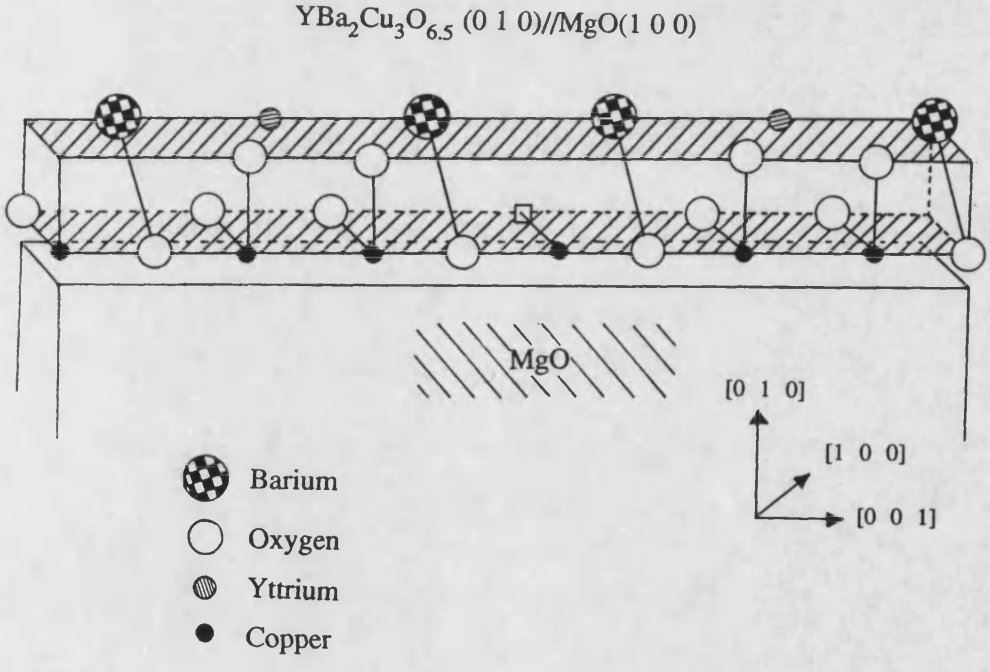

Figure 7.18 Diagrammatic representation of; (a) $YBa_2Cu_3O_{6.5}$ (100)//MgO(100). (b) $YBa_2Cu_3O_{6.5}$(010)//MgO(100). For ($YBa_2Cu_3O_{6.5}$ type A) interfaces with CuO ions terminating the $YBa_2Cu_3O_{6.5}$ at the interface region.

interface. Because of the difficulty in minimising these interfaces together with the large primitive unit cell size, a rigid ion approach was employed.

Table 7.7 shows the calculated unrelaxed and relaxed energies of the $YBa_2Cu_3O_{6.5}$(100)//MgO(100) and $YBa_2Cu_3O_{6.5}$(010)//MgO(100) interfaces with CuO or YBaO planes terminating the $YBa_2Cu_3O_{6.5}$ at the interface region, for 1 $YBa_2Cu_3O_{6.5}$ layer on the MgO surface. The calculated energies represent the energy of the interface relative to the energy of the MgO surface and the $YBa_2Cu_3O_{6.5}$(100) or $YBa_2Cu_3O_{6.5}$(010) thin films 'in space'. The relaxed energy values suggest the $YBa_2Cu_3O_{6.5}$(100)//MgO(100) interface is more stable than the $YBa_2Cu_3O_{6.5}$(010)//MgO(100) interface independent of whether the $YBa_2Cu_3O_{6.5}$ is terminated with a CuO or YBaO plane at the interface region. Furthermore the $YBa_2Cu_3O_{6.5}$(100)//MgO(100) interface is more stable when terminated with a CuO plane at the interface. The unrelaxed energy values however suggest the interfaces with a CuO plane terminating the $YBa_2Cu_3O_{6.5}$ at the interface are more stable than with a YBaO plane terminating the $YBa_2Cu_3O_{6.5}$ at the interface for both $YBa_2Cu_3O_{6.5}$(100)//MgO(100) and $YBa_2Cu_3O_{6.5}$(010)//MgO(100) with the $YBa_2Cu_3O_{6.5}$(100)//MgO(100) interface the most stable.

Figure 7.19a,b shows the unrelaxed and relaxed structures of the $YBa_2Cu_3O_{6.5}$(010)//MgO(100) interface structures with a CuO plane terminating the $YBa_2Cu_3O_{6.5}$ at the interface (figure 7.19a) and a YBaO plane terminating the $YBa_2Cu_3O_{6.5}$ at the interface (figure 7.19b). Figures 7.19a,b exhibit substantial structural modifications of the $YBa_2Cu_3O_{6.5}$ structure after relaxation with ionic displacements of up to 3.6Å! The relaxation is so substantial for the $YBa_2Cu_3O_{6.5}$(010)//MgO(100) interface with YBaO terminating the $YBa_2Cu_3O_{6.5}$ at the interface (figure 7.19b), that the relaxed $YBa_2Cu_3O_{6.5}$ structure is incomparable to the

$YBa_2Cu_3O_{6.5}$ Plane	Interfacial ions	Energy / Jm^{-2} Initial	Final
(1 0 0)	CuO	+0.56	+1.17
(1 0 0)	YBaO	-2.92	+1.03
(0 1 0)	CuO	+0.37	+0.82
(0 1 0)	YBaO	-3.12	+0.12

Table 7.7 Calculated interfacial energies of the $YBa_2Cu_3O_{6.5}$(100)//MgO(100) and $YBa_2Cu_3O_{6.5}$(010)//MgO(100) interfaces for $YBa_2Cu_3O_{6.5}$ structural type A, with CuO and YBaO ions terminating the $YBa_2Cu_3O_{6.5}$ at the interface region.

Figure 7.19 Unrelaxed and relaxed structures of the $YBa_2Cu_3O_{6.5}(010)//MgO(100)$ interface with 1 $YBa_2Cu_3O_{6.5}$ (type A) layer on the surface. (a) CuO ions terminating the $YBa_2Cu_3O_{6.5}$ at the interface region. (b) YBaO ions terminating the $YBa_2Cu_3O_{6.5}$ at the interface region. Oxygen is coloured red, barium is white, yttrium is yellow, copper, blue and magnesium purple.

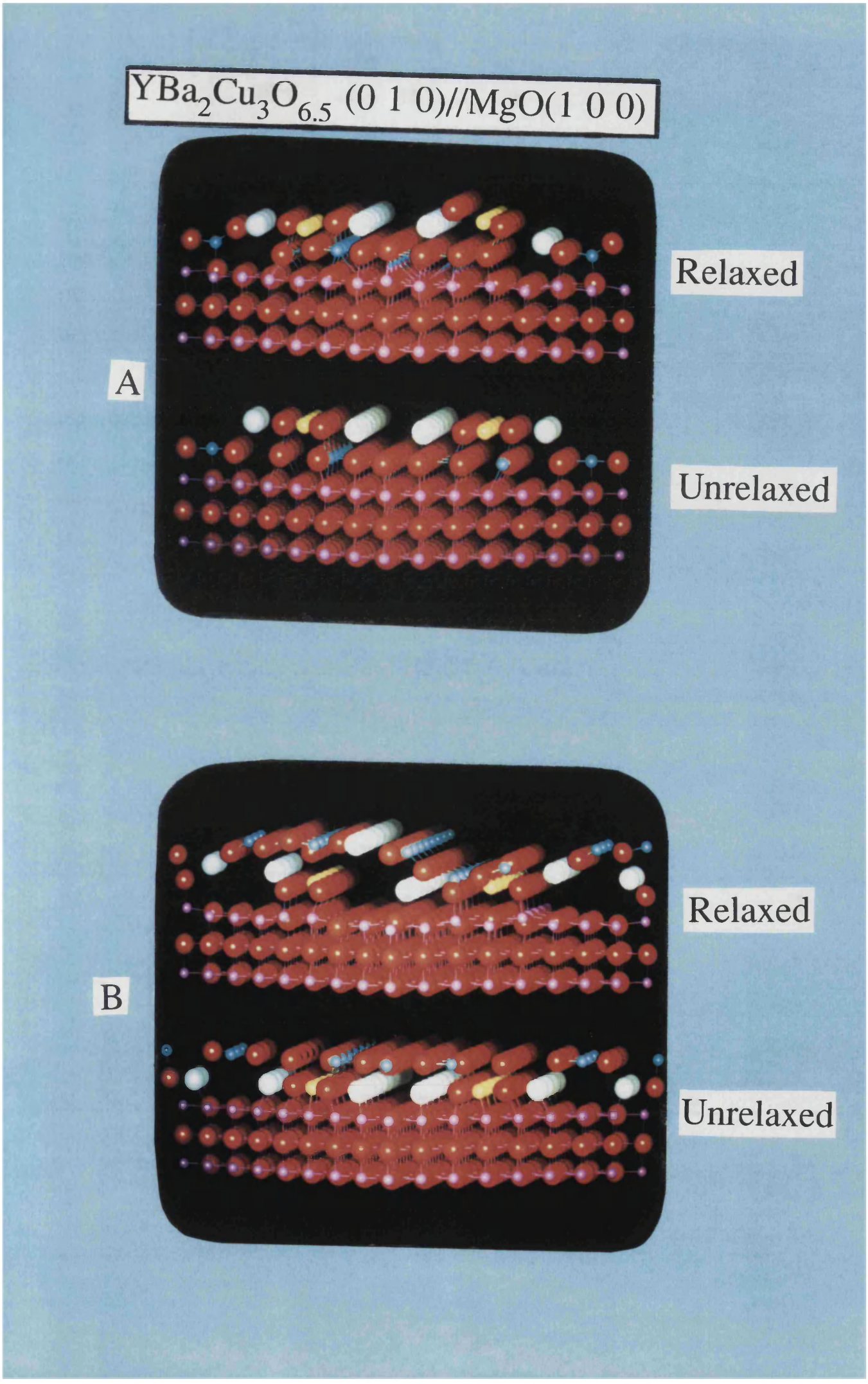
$YBa_2Cu_3O_{6.5}$ (0 1 0)//MgO(1 0 0)
A
Relaxed
Unrelaxed
B
Relaxed
Unrelaxed

original $YBa_2Cu_3O_{6.5}$ (type A) structure with the $YBa_2Cu_3O_{6.5}$ thin film exhibiting a wave-like configuration on the MgO substrate. This relaxational behaviour is reminiscent of the relaxational behaviour observed in the BaO(100)//MgO(100) interface in chapter 6, where the overlaying thin film must be compressed to accommodate the misfit and the strain energy was alleviated by the corrugation of the thin film to reduce the interfacial area. This is not however an explanation of the $YBa_2Cu_3O_{6.5}$ thin film behaviour as the $YBa_2Cu_3O_{6.5}$ was artificially expanded to accommodate the misfit. The driving force for the relaxational behaviour and substantial structural modifications is probably the reduction of the dipole moment. For the $YBa_2Cu_3O_{6.5}$(100) interface with a CuO plane at the interface, the relaxation was calculated to have reduced the dipole in the system by 85% to increase the stability of the interface. The relaxation will never remove the dipole totally. Indeed for surface relaxations a dipole moment is introduced because of the rumpling of the surface ions.

7.6.1 $YBa_2Cu_3O_{6.5}$//MgO Multilayers

In this section we examine the effect of increasing the $YBa_2Cu_3O_{6.5}$ thin film thickness on the interfacial energies and ionic relaxation of the $YBa_2Cu_3O_{6.5}$(100)//MgO(100) and $YBa_2Cu_3O_{6.5}$(010)//MgO(100) interfaces. The most stable monolayer interfaces with the $YBa_2Cu_3O_{6.5}$ c-axis parallel to the MgO(100) surface, require the $YBa_2Cu_3O_{6.5}$ to be terminated with a CuO plane at the interface region. It was therefore assumed that terminating the $YBa_2Cu_3O_{6.5}$ with a CuO plane at the interface will result in the most stable multi-layer $YBa_2Cu_3O_{6.5}$//MgO interfaces. Indeed, if the thin film is grown from a monolayer, the calculations show that the CuO will always terminate the $YBa_2Cu_3O_{6.5}$ at the interface.

The stability of the $YBa_2Cu_3O_{6.5}$(100)//MgO(100) and $YBa_2Cu_3O_{6.5}$(010)//MgO(100) interfaces with a CuO plane terminating the $YBa_2Cu_3O_{6.5}$ at the interface were

calculated for 1 to 6 $YBa_2Cu_3O_{6.5}$ layers. The energy of these interfaces relative to the energy of a pure MgO surface and an $YBa_2Cu_3O_{6.5}$ thin film 'in space' is given in figure 7.20 for the $YBa_2Cu_3O_{6.5}$(100)//MgO(100) (1 to 6 layers) and figure 7.21 for the $YBa_2Cu_3O_{6.5}$(010)//MgO(100) (1 to 5 layers) interfaces.

From figure 7.20, $YBa_2Cu_3O_{6.5}$(100) monolayer coverage of the MgO(100) substrate appears to result in the most stable interface, with increased layers the stability decreases to reach a minimum at 3 layers. Increasing the thin film thickness further results in a sharp increase in stability attaining a further maximum at 5 layers. Figure 7.21 shows that $YBa_2Cu_3O_{6.5}$(010) monolayer coverage is calculated to be the most stable interface, with increased layers the interfacial stability decreases steadily with 5 $YBa_2Cu_3O_{6.5}$ layers the most unstable. This behaviour is expected because the thin film has a dipole associated with it which will destabilise the interface. For one $YBa_2Cu_3O_{6.5}$ layer the relaxational freedom of the ions enable this dipole to be much reduced, however for further layers the relaxation is inhibited by the further addition of $YBa_2Cu_3O_{6.5}$ layers providing a constraint to the relaxation.

The calculated interfacial energies of these interfaces are relative to the relaxed energy of the $YBa_2Cu_3O_{6.5}$(100) or $YBa_2Cu_3O_{6.5}$(010) thin film 'in space'. The relaxed structural configuration and energy of this hypothetical thin film 'in space' is heavily dependent on the initial (unrelaxed starting configuration) $YBa_2Cu_3O_{6.5}$ structure with many 'local' relaxed minima (with energies varying by as much as 1%) identified with slightly modified unrelaxed starting configurations. The question of which local minima should be employed to ascertain the energy of the interface then arises as the resulting interfacial energy may vary by up to 50% depending on which 'local' energy value of the $YBa_2Cu_3O_{6.5}$ thin film is employed. Furthermore the initial configuration of the interface may also lead to the identification of many local minima. The resulting

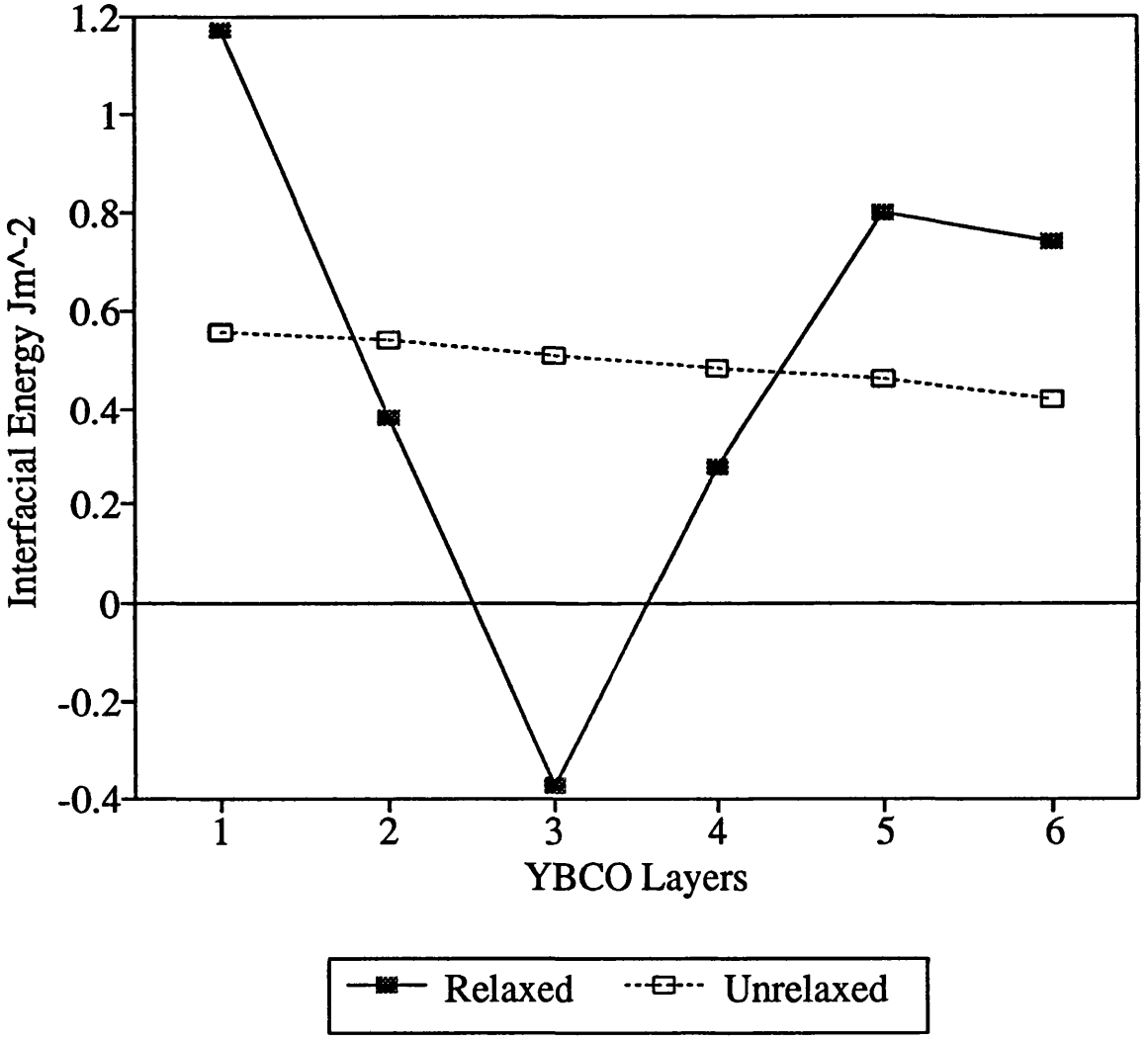

Figure 7.20 Variation of $YBa_2Cu_3O_{6.5}$(100)//MgO(100) ($YBa_2Cu_3O_{6.5}$ type A) interface energy as a function of $YBa_2Cu_3O_{6.5}$ thin film thickness with CuO ions terminating the $YBa_2Cu_3O_{6.5}$ at the interface region.

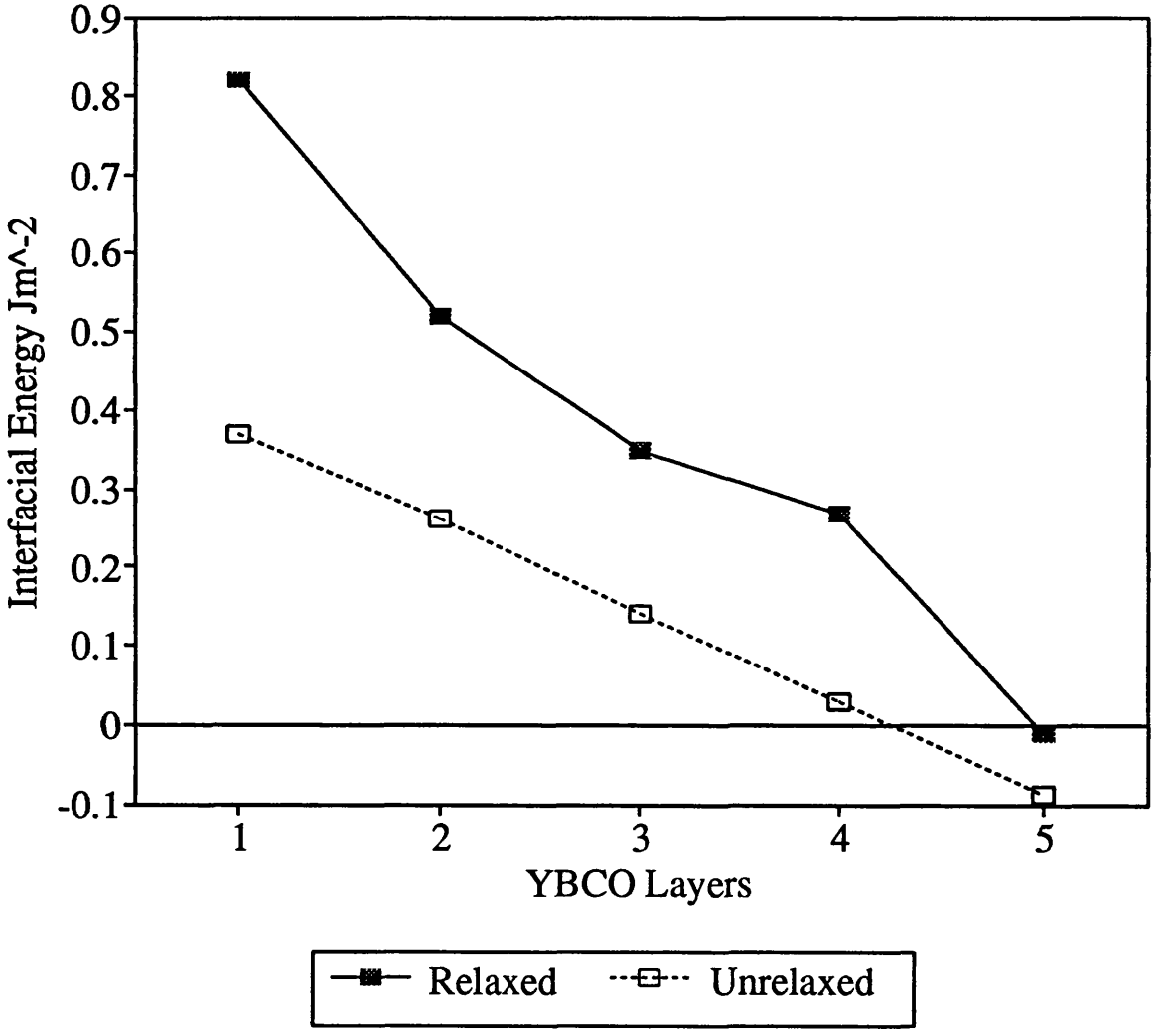

Figure 7.21 Variation of $YBa_2Cu_3O_{6.5}$(010)//MgO(100) ($YBa_2Cu_3O_{6.5}$ type A) interface energy as a function of $YBa_2Cu_3O_{6.5}$ thin film thickness with CuO ions terminating the $YBa_2Cu_3O_{6.5}$ at the interface region.

interfacial energies must therefore be treated with some caution.

Figure 7.22a,b shows the unrelaxed (7.22a) and relaxed (7.22b) structures of the $YBa_2Cu_3O_{6.5}$(100)//MgO(100) interfaces with 3 $YBa_2Cu_3O_{6.5}$ layers. The copper Cu(1) and oxygen O(4) ions have migrated from the top CuO(100) plane to the surface YBaO plane leaving channels through the $YBa_2Cu_3O_{6.5}$ in the [0 1 0] direction. Figure 7.22c,d shows the unrelaxed (7.22c) and relaxed (7.22d) structures of the $YBa_2Cu_3O_{6.5}$(010)//MgO(100) interfaces with 5 $YBa_2Cu_3O_{6.5}$ layers. The relaxational behaviour of this interface has resulted in the $YBa_2Cu_3O_{6.5}$ surface appearing wave-like.

7.7 Summary

The major objective of this chapter is not to characterise the $YBa_2Cu_3O_{6.5}$//MgO interfaces explicitly, but to ascertain the factors conducive to interfacial stability and to develop a method which will enable a complex interface to be constructed and examined theoretically. The $YBa_2Cu_3O_{6.5}$//MgO system was chosen to be a model system representative of a complex heteroepitaxial ceramic interface in an attempt to elucidate factors, conducive to the interfacial stability, which may not have been identified by examining the more simple systems considered in the previous chapters.

The near coincidence site lattice theory was employed to investigate the $YBa_2Cu_3O_{6.5}$(001)//MgO(100) interfaces and has enabled the interfacial stability of the various interfaces, observed experimentally (Ravi et al. 1990, Hwang et al. 1990), to be calculated. Furthermore the calculations have shown the $YBa_2Cu_3O_{6.5}$(001)//MgO(100) interface to exhibit maximum stability if the $YBa_2Cu_3O_{6.5}$ is terminated with the CuO plane at the interface. The $YBa_2Cu_3O_{6.5}$(001)//MgO(100) interfacial stabilities are calculated to increase with decreasing misfit in accordance with the results in chapter 6, with the Σ^P = 20/17 β (Θ = 12.529°) with the lowest associated misfit of -0.07%

Figure 7.22 (a, b) Unrelaxed and relaxed structures of the $YBa_2Cu_3O_{6.5}$(100)//MgO(100) interface with 3 $YBa_2Cu_3O_{6.5}$ (type A) layers on the surface and CuO ions terminating the $YBa_2Cu_3O_{6.5}$ at the interface region. (c, d) Unrelaxed and relaxed structures of the $YBa_2Cu_3O_{6.5}$(010)//MgO(100) interface with 5 $YBa_2Cu_3O_{6.5}$ (type A) layers on the surface and CuO ions terminating the $YBa_2Cu_3O_{6.5}$ at the interface region. Oxygen is coloured red, barium is white, yttrium is yellow, copper, blue and magnesium purple.

$YBa_2Cu_3O_{6.5}$ (1 0 0)//MgO(1 0 0)

A

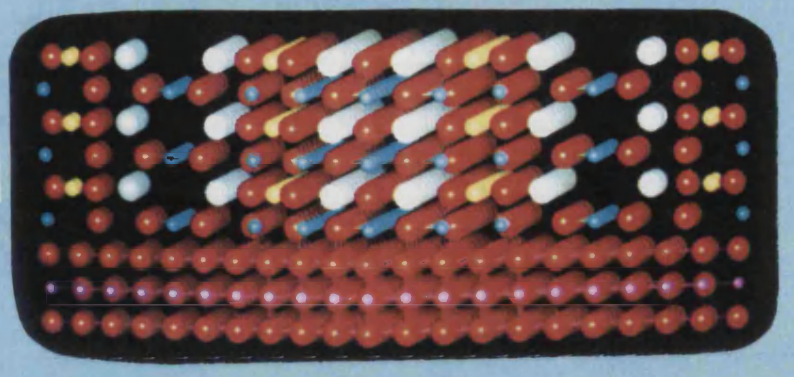

Unrelaxed Structure

3 Layers

Relaxed Structure

B

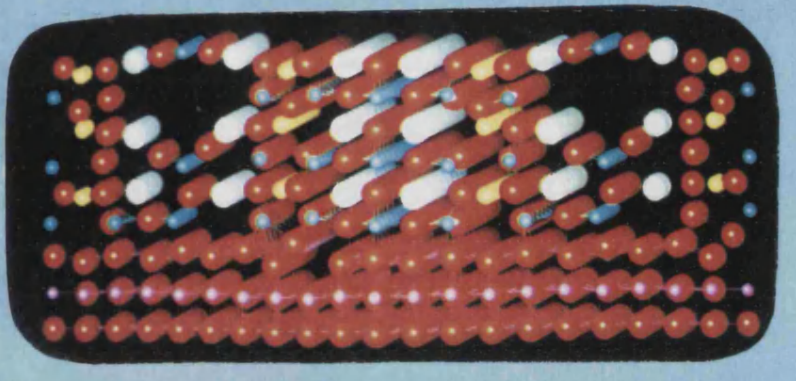

$YBa_2Cu_3O_{6.5}$ (0 1 0)//MgO(1 0 0)

C

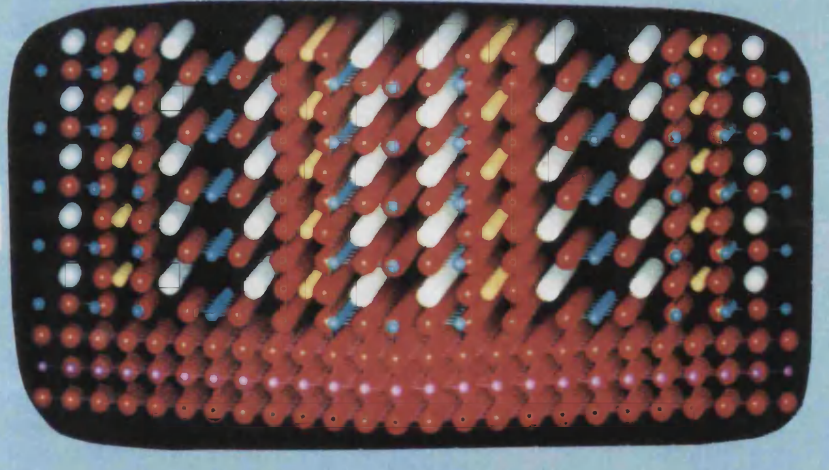

Unrelaxed Structure

5 Layers

Relaxed Structure

D

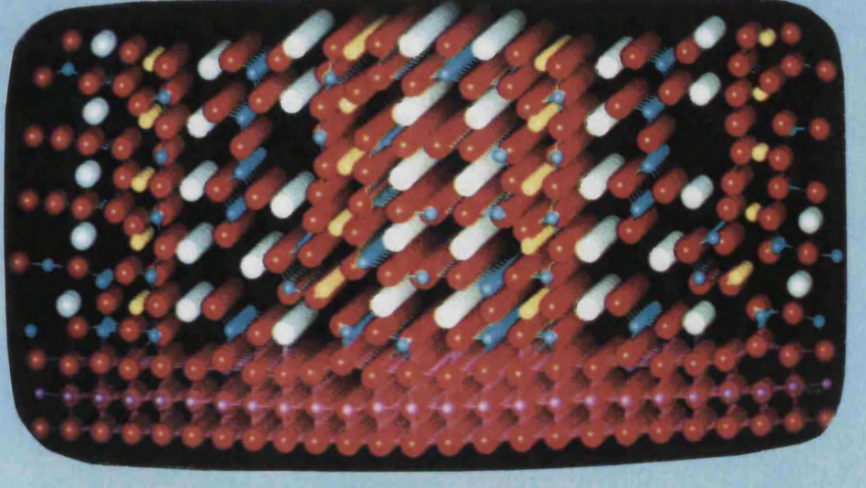

exhibiting the highest interfacial stability of +0.55 Jm^{-2}.

The ionic relaxation of the $YBa_2Cu_3O_{6.5}$ when interfaced to the MgO for the $YBa_2Cu_3O_{6.5}$(001)//MgO(100) interfaces show deviations from the perfect $YBa_2Cu_3O_{6.5}$ crystal structure with bond length modifications of up to 10% with serious implications to the superconducting properties of the material including T_c (Miceli et al. 1988, Islam and Baetzold 1989, Zhang and Catlow 1992). However experimental work by Ramesh et al. (1990) suggests thin film growth beyond the first unit cell (12Å) occurs without any influence of the lattice mismatch.

The reduction in symmetry for the more complex oxide $YBa_2Cu_3O_{6.5}$, compared to BaO, results in more surfaces which may be interfaced to the substrate material. $YBa_2Cu_3O_{6.5}$(100) and $YBa_2Cu_3O_{6.5}$(010) surfaces provide alternative faces with which to interface to a substrate and have been observed experimentally. These interfaces can be investigated theoretically. However a dipole, normal to the interface, is associated with these interfaces. The resulting relaxed interfacial structures exhibit substantial modification of the $YBa_2Cu_3O_{6.5}$ thin film as the relaxation reduces the dipole by up to 85%. The effect of multiple $YBa_2Cu_3O_{6.5}$ layers inhibits this relaxation and as a consequence the interfacial stability is reduced as a result of the dipole (see chapter 4).

The initial, unrelaxed, interfacial configuration was found to be critical to the relaxed structural configuration, with respect to both the interfacial stability and the ionic relaxation, with many local minima located with only slight modifications in the initial structural configuration. These local minima will inevitably arise when one considers these more complex systems and will increase the difficulty in the interpretation of the calculated results. A consolation however is the local minima may indeed occur naturally.

Chapter 8

The Metal - Oxide Interface

8.1 Introduction

The work presented in this thesis thus far, has been concerned with interfaces between two oxide materials. In this final chapter we consider a theoretical treatment of an interface between a metal and an oxide. Indeed the metal - oxide interface is probably more technologically important than the interface between two oxide materials. For example in catalysis, a metal may be supported by a high surface area oxide and the catalytic properties influenced by the so-called strong metal support interaction. Corrosion of metals depends on the stability of the growing oxide film on the metal substrate and the diffusion of ions along the metal - oxide interface. The metal - oxide interface also has extensive applications in the electronics and semiconductor industries. However the theoretical treatment of metal - oxide interfaces has inevitably lagged behind that of interfaces within a single class of materials such as oxides. In this thesis we have developed, at an atomistic level, models which predict the structure and properties of oxide interfaces between two dissimilar oxides and have elucidated the factors that determine the interfacial stability. Such a treatment of the metal - oxide interfaces would be of great value. However modelling these interfaces provides the simulator with a formidable task. The models that describe the interactions in either the metal or the oxide are fundamentally different from and inappropriate to the other material. In an ionic material, the potential model consists of a Coulombic contribution with repulsive short range potentials and the shell model to describe the ionic polarisability. In contrast, metals can be described by a simple pair potential and a volume dependent term. However, the interaction between the two materials has not been understood well enough to derive simple potentials which include the essential physics of the bonding across the metal - oxide interface.

In this thesis we employ the image charge theory to describe the long range interactions across the metal - oxide interface. To ascertain the position of the image plane, the BaO//MgO interface is considered and the image plane position adjusted until the Coulombic interactions are equal to the image terms. The advantage of this approach is that the image charge theory can be compared directly with atomistic simulation. Image theory is then employed to describe the long range attractive interaction between a metal and an oxide material. Modifications to the image interactions are introduced into the calculations to help screen the image terms. The Ag//MgO and Au//MgO interfaces are then modelled using the modified image terms. The approach is tested by examining the metal-oxide interfaces and comparing with the experimental metal-oxide interface contact angle.

8.1.1 Contact Angles and the Wetting by Liquid Metals

The driving force for formation of a metal-oxide interface is the yield in energy when intimate contact is established between the metal and the oxide surface. The simplest description of the physical interaction between a metal and a oxide is the work of adhesion W_{ad}. Specifically, when clean, defect free surfaces are brought together, energy is released in accordance with the Dupré equation:

$$W_{ad} = \sigma_o + \sigma_m - \sigma_{mo} \qquad (8.1)$$

where σ_o and σ_m are the surface energies of the oxide and metal respectively and σ_{mo} represents the interfacial energy. From the interfacial energies it is possible to calculate a wetting angle of the metal on the oxide.

The wetting angle (Θ) is given by;

$$\cos\Theta = (\sigma_o - \sigma_{mo})/\sigma_m \qquad (8.2)$$

The measurement of the contact angle between the oxide and the metal can be performed experimentally and therefore useful comparisons may be made with the calculated contact angles.

First however a model is required to simulate the interface; A complete quantum mechanical description would be appropriate, however the computer time required is extensive. Instead, the fundamental characteristics of the metal - oxide interfaces are examined to identify the dominant physical processes that contribute to the adhesion.

One of the most striking features of the metal - oxide interface is the dielectric discontinuity between the two materials; Whilst the metal has an almost infinite dielectric constant, the typical dielectric constant of the oxide is around 10. Furthermore, the oxide material may have a high degree of ionic bonding and can therefore support charged defects and impurities. A leading attractive interaction between the metal and the oxide can therefore be described in terms of classical image interactions.

8.2 Image Theory

If we consider an interface between two materials of dielectric constants ϵ_1 and ϵ_2, then the presence of a charge, Q, introduces an additional term in the interfacial energy;

$$E_{im} = \left(\frac{Q^2}{4\epsilon_1 r} \right) \left(\frac{\epsilon_1 - \epsilon_2}{\epsilon_1 + \epsilon_2} \right) \tag{8.3}$$

Where r is the distance from the boundary or image plane. From equation (8.3) we can see that if region 2 is a metal ($\epsilon_2 = \infty$) then the additional term lowers the boundary energy and is attractive. If we consider a free surface ($\epsilon_2 = 1$), then the additional term is repulsive and destabilises the surface.

If we consider an ionic or partly ionic material being brought up to a metal surface, there are two sources of image interaction. Firstly, the ionic charges of the ionic material will gain stabilisation through the proximity of the metal. Secondly, there will be additional attraction if charged defects or impurities are near the ionic surface. This phenomena was observed in the calculations presented in chapter 4, where the image charge contribution enhanced the interfacial stability when charged defects approach the interface from the material with the lower dielectric constant.

At large distances, the image interaction gives a good representation of the attractive interaction. Indeed the description is accurate down to about 2Å although the position of the image plane presents problems (Finnis 1992). In the next section, the BaO//MgO interface is employed to identify the position of the image plane.

8.3 Image Plane Position

To ascertain the position of the image plane, the BaO//MgO interface was considered with the Coulombic contribution to the interfacial energy across the interface replaced by image terms. (The introduction of image interactions was facilitated by a modification of the MIDAS codes). The position of the image plane can thus be identified when the image terms are exactly equal to the Coulombic contribution.

For these calculations the BaO is considered only as a dielectric continuum and therefore the short range potentials within the BaO are neglected (the short range repulsive interactions between the BaO and MgO ions across the interface are included to balance the image interactions). The Coulombic contribution to the interfacial energy is obtained by positioning an image plane above the MgO surface and calculating the interactions of the magnesium and oxygen ions with their images. The position of the image plane can then be adjusted until the image terms exactly match the Coulombic contribution from the full atomistic simulation. Two locations of the image plane were considered. The plane was placed, first, equidistant from the termination of the two materials at the interface and second on the first plane of BaO ions (figure 8.1). Table 8.1 shows the unrelaxed and relaxed energies of the image calculations compared to the standard calculation with the Coulombic terms describing the contribution to the interfacial energy across the interface. The calculations were performed for two interfacial configurations, (i) with the BaO over the magnesium sublattice of the MgO and (ii) with the BaO over the oxygen sublattice of the MgO. 'Imagehalf' is with the image plane half way between the surfaces of the MgO and the BaO at the interface and 'imagetop' is with the image plane located on the first plane of the BaO block (figure 8.1).

The energies clearly indicate that the image terms provide the best representation of the

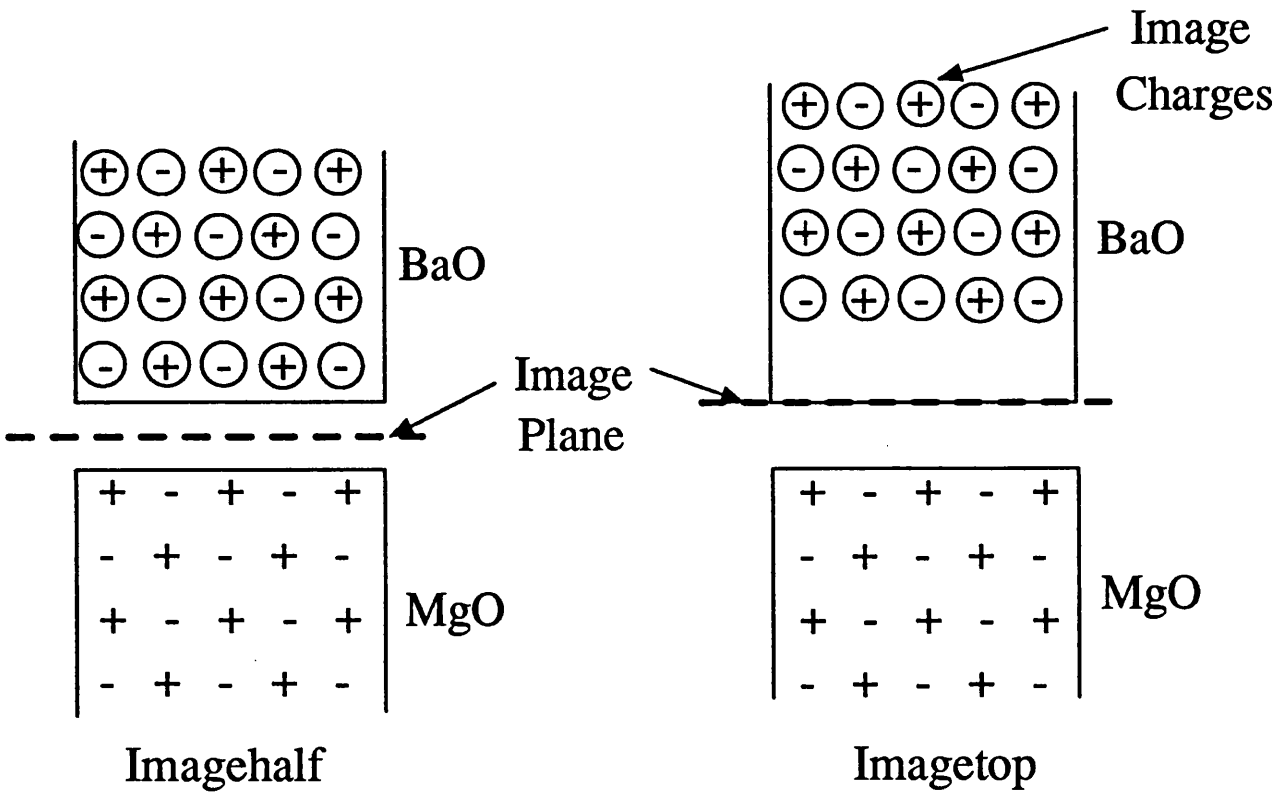

Figure 8.1 Diagrammatic representation of the location of the image plane.

Table 8.1 Comparison between the unrelaxed and relaxed interface energies using the classical image approach and a full atomistic calculation. The BaO is considered to be a dielectric continuum.

	Over Magnesium Sublattice		Over Oxygen Sublattice	
	Unrelaxed	Relaxed	Unrelaxed	Relaxed
Full Atomistic	-242.06	-247.66	-243.93	-247.81
imagehalf	-246.69	----	-245.50	----
Imagetop	-242.24	-247.83	-244.15	-247.83

Coulombic interactions when the image plane is located at the 'imagetop' position and give an excellent representation of the Coulombic terms. Positioning of the image plane at the 'imagehalf' position results in a poor representation of the Coulombic interactions with the interface energy before minimisation incorrectly calculated by up to 4.7eV (for the BaO above the magnesium sublattice of the MgO substrate). Furthermore the minimisation was unsuccessful. This is because the repulsive forces are much weaker than the image terms with the image plane in the 'imagehalf' position and are therefore unable to balance the strong image interactions. The image terms therefore dominate the relaxation and the BaO block is forced into the surface of the MgO crystal!

A major limitation of employing the method of images to replace the Coulombic interaction can be seen when one considers the detailed atomic relaxation of the ions at the interface region. For the 'full atomistic' calculation, after relaxation, the magnesium ions are displaced towards the oxygens of the BaO lattice at the interface region, with the driving force for this behaviour being the Coulombic interaction between the positive charge on the magnesium and the negative charge on the oxygen. When the Coulombic terms are replaced by image interactions, there is no such association between the magnesium ions and the oxygen ions of the BaO lattice and therefore the relaxation is driven by the repulsive short range interaction between these two ions and subsequently the magnesium ions are displaced away from the oxygen ions of the BaO lattice. This argument can be applied to all such ionic relaxations across the interface region, where, although the interfacial energy is very similar, the ionic relaxation at the interface is very different. The good correlation between the full atomistic and the 'image' calculations may therefore be fortuitous and therefore further systems must be considered to ascertain whether this image plane position is reproducible for alternative systems.

The next system considered was the BaO//$SrTiO_3$ interface. Again for this interface, the BaO was considered to be a dielectric discontinuity and the image charges induced into the BaO from the $SrTiO_3$ were employed to describe the long range attractive interactions across the interface. With the image plane located at the 'imagehalf' position, the image interactions again proved too attractive to be balanced by the repulsive forces. However, with the image plane located at the 'imagetop' position, the image contribution gives an excellent representation of the Coulombic interactions with a discrepancy of only 0.2eV or 0.03% after relaxation.

A further problem one must address is whether the image interaction is attractive or repulsive. For BaO on MgO, as BaO has the higher dielectric constant, the interaction (equation 8.1) is attractive, similarly for BaO on $SrTiO_3$ the image interaction is attractive. However if one considers MgO on BaO where the images from BaO are induced into the MgO lattice, the image interaction is repulsive and should destabilise the interface. A similar calculation was therefore performed where the MgO is considered to be the dielectric continuum and the images from the BaO are employed to describe the long range contribution to the interfacial energy and the interfacial energies are given in table 8.2. The results from this table indicates that the image interaction remains a good representation of the Coulombic terms however from equation 8.1 the image interactions should destabilise the interface as the dielectric constant of BaO is greater than MgO. On closer inspection, the interface energies are all higher (more unstable) with the image contribution than with the normal Coulombic contribution, both before and after relaxation. Inspection of the detailed atomic structures of the interface reveals that the distance between the BaO and MgO has increased substantially from 2.4Å to 5.0Å for both interfaces whether BaO is over the magnesium or oxygen sublattice of the MgO lattice. Furthermore at this distance, the image interaction is

Table 8.2 Comparison between the unrelaxed and relaxed interface energies using the classical image approach and a full atomistic calculation. The MgO is considered to be a dielectric continuum.

	Over Magnesium Sublattice		Over Oxygen Sublattice	
	Unrelaxed	Relaxed	Unrelaxed	Relaxed
Full Atomistic	-309.1	-312.4	-308.7	-312.5
Imagetop	-308.9	-312.1	-308.6	-312.0

actually slightly attractive. This can be explained by considering the sum of the contribution of the four neighbouring image charges with the ion in question is greater that the repulsive interaction between the ion and its own image (figure 8.2). The slightly attractive image terms therefore prevents the two crystals from dissociating from each other and balances the short range repulsive terms which are also very small at this distance. The primary reason for addressing image interactions is their application to the metal - oxide interaction. As the metal will always have a higher dielectric constant than the support oxide material, the image interaction will always be attractive. However the above argument suggests that if the metal is further than a certain distance away from the oxide surface, the sum of the image contributions from neighbouring ions may indeed be repulsive, although this distance will obviously be dependent on the structure of the oxide material.

8.4 The Metal - Metal Oxide Interface

In this section we employ the image charge interactions to describe the long range attractive interactions between the metal and the metal oxide. The success of the image terms in correctly representing the Coulombic contribution to the interfacial energy suggests that the position of the image plane should be located at the bottom plane of the metal ions with the interactions between the ions of the oxide material and the induced image charges in the metal images of the oxide material providing the leading attractive terms in the interfacial energy.

The first metal - oxide interface considered is the Ag(100)//MgO(100). The silver is considered to be a dielectric continuum and therefore interatomic potentials for the silver are neglected. The short range repulsive interactions across the interface are derived by Harding at AEA Harwell (1991) and are given in table 8.3. The next question to address

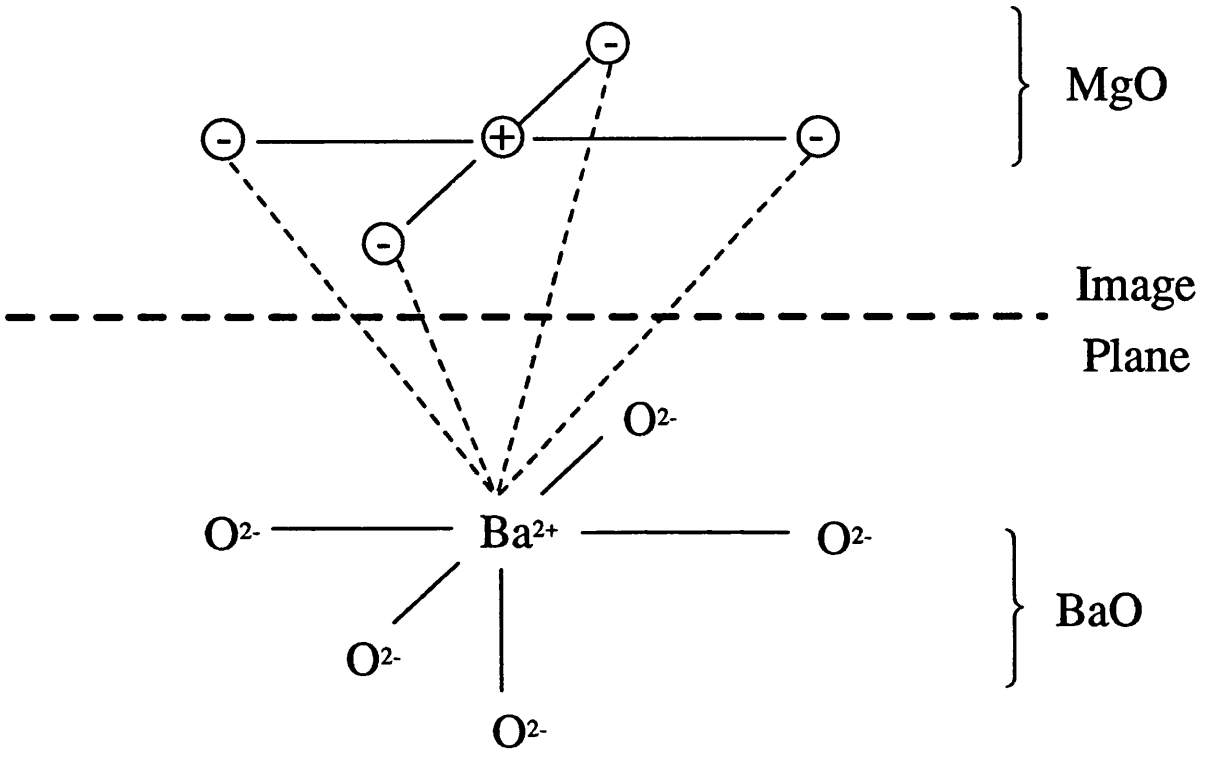

Figure 8.2 Diagrammatic representation of the interaction of barium with images from adjacent oxygen ions.

Table 8.3 Short range repulsive interatomic potential parameters fitted to a Buckingham form (Harding 1991).

Species	A(eV)	ρ(Å)	C(eV/Å^6)
Ag(0) - Mg(2+)	1045.7	0.33952	0.00
Ag(0) - O(2-)	1419.3	0.34788	0.00

$$\Phi(r_{ij}) = A\exp[(-|r_i-r_j|)/\rho] - Cr^{-6}$$

is the epitaxial configuration of the silver on the MgO. Because of the near equality of the lattice vectors of MgO and silver (4.2 and 4.085Å respectively), the silver ions can be positioned either over the oxygen or magnesium sublattice of the MgO substrate or alternatively at the interstitial positions.

The relaxation of the silver - MgO interface was unsuccessful as the repulsive interactions between the silver and the MgO were much stronger than the image interactions and the silver ions were displaced from the MgO surface until the interfacial distance was greater than the short range potential cutoff. This result suggests that the location of the image plane is wrong and our initial assumption that the image plane position can be transferred from the image calculations performed on the BaO//MgO interface is incorrect. A further calculation was performed with the image plane located at the 'imagehalf' position. In this case the image interactions were much too strong to balance the repulsive interactions and the silver ions collapsed into the MgO surface. It may be possible to identify an image plane position where the very delicate balance between the short range repulsive forces and the image forces are balanced. However we now turn to the limitations of the classical image theory in an attempt to elucidate whether the image interactions can be modified to reduce this fine balance and produce a more robust method for investigating metal - oxide interfaces.

8.4.1 Limitations of the Classical Image Charge Theory

From classical image theory, a charge q a distance z_o from the surface of the metal induces a charge distribution of the form

$$\rho(r) = z_o q/2\pi(z_o^2 + r^2)^{3/2} \qquad (8.4)$$

on the metal surface. Here r is the distance parallel to the surface. Such a charge distribution results in a potential of the form

$$V(r,z) = -q/(r^2 + (z_o + z)^2)^{1/2} \qquad (8.5)$$

at a site (r,z).

This description is accurate for large values of z_o, however as the charge approaches near to the metal surface (small z_o), the classical image potential diverges to $-\infty$. This cannot be true as the potential energy inside a conductor V_o is finite and the potential energy function should saturate to this value, as the charge passes into the metal (figure 8.3). The value of V_o is given by Lang and Kohn (1970) as

$$V_o = E_f + W \qquad (8.6)$$

Where E_f is the Fermi energy of the metal and W is the work function of the specific metal surface.

Recent work by Duffy, Harding and Stoneham (1992) on the modelling of metal/oxide interfaces addresses this problem and they remove the divergence in the classical image potential by suppressing fluctuations of the induced charge density which have wavelengths longer than the Fermi wavevector. The potential V(r,z) at a site (r,z) of a charge distribution, induced by a charge q at $(z_o,0)$, with all Fourier components with wave vector greater than the Fermi wavevector (K_f), in the direction parallel to the interface, eliminated is given by Duffy et al. (1992) as;

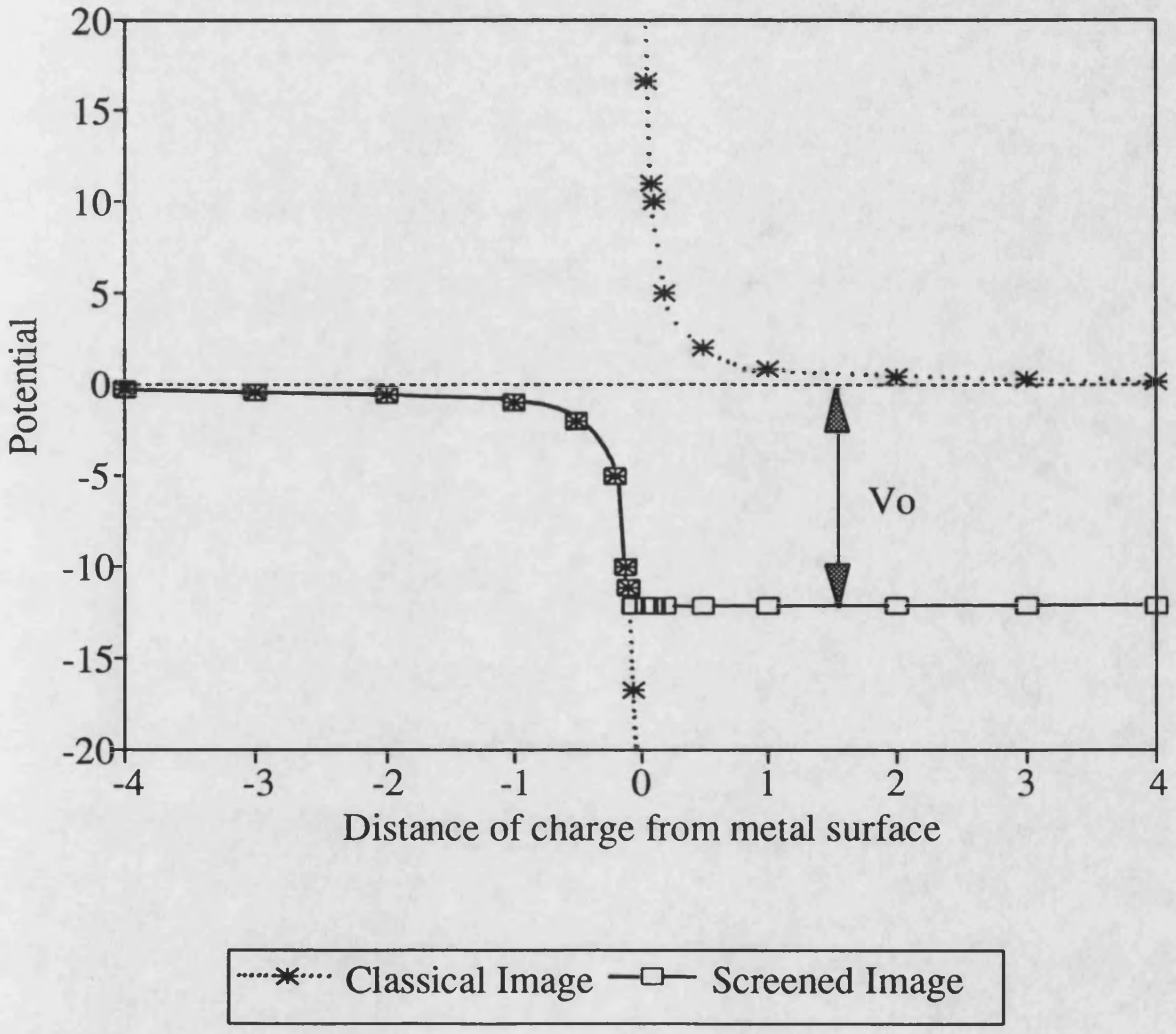

Figure 8.3 Comparison between the classical image potential and the screened image potential.

$$V(r,z) = -q/(r^2 + z'^2)^{1/2} + (q/2\pi)\int_0^{2\pi} \frac{\{\exp[-K_f(z' + ir\cos\phi)]\}}{[z' + ir\cos\phi]}\, d\phi \qquad (8.4)$$

Here $z' = z + z_o$ and z_o is the perpendicular distance between the charge and interface. This expression reduces to the classical form for large K_f. This integral reduces the magnitude of the potential and acts as an effective screening term. In addition it eliminates the divergence of the $r = 0$, $z' = 0$ case.

The potential for the case where short wavelength fluctuations are eliminated in both the perpendicular and parallel directions has also been calculated. The resulting potential takes the form of a 3-dimensional integral which cannot be written in the form of the classical result with a correction, however the integral can be calculated numerically (Duffy et al. 1992).

In this thesis we adopt a much simpler method to screen the image interaction such that the potential does not diverge when a charge approaches very close to a metal surface. To achieve this the image plane is never allowed to approach so close to the MgO such that the image interaction is greater than V_o (figure 8.3). This effectively introduces a cutoff into the image interaction which screen the image interactions.

The minimum distance that image plane can approach the MgO substrate can be calculated for the Ag(100)//MgO(100) interface as follows from equation 8.4. The Fermi energy for silver is 5.48 eV and the work function for the (100) surface of silver is 4.64 eV (Kittel 1989). The inner potential of the metal (V_o) is then 10.12 eV and from equation 8.3, the minimum distance the image plane must be from the top of the MgO

surface is calculated to be 0.7114 Å.

From the work by Duffy et. al. (1992) a further complication arises; the initial calculations of the short range interactions were performed within the electron gas approximation. This was found by Duffy et. al. to be unsatisfactory as the potential was too repulsive. The reason for this failure is discussed by Wood and Pyper (1981). The electron gas method, since it only uses the density, includes certain interactions between orbitals which are forbidden by the symmetry of the wavefunctions. More accurate Dirac-Fock methods developed by Wood and Pyper (1986) were therefore employed by Duffy et. al. For the work in this thesis we have also employed these more accurate short range interactions.

In the next section we employ the modified image interaction (with the cutoff to screen the image interactions) and also the more accurate short range interactions which were derived by Duffy et. al. (1992) for silver and gold, to investigate the Ag//MgO and Au//MgO interfaces. The relevant potential parameters are given in table 8.4.

8.4.2 The Ag(1 0 0)//MgO(1 0 0) interface

For the Ag(1 0 0)//MgO(1 0 0) interface, three configurations can be envisaged. Firstly with the silver over the magnesium ions of the MgO, second with the silver over the oxygen ions, and third with the silver accommodating interstitial positions between the oxygen and magnesium ions. The relaxed structures and energies of the Ag(1 0 0)//MgO(1 0 0) interfaces were calculated for all three positions for a number of different initial interfacial separations. The results of these calculations are summarised in table 8.5. The result of the silver accommodating interstitial positions is not given as the relaxation resulted in a migration of the silver ions to positions above the oxygen

Table 8.4 Short range interatomic potential parameters derived using Dirac-Fock methods by Harding (1991).

Species	A(eV)	ρ(Å)	C(eV/Å^6)
Ag(0) - O(2-)	21612.51	0.23996	375.73
Au(0) - O(2-)	9030.42	0.2789	444.28
Ag(0) - Mg(2+)	553.465	0.39413	0.00
Au(0) - Mg(2+)	2026.92	0.31769	0.00

$\Phi(r_{ij}) = A\exp[(-|r_i-r_j|)/\rho] - Cr^{-6}$

$V_o(Ag) = 10.12$ eV

$V_o(Au) = 10.12$ eV

Table 8.5 Calculated work of adhesion, interfacial separation and contact angles for the Ag(1 0 0)//MgO(1 0 0) and Au(1 0 0)//MgO(1 0 0) interfaces.

Ag(1 0 0)//MgO(1 0 0)

	Work of Adhesion /Jm^{-2}	Metal-Oxide Separation / Å	Contact Angle
Over Oxygen	2.1	2.20	126°
Interstitial	---	---	---
Over Magnesium	1.0	2.45	84°

Au(1 0 0)//MgO(1 0 0)

	Work of Adhesion /Jm^{-2}	Metal-Oxide Separation / Å	Contact Angle
Over Oxygen	2.2	2.29	130°
Interstitial	1.9	2.26	117°
Over Magnesium	1.5	2.44	102°

$\sigma_{MgO(1\,0\,0)} = 1.16\ Jm^{-2}$ (calculated)

$\sigma_{Ag(1\,0\,0)} = 1.59\ Jm^{-2}$ (Wawra 1975)

$\sigma_{Au(1\,0\,0)} = 1.63\ Jm^{-2}$ (Ercolessi 1987)

ions of the MgO.

The results suggest that the most stable configuration is with the silver over the oxygen positions, in accordance with the results of Schonberger and Anderson (1992) who calculated energies of the MgO(100)//Ag interface using a linearized Muffin Tin Orbital Method. These detailed electronic calculations give predictions about the electronic density of states at the interface, in addition to the detailed geometry and interfacial energies. Furthermore our calculated value of the wetting angle (126°) is in excellent agreement with the measured value of 139° (Kingery 1976).

8.4.3 The Au(100)//MgO(100) interface

As with the Ag(100)//MgO(100) interfaces, three configurations were considered for the Au(100)//MgO(100) interfaces. The results are given in table 8.5.

The most stable configuration is with the gold ions accommodating positions above the oxygen sublattice of the MgO. For this configuration the interfacial distance is 2.29Å with a contact angle of 130°, therefore showing a similarity with the Ag(100)//MgO(100) interface. This is not surprising since the image terms for the two interfaces are identical and the short range potentials are comparable.

8.4.4 The Au(110)//MgO(110) Interface

There are several interfacial configurations the Au(110)//MgO(110) can adopt, four of these are illustrated in figure 8.4. These four systems were relaxed and the results are summarised in table 8.6. The contact angles for all these systems were calculated to be less than 90° and therefore the metal is not expected to spread over the surface of the MgO therefore suggesting island formation.

Table 8.6 Calculated work of adhesion, interfacial separation and contact angles after relaxation, for the Au(1 1 0)//MgO(1 1 0) interface for four initial configurations (figure 8.4).

Au(1 1 0)//MgO(1 1 0)

Interface Type (fig 8.4)	Work of Adhesion /Jm^{-2}	Metal-Oxide Separation / Å
A (Over Magnesium)	2.9	1.69
B (Over Oxygen)	2.1	2.14
C (Over Oxygen)	1.5	1.87
D (Over Magnesium)	1.2	2.29

$\sigma_{MgO(1\,1\,0)} = 2.94\ Jm^{-2}$ (calculated)

$\sigma_{Au(1\,1\,0)} = 1.72\ Jm^{-2}$ (Ercolessi 1987)

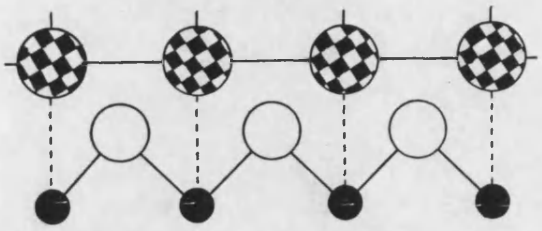

Over Magnesium Ions

A

Over Oxygen Ions

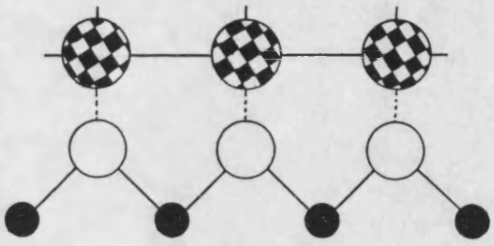

B

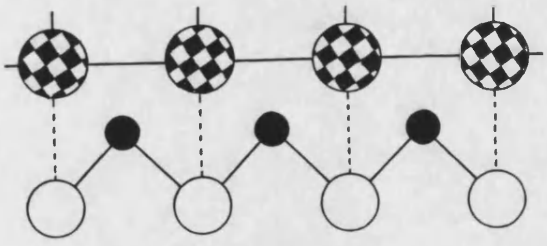

Over Oxygen Ions

C

Over Magnesium Ions

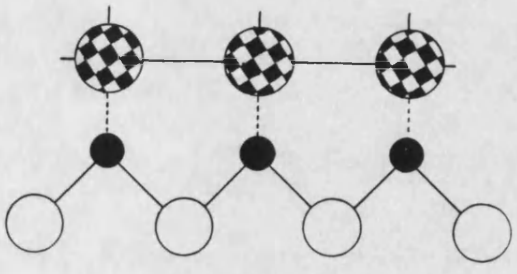

D

Figure 8.4 Four configurations of the Au(1 1 0)//MgO(1 1 0) interface. Gold is represented by the large patterned balls, magnesium ions are the small filled balls and oxygens are the open balls.

The interfacial stability for the Au(110)//MgO(110) interface is calculated to be 2.9 Jm^{-2}, with an interfacial separation of 1.69Å. This compares to 2.2 Jm^{-2} for the Au(100)//MgO(100) interface with an interfacial separation of 2.29 Å, suggesting the (110) interfaces are more tightly bound than the (100) interfaces in accordance with the work of Duffy et al. (1992)

8.4.5 The Au(111)//MgO(111) Interface

The Au(111)//MgO(111) interface is much more difficult to simulate than the (100) or (110) interfaces as the MgO(111) is a dipolar or type 3 surface (see chapter 4). To enable the (111) interface to be modelled, the dipole in the repeat unit perpendicular to the surface was removed by transferring half the magnesium ions from the top of the MgO surface to the bottom surface of the crystal (figure 8.5). The interface was then constructed by placing the gold on top of the MgO(111) surface. For the Au(111)//MgO(111) interface various interfacial configurations can be constructed, however the minimisation persisted in locating a certain configuration from whatever starting or initial configuration was imposed on the interface.

Figure 8.6 shows diagrammatically the relaxed structure of the Au(111)//MgO(111) interface. Figure 8.6a is a side view of the interface and figure 8.6b is a view looking normal to the interface (only 1 gold layer is shown in this view for clarity).

The interfacial stability of the Au(111)//MgO(111) interface was calculated to be 1.81 Jm^{-2} with an interfacial separation 0f 2.06 Å. The surface energy of the MgO(111) was calculated to be 4.01 Jm^{-2} (σ_o) and the surface energy of the Au(111) is given by Ercolessi et al. (1987) as 1.44 Jm^{-2} (σ_m). From this data the contact angle is calculated to

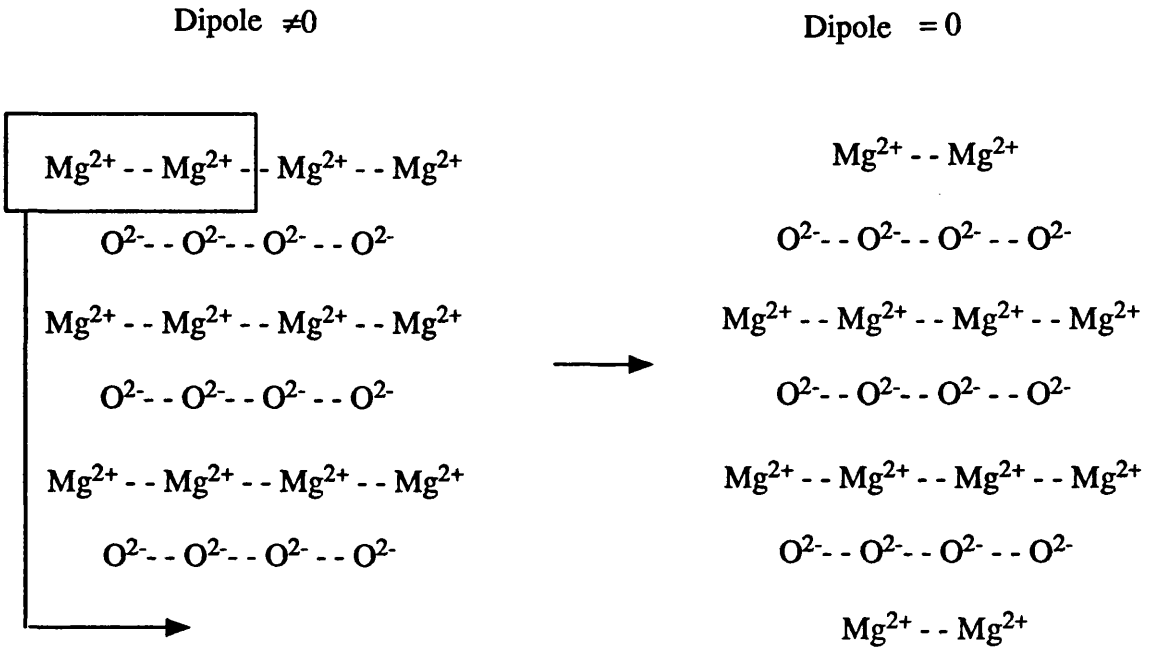

Figure 8.5 MgO(1 1 1) surfaces with half the magnesium ions transferred from the surface magnesium plane to the bottom of the crystal enabling the formation of a stable type 2 surface (Tasker 1979).

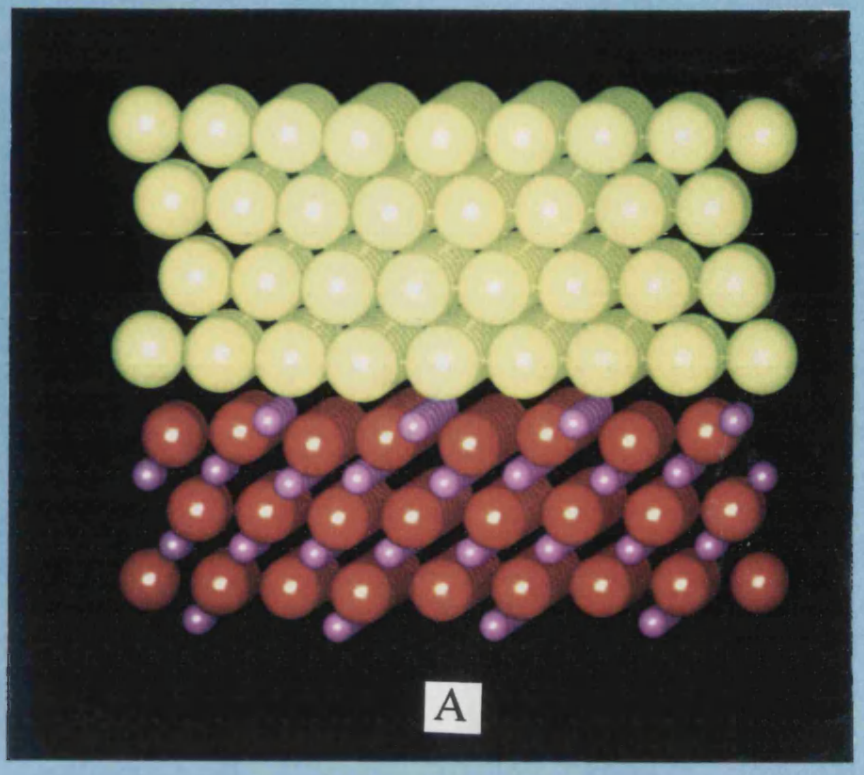
A

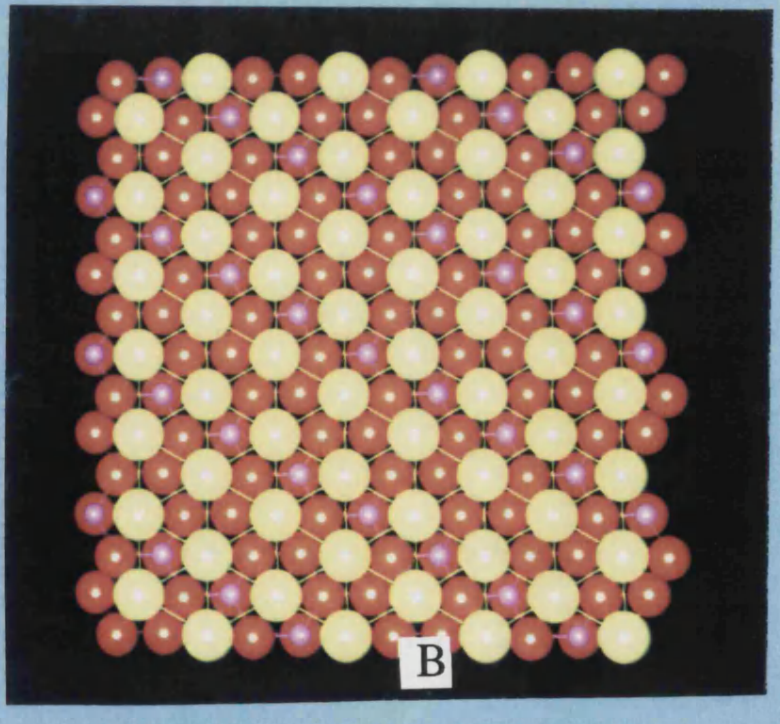
B

be less than 90° and therefore the metal is not expected to spread over the surface of the MgO.

8.5 Summary

In summary we have shown that the image terms provide an excellent representation of the long range Coulombic interactions across the interface for oxide - oxide interfaces if the image plane is located at the first atomic plane of the second material. The detailed ionic displacements of ions at the interface are not however correctly described when the image terms are employed to replace the Coulombic terms. This is perhaps not too surprising as we have discarded detail of the atomic arrangements and moved to a continuum approach.

In simulating the metal - oxide interface, the repulsive interactions between the metal and the oxide are too strong for the image terms to balance, when the image plane is located at the first atomic plane of the second material. Positioning of the image plane equidistance between the termination of the two materials at the interface regions results in the image interactions being too strong to be balanced by the repulsive interactions between the metal and the oxide and the metal ions are observed to relax into the surface of the MgO substrate.

A solution to this problem was obtained by introducing modified image terms. This was facilitated by ensuring that the maximum image term is equal to the inner potential of the metal, which can be calculated as the sum of the Fermi energy of the metal and the work function of the specific metal plane which is to be interfaced. This effectively screens the image terms and the image terms can be balanced by the repulsive interactions between the metal and the oxide.

The calculated contact angle for the Ag(100)//MgO(100) interface using the modified image terms is found to be in excellent agreement with the experimentally observed value. Furthermore the most stable configuration is found to be with the silver over the oxygen ions of the MgO substrate in agreement with recent detailed electronic calculations.

Conclusion

This thesis has been concerned with the application of atomistic computer simulation to the study of heteroepitaxial interfaces. The primary aim has been to develop a procedure such that any two oxides can be routinely examined using the simulation techniques available.

In chapter 4, the BaO//MgO interface was considered as a model system representative of a heteroepitaxial interface. The defect calculations on this interface showed that the vacancies are not defects in some ideal structure, but are identified as an integral part of the low temperature interface configuration.

In chapter 5, interfaces between materials adopting the perovskite structure were considered. Unlike the rocksalt {001} surfaces, the perovskite {001} surfaces offer two planes which may terminate the crystal at the interface. The calculations on $SrTiO_3$ and $BaTiO_3$ showed that the interfaces with the TiO_2 plane terminating the crystal at the interface region resulted in the most stable interfaces.

The interfacial stability was found to depend heavily on the misfit between the two materials determined from the bulk lattice parameters of the two materials. For a monolayer in 'free space', the material adopts a lower lattice parameter than in the bulk material therefore for thin film interfaces, the 'contracted' lattice parameter of the material as opposed to the bulk lattice parameter must be considered to calculate the misfit between the two materials. Furthermore, the substrate material must exhibit its natural bulk lattice parameter with the overlayer accommodating the full misfit. For bulk interfaces, the accommodation of the misfit is associated with a **local** expansion and contraction of the two materials. Far from the interface into the bulk crystals, the materials adopt their natural lattice parameter and therefore a strain gradient is

introduced into the interface system. This has also been observed experimentally for the Co-Cu interfaces. The discrepancy between the coefficients of linear expansion of the two materials may enable a perfect match (no misfit) at a certain temperature. However the calculations have shown that cracks may form on returning to a lower temperature.

In chapter 6, a coincidence site lattice theory is employed, to identify alternative interfacial configurations, based purely on geometrical considerations. This theory, coupled with the atomistic simulation techniques, has enabled accurate predictions of the occupation levels for MgO(100)//MgO(100) twist grain boundaries. Defects were found to stabilise these interfaces, giving further evidence that defects are an integral part of the low temperature interface structure.

Near coincidence site lattice theory was employed to investigate the BaO thin film formation on an MgO(1 0 0) substrate. For interfaces with a positive misfit (the BaO must be expanded), the BaO was seen to form islands on the MgO surface, with the BaO adopting its natural lattice spacing within these islands. For interfaces with negative misfits (BaO artificially compressed to accommodate the misfit), the BaO overlayer was observed to corrugate, facilitating a reduction in the 2-dimensional surface area (from which it would naturally adopt), to accommodate the misfit strain energy.

The value of the misfit was found to almost dominate the resulting stability of the interface, with interfaces with low misfits being the most stable. This suggests that the interfacial stability may be predicted on purely geometrical criterion. However, at very low misfits < 2%, other factors contribute to the stability, such as relaxation and ionic interactions at the interface. High planar densities of coincidence sites (Σ_p) and low rotational angles were also observed to be conducive to the interfacial stability. However, these factors are a consequence of the ionic positions at the interface and are

therefore treated explicitly within the atomistic simulation.

In chapter 7, a superconducting thin film of $YBa_2Cu_3O_{6.5}$ was interfaced to an MgO substrate. The effect of the relaxation was to modify several Ba-O and Cu-O bond lengths in the $YBa_2Cu_3O_{6.5}$ with severe implications to the superconducting properties of the material.

Finally in chapter 8, we have found that the image terms provide an excellent representation of the long range Coulombic interactions within the oxide-oxide interface. For the metal-oxide interface, the image terms are too strong to balance the repulsive forces across the interface and therefore the image terms were screened. This screening was facilitated by ensuring that the maximum image term is smaller or equal to the sum of the Fermi energy and work function of the metal. The application of this modified image term enabled an excellent agreement between the calculated and experimentally measured value of the contact angle between the Ag(100)//MgO(100) interface.

To conclude, the work described in this thesis shows that computer simulation can be successfully employed to study interfaces at the atomic level of both the oxide-oxide and metal-oxide interfaces. Furthermore the work has enabled a systematic investigation of simulating the interface between two oxide materials to be made. This procedure is detailed in figure C1 and briefly outlined below.

(1) TWO MATERIALS: Obtain potential models for the two materials to be interfaced, to correctly describe their crystal properties.

(2) OVERLAYER CONTRACTION: for thin film interfaces with n overlayers on the substrate material, calculate the lattice contraction of the overlayer for a block of n layers.

(3) NCSL THEORY: Using the bulk lattice parameter of the substrate and the contracted lattice parameter of the overlaying materials, calculate and construct interfaces using a near coincidence site lattice theory. The misfit must be fully accommodated by the overlaying material only.

(4) POTENTIAL ENERGY SURFACES: Calculate the potential energy surface of the overlayer on the substrate to ascertain the starting configuration prior to relaxation.

(5) MINIMISATION: Perform a full energy minimisation on the interface to obtain the interfacial stability for **n** overlayers.

DEFECTS/REDUCED DENSITY: Include defects to identify whether the interfacial stability is increased and repeat procedural from step 4.

(6) N+1 LAYERS: Increase the thickness of the thin film to obtain the interfacial stability of n+1 layers and repeat procedure from step 3.

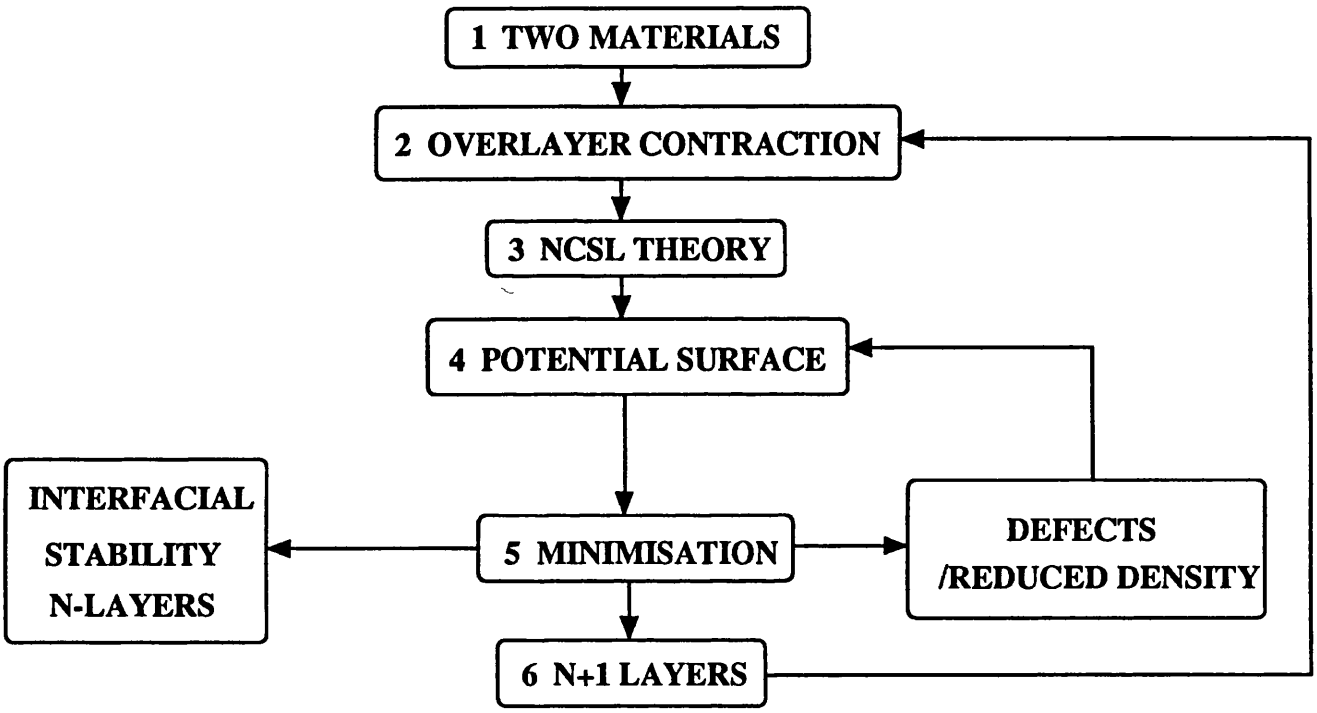

Figure C1 Systematic procedure outlining the various steps to investigate the interface between two oxide materials.

References

B.J. Alder, T.W. Wainwright, J. Chem. Physics, **31** (1959) 459.

N.L. Allan, P.R. Kenway, W.C. Mackrodt, S.C. Parker, J. Phys.: Condens. Matter. **1** (1989a) SB119.

N.L. Allan, W.C. Mackrodt, J. Chem. Soc., Faraday Trans. 2 **85**(5) (1989b) 385.

S. Amelinckx, G. Van Tendeloo, J. Van Landuyt, Supercond. Sci. Technol. **4** (1991) S19.

A. Atkinson, R.I. Taylor, Phil. Mag. A, **39** (1979) 581.

A. Atkinson, R.I. Taylor, J. Phys. Chem. Solids, **47** (1986) 315.

R.C. Baetzold, Phys. Rev. B. **38** (1988) 11,304.

R.C. Baetzold, Phys. Rev. B. **42** (1990a) 56.

R.C. Baetzold, J. Am. Ceram. Soc. **73** (1990b) 3185.

R.C. Baetzold, Physica C **181** (1991) 252.

O.M. Bakunin, S.M. Klotsman, S.A. Matveev, K.A. Stepanov, Appl. Phys. Lett., **55** (1989) 78.

R.W. Balluffi, A. Brokman, A.H. King, Acta. Metall., **30** (1982) 1453.

M.A. Beno, L. Soderholm, D.W. Capone, D.G. Hinks, J.D. Jorgensen, I.K. Schuller, C.U. Segre, K. Zhang, J.D. Grace, Appl. Phys. Lett. **50** (1987) 1688.

A.B. Berezin, C.W. Yuan, A.L. de Lozanne, Appl. Phys. Lett. **57** (1990) 90.

F. Bertaut, Compt. Rendu., **246** (1958) 3447.

G.Binning, C.F. Quate, Phys. Rev. Lett., **56** (1986) 930.

G.Binnig, CH. Gerber, E.Stoll, T.R.Albrecht, C.F. Quate, Europhys. Lett., **3** (1987) 1281.

P. Blochl, G.P. Das, H.F. Fischmeister, U. Schönberger. "Metal-Ceramic Interfaces". (Ed. M. Ruhle, A.G. Evans, M.F. Ashby, J.P. Hirth) Oxford, Pergamon Press. p9, 1989.

G.E. Blumberg, E.M. Fefer, T. Fimberg, E. Joon, A. Laht, R. Stern, L.A. Rebane, Sol. St. Comm., **70** (1989) 647.

W. Bollmann, "Crystal Defects and Crystalline Interfaces." Springer, Berlin (1970).

M. Born, K. Hwang, "Dynamical theory of crystal lattices" (Oxford university press 1954).

D.G. Brandon, B.Ralph, S. Ranganathan, M.S. Wald, Acta. Metall., **12** (1964) 813.

L.A. Bursill, X.D. Fan, Phys. Stat. Sol., **107** (1988) 503.

W.R. Busing, Acta. Crystallogr. A **28** (1970) 252.

R. Car, M. Parrinello, Phys. Rev. Lett., **55** (1985) 2471.

C.R.A. Catlow, W.C. Mackrodt (eds.), Lecture Notes in Physics, **166** (1982).

C.R.A. Catlow, Ann. Rev. Mater. Sci., **16** (1986) 517.

C.R.A. Catlow, C.M. Freeman, B. Vessal, S.M. Tomlinson, M. Leslie, J. Chem. Soc. Faraday Transactions, **81** (1991) 1947.

R.J. Cava, A.W. Hewat, E.A. Hewat, B. Batlogg, M. Marezio, K.M. Rabe, J.J. Krajewski, W.F. Peck, L.W. Rupp, Physica C**165** (1990) 419.

M. Causer, Surf. Sci., **175** (1986) 551.

C.C. Chang, X.D. Wu, R. Ramesh, X.X. Xi, T.S. Ravi, T. Venkatesan, D.M. Hwang, R.E. Muenchausen, S. Foltyn, N.S. Nogar, Appl. Phys. Lett., **57** (1990) 1814.

C.H. Chen, J. Kwo, M.Hong, Apll. Phys. Lett., **52** (1988) 841.

E.A. Colbourn, W.C. Mackrodt, Physica **131B** (1985) 41.

L. Cota, L. Morales de la Garza, G. Hirata, L. Martinez, E. Orozco, E. Carrillo, A. Mendoza, J.L. Albarran, J. Fuentes-Maya, J.L. Boldu, J.G. Perez-Ramierez, R. Perez, R.Reyes Gasga, M. Avalos, M. Jose-Yacaman, J. Mater. Res. **3** (1988) 417.

M. Cotter, S. Campbell, R.G. Egdell, W.C. Mackrodt, Surf. Sci., **197** (1988) 208.

M. Cotter, S. Campbell, L.L. Cao, R.G. Egdell, W.C. Mackrodt, Surf. Sci., **208** (1989) 267.

K. Le Dang, P. Veillet, Phys. Rev. B **41** (1990) 12902.

W.C. Davidson, AEC Report, ANL-5990 (Rev) (1959).

M.J. Davies, P.R.Kenway, P.J.Lawrence, S.C. Parker, W.C. Mackrodt, P.W. Tasker, J. Chem. Soc. Faraday Trans. 2 **85** (1989) 555.

B.G. Dick, A.W. Overhauser, Phys. Rev. **112** (1958) 90.

D.Dimos, P.Chaudhari, J. Mannhart, F.K. Legouse, Phys. Rev. Lett., **61** (1988) 1653.

D.Dimos, P.Chaudhari, J. Mannhart, Phys. Rev. B, **41** (1990) 4038.

D.M. Duffy, P.W. Tasker, Harwell Report, AERE-TP953 (1982).

D.M. Duffy, P.W. Tasker, Harwell Report, AERE-R11059 (1983a).

D.M. Duffy, P.W. Tasker, Phil. Mag. A, **47** (1983b) 817.

D.M. Duffy, J. Hoare, P.W. Tasker, J. Phys. C: Solid State Phys., **17** (1984) L195.

D.M. Duffy, J. Phys. C: Solid State Phys., **19** (1986) 4393.

D.M. Duffy, J.H. Harding, A.M. Stoneham, Acta Metallurgica 1992 in press.

C. Duriez, C. Chapon, C.R. Henry, J.M Rickard, Surf. Sci. **230** (1990) 123.

O. Eibl, H.E. Hoenig, J.-M. Triscone, Ø. Fischer, L. Antognazza, O. Brunner, Physica C, **172** (1990a) 365.

O. Eibl, H.E. Hoenig, J.-M. Triscone, Ø. Fischer, L. Antognazza, O. Brunner, Physica C, **172** (1990b) 373.

F. Ercolessi, A. Bartolini, M. Garofalo, M. Parrinello, E. Tosatti, Surf. Sci., **189/190** (1987) 636.

P.P. Ewald, Ann. Physik, **64** (1921) 253.

I.D. Faux, J. Phys. C **4** (1971) L211.

M.W. Finnis, Surface Science, **241** (1991) 61.

M.W. Finnis, Acta. Met. in press (1992).

P. Fischer, J. Karpinski, E. Kaldis, E. Jilek, S. Rusieki, Sol. St. Comm. **69** (1989) 531.

R. Fletcher, M.J.D. Powell, Computer J., **6** (1963) 16.

P.W. Fowler, P.A. Madden, Mol. Phys., **49** (1983) 913.

A.J. Freeman, C. Li, C.L. Fu, "Metal-Ceramic Interfaces" (ed. M. Ruhle, A.G. Evans, M.F. Ashby, J.P. Hirth) Oxford, Pergamon Press p2, 1989.

Y. Fujiwara, S. Hirata, M. Iyori, T. Kobayashi, Solid State Communications, **74** (1990) 641.

Y. Gao, P. Shewmon, S.A. Dregia, Scripta Metallurgica, **22** (1988) 1521.

F.H. Garzon, I.D. Raistrick, in "Chemistry of electonic materials", Proc. Int. Conf., 17-22 Aug 1990, Natl. Inst. Standards Technol. Spec. Publ. **804** (1991) 373.

M.J. Gillan, M.J. Dixon, J. Phys. C, **13** (1980) 1901.

M.J. Gillan, Physica, **131B** (1985) 157.

R.G. Gordon, Y.S. Kim, J. Chem. Phys., **56** (1972) 3122.

H. Grimmer, W. Bollmann, D.H. Warrington, Acta. Cryst., **30** (1974) 197.

R. Gronsky, National Centre for Electron Microscopy, Lawrence Berkeley Laboratory.

R.O.A. Hall, M.J. Mortimer, D.A. Mortimer, Report AERE-R 11774 (1985)

C.A. Handwerker, M.D. Vaudin, J.E. Blendell, Journal De Physique, C5 **49** (1988) 367.

J.H. Harding, A.H. Harker, Harwell report, AERE-R10425 (1982).

J.H. Harding, Harwell Report, AERE-R14300 (1988).

J.H. Harding, Rep. Prog. Phys., **53** (1990) 1403.

J.H. Harding, Private Communication 1991.

T. Hasegawa, K. Kishio, M. Aoki, N. Ooba, K. Kitazawa, K. Fueki, Jap. J. Appl. Phys. **26** (1987) L337.

V.E. Henrich, Rep. Prog. Phys. **48** (1985) 1481.

A.W. Hewat, P Fischer, E. Kaldis, J. Karpinski, S. Rusiecki, E. Jilek, Physica C **167** (1990) 579.

Z. Hiroi, M. Takano, Y. Takeda, R. Kanno, Y. Bando, Jpn. J. Appl. Phys. **27** (1988) L580.

S. Horn, J. Cai, S.H. Shaheen, Y. Jeon, M. Croft, C.L. Chang, M.L. denBoer, Phys. Rev., B **36** (1987) 3985.

D.M. Hwang, T.S. Ravi, R.Ramesh, Siu-Wai Chan, C.Y. Chen, L. Nazar, X.D. Wu, A. Inam, T.Venkatesan, Appl. Phys. Lett. **57** (1990) 1690.

M.S. Islam, R.C. Baetzold, Phys. Rev. B. **40** (1989) 10,926.

M.S. Islam, Supercond. Sci. Technol. **3** (1990) 531.

M.S. Islam, C. Ananthamohan, Phys. Rev. B. **44** (1991) 9492.

R. James, PhD Thesis, University College, London (1978).

P.W. Jennings, R.O. Jones, Advances in Physics, **37** (1988) 341.

D.C. Johnston, J.P. Stokes, D.P. Goshorn, T.J. Lewandowski, Phys. Rev., **36** (1987) 4007.

J.D. Jorgensen, B.W. Veal, A.P. Paulikas, L.J. Nowicki, G.W. Crabtree, H. Claus, W.K. Kwok, Phys. Rev. B. **41** (1990) 1863.

J.D. Jorgensen, Physics Today, **44** (1991) 34.

P.R. Kenway, S.C. Parker, W.C. Mackrodt, Molecular Simulation, **4** (1989) 175.

P.R. Kenway, PhD Thesis, University of Bath (1991).

R. Kern, Crystal growth in science and technology, Ed. H. Arend, J. Hullinger (NATO ASI series, NY plenum) pp143-169 (1989).

W.D. Kingery, H.K. Bowen, D.R. Uhlmann, "Introduction to Ceramics", Wiley, New York, (1976).

C. Kittel, "Introduction to Solid State Physics", Sixth edition, Pub. J. Wiley & Sons Inc. (1989).

J. Kondo, J. Phys. Soc. Jpn. **59** (1990) L819.

E. Kotomin, A.Schluger, M.Causa, R.Dovesi, F.Ricca, Surf. Sci., **232** (1990) 399.

S.A. Kramer, G. Kordas, J. McMillan, G.C. Hilton, D.J. Van Harligen, Appl. Phys. Lett. **53** (1988) 156.

J. Kwo, T.C. Hseih, R.M. Fleming, M. Hong, S.H. Liou, B.A. Davidson, L.C. Feldman, Phs. Rev. B, **36** (1987) 4039.

A. Lamagna, S. Nicoletti, M. Sanchez Balmaseda, A. Migliori, R. Fabbri, L. Correra, Supercond. Sci. Technol., **5** (1992) 117.

N.D. Lang, W. Kohn, Phys. Rev. B. **1** (1970) 4555.

D. Larbalestier, Physics Today, **44** (1991) 74.

P.J. Lawrence, PhD Thesis, University of Bath (1988)

V.B. Lazarev, K.S. Gavrichev, V.E. Gorbunov, J.H. Greenberg, P.Z. Slutskii, Ju.G. Nadtochii, I.S. Shaplygin, Thermochim. Acta, **174** (1991) 27.

F.K. LeGoues, Phil. Mag. B., **57** (1988) 167.

M. Leslie, SERC Daresbury Report, DL/SCI/TM31T (1982), SERC Daresbury Laboratory, UK.

G.V. Lewis, C.R.A. Catlow, Radiation Effects, **73** (1983) 307.

G.V. Lewis, C.R.A. Catlow, R.E.W. Casselton, J. Am. Ceram. Soc., **68** (1985a) 555.

G.V. Lewis, Physica **131B** (1985b) 114.

G.V. Lewis, C.R.A. Catlow, J. Phys. C. **18** (1985c) 1149.

D.J. Li, J.P. Zhang, J.P. Thiel, L.D. Marks, J. Sol. St. Chem., **81** (1989a) 165.

Q. Li, O. Meyer, X.X. Xi, J. Geerk, G. Linker, Appl. Phys. Lett., **55** (1989b) 310.

A.B. Lidiard, M.J. Norgett, "Computational Solid State Physics", Eds. F. Hermann, N.W. Dalton, T.R. Koehler (Plenum, NY, 1972) pp385.

S.M.P. Lyddane, A. Herzfield, Phys. Rev. **54** (1958) 846.

W.C. Mackrodt, J. Chem. Soc. Farad. Trans. 2., **85** (1989a) 541.

W.C. Mackrodt, Supercond. Sci. Technol. **1** (1989b) 343.

Y. Maeno, M. Kato, Y. Aoki, T. Nojima, T. Fujita, Physica B. **148** (1987) 357.

G.D. Mahan, Solid state ionics, **1** (1980) 29.

P.A. Makasym, Surf. Sci. **149** (1985) 157.

M. Matsui, K. Yamamoto, M. Nakajima, T. Shimano, H. Matsuba, Supercond. Sci. Technol. **5** (1992) S427.

P.F. Miceli, J.M. Tarascon, L.H. Greene, P. Barboux, F.J. Rotella, J.D. Jorgensen, Phys. Rev. B **37** (1988) 5932.

S. Miraglia, F. Beech, A. Santoro, D. Tran Qui, Mat. Res. Bull., **22** (1987) 1733.

B.H. Moeckly, S.E. Russek, D.K. Lathrop, R.A. Buhrman, M.G. Norton, C.B. Carter, Appl. Phys. Lett. **57** (1990) 2951.

I. Monot, M. Lepropre, J. Provost, H. Hervieu, G. Desgardin, B. Raveau, Supercond. Sci. Technol., **5** (1992) 60.

N.F. Mott, M.J. Littleton, Trans. Faraday Soc. **34** (1938) 485.

J.H. Muller, W. Mertin, R.Gruehn, Supercond. Sci. Technol. **3** (1990) 273.

H. Mykura, P.S. Bansal, M.H. Lewis, Phil. Mag. **A42** (1980) 225.

Y. Nakazawa, M. Ishikawa, Physica C **158** (1989) 381.

J. Narayan, S. Sharan, R.K. Singh, K. Jagannadham, Mater. Sci. Eng., **B2** (1989) 333.

M. Needels, M.C. Payne, J.D. Joannopoulos, Phys. Rev. Lett., **58** (1987) 1765.

M.J. Norgett, A.B. Lidiard, Phil. Mag., B **18** (1968) 1193.

M.J. Norgett, J. Phys. C, **4** (1971) 298.

M.J. Norgett, Harwell Report AERE-R7015 Unpublished (1972).

M.J. Norgett, Harwell Report AERE-R7650 Unpublished (1974).

E. Olsson, A. Gupta, M.D. Thouless, A. Segmüller, D.R. Clarke, Appl. Phys. Lett. **58** (1991) 1682.

H. K. Onnes, Akad. van Wetenschappen (Amsterdam) **14**, 113 (1911) 818.

S.C. Parker, G.D. Price, NATO A.S.I. Series C, **225** (1988) 591, (Ed. E.K.H. Salje), D. Reidel Publ. Company, Dordrecht.

D.E. Parry, Surf. Sci., **49** (1975a) 433.

D.E. Parry, Surf. Sci., **54** (1975b) 195.

M.C. Payne, P.D. Bristowe, J.D. Joannopoulos, Phys. Rev. Lett. **58** (1987) 1348.

S.D. Pickett, A.K. Nowak, J.M. Thomas, B.J. Peterson, J.F.P. Swift, A.K. Cheetham, C.J.J. den Ouden, B. Smit, M.F.M. Post, J. Phys. Chem., **94** (1990) 1233.

R.C. Pond, D.A. Smith, Scripta Metall., **11** (1977) 77.

G.D. Price, S.C. Parker, M. Leslie, Phys. Chem. Minerals, **15** (1987) 181.

A. Rahman, "Fast Ion Transport in Solids" (Ed. Vashishta, Mundy, Shenoy) Elsevier, North Holland, pp643 (1979).

R. Ramesh, D. Hwang, T.S. Ravi, A. Inam, J.B. Barner, L.Nazar, S.W. Chan, C.Y. Chen, B. Dutta, T. Venkatesan, X.D. Wu, Appl. Phys. Lett., **56** (1990) 2243.

T.S. Ravi, D.M. Hwang, R. Ramesh, S.W. Chan, L. Nanar, C.Y. Chen, A. Inman, T. Venkatesan, Phys. Rev. B **42** (1990) 10,141.

W.T. Read, W. Schottky, Phys. Rev., **78** (1950) 275.

M. Ruhle, Proceedings of an international workshop, Santa Barbera, California U.S.A. 16-18 Jan 1989a, Ed. M. Ruhle, A.G. Evans, M.F. Ashby, J.P. Hirth., Pub, Pergamon Press.

M. Ruhle, A.H. Evans, Mat. Sci. Eng. **A107** (1989b) 187.

K.H. Reider, Surf. Sci. **118** (1982) 57.

M.J.L. Sangster, A.M. Stoneham, Phil. Mag. **43** (1980) 597.

A. Santoni, D.B. Tran Thoai, J. Urban, Solid State Communications **68** (1988) 1039.

M. Sautter, H. Gliter, G. Bäro, Acta. Metall., **25**, (1977) 467.

U. Schonberger, O.K. Andersen, Acta. Met. in Press (1992).

M.W. Shafer, T. Penney, B.L. Olson, Phys. Rev. B **36** (1987) 4047.

H. Shaked, J.D. Jorgensen, J. Faber, D.G. Hinks, B. Dabrowski, Phys. Rev. B **39** (1989) 7363.

R. Simon, Physics Today, **44** (1991) 64.

A.W. Sleight, Physics Today, **44** (1991) 24

D.A. Smith, R.C. Pond, Int. Metall. Rev., **205** (1976) 61.

C.P. Sun, R.W. Balluffi, Phil. Mag., **A46** (1982a) 49.

C.P. Sun, R.W. Balluffi, Phil. Mag., **A46** (1982b) 63.

A.P. Sutton, R.W. Balluffi, Acta. Metall., **35** (1987) 2177.

A.M. Stoneham, P.W. Tasker, From: "Ceramic Microstructures '86" Ed. A. Joseph, A. Pask, A.G. Evans. pp155-165. Plenum Publishing Corporation (1986).

A.M. Stoneham, P.W. Tasker, Phil. Mag. B., **55** (1987) 237.

A.M. Stoneham, P.W. Tasker, Journal de Physique, C5 **49** (1988) C5-99.

J. Talvacchio, G.R. Wagner, H.C. Pohl, Physica **C162** (1989) 659.

T. Takabatake, M. Ishikawa, Y. Nakazawa, K. Koga, Physica C **152** (1988) 424.

S. Tanaka, H. Nakanishi, K. Higaki, H. Itozaki, Jap. J. Appl. Phys., **29** (1990) 1059.

J.M. Tarascon, P. Barboux, P.F. Miceli, L.H. Greene, G.W. Hull, M. Eibschutz, S.A. Sunshine, Phys. Rev. B **37** (1988) 7458.

P.W. Tasker, Harwell Report, AERE-R9130 (1978).

P.W. Tasker, J. Phys. C: Solid State Phys., **12** (1979) 4977.

P.W. Tasker, E.A. Colbourn, W.C. Mackrodt, J. Am. Ceram. Soc., **68** (1985) 74.

P.W. Tasker, A.M. Stoneham, Journal de Chemie Physique., **84** (1987) 149.

J.O. Titiloye, S.C. Parker, D.C. Sayle, F.S. Stone, C.R.A. Catlow, Studies in Surface Science and Catalysis **52** (1989) 271.

J.O. Titiloye, S.C. Parker, D.J. Osguthorpe, S. Mann, J. Chem. Soc. Chem. Commun., **20** (1991) 1494.

Y. Tokura, J.B. Torrance, T.C. Huang, A.I. Nazzal, Phys. Rev. B **38** (1988) 7156.

S.-Tong Lee, S. Chen, L.S. Hung, G. Braunstein, Appl. Phys. Lett. **55** (1989) 286.

P. Tschaufeser, PhD Thesis, University of Bath, (1992).

P. Tschaufeser, Private Communication.

L.E.C. Van De Leemput, P.J.M. Van Bentum, L.W.M. Schreus, H. Van Kempen, Physica C **152** (1988) 99.

B.W. Veal, A.P. Paulikas, J.W. Downey, H. Claus, K. Vandervoort, G. Tomlins, H. Shi, M. Jensen, L. Morss, Physica C **162** (1989) 97.

Z.Z. Wang, Phys. Rev. B **36** (1987) 7222.

G.W. Watson, S.C. Parker, A. Wall, J. Physics Condensed Matter **4** (1992) 2097.

H. Wawra, Z. Metallkd. **66** (1975) 395.

P.T. Wedepohl, Proc. Phys. Soc., **92** (1967) 79.

M.R. Welton-Cook, W. Berndt, J. Phys. C: Solid state Phys., **15** (1982) 5691.

D. Wolf, R. Benedek, Adv. Ceram., **1** (1981) 107.

D. Wolf, J. Physique Coll., **43** C6 (1982) 45

D. Wolf, Physica, **131B** (1985) 53.

C.P. Wood, N.C. Pyper, Molec. Phys., **43** (1981) 1376.

C.P. Wood, N.C. Pyper, Phil. Trans. A **320** (1986) 71.

A.B. Woods, W. Cochran, B.N. Brockhouse, Phys. Rev. B **119** (1960) 980.

H.W. Zandbergen, R. Gronsky, K. Wang, G. Thomas, Nature **331** (1988) 596.

H.W. Zandbergen, G. Van Tendeloo, T. Okabe, S. Amelinkx, Phys. Stat. Sol., **103** (1987) 45.

J.X. Zhang, G.M. Lin, W.G. Zeng, K.F. Liang, Z.C. Lin, G.G. Siu, M.J. Stokes, P.C.W. Fung, Supercond. Sci. Technol. **3** (1990) 113.

X. Zhang, C.R.A. Catlow, Physica C **193** (1992) 221.